Experimental Evaluation and Control of Two-Phase Multi-Microchannel Evaporator Cooling Systems for High Efficiency Data Center

PAR

Duan WU

ÉCOLE POLYTECHNIQUE
FÉDÉRALE DE LAUSANNE

Suisse
2012

三人行，必有我师焉。

"When I walk along with two others, from at least one I will be able to learn."

−−《论语·述而》

Confucius

Acknowledgements

Working on the Ph.D. has been a wonderful and often overwhelming experience. It is difficult to say whether it has been grappling with the project itself which has been the real learning process, or struggling with how to write papers and reports, stay up running experiments until birds start singing. In any case, I would like to express my deep gratitude to many people for making the time of my Ph.D. precious.

First and foremost I would like to express my sincere acknowledgement in the support and help of my thesis director Prof. Thome, his encouragement, support and fruitful conversation over the past three and half years made my dream become true. Also, I would like to thank my thesis co-director Dr. Marcinichen who had laid out the concrete foundation for my thesis and helped me along my study, his long-lasting trust and warm-hearted guidance will be well kept in my memory.

I would like to thank my jury members, including Prof. Püttgen for having organized my oral exam and shared his open-minded thoughts with me, Prof. Favrat, Prof. Bandarra Filho and Dr. Agostini for their precious time and valuable efforts reading through my thesis carefully and giving me insightful and constructive comments and suggestions to improve the quality of my work.

It is my great pleasure to thank all my LTCM colleagues, with whom I spent many joyful days and wonderful time together, special thanks go to Nathalie Matthey-de-l'Endroit, and Cécile Tavernay for their administrative work with great patience and thoughtful caring, and also to our first assistant Dr. Navid Borhani for his constant help and support; to Jean-Pierre Bougnon and Laurent Chevalley for their dedication on building the new

Abstract

Thermal designers of data centers and server manufacturers are showing a greater concern regarding the cooling of the new generation data centers, which consume considerably more electricity and dissipate much more waste heat, a situation that is creating a re-thinking about the most effective cooling systems for the future beyond conventional air cooling of the chips/servers. Potentially, a significantly better solution is to make use of on-chip two-phase cooling, which, besides improving the cooling performance at the chip level while also consuming less energy to drive the cooling process, also adds the capability to reuse the waste heat in a convenient manner, since higher evaporating and condensing temperatures of the two-phase cooling system (from 60-95 °C) are possible with such a new "green" cooling technology. In the present thesis, three such two-phase cooling cycles using micro-evaporation technology were experimentally evaluated with specific attention being paid to (i) controllability of the two-phase cooling system, (ii) energy consumption and (iii) overall exergetic efficiency, with the emphasis on (i). The controllers were evaluated by tracking and disturbance rejection tests, which were shown to be efficient and effective. The average temperatures of the chips were maintained below the upper limit of 85 °C of computer CPU's for all tests evaluated in steady state and transient conditions. In general, simple SISO and SIMO strategies were sufficient to attain the requirements of control. Regarding energy and exergy analyses, the experimental results showed that all these systems can be thermodynamically improved since only about 6% of the exergy supplied is in fact recovered in the condenser in the present setup. Additionally, a series of tests covering a wide range of operating conditions under steady state regime were done. The main idea was to generate a "map of performance" of the different cooling systems in terms of energy consumption, energy recovery at the condenser and heat exchanger

performance. A total of 120 tests were done which considered all combinations of the variables involved. Finally, empirical and semi-empirical correlations for overall thermal conductance and performance of all components and piping of all these systems were developed based on the experimental results obtained, which can be used for simulations and validations of potential codes developed to design and/or evaluate performance of cooling systems. An overall energy balance analysis for each system using the correlations developed showed that 99.17% of the experimental data were bounded within ± 10%.

Keywords: Data center, high performance computers, high heat flux, two-phase on-chip cooling, microevaporator, cooling system, controller, energy recovery.

Résumé

Les concepteurs thermiques et les fabricants de serveurs font preuve de plus en plus de préoccupation en ce qui concerne le refroidissement des centres informatiques de nouvelle génération. Ces centres de donnée consomment en effet de plus en plus d'électricité et dissipent de ce fait de plus en plus de chaleur. Cette situation implique une nouvelle façon de penser les futurs systèmes de refroidissement, au-delà des systèmes conventionnels de refroidissement à air des processeurs/servers. Potentiellement, l'utilisation de systèmes de refroidissement diphasique « on-chip » semble être une solution attrayante. En plus d'améliorer les performances du refroidissement au niveau du processeur en consommant moins d'électricité, ils permettent la réutilisation de la chaleur résiduelle issue des processeurs. De hautes températures d'évaporation et de condensation (de 60 à 95 °C) sont en effet obtenues avec cette technologie « verte » de refroidissement diphasique.

Dans la thèse présentée, trois de ces cycles de refroidissement diphasiques utilisant des micro-évaporateurs ont été testés expérimentalement en accordant une attention particulière à (i) la contrôlabilité du système diphasique, (ii) la consommation d'énergie et (iii) l'efficacité éxergétique globale, en mettant l'accent sur (i). Des tests de suivi et de rejet de perturbation ont permis d'évaluer les contrôleurs qui se sont montrés efficaces et efficient. Les températures moyennes des processeurs ont été maintenues en dessous de la limite maximale de 85 °C (pour CPU d'ordinateur) pour tous les tests que ce soit à l'état stationnaire ou durant les états transitoires. En général, de simples stratégies SISO et SIMO ont été suffisantes pour obtenir la contrôlabilité exigée. En ce qui concerne les analyses énergétiques et éxergétiques, les résultats expérimentaux montrent que ces systèmes peuvent être thermodynamiquement améliorés puisque seulement 6% de l'éxergie apportée au système est récupérée dans le condenseur. En outre, une série de tests

couvrant un large éventail de conditions opératoires à l'état stationnaire a été effectuée. L'idée principale était de générer une «carte de performance» pour les différents systèmes de refroidissement en termes de consommation énergétique, d'énergie récupérée au condenseur et de performances de ce condenseur. Un total de 120 tests considérant toutes les combinaisons possibles des variables impliquées a été réalisé. Finalement, des corrélations empiriques et semi-empiriques pour la conductance thermique globale et les performances de tous les composants (tuyaux inclus) ont été développés sur la base des résultats expérimentaux. Ces corrélations peuvent être utilisées pour la validation de codes potentiels développés pour la conception / évaluation de ces systèmes de refroidissement. Un bilan énergétique global pour chaque système utilisant les corrélations développées montre que 99.17% des données expérimentales sont bornées à ±10% par ces corrélations.

Mots-clés: centre de données, ordinateurs de haute performance, flux de chaleur élevé, refroidissement diphasique « on-chip », micro-évaporateur, contrôleurs, récupération d'énergie.

Contents

List of figures

List of tables

Nomenclature

Rome

A_{SMV}	stepper motor valve aperture, %
b	elemental systematic uncertainty
B	systematic uncertainty
d_i	internal channel diameter, m
EX	exergy, W
g	gravitational acceleration, m/s^2
G	transfer function of the system or mass velocity, kg/(m^2·s)
h	specific enthalpy, kJ/kg
h_i	MME inlet specific enthalpy, kJ/kg
h_o	MME outlet specific enthalpy, kJ/kg
K_C	PI proportional gain
K_I	PI integral gain
K_P	static gain of the system
LPS_C	cooling loop's liquid pump speed, rpm
LPS_W	water loop's liquid pump speed, rpm
$\dot{m}$	mass flow rate, kg/s
N	speed, rpm/s
P_{cond}	condensing pressure, bar
P_i	MME inlet pressure, bar
P_o	MME outlet pressure, bar
q	heat flux, W/m^2
Q_{cond}	heat transfer rate of condenser, W
Q_p	pumping power, W
Q_t	dissipated heat, W

R_{th}	thermal resistance of heat sink, °C/W
T_i	MME inlet temperature, °C
T_I	integral time, s
T_o	dead state temperature, °C
T_{cond}	condensing temperature, °C
UA_{cond}	overall conductance of condenser, W/°C
V_d	dead volume of compressor, m^3
V_{sw}	swept volume of compressor, m^3
v_{dis}	specific volume at discharge line, m^3/kg
v_{suc}	specific volume at suction line, m^3/kg
W_e	Webber number
x_o	MMEs' outlet vapor quality
Z	position of the zero in the complex plan

Greek

α	heat transfer coefficient, W/(m^2·K)
θ	transport delay, s
τ	time constant, s
τ_D	desired closed-loop time constant, s
η_c	cooling cycle efficiency
η_{hr}	heat recovery efficiency
η_{ise}	isentropic efficiency
η_v	volumetric efficiency
ε_{cond}	condenser effectiveness
δ	the annular liquid film thickness, m
ΔT_{cond}	minimum approach temperature, which is the temperature difference between outlet water flow and inlet working fluid flow of the condenser in this thesis, °C
$\Delta \delta$	liquid film wave height, m

κ	isentropic exponent
λ	conductivity, $W/(m\cdot K)$
u_V	the mean velocity of the vapor, m/s
u_{Vo}	the vapor only velocity, m/s
u_L	the mean velocity of the liquid, m/s
u_{Lo}	the liquid only velocity, m/s
ρ_L	liquid density, kg/m^3
ρ_v	vapor density, kg/m^3
Υ_P	pressure ratio

Acronyms

CHF	critical heat flux, W/cm^2
COP	coefficiency of performance
CPU	central processing unit
EEV	electric expansion valves
HL	heat load or heat loss, W
iHEx	internal heat exchanger
LA	liquid accumulator
LS	liquid separator
LPC	liquid pump in the refrigerant cooling loop
LPW	liquid pump in the water loop
LPR	low pressure receiver
MME	multi-microchannel evaporator
MIMO	multiple input multiple output
SMV	stepper motor valve
SIMO	single input multiple output
SISO	single input single output
SEE	the standard error of estimate of a least squares regression or curve fit

VC	vapor compression
VSC	variable stroke/speed compressor

VSC	variable stroke/speed compressor

1 Introduction

Cooling of data centers can represent up to 45% (Koomy 2007) of the total energy consumption using current cooling technologies (air cooling). Currently, data centers consume approximately 2% of the total electricity generated in the US. This relates to an estimated 45 billion kWh usage by 2011 with an annual cost of $3.3 billion, or $648 billion with the inclusion of a carbon tax. And this is just for cooling. This problem is aggravated by the current growth rate of data centers, being between 10-20% per annum, with the US having an annual increase of total electrical generation of approximately 1.5%.

Most data centers make use of air-cooling technologies to ensure the correct running of the servers contained within. Air, however, is a very inefficient source of cooling due to its very low capacity for transporting heat and its low density, both which drive large power requirements. The limits of air-cooling are also being approached due to the power density increase in the microprocessors (CPUs) in the servers, which will have heat fluxes on the order of 100 W/cm^2 in the not too distant future. It was shown that air has a maximum heat removal capacity of about 37 W/cm^2 (Saini and Webb 2003). The problem is made worse with servers being more densely packed, such as blade centers with racks that will be generating in excess of 60 kW of heat, while today's data centers are designed for cooling capacities on the order of 10-15 kW per rack (Samadiani *et al.* 2008). Hence, if data centers want to become green, other solutions rather than air cooling are required.
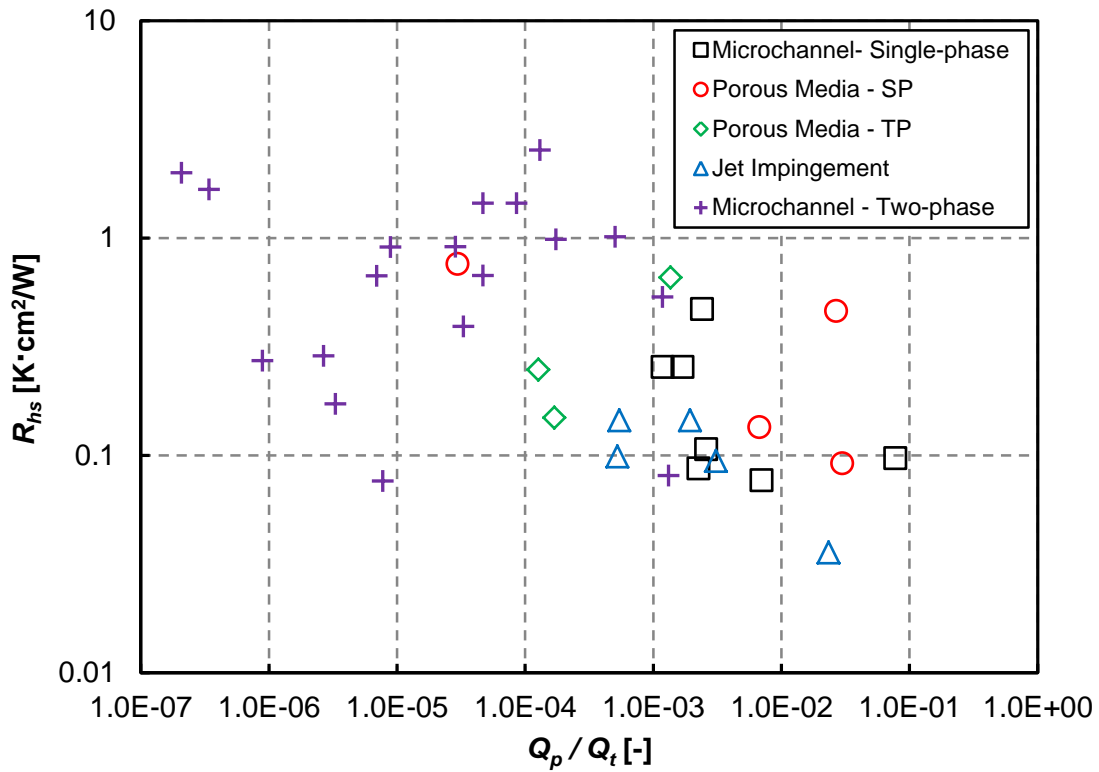
Figure 1.1 Thermal resistance of heat sinks (R_{hs}) for diverse cooling technologies versus the ratio of the pumping power (Q_p) and the dissipated heat (Q_t) (Agostini *et al.* 2007)

One long-term solution is to go to direct on-chip cooling. Recent publications show the development of primarily four competing technologies for on-chip cooling: microchannel single-phase flow, porous media flow, jet impingement and microchannel two-phase flow. Leonard and Phillips (2005) showed that the use of such new technology for cooling of chips could produce savings in energy consumption of over 60%. Agostini *et al.* (2007) highlighted that the most promising of the four technologies was microchannel two-phase cooling, where Figure 1.1 shows the heat sink thermal resistances for diverse cooling technologies as a function of the pumping power to the dissipated thermal power ratio. Using this criterion, the best heat sink solution should be that nearest the lower left corner because it represents the lowest thermal resistance at the lowest pumping power of the cooler (*attention*: not the pumping power of the entire cooling system). It is clear that two-phase microchannel cooling is the best performing technology in this confrontation from this perspective.

The current thesis aims mainly at studying two-phase electronic cooling systems which utilize multi-microchannel evaporators to cool high heat flux microprocessors and are driven by a liquid pump or a variable stroke compressor or both together. An integrated experimental facility has been built at LTCM which consists of these three independent cycles. The main objectives of this thesis are to answer the following questions:

- What kinds of systems are viable to implement multi-microchannel evaporator for cooling blade server? How do they work to satisfy the cooling requirements and also heat recovery functions?
- What are the critical parameters to guarantee the basic safety measurements? What are the important perspectives for controlling the system?
- How do these cycles respond to dynamic changes such as transient heat load which commonly happen during the normal operation in the blade servers?
- What about the performance of these cycles regarding the energetic and exergetic perspectives? What are the options to minimize the energy consumption and to improve the overall performance?

To answer these questions, a series of system dynamic tests have been done and controllers were developed for running the cycles to achieve and maintain the desired setpoints of control variables. A thorough comparative analyses among these novel systems from energetic and exergetic perspectives were done (although not a highly detailed exergy analysis). Then, performance mapping tests were carried out for more detailed energetic analysis and comparison. The main contributions of the thesis are the successful control of the two-phase cooling systems studies, characterized by their simplicity, high efficiency and effectiveness; and also the performance evaluation and comparison of the proposed cycles.

Finally, the thesis is outlined as follows:

- Chapter 1: Introduction
- Chapter 2: Literature review
- Chapter 3: Experimental facility
- Chapter 4: Controls

- Chapter 5: Energy and exergy analysis
- Chapter 6: Map of performance
- Chapter 7: Conclusions and recommendations

2 Literature review

The present chapter will address two general subjects: the fundamental issues controlling the proper operation of a multi-microchannel evaporator including critical heat flux, flow distribution and flow stability, and hot spot management and a state-of-the-art review on data center two-phase cooling systems.

2.1. Multi-microchannel evaporators

In the previous chapter, the microchannel two-phase cooling was presented as a promising solution for tackling the energy issues in the data centers, in order to better understand the characteristics of microchannel evaporators which are closely related to such applications, some fundamental issues will be explained as following.

2.1.1 Critical heat flux

For high heat flux cooling applications using multi-microchannel cooling channels, the critical heat flux (CHF) in saturated flow boiling conditions is a very important operational limit. CHF signifies the maximum heat flux that can be dissipated at the particular operating conditions by the evaporating fluid. Surpassing CHF means that the heated wall becomes completely and irrevocably dry, and is associated with a very rapid and sharp increase in the wall temperature due to the replacement of liquid by vapor adjacent to the heat transfer surface, typically resulting in "burnout" of the electronics. Only a brief summary is presented below.

Revellin and Thome (2008) proposed the first partially theoretically based model for predicting critical heat flux in microchannels. Their model is based on the premise that

CHF is reached when local dry out occurs during evaporation in annular flow at the location where the height of the interfacial waves matches that of the annular film's mean thickness. To implement the model, they first solve one-dimensionally the conservation of mass, momentum and energy equations assuming annular flow to determine the variation of the annular liquid film thickness δ along the channel. Then, based on the slip ratio given by the velocities of the two phases (liquid and vapor) and a Kelvin-Helmoltz critical wavelength criterion (assuming the height of the waves scales proportionally to the critical wavelength), the wave height was predicted with the following empirical expression:

$$\Delta\delta = 0.15 \left(\frac{u_V}{u_L}\right)^{-\frac{3}{7}} \left(\frac{g(\rho_L - \rho_V)(d_i/2)^2}{\sigma}\right)^{-\frac{1}{7}} \qquad 2.1$$

where u_V, u_L, g and d_i are the mean velocities of the vapor and liquid phases, the acceleration due to gravity and the internal channel diameter, respectively.

Then, when δ equals $\Delta\delta$ at the outlet of the microchannel, CHF is reached. Refer to Figure 2.1 for a simulation. The leading constant and two exponents were determined with a database including three fluids (HFC134a, HFC245fa and CFC113) and three circular channel diameters (0.509 mm, 0.790 mm and 3.15 mm) taken from the CHF data of Wojtan *et al.* (2006) and data from the Argonne Laboratory by Lazarek and Black (1982). Their model also satisfactorily predicted the Purdue CFC113 data of Bowers and Mudawar (1994) for circular multi-microchannels with diameters of 0.510 and 2.54 mm of 10 mm length. Furthermore, taking the channel width as the characteristic dimension to use as the diameter in their 1-D model, they were also able to predict the Purdue rectangular multi-microchannel data of Qu and Mudawar (2004) for water. Altogether, 90% of the database was predicted within ±20%. This model also accurately predicted the HFC236fa multi-microchannel data of Agostini *et al.* (2008). Additionally, this model also predicts CHF data of CO_2 in microchannels from three additional independent studies as well as other fluids.
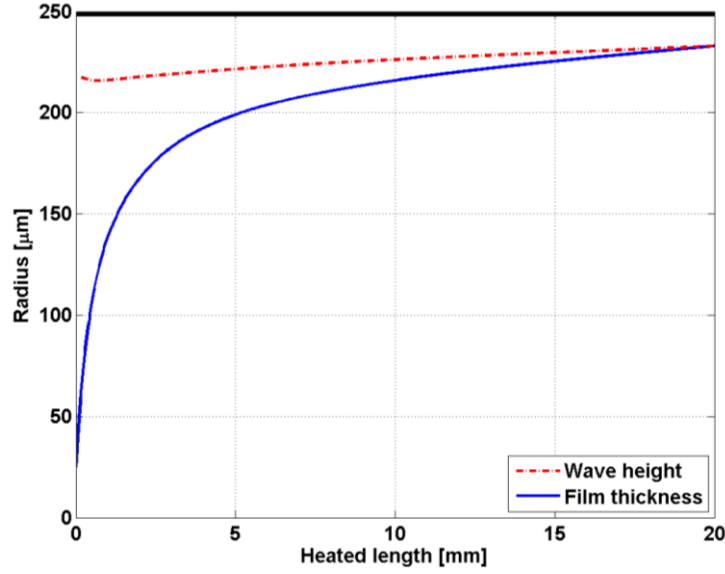
Figure 2.1 CHF model showing the annular film thickness variation along the channel plotted versus the wave height (Revellin and Thome 2008)

Notably, the above 1-D numerical method can also be applied to non-uniform wall heat flux boundary conditions when solving for the annular liquid film profile. Hence, it can tentatively simulate the effects of single or multiple hot spots, their size and location, etc. or it can use, as an input, a CPU chip's heat dissipation map to investigate if the locally high heat fluxes will locally trip CHF.

Regarding simpler empirical methods, Ong (2010) has more recently updated the CHF correlation developed by Wojtan *et al.* (2006) for a wider range of operating parameters and fluid properties. This correlation is given as

$$q_{chf} = 0.12 G h_{LV} \left(\frac{\mu_{LO}}{\mu_{VO}}\right)^{0.183} \left(\frac{\rho_{VO}}{\rho_{LO}}\right)^{0.062} We_{LO}^{-0.141} \left(\frac{L_{ev}}{d_i}\right)^{-0.7} \left(\frac{d_i}{d_{th}}\right)^{0.11} \qquad 2.2$$

where the threshold d_{th} is defined as

$$d_{th} = \frac{1}{Co} \sqrt{\frac{\sigma}{g(\rho_{LO} - \rho_{VO})}} \qquad 2.3$$

and the confinement number is $Co = 0.5$. We_{LO} is the liquid-only Weber number defined as

$$We_{LO} = \frac{G^2 L_{ev}}{\sigma \rho_{LO}} \qquad\qquad 2.4$$

G is the mass velocity per unit cross-sectional tube area of the fluid, σ the fluid surface tension, ρ_{LO} and ρ_{VO} the liquid-only and vapor-only densities, μ_{LO} and μ_{VO} the liquid-only and vapor-only viscosities, h_{LV} the latent heat of vaporization, L_{ev} the heated length of the channel and d_i the inner channel diameter. This correlation is valid for $0.35 < d_i < 3.04$, $84 < G < 3'736$, $7 < We_{LO} < 201'232$, $14.4 < \frac{\mu_{LO}}{\mu_{VO}} < 53.1$, $0.024 < \frac{\rho_{VO}}{\rho_{LO}} < 0.036$ and $22.7 < \frac{L_{ev}}{d_i} < 177.6$.

This correlation predicted 94.4% of the data on which it was based and that of Wojtan *et al.* (2006) for single microchannels to within ±30% with a mean absolute error of 13.6%. It also predicted 100% of the split flow multi-microchannel data of Mauro *et al.* (2010) and Agostini *et al.* (2008) to within ±30% with a mean absolute error of 20.7% and 15.6%, while also predicting 91.9% of the once-through flow multi-microchannel data of Park (2008) to within ±30% with a mean absolute error of 16.1%. Notably, like any empirical CHF correlation, it is only applicable to uniform heat flux boundary conditions.

2.1.2 Flow distribution and flow stability

Multi-microchannel flow boiling test sections can suffer from flow maldistribution among the numerous parallel channels, two-phase flow instabilities and even backflow effects. The flow may in fact flow back into the inlet header and some channels may become prematurely dry from too low of an inlet liquid flow rate.

Figure 2.2 shows a sequence of video images to demonstrate backflow and parallel channel instability in multi-microchannel test section (something to be avoided). A slug bubble was observed at the inlet of the topmost channel in (a). If the flow in the channel is pushed upstream by a bubble growth downstream, the bubble goes back into the inlet plenum in (b), as there is no restriction at the channel inlet of the channel to prevent this. This reverse flow bubble quickly moves to one of the adjacent channels, (c), and breaks down into

smaller parts before entering these channels, (d). Depending on its location, the inserted bubble becomes stagnant, (e) and (f), before moving forwards or backwards again.

(a) t = 2.5 ms   (b) t = 5.0 ms   (c) t = 7.5 ms

(d) t = 10.0 ms   (e) t = 12.5 ms   (f) t = 15.0 ms
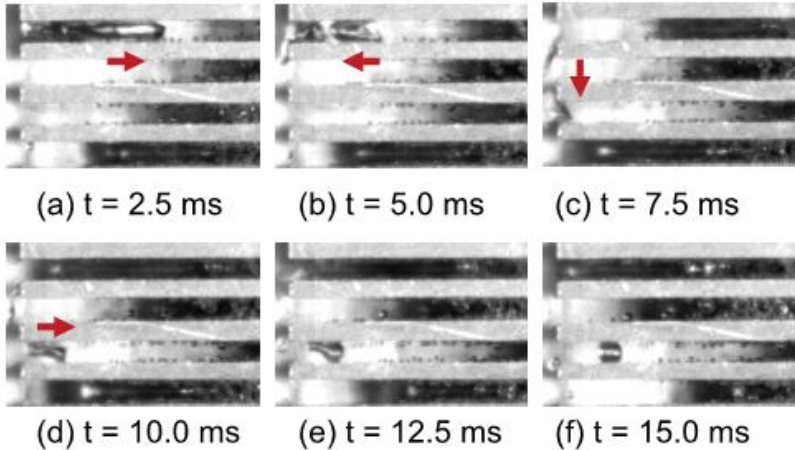
Figure 2.2 Dramatic effect that maldistribution can have on the heat transfer process (Park 2008)

Micro-inlet orifices can completely prevent backflow, flow instabilities and maldistribution. Figure 2.3 shows the maldistribution effect when no inlet orifice is used, with a large dry zone being visible in the top right corner. A critical heat flux of only 115 W/cm^2 was achieved.
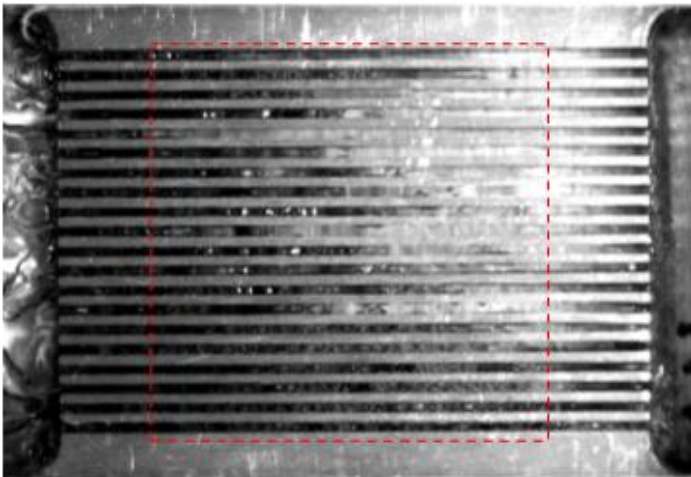
Figure 2.3 Without orifice by Park (2008)

Figure 2.4 shows that maldistribution is avoided when making use of micro-inlet orifices at the entrance of each channel (created by placement of an insert in the entrance plenum), with heat fluxes in excess of 350 W/cm^2 being obtainable…this is equivalent to cooling of 35'000 100-Watt light bulbs per meter squared of surface area! Hence, microscale flow boiling can dissipate very high heat fluxes as long as proper attention is paid to obtain good flow distribution and stable flow by use of micro-orifices. Such orifices often make up about 10-30% of the pressure drop of the micro-evaporator cooling element, according to LTCM lab simulations; however, this pressure drop penalty is not all that significant when compared to the total pressure drop of the entire two-phase cooling loop.
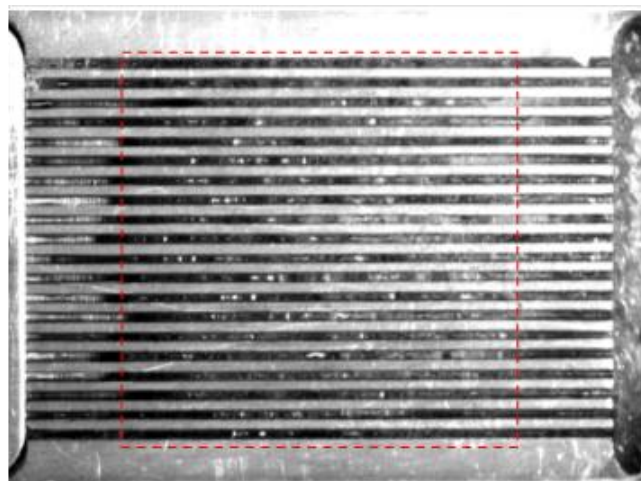
Figure 2.4 With orifice by Park (2008)

Figure 2.4 also depicts some flashing of the nearly saturated inlet liquid into a small fraction of vapor, visible at the left of the image in some channels. This flashing process is also an important feature of the inlet orifices as this takes slightly subcooled inlet liquid directly into the flow boiling regime by suppressing the onset of nucleate boiling, the latter which requires a large wall superheat (with respect to the saturation temperature) to activate the boiling process and hence is to be avoided in electronics cooling because of the temperature overshooting involved.

10

2.1.3   Hot-spot managements

Non-uniform power dissipation across a chip leads to local hot-spots, resulting in elevated temperature gradients across the silicon die. These hot-spots could result in the degradation of reliability and performance of the chip (Karajgikar *et al.* 2010), with a complete thermal breakdown of the chip also being possible. The reliability of a chip decreases by 10% for every 2 °C rise in temperature (Bar-Cohen *et al.* 1983). An example of a temperature map showing the results of non-uniform power dissipation is given in Figure 2.5. In this example the temperature gradient is approximately 50 K.
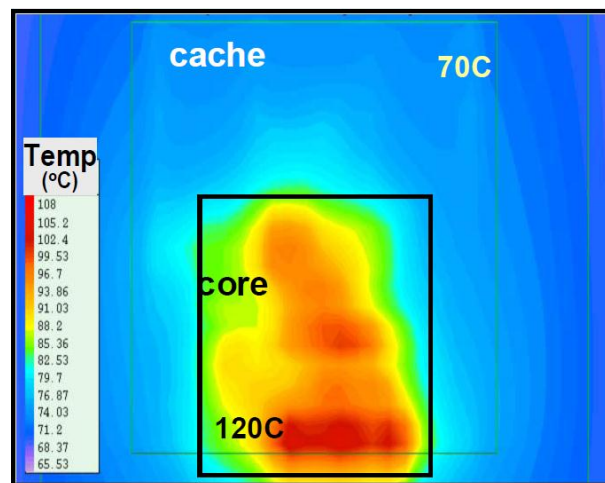
Figure 2.5 Temperature map of a typical chip (Borkar *et al.* 2003)

From the numerous experimental data obtained in the last decade, various trends regarding microchannel two-phase flow boiling have been observed by Agostini and Thome (2005). One of these trends is that the local heat transfer coefficient for microchannel flow boiling at low to intermediate vapor qualities increases proportionally with the heat flux, essentially in the isolated bubble and coalescing bubble flow regimes but not in the annular flow regime as noted by Ong and Thome (2011). In general it has been found that it approximately increases as $\alpha \propto q^{0.7}$ in the bubble and coalescing bubble (slug flow) regimes. More recent results by Costa-Patry *et al.* (2010), focusing on cooling of hot-spots of a pseudo-chip with 35 local heaters and temperature sensors cooled with a silicon multi-microchannel evaporator, have shown that this proportionality is closer to $q^{0.4}$ for his test geometry of high aspect ratio rectangular microchannels, with conduction (heat

spreading) effects within the evaporator being the main differentiating factor. One such result is shown in Figure 2.6, which is the thermal profile of their pseudo-chip being cooled by a two-phase refrigerant evaporating in 135 parallel microchannels of 85 micron width engraved in the face of the silicon die. For a hot-spot heat flux in the outlet row 5 being 10 times higher than the base heat flux in rows 1 to 4 (with fluid inlet at the left and exit at the right), the hot-spot heat transfer coefficient was measured to be 2 times higher with consequently a wall superheat of only 4.5 times higher (Costa-Patry *et al.* 2012). Hence, two-phase cooling has been proven experimentally to have a built-in passive hot-spot cooling mechanism, unlike single-phase cooling.
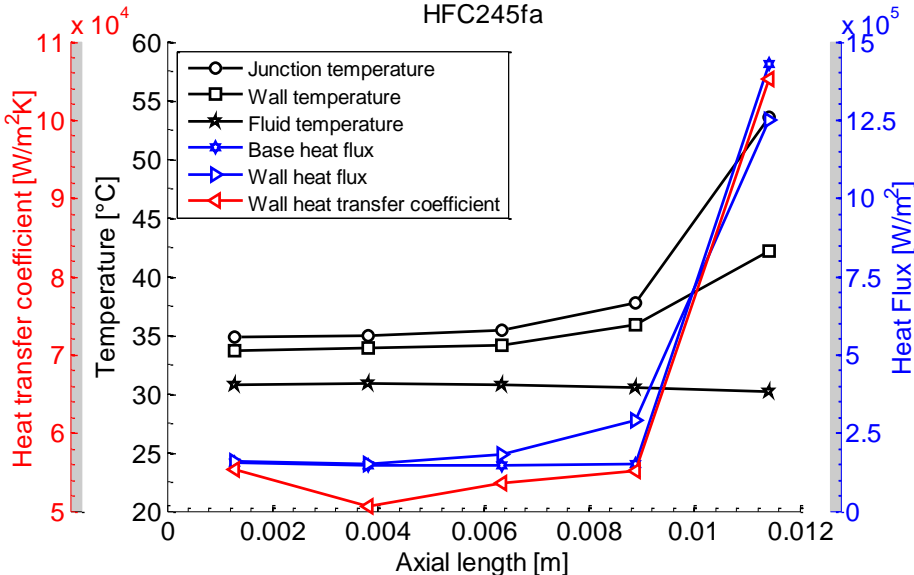
Figure 2.6 Thermal profile of a pseudo-chip (Costa-Patry *et al.* 2012)

Figure 2.7 and Figure 2.8 show the results of simulations using a multi-purpose internal LTCM lab code considering the presence of 3 hot spots on a chip of 20 mm length. Base and hot-spot heat fluxes of 50 W/cm^2 and 200 W/cm^2 were considered, respectively. HFC134a, water and 50% water-ethylene glycol were evaluated as working fluids with microchannels of 1.7 mm height and 0.17 mm width, fins 0.17 mm thick and a base of 1 mm thickness to the junction for a copper cooling element. The results, as expected, show an increase of heat transfer coefficient when using HFC134a two-phase flow boiling, resulting in a much lower increase of junction temperature than for the other two working fluids, which do not

12

have an effect of the hot-spot on their heat transfer coefficient (except for the change in their physical properties with the locally rising liquid temperature).
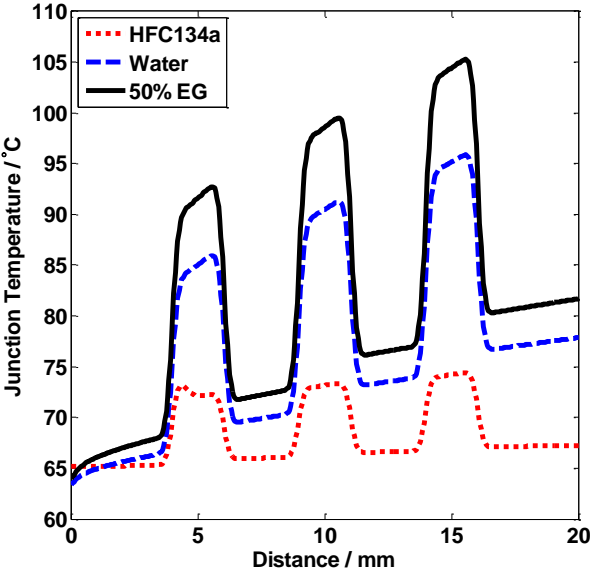
Figure 2.7 Junction temperature for non-uniform heat flux (Costa-Patry *et al.* 2012)
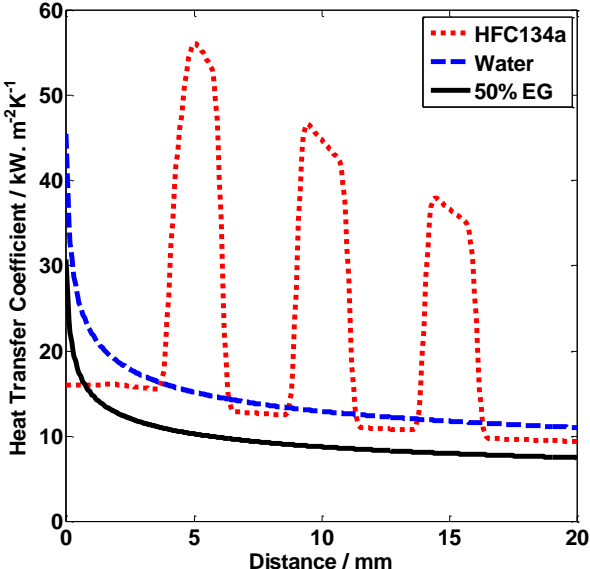
Figure 2.8 Heat transfer coefficient for non-uniform heat flux (Costa-Patry *et al.* 2012)

2.2 Two-phase cooling system

Heydari (2002) developed a simplified simulation program to design and evaluate the performance of miniature refrigeration systems for high performance computers. Due to space limitations in some high performance computer servers, a miniature refrigeration system composed of a compressor, capillary tube, a compact condenser, and a cold-plate evaporator heat exchanger is used. Mathematical multi-zone formulations for modeling thermal-hydraulic performance of its heat exchangers (condenser and evaporator) are presented. The throttling device is a capillary tube for which a mathematical formulation for predicting the refrigerant mass flow rate is presented. To simulate the performance of the miniature compressor a physically based formulation is used. An efficient iterative numerical scheme with allowance for utilization of various refrigerants was developed to solve the governing system of equations. Using the simulation program, the effects of parameters such as the choice of working fluid, evaporating and condensing temperatures, and overall efficiency of system were studied. In addition, a RAS (reliability, availability and serviceability) discussion of the proposed CPU-cooling refrigeration solution was presented. The results of analysis show that the new technology not only overcomes many shortcomings of the traditional fan-cooled systems, but also has the capacity of increasing the cooling system's coefficient of performance. The analysis of the system was based on a steady-state modeling of four components, i.e. compressor, condenser, evaporator and capillary tube. The two main points observed in the simulations were: i) HFC134a is the most favorable refrigerant for CPU-cooling in combination with a vapor compression refrigeration system and ii) the condensing temperature has a much greater effect on the overall system efficiency than the evaporating temperature, with much higher COPs being observed at lower condensing temperatures.

Hannemann *et al.* (2004) have proposed a pumped liquid multiphase cooling system (PLMC), to cool microprocessors and microcontrollers of high-end devices such as computers, telecommunications switches, high-energy laser arrays and high-power radars. According to them, their system could handle applications with 100 W heat loads (single computer chip) as well as applications with short time periods of kW heat loads (radar). Their PLMC consisted basically of a liquid pump, a high performance cold plate

(evaporator) and a condenser with a low acoustic noise air mover to dissipate the heat in the ambient air, as shown in Figure 2.9. A comparison between a single-phase liquid loop (water) and the system proposed with HFC134a was made for a 200 W heat load. The HFC134a system had a mass flow rate, a pumping power and a condenser size that were 4.6, 10 and 2 times smaller than the water-cooled system. The coolant temperature rise was 10 K for the water but negligible for HFC134a. In their study, a demonstration radar cooling unit was also designed and built for a 6.4 kW heat load (sixteen 400 W cold plates with convoluted fins). For 25 °C ambient air temperature, the working fluid saturation temperature was maintained at 32 °C with a total volumetric liquid flow rate of 376 L/h and a cold plate outlet vapor quality of 30%, providing a safety factor for dry-out. The system was stable, easily controllable and provided essentially isothermal conditions for all the cold plates. They emphasized the significant benefits from efficiency, size and weight that were provided with the PLMC solution.
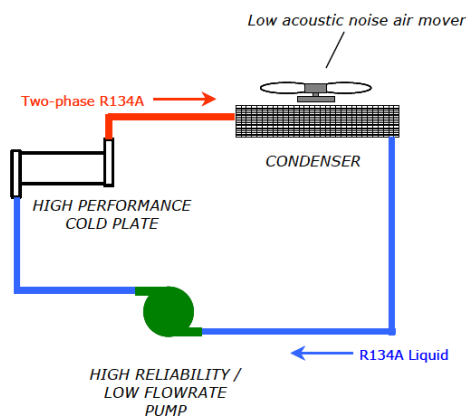
(a) flow loop   (b) 1U mockup

Figure 2.9 PLMC flow loop and 1U mockup (Hannemann *et al.* 2004)

Mongia *et al.* (2006) designed and built a small-scale refrigeration system applicable for a notebook computer, as shown in Figure 2.10. The system basically included a mini-compressor, a microchannel condenser, a microchannel evaporator and a capillary tube as the throttling device and is considered to be the first refrigeration system developed that can fit within the tight confines of a notebook and operate with high refrigeration efficiencies. HC600a (isobutane) was the working fluid, chosen from an evaluation of 40

candidate refrigerants. According to them, HC600a presented the best efficiency at a low pressure ratio and was readily available, although flammable, but the system required only a very small fluid charge (a few milliliters). Two evaporators were used, the first one a microchannel evaporator to cool the high heat flux component (chip) and the second one a superheater (conventional finned evaporator) to cool lower heat flux components, such as memories, which also guaranteed that superheated vapor was delivered to the mini-compressor inlet. Two thermal test vehicles were used to simulate the chip and the power components. For a baseline operating condition, when the evaporator and condenser temperatures and the heat load were 50 °C, 90 °C and 50 W, the coefficient of performance (COP) obtained was 2.25. The COP reached 3.70 when the evaporator and condenser temperatures increased and decreased by 10 °C from the baseline conditions and the heat load was reduced to 44 W. The small-scale refrigeration system achieved 25-30% of the Carnot efficiency (ideal COP for a Carnot cycle), values comparable with those obtained in today's household refrigerators.
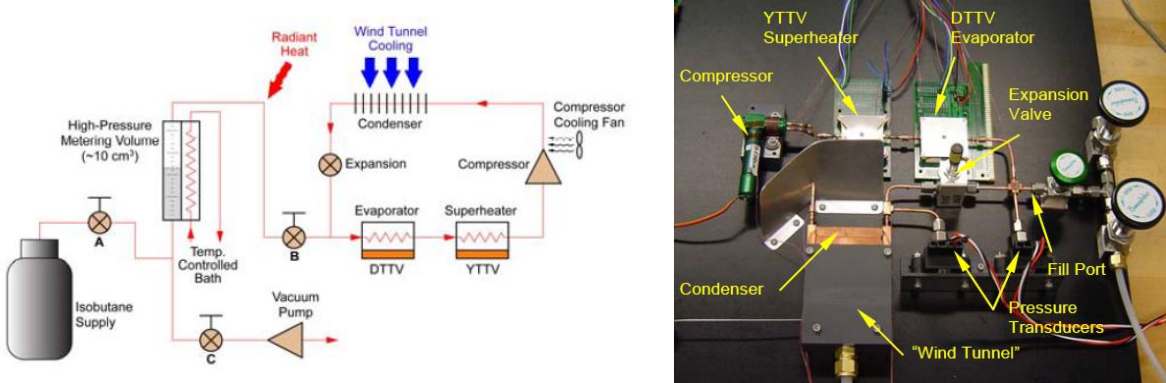
(a) system scheme and main compoents   (b) testing system

Figure 2.10 Form factor loop for refrigeration system (Mongia *et al.* 2006)

Trutassanawin *et al.* (2006)) designed, built and evaluated the performance of a miniature-scale refrigeration system (MSRS) suitable for electronics cooling applications. Their MSRS had the following components: a commercial small-scale compressor, a microchannel condenser, a manual needle valve as the expansion device, a cold plate microchannel evaporator, a heat spreader and two compressor cooling fans, the schematic is shown in

16

Figure 2.11. A suction accumulator to avoid liquid flow to the compressor, an oil filter to return oil to the compressor and guarantee good lubrication, and heat sources to simulate the chips were also installed. HFC134a was the working fluid. System performance measurements were conducted at evaporator temperatures from 10 °C to 20 °C and condenser temperatures from 40 °C to 60 °C. The cooling capacity of the system varied from 121 W to 268 W with a COP of 1.9 to 3.2 at pressure ratios of 1.9 to 3.2. Their MSRS was able to dissipate CPU heat fluxes of approximately 40-75 W/cm^2 and keep the junction temperature below 85 °C for a chip size of 1.9 cm^2. It was concluded that a new compressor design for electronics cooling applications was needed to achieve better performance of the system (the most significant losses occurred in the compressor, which was not designed for the operating conditions of electronics cooling). It was also recommended to study the development of an automatic expansion device and a suitable control strategy for the MSRS.

Trutassanawin *et al.* (2006) also mentioned some alternative cooling approaches such as heat pipes, liquid immersion, jet impingement and sprays, thermoelectrics and refrigeration. For refrigeration, the following possible advantages were cited: (i) one of the only methods which can work at a high ambient temperature, (ii) chip to fluid thermal resistances are considerably lower, resulting in lower junction temperatures, which could lead to higher heat fluxes being dissipated, and (iii) lower junction temperatures can also increase the microprocessor's performance and increase the chip's reliability. Possible "disadvantages" were characterized to be: (i) an increase in the complexity and cost, (ii) possible increase in the cooling system volume and (iii) uncertainties in the system reliability (moving parts in the compressor).
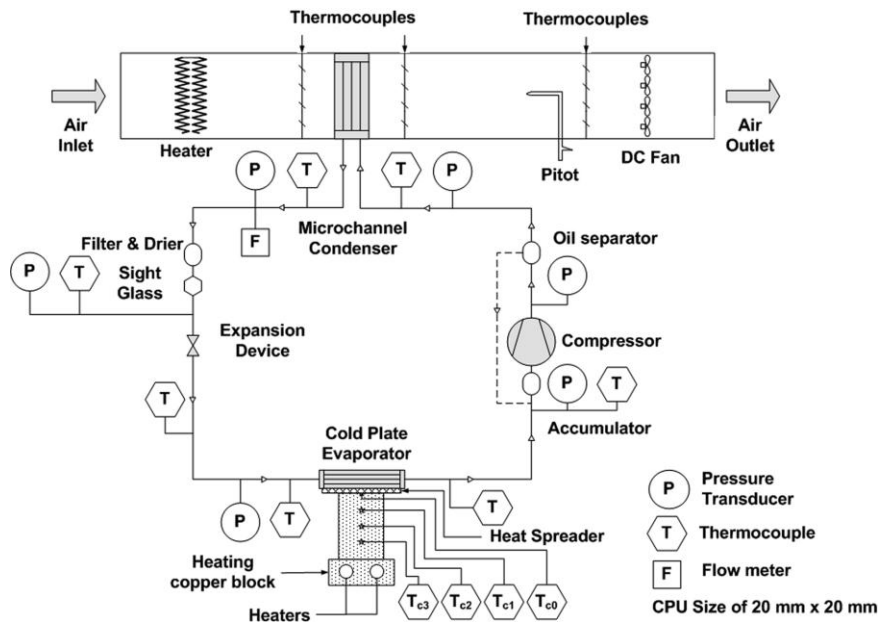
Figure 2.11 Schematic of bread board of miniature-scale refrigeration system
(Trutassanawin *et al.* 2006)

Agostini *et al.* (2007) surveyed the advances in thermal modeling for flow boiling of low pressure refrigerants in multi-microchannel evaporators for cooling of microprocessors. According to them, multi-microchannel evaporators hold promise to replace the actual air cooling systems and can compete with water-cooling to remove high heat fluxes, higher than 300 W/cm^2, while maintaining the chip safely below its maximum working temperature, providing a nearly uniform chip base temperature (Agostini *et al.* 2008) and minimizing energy consumption. Variables such as critical heat fluxes, flow boiling heat transfer coefficients and two-phase friction factors were evaluated and characterized as important design parameters to the micro-evaporator for high heat flux applications.

Thome and Bruch (2008) simulated two-phase cooling elements for microprocessors with micro-evaporation. Heat fluxes of 50 W/cm^2 and 150 W/cm^2 in a micro-evaporator with channels 75 μm wide, 680 μm high and 6 mm long with 100 μm thick fins were simulated for flow boiling. The size of the chip was assumed to be 12 mm by 18 mm and the micro-evaporator was considered with the fluid inlet at the centerline of the chip and outlets at both sides, i.e. a split flow design to reduce the pressure drop and increase the critical heat flux. Results of pumping power, critical heat flux, and junction and fluid temperatures were

generated for HFC134a at an inlet saturation temperature of 55 °C (chosen to allow for heat recovery). The following conclusions were reached: i) the influence of mass flux on the fluid, chip and wall temperatures was small, ii) for the heat flux of 150 W/cm^2, the chip temperature was 70 °C or less, i.e. well below its operational limit of 85 °C, iii) for the heat flux of 150 W/cm^2, the junction-to-fluid temperature difference was only 15 K, which is lower than that with liquid cooling systems, iv) the fluid temperature could still be raised more while rejecting heat at 65 °C for reuse, and v) the critical heat flux increased with the mass flux and the lower limit was about 150 W/cm^2 for 250 kg/(m^2·s). The channel width had a significant effect on the wall and junction temperatures, and there was a turning point at about 100 μm when considering 1000 kg/(m^2·s) of mass flux and 150 W/cm^2 of base heat flux, at which these temperatures reached a minimum. For the same mass flux and base heat flux, the reduction of channel width also reduced the energy consumption to drive the flow (pumping power).

From a system viewpoint, Thome and Bruch (2008) showed an approximate comparison of performances of liquid water cooling versus two-phase cooling. For the same pumping power consumption to drive the fluids, two-phase cooling allowed the chip to operate about 13 K cooler than water-cooling or it could operate at the same junction temperature but consume much less pumping power using a lower refrigerant flow rate. The two-phase cooling system appeared to be more energy-efficient than classical air cooling or direct liquid cooling systems while also exhausting the heat at higher reusable temperatures. Regarding the choice between a pump or a compressor as the driver for a micro-evaporation heat sink system, they emphasized that the choice depends on the economic value of the re-used energy. The system with a compressor is ideal for energy re-use because of the higher heat rejection temperature; however the additional energy consumed by the compressor compared to the pump has to be justified by the re-use application.

Zhang *et al.* (2010) evaluated the effect of transient heat loads on inherent pressure drop flow instabilities in two-phase refrigeration cooling systems. The authors justify such instabilities with the negative slope of the boiling flow pressure drop with the increasing of mass flux. The idea would be to develop a controller able to compensate the portion of the boiling flow pressure drop curve with a negative slope, so that no flow excursion or

oscillation would take place, i.e. the combined system pressure drop increases monotonically with mass flux. A two-loop refrigeration system designed for two-phase cooling of ultra-high power electronics components was used for the simulations. Such a system is composed in the primary loop by a pump, a surge tank, an accumulator and cartridge heaters immersed in the refrigerant (HFC134a) to emulate the evaporator. The second loop is a secondary vapor compression cycle, which is used to dissipate the heat to the ambient by using a fluid-to-fluid heat exchanger. A set of active control strategies were developed to suppress compressible flow boiling oscillations and to maintain reasonable electronics wall temperature under transient heat load changes. Simplified two-phase friction and heat transfer correlation were used to design and simulate the controllers, since no widely-accepted transient two-phase heat transfer model was found in the literature. Periodic heat load changes for period varies from 2 s, to 5 s, and to 10 s within the simulation time range (10 - 50 s) and the heat load variation amplitude of 500 W were simulated. Two actuators were evaluated, a valve before the heated channel and a supply pump. According to the authors, although the valve can suppress the compressible flow instability, it suffers from high pressure loss and high supply pumping power. The use of a positive displacement pump can also regulate the downstream flow and the valve could be removed so that no additional pressure loss is induced. In summary, the results of simulations showed that both actuators were efficient and effective to control the flow oscillations. However, only simulations were done no experimental evaluations were done to confirm such a performance.

Mauro *et al.* (2010) evaluated the performance of a multi-microchannel copper heat sink with respect to critical heat flux (CHF) and two-phase pressure drop. A heat sink with 29 parallel channels (199 μm wide and 756 μm deep) was tested experimentally with a split flow system with one central inlet at the middle of the channels and two outlets at either end. Three working fluids were tested (HFC134a, HFC236fa and HFC245fa) and also the parametric effects of mass velocity, saturation temperature and inlet temperature. The analysis of their results showed that a significantly higher CHF was obtainable with the split flow system compared to the single inlet-single outlet system (Park and Thome, 2010), providing also a much lower pressure drop. For the same mass velocity, the increase in CHF exceeded 80% for all working fluids evaluated due to the shorter heated length of a

split system design. For the same total refrigerant mass flow rate, an increase of 24% for HFC134a and 43% for HFC236fa were obtained (no comparable data were available for HFC245fa). They concluded that the split flow system had the benefit of much larger CHF values with reduced pressure drops and further developments in the design of split flow system could yield an interesting energetic solution for cooling of computer chips.

Zhou *et al.* (2010) developed a steady state model of a refrigeration system for high heat flux electronics cooling. The refrigeration system proposed consisted of multiple evaporators (microchannel technology), a liquid accumulator with an integrated heater, a variable speed compressor, a condenser and electric expansion valves (EEV). To obtain more efficient heat transfer and higher critical heat flux, the evaporators were considered to operate only with two-phase flow. To guarantee the safe operation of the refrigeration system the authors considered the presence of an integrated heater-accumulator to fully evaporate the two-phase flow coming out of the evaporator, which naturally represents a decrease of the cycle COP. A parametric study to evaluate the effects of external inputs on the system performance (secondary fluid temperature in the condenser, evaporator heat load, compressor speed, EEV percentage opening and heat supplied to the accumulator) and a Pareto optimization to find the optimal system operating conditions were also developed. A heat load of 1500 W and 2500 W, which represent respectively a heat flux of 94 kW/m^2 and 156.6 kW/m^2 were considered. The main points observed were: i) the system COP can be improved without compromising the critical heat flux when handling higher heat flux, ii) higher critical heat fluxes are achieved with a smaller EEV opening and higher heat input supplied to the accumulator and iii) a trade-off between the system COP and CHF is necessary to prevent the device burnout, i.e., the imposed heat flux must be lower than the CHF considering a safety margin. Finally, they presented a preliminary validation of the model with initial experimental data showing a satisfactory prediction ability of the model. The authors do not mention anything about the geometry assumed for the evaporators.

Marcinichen and Thome (2010) by means of a simulation code developed to evaluate electronic cooling cycles, performed thermo-hydrodynamic simulations of a vapor compression cycle (VC cycle) and a liquid pumping cooling cycle (LP cycle) using on-chip

cooling with multi-microchannel coolers. Water and different working fluids were simulated. Their results showed that for the LP cycle, the pumping power consumption when using water was 5.5 times that obtained for two-phase HFC134a. The simulation of VC cycle showed higher driving energy consumption than that with LP cycle; however, this cycle was justified when the waste heat at the condenser is recovered for applications such as district heating and preheating of boiler feedwater. The highest condensing temperature (higher secondary fluid temperature) and heat transfer rate (associated with the work imparted by the compressor) represents a higher economic value than that obtained with the LP cycle.

Marcinichen J.B. *et al.* (2012) designed and built two candidate two-phase cooling cycles, and experimentally evaluated the functionality and controllability for both cycles which were driven by a liquid pump and by a compressor. Firstly, specific controllers for the multi-microchannel outlet vapor quality, condensing/evaporating pressure and difference of temperature between outlet water flow and inlet working fluid flow in the condenser were designed. Then, these controllers were evaluated by tracking and disturbance rejection tests, which proved be efficient and effective. The average temperatures of the pseudo-chips, which were specifically designed to simulate a CPU on a blade server, were maintained below of the limit of 85 °C for all tests evaluated in steady state and transient conditions. Additional tests were also done considering a periodic step change of heat load, where the maximum variation observed in the average pseudo-chips temperatures was only 1.5 K. In general, simple SISO strategies were sufficient to achieve the requirements of control, and more complex MIMO strategies were not necessary for this application. Regarding energy and exergy analyses, the experimental results showed that both systems can be thermodynamically improved since only about 10% of the exergy supplied was in fact recovered in the condenser.

Ohadi *et al.* (2012) provided performance comparison analysis for cooling of electronics in data centers by air, liquid and two-phase on-chip cooling. Advantages and disadvantages of each of the methods were also discussed. It was demonstrated that air cooling may remain very attractive for select locations where a cool air climate is available most of the year. For optimum two-phase cooling, a proprietary manifolded microchannel cooling technology

22

was introduced. From the results obtained and highlighted in Figure 2.12, it was showed that the two-phase flow cooling provides substantially reduced thermal resistance, as much as an order of magnitude less than that of air and significantly below that of liquid cooling. Additionally, the two-phase cooling by the force-fed manifolded microchannels has 20 times lower thermal resistance than liquid cooling at 5 times lower pumping power consumption. This is contrary to the generally held view that two-phase cooling flows require higher pumping power than single-phase cooling flows. The main reason for this behavior was justified by the fact that the governing regime in the microchannels is a combination of forced convection boiling and thin film evaporation over high aspect ratio microchannels with limited fluid flow running length. Based on such preliminary analysis they concluded that future data centers utilizing advanced phase change cooling systems will have a significant competitive advantage over conventional systems, due to their lower capital costs, operating costs, and energy savings appeal. Moreover, such systems would allow reductions in the sizes of servers by eliminating the need for air flow within the server housing and of cabinets. These space savings could be combined with corresponding reductions in the open space around the data center cabinets to generate savings in real estate and building expenses. Even without realizing all of these advantages, the total energy savings from a redesign of an integrated cooling system could lead to potential energy savings of 75% or higher compared to a traditional air cooling data center.
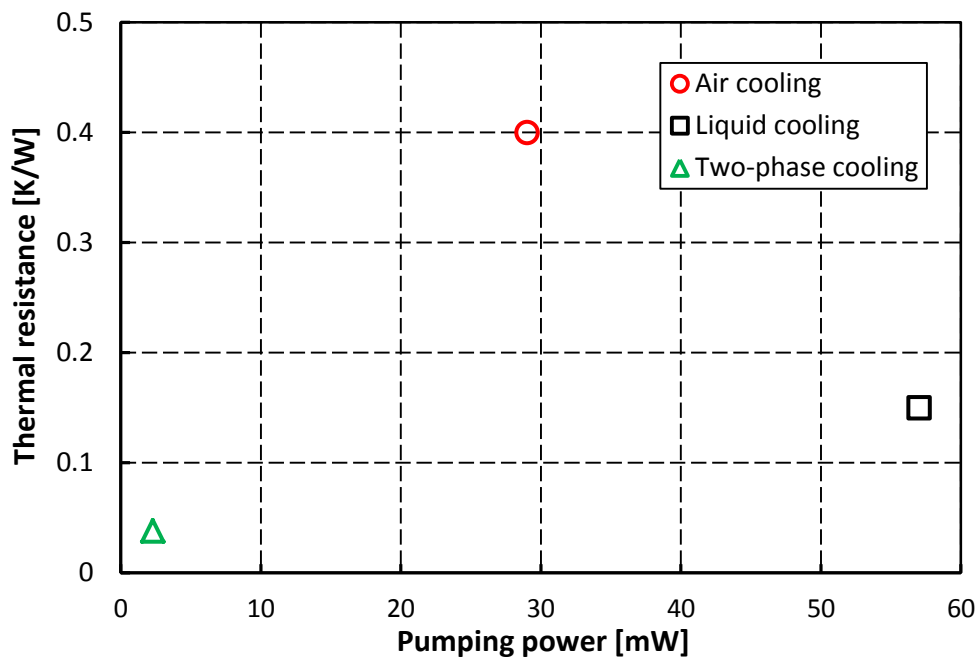
Figure 2.12 Comparison of thin film manifold microchannel cooling with air cooling and liquid cooling (Ohadi *et al.* 2012)

Marcinichen J.B. *et al.* (2012) proposed and simulated a hybrid two-phase cooling cycle to cool microprocessors and auxiliary electronics of blade server boards with two-phase evaporating flow in the micro-evaporator cooling elements. A simulation code was developed and 5 cases were simulated considering 3 different working fluids (HFC134a, HFO1234ze and water in an analogous single-phase cooling cycle) and different internal diameters of the pipes and elbows joining the components. The results showed that the liquid water cooling cycle has a pumping power consumption 5.5 times that obtained for the two-phase HFC134a cooling cycle, both considering a liquid pump as the driver of the fluid. When compared with the HFO1234ze cooling cycle the difference drops to 4.4 times. The simulation of the vapor compression cooling cycle showed higher pumping power consumption when compared with the other cycles simulated. However, this cycle was justified when the waste heat at the condenser is recovered for applications such as district heating and preheating of boiler feedwater. An exergy analyses of the cooling cycles, regarding the potential of exergy recovery at the condenser, showed a low overall exergetic efficiency (lower than 50%), meaning that improvements can be done to increase the

thermodynamic performance of the cycles. It was also shown that the overall exergetic efficiency of the vapor compression cooling cycle is strongly influenced by the compressor overall efficiency, which showed to be more exergeticaly efficient than the liquid pumping cooling cycle for an overall efficiency higher than 67%. Finally, a case study was developed to investigate the potential savings in energy that can be achieved a data center by implementing on-chip cooling with waste heat recovery. As an application for the waste heat, the preheating of boiler feedwater in a coal fired power plant was analyzed. The results showed that, when compared with traditional air-cooling systems, the energy consumption of the data center could be reduced by as much as 50% when using a liquid pumping cycle and 41% when using a vapor compression cycle. The overall consumption can be reduced even further if the recovered energy is sold to a secondary application, such as to a thermal power plant. It was showed that power plant thermal efficiency improvements on the order of 2.2% are possible if data center waste heat is incorporated in the power plant's feedwater (*viz.* Figure 2.13). This could imply huge savings in terms of fuel as well as carbon tax due to a reduced carbon footprint.
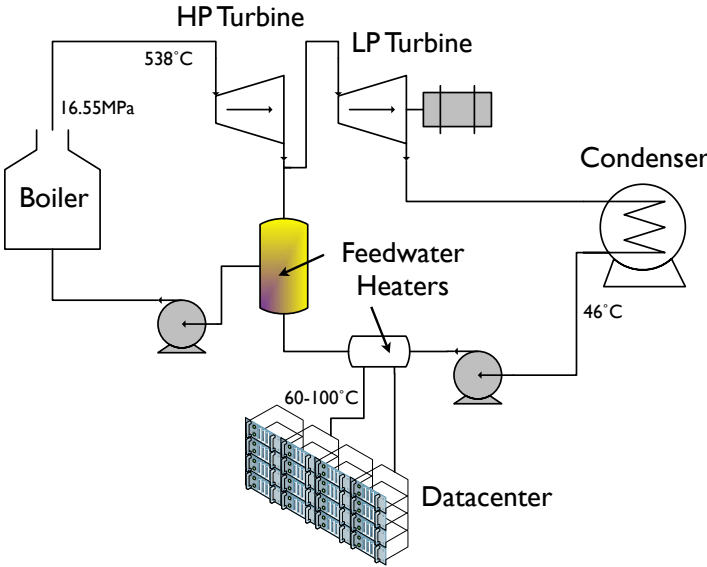
Figure 2.13 Case study: data center integrated in a power utility (Marcinichen J.B. *et al.* 2012)

Table 2.1 summarizes the studies on two-phase cooling systems. However, none of them has experimentally evaluated the behavior during transients which represents the typical operational condition in the servers, i.e. variable clock speed, which can affect considerably the performance of the cooling system and the reliability of the chip, which will be one of the major objectives of the current study. Also, the current thesis will give a thorough analysis from energetic and exergetic perspectives and also present an operational performance evaluation, which are missing out in these previous studies.

Table 2.1 Studies in two-phase cooling system

Author	Experiment or simulation?	Application	Working fluid	Driver	Tevp [°C]	Tcond [°C]	Cooling capacity [W]	Qcond [W]	COP [-]
Heydari (2002)	simulation	computers	R134a	compressor	20	60	--	170	~3.0
Hannemann *et al.* (2004)	experiment	microprocessors /microcontrollers	R134a	liquid pump	32	33	6400	--	--
Mongia *et al.* (2006)	experiment	notebook	R600a	compressor	50	90	50	--	>2.25
Trutassanawin *et al.* (2006))	experiment	1-U rack	R134a	compressor	10 ~ 20	40 ~ 60	121 ~ 268	225	2.8~4.7
Zhou *et al.* (2010)	simulation and experiment	electronics	R134a	compressor	-10~10	30~40	500~5000	--	1.0~2.6
Phelan *et al.* (2004)	experiment	high power microelectronics	NH3 R134a R22	compressor	-15~0	25~55	100~300	--	2~6.6
Marcinichen and Thome (2010)	simulation	server/data center	HFC236fa, HFC245fa, HFC134a,	liquid pump	~60	~60	146~162	--	--
			HC600a-isobutane	compressor	~60	~90	146~162	--	--
Ohadi *et al.* (2012)	simulation	server/data center	R245a	--	76.5	--	50~200	--	--
Lee and Mudawar (2006)	experiment	high-power-density devices	R134a	compressor	-18~24	--	100~600	--	1.2~2.9

3 Experimental facility

In this chapter, a general description of the newly built experimental facility, which includes the flow loop of three specific cycles, major components and instrumentation will be presented.

3.1 Description

Figure 3.1 depicts a diagram of the experimental facility. There are three different cooling cycles integrated to the facility (3 flow loops), which will be explained in the next section. In order to switch from one cycle to another cycle, several ball valves were installed (not shown in Figure 3.1). A more detailed schematic with all the measurement transmitters can be found in Appendix B. In the diagram, MME1 and MME2 are multi-microchannel evaporators and each one was assembled with a pseudo-chip to emulate the CPU on the real server board. The oil-free compressor is a linear reciprocating compressor. The oil-free gear pump is a positive displacement gear pump.
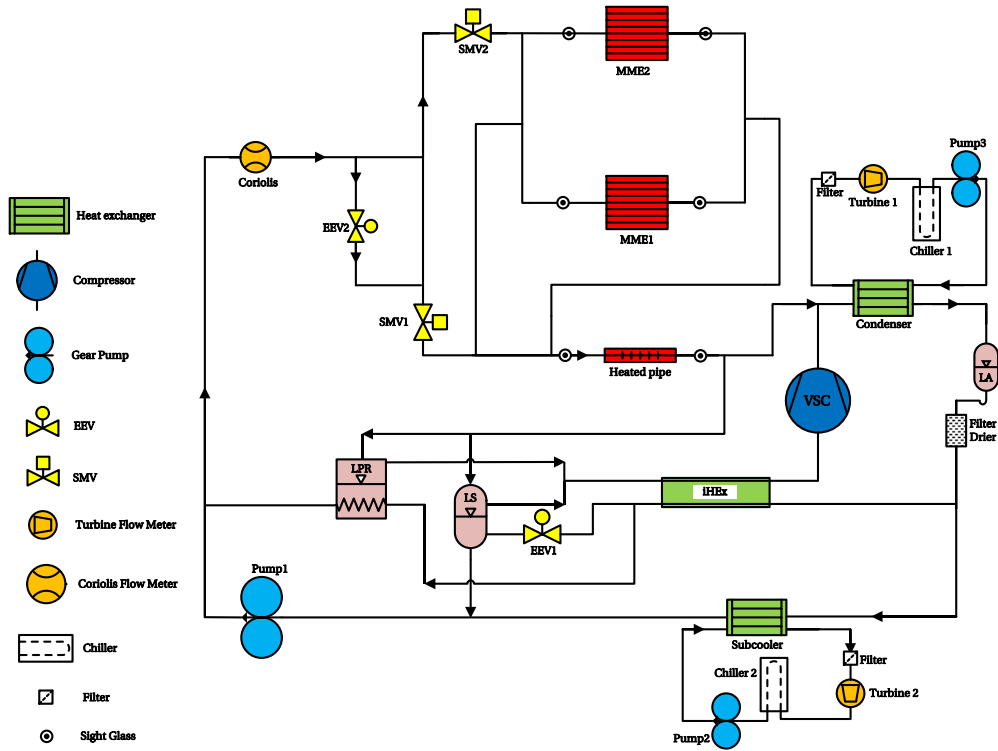
Figure 3.1 Schematic of experimental facility

The three cycles are basically differentiated by the drivers, which are a gear pump (liquid pumping cycle), a linear compressor (vapor compression cycle) and both operating simultaneously in a so-called hybrid cycle.

The experimental facility was built through a breadboard concept, i.e. the main components can be easily changed allowing the impact evaluation of different design on the overall performance of cooling cycles. Figure 3.2 shows the final assembly of the experimental facility.
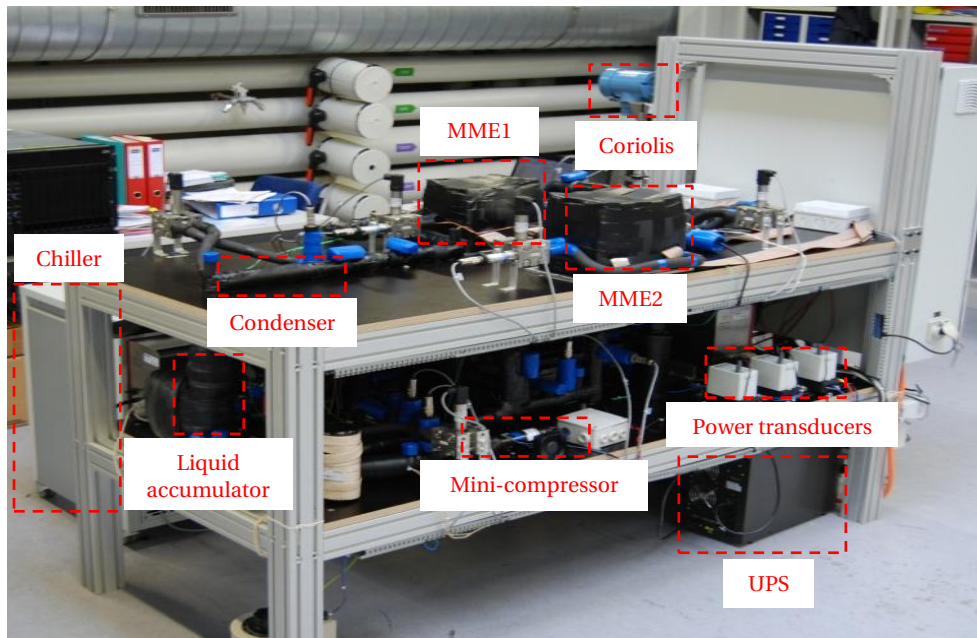
Figure 3.2 Experimental facility at LTCM

3.1.1 Liquid pumping cycle

The liquid pumping cycle uses a gear pump as the driver, and the major components and loop diagram are shown in Figure 3.3. The P-h diagram (Figure 3.4), which was drawn for low pressure refrigerant HFC245fa, shows the thermodynamic conditions for specific points along the cooling cycle, considering 9.9 K and 60 °C for the subcooling and evaporating temperature at the MME (Multi-Microchannel Evaporator) inlet, respectively. The pressure drops in the multi-microchannel evaporator and the post heater were simulated to be on the order of 0.5bar and 0.0bar (it is negligible), respectively, based on preliminary calculations. These values are representative and were defined only for cycle interpretation. The components considered and their main functions are presented below:

a. Variable speed liquid pump: circulates and modulates the working fluid in the refrigerant loop.
b. Stepper motor valve (SMV): controls the liquid flow rate in order to control the outlet vapor quality in each micro-evaporator (0% to 100%).

c. Multi-microchannel evaporator (MME): transfers the heat generated by the pseudo-chip to the refrigerant while keeping the junction temperature below the limit at 85°C (Brunschwiler *et al.* 2009).

d. Post heater: emulates the additional heat dissipating components of a reservoir such as the memories, power suppliers, etc. and uses the remaining latent heat, which is available due to the limitations enforced on the multi-microchannel evaporator.

e. Condenser: counter-flow tube-in-tube exchanger.

f. Liquid accumulator (LA): guarantees that there is only saturated liquid at the liquid pump inlet, independent of changes in thermal load.
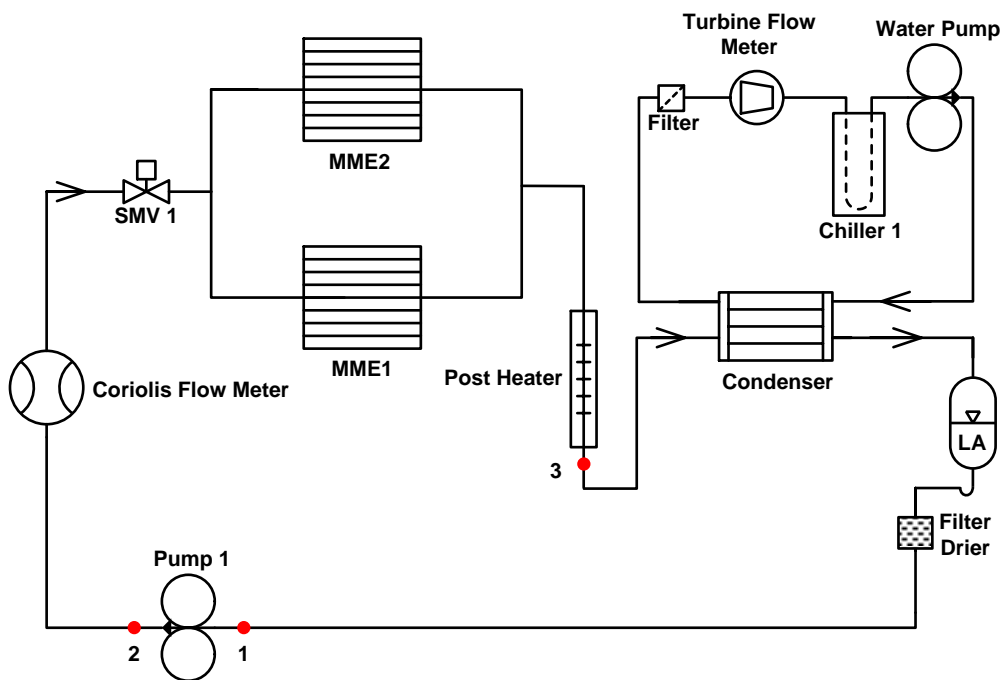
Figure 3.3 Schematic of liquid pumping cooling cycle
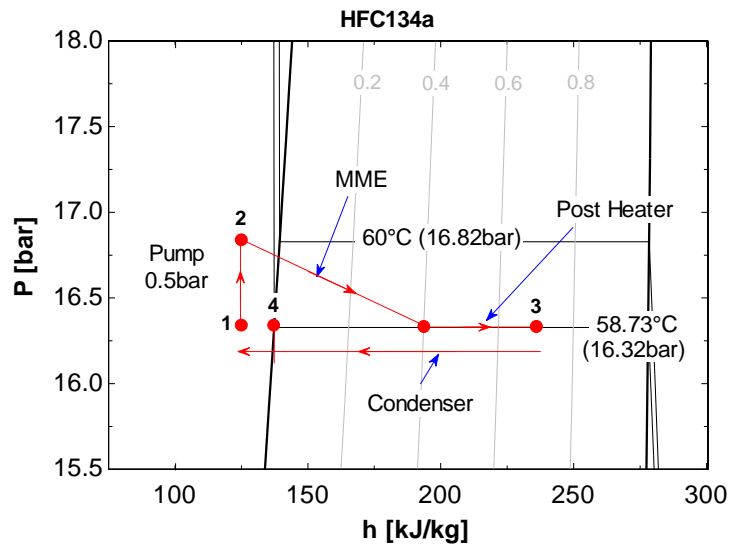
Figure 3.4 HFC134a P-h diagram of the liquid pump cooling cycle

In summary the cycle consists of a liquid pump as the driver to circulate the fluid, one stepper motor valve for controlling the flow, multi-microchannel evaporators for cooling the chips, and a post heater to simulate the other heat dissipating components on blade server board. It is worth noting that the evaporating and condensing temperature are almost the same the pressure drop along evaporators and pipings is ignored, i.e. a "pumped" heat pipe.

This cycle is characterized by having a low initial cost, a low vapor quality at the MME outlet, a high overall efficiency, low maintenance costs and a low condensing temperature similar to that of the electronics being cooled. This is a good operating option when the energy dissipated in the condenser is not necessary to be recovered for other particular higher temperature applications, typically during the summer season. However, the heat can still be recovered if there is an appropriate demand for low quality heat (low exergy), such as heating of building.

3.1.2 Vapor compression cycle

Figure 3.5 shows the two-phase cooling cycle where an oil-free linear vapor compressor is the driver of the working fluid. The P-h diagram (Figure 3.6), which was also drawn for low pressure refrigerant HFC245fa, shows the thermodynamic conditions for specific points

along the cooling cycle, considering 0.69 K and 60 °C for the subcooling and evaporating temperature at the MME inlet, respectively. For the condensing temperature 90 °C was chosen as the target, from heat recovery point of view 90 °C is in the promising range for secondary application such as power co-generation, adsorption cycle, etc; on the other hand, the pressure ratio is 1.9 under such condition which is practical and viable for the compressor. The pressure drops in the MME and the post heater were considered to be the same as for the liquid pumping cycle above. The components considered and their main functions are:

a. Variable speed compressor (VSC): it circulates and modulates the working fluid, and raises the condensing temperature for heat rejection to the water loop for heat recovery.
b. Condenser: counter-flow tube-in-tube exchanger.
c. Liquid accumulator: it guarantees that there is only saturated liquid at the internal heat exchanger (iHEx) inlet.
a. Internal heat exchanger liquid line/suction line (iHEx): it increases the performance of the cooling system. Figure 3.7 shows the ratio of the isentropic COP with superheating at the inlet of the VSC relative to the saturation COP_{sat} (as defined by Gosney (1982)). Condensing and evaporating temperatures of 90 °C and 60 °C were considered, respectively. It is worth noting that for the four potential working fluids analyzed, the ratio increases with higher superheating, although some fluids, such as ammonia, shows decreasing performance (Gosney 1982).
b. Electric expansion valve (EEV): expansion device.
c. Low pressure receiver (LPR): initially to guarantee that only saturated vapor enters the iHEx and then superheated vapor into compressor, which eventually improves the safety operation for the compressor and whole system; additionally it also can be seen as a second internal heat exchanger liquid line/suction line, as shown in Figure 3.6.
d. Stepper motor valve: it modulates the liquid flow rate.
e. Post heater: it emulate the additional heat dissipating components in a server.
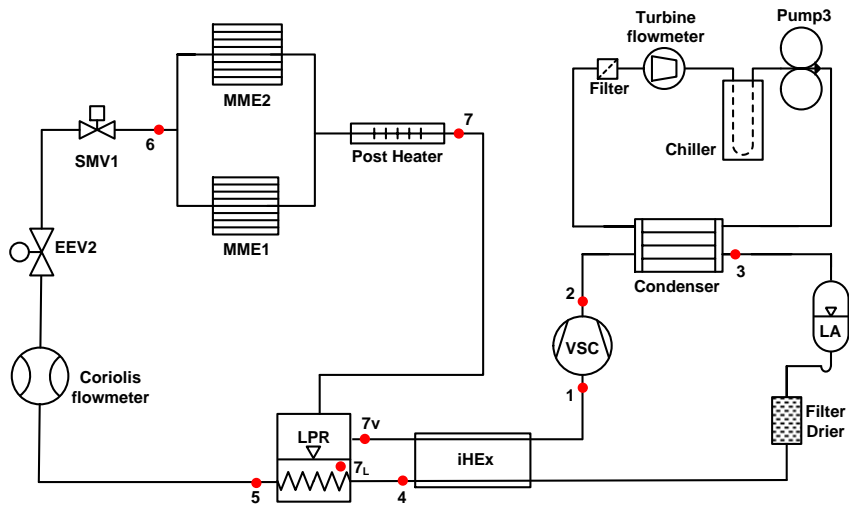
Figure 3.5 Schematic of vapor compression cooling cycle
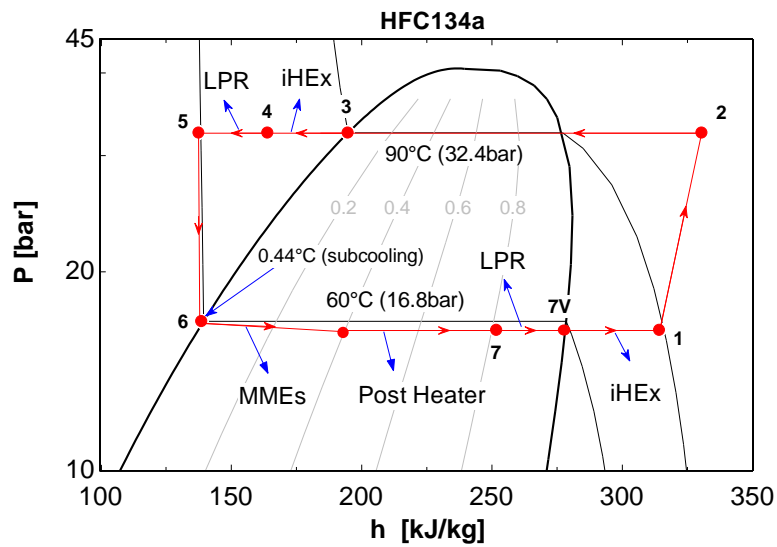
Figure 3.6 HFC245fa P-h diagram of the vapor compression cooling cycle (assuming isentropic compression)

Effect of Superheating
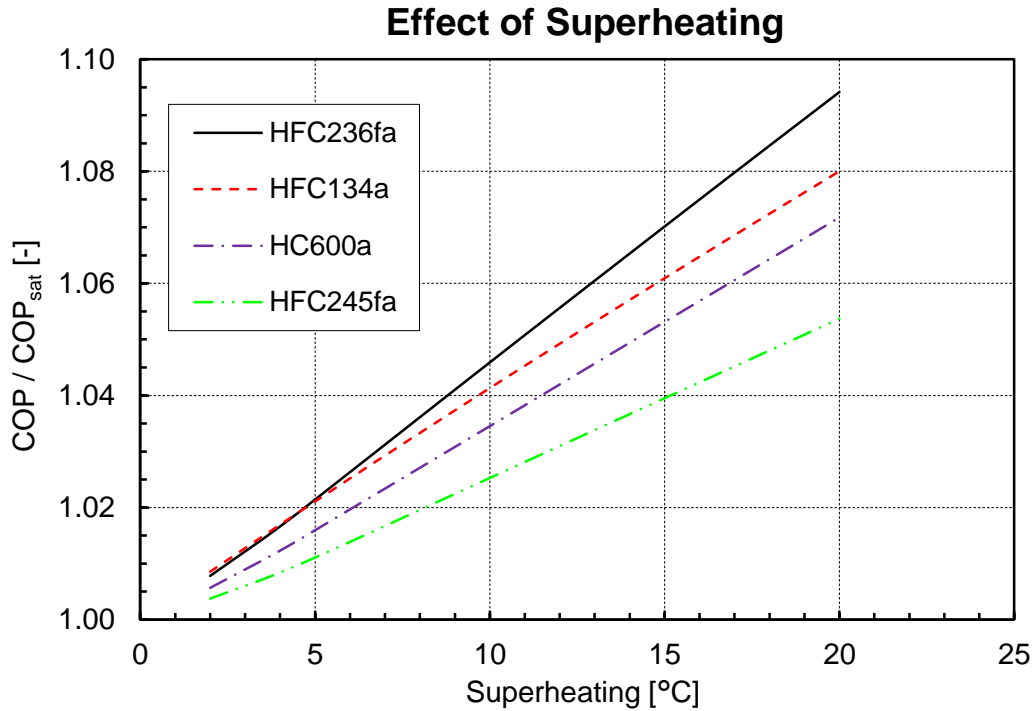
Figure 3.7 Effect of superheating at the inlet of the VSC on the isentropic COP

In summary this cycle consists of an oil-free mini-compressor (VSC) as the driver to circulate the working fluid and raise the condensing temperature for rejecting the heat at a higher temperature, one electric expansion valve (EEV) as the expansion device and one stepper motor valve for finely tuning the flow, multi-microchannel evaporators for cooling the chips, a post heater to simulate other heat dissipating components on the blade server board, a condenser to reject the heat into the secondary fluid, a liquid accumulator, a low pressure receiver (LPR) and an internal heat exchanger to improve the overall efficiency.

This cycle is characterized by a high condensing temperature (high heat recovery potential), a high range of controllability of the MME inlet subcooling (characteristic of systems with VSC and EEV), a medium overall efficiency when compared with the liquid pumping cooling cycle (depends on the potential for heat recovery in the condenser). This is a good operating option when the energy dissipated in the condenser is recovered for other use, typically during the winter season when considering a district heating application (high exergy).

34

3.1.3 Hybrid cycle

Figure 3.8 shows the two-phase cooling cycle where a vapor compressor and a liquid pump are the drivers of the working fluid. This cycle considers the following components and functions:

a. Variable speed compressor (VSC): it circulates and modulates the refrigerant in the *condensing loop* and raises the condensing temperature for heat rejection to the *water loop* for heat recovery.

b. Variable speed liquid pump: it circulates and modulates the working fluid in the *cooling loop* to cool the pseudo-chips.

c. Condenser: counter-flow tube-in-tube exchanger.

d. Liquid accumulator (LA): it guarantees that there is only saturated liquid at the internal heat exchanger (iHEx) inlet.

e. Internal heat exchanger liquid line/suction line (iHEx): it increases the performance of the cooling system.

f. Electric expansion valve (EEV): expansion device in the condensing loop.

g. Liquid separator: it guarantees that liquid working fluid enters the pump and vapor working fluid enters the iHEx.

h. Stepper motor valve (SMV): it modulates the liquid flow rate.

i. Multi-microchannel evaporator (MME): it transfers the heat away from the pseudo-chip.

j. Post heater: it emulates the additional heat dissipating components.
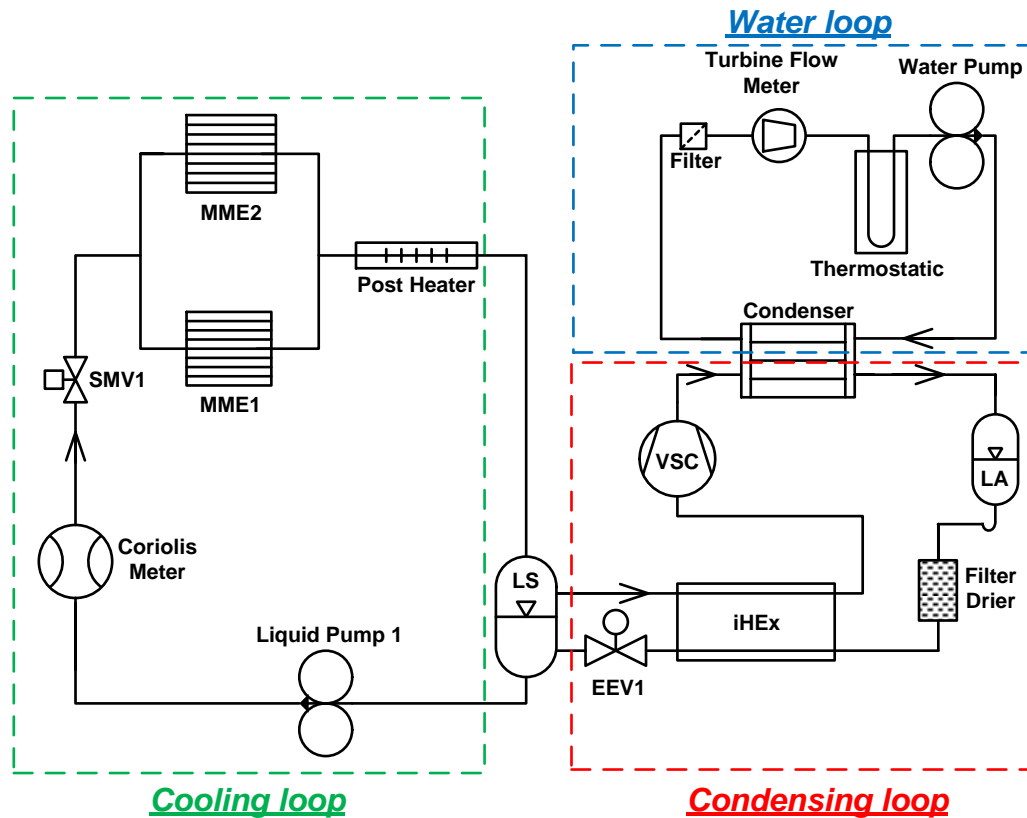
Figure 3.8 Schematic of hybrid cooling cycle

This cycle utilizes both types of drivers working simultaneously (a very versatile solution). Basically it can be seen as two sub-loops on the refrigerant side, one is the *cooling loop* which consists of a liquid pump to circulate the fluid, one stepper motor valve for controlling the flow, micro-evaporators for cooling the chips, and a post heater to simulate other heat dissipating components on the blade server board. The other sub-loop is the *condensing loop* which consists of an oil-free mini-compressor (VSC) as the driver, a condenser to reject the heat into the *water loop* at high temperature, a liquid accumulator, an internal heat exchanger to improve the overall efficiency and an electric expansion valve (EEV). The *condensing loop* functions are to remove the heat transferred to the *cooling loop*, raise it to a higher exergy level (temperature) and, finally, to reject the heat to the external water loop. The two sub-loops on the refrigerant side are connected by a liquid separator (LS).

There are several significant advantages in this cycle, such as a high condensing temperature (larger heat recovery potential), better controllability with more actuators, wide operating conditions (applicable for summer and winter with optimal running modes including free-cooling), adaptable configurations (capable to run only with liquid pump driven cycle with flexible design). There are also few disadvantages such as complexity, cost, and maintenance.

3.2 Components

The main components installed in the experimental facility are described below.

3.2.1 Multi-microchannel evaporator

Two multi-microchannel evaporators were assembled in parallel in the experimental facility and each one cooled one pseudo-chip, the latter which consisted of 35 heaters and temperature sensors (2.5 mm by 2.5 mm in size) to represent those on typical blade servers with two CPUs, as shown in Figure 3.9. The pseudo-chip can generate heat as required by controlling the input voltage. The final assembly is showed in Figure 3.10 with the thermal insulation removed.
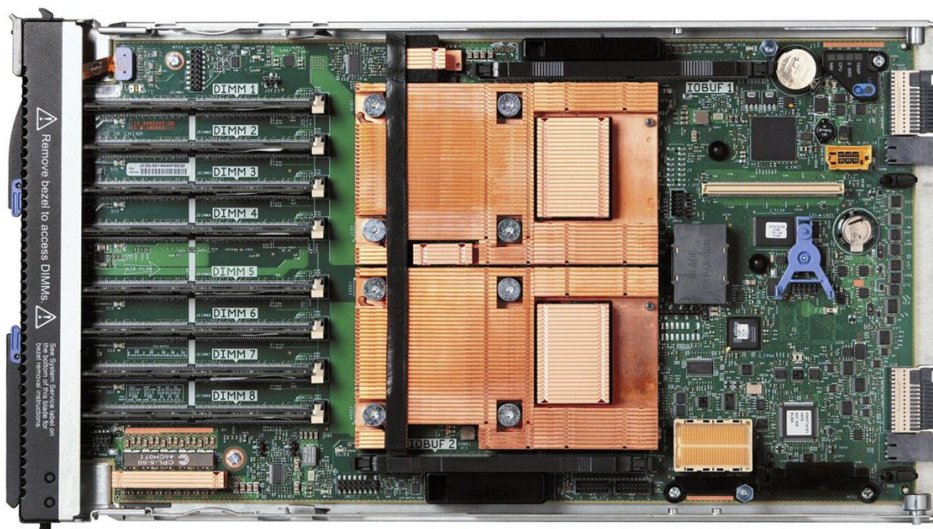
Figure 3.9 Typical blade with two microprocessors and a heat generation capacity higher than 300W setup for air cooling (IBM 2011)

Figure 3.10 Pseudo-chips and multi-microchannel evaporators assembly

A same design of pseudo-chip/MME assembly used in this facility has been extensively tested to study flow boiling heat transfer, two-phase pressure drops, hot spot cooling with non-uniform heat fluxes, transient cooling, etc. by Costa-Patry *et al.* (2011) and Madhour *et al.* (2011), with simulations being performed by Olivier *et al.* (2011). The copper MME was manufactured by Wolverine Tube Inc. to LTCM's specification using a micro-deformation technology. Figure 3.11 and Figure 3.12 show respectively the MME's top view and the schematic of a multi-microchannel evaporator, and Table 3.1 lists the detailed dimensions. The manufacturing process, in summary, is: i) raise the fins from a copper block, and ii) mill a copper surface around the fins to the desired thickness, and iii) close the channels' extremities by brazing a copper cover plate over the fins on the copper surface.
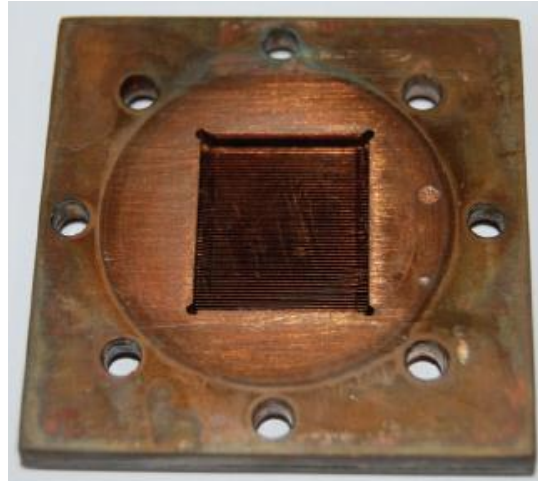
Figure 3.11 Top view of copper MME
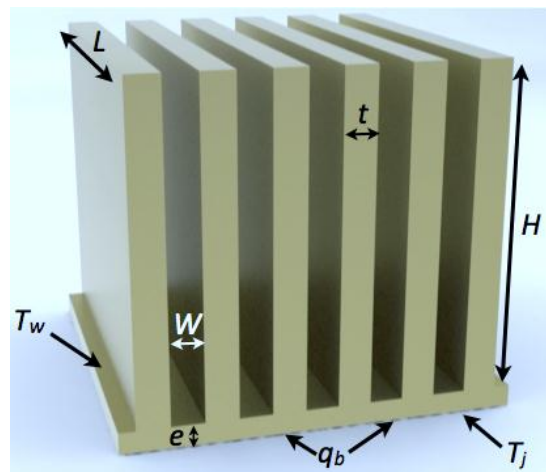
Figure 3.12 Schematic of a multi-microchannel evaporator

Table 3.1 Dimensions of MME

Parameter	Value
Fin height (H)	1.7 mm
Fin thickness (t)	0.17 mm
Channel width (W)	0.17 mm
Base thickness (e)	1 mm
Number of fins (N)	53
Heated length	13.5 mm
Heated width	18.5 mm

It is worth mentioning that the applicability of the cooling cycles described are not restricted to only two microprocessors as built in this facility but can be applied to blade servers[1] and clusters, which may have up to 64 blades or more per rack cabinet. Thus, each blade can have two (or more) microprocessors with a heat generation higher than 150W. If the auxiliary electronics (memories, DC/DC converters, etc.) on the blade are considered, the total heat generation per blade can be 300W or higher. Thus, the post heater described in the cooling cycles has the function to emulate and cool these auxiliary electronics that can represent about 60% of the total heat load on the blade, but have a larger surface area compared to the CPU and thus a lower heat flux.

Between the micro-evaporators and pseudo-chips, a thin layer of thermal interface material (TIM) was applied. The TIM was a high thermal conductivity liquid metal alloy made of gallium, indium and tin (62.5Ga-21.5In-16.0Sn) with a melting temperature of 10.7 °C. The measured bulk thermal conductivity is 35 W/(m·K) (Costa-Patry 2011).

3.2.2 Mini-compressor

The oil-free linear mini-compressor is manufactured by Embraco and shown in Figure 3.13.

Figure 3.13 Oil-free mini-compressor

---

1 A blade server is a server chassis housing multiple thin, modular electronic circuit boards, known as server blades. Each blade is a server in its own right, often dedicated to a single application. The blades are literally servers on a card, containing processors, memory, integrated network controllers etc.

It is characterized by a variable swept volume whose maximum is 0.267 cm^3 and a dead volume of 0.007854 cm^3, and fixed operating frequency of 336.4 Hz. These parameters will be used to experimentally adjust a semi-empirical equation for the volumetric efficiency. This compressor was designed for normal operation conditions of domestic refrigeration systems, not the much higher temperatures employed here. It is worth to mention that the oil-free design can make the system simple without additional components such as oil separator, etc, which also means the cost can be reduced; on the other hand, since the multi-microchannel evaporator is in micro scale, potentially certain lubricant will remain on the surface of the channel which will jeopardize the performance of the evaporator. This compressor is controlled by changing its stroke length (at constant frequency) and thus changes the capacity.

3.2.3 Liquid pump

Three positive displacement gear pumps were installed in the experimental facility, made by Ismatec. For the liquid pumping and hybrid cycles the pump is used for driving the subcooled working liquid to MMEs for cooling the pseudo-chips and other heat dissipating components; another two pumps were installed in the water loops (condenser and subcooler) for precise control of the water flow rate for heat recovery. All these pumps are speed controlled.

The pumps used in this facility were manufactured by ISMATEC. The model of the drives is MCP-Z process, and the headers are Z-1830.

3.2.4 Condenser

A tube-in-tube condenser model HE 0.5 manufactured by Danfoss was used. The drawing and dimensions of the condenser are shown in Figure 3.14 and Table 3.2, respectively.
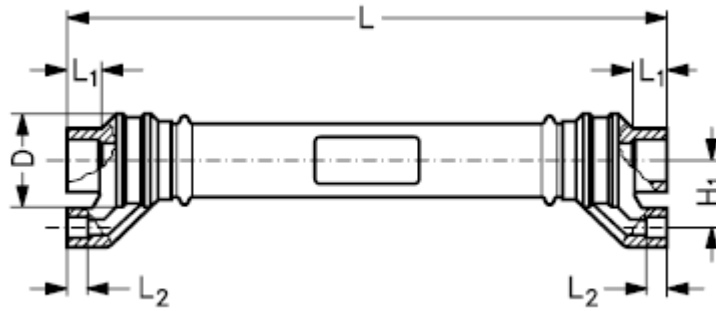
Figure 3.14 Drawing of tube-in-tube condenser

Table 3.2 Dimensions of tube-in-tube condenser

Type	H1(mm)	L (mm)	L1 (mm)	L2 (mm)	ØD (mm)	Weight (kg)
HE 0.5	20	178	10	7	27.5	0.3

3.2.5 Electric expansion valve

An EEV model HP120 and manufactured by Sporlan was used in the vapor compression and hybrid cycles after the iHEx (high pressure line), made by Sporlan. It is a pulse width modulated design, i.e. the plunger operates with a constant frequency of on-off (typically 0.5 – 2 Hz) and a duty cycle is possible to be modulated (0-100%) which permits controlling the ratio of expansion. Originally, for the vapor compression cycle, such a valve was used as an expansion device. However, due to the pulsating characteristics, which affect the MME performance, the valve was eliminated and the expansion function was developed by the stepper motor valve (SMV, *viz*. Figure 3.1), which poses two functions, i.e. expansion and control of outlet vapor quality in the MMEs.

3.2.6 Stepper motor valve

The stepper motor valve (SMV) was used for modulate the mass flow rate of working fluid entering the multi-microchannel evaporators (MMEs). In this type of valve, the position of "plunger" is controlled by a digital electrical circuit which associates the number of steps with a function of one revolution of the motor. The number of steps sent by the controller is "memorized" by the controller, so that the valve can be returned to any previous position at any time, which guarantees an extremely fine control. Additionally, an important

characteristic of this step motor valve is the quick and accurate response, which is desired for the current application.

The model of SMV used in the facility is SEI.5, made by Sporlan. It has 1,596 steps and a travel length of 3.2 mm with resolution of 0.002 mm/step and valve aperture of 0.5 mm.

3.2.7 Thermostatic bath

Two thermostatic baths were connected with independent water loops in the condenser and subcooler to emulate the secondary fluid used for heat rejection and heat recovery. The manufacturer is Lauda and the specifications are listed in Table 3.3.

Table 3.3 Specification of chillers

Model	Description
WK500 (subcooler)	according to DIN 12876 (DEUTSCHES_INSTITUT_FUR_NORMUNG 2001) Working temperature range 0°C ... 40 °C Ambient temperature range 5 °C... 40 °C Temperature control ± 0.5 °C Cooling capacity at 20 °C 0.5 kW
WK2000 (condenser)	according to DIN 12876 (DEUTSCHES_INSTITUT_FUR_NORMUNG 2001) Working temperature range -10 °C ... 40 °C Ambient temperature range 5 °C ... 40 °C Temperature control ± 1.0 °C Cooling capacity at 20 °C 2.2 kW

3.2.8 DC power supply

Each pseudo-chip was powered by a dedicated power supplier, manufactured by Agilent and connected with the computer by adopting a USB 2.0 interface for controlling the voltage and current via the LabVIEW program. The specification of the power suppliers are listed in Table 3.4.

Table 3.4 Performance specification of DC power supplier

Model	N5748A
DC output ratings	Voltage 80 V
	Current 9.5 A
	Power 760 W
Output ripple and noise	CV p-p 80 mV
	CV rms 8 mV
Load effect	Voltage 10 mV
	Current 6.9 mA
Programming accuracy	Voltage 40 mV
	Current 9.5 mA
Measurement accuracy	Voltage 80 mV
	Current 28.5 mA
Command response time	55 ms

3.3   Instrumentation and measurement

The experimental facility was equiped with National Instrument data acquisition system (NI DAQ) which was connected with a computer and running via LabVIEW software. The measurement transmitters for temperature, pressure, differential pressure, mass flow rate, etc. were connected with the NI DAQ. The period of data acquisition was fixed at 0.75 s and the number of samplings for each acquisition was 850 at a rate of 1000 Hz.

A NI SCXI-1001 was installed to house, power, and control the SCXI modules, and also routes analog and digital signals and acts as the communication conduit between modules. Table 3.5 lists the main components of NI DAQ.

Table 3.5 NI DAQ system components

Module	Description
SCXI-1001	12-Slot Chassis.
PCI-6221	RS232 serial interface, 16-Bit, 250 kS/s, 16 analog inputs with 37-Pin D-Sub.
SCXI-1112	8-channel thermocouple input module with Cold-junction compensation per channel.
SCXI-1160	16 independent SPDT electromechanical relays
SCXI-1102	32-channel amplifier, designed for high-accuracy thermocouple measurements, also can acquire millivolt, volt, 0 to 20 mA, and 4 to 20 mA current input signals.
SCXI-1124	6-channel isolated source for static DC (low bandwidth) voltage or current signals.

The measurement sensors will be explained briefly as in following section, more details regarding the calibration and uncertainty analysis will be detailed in Appendix A.

3.3.1 Temperature

K-Type thermocouples, made by Thermocoax, were used in the experimental facility. Cold junction compensated connection blocks of NI, especially made for thermocouple measurements, were used to eliminate the effect of ambient temperature instability. For these blocks, NI acquisition software provides built-in calibration curves for thermocouples. To eliminate the actual deviation from these built-in functions, an in-house thermocouple calibration was carried out.

The calibrations of diode sensors in the pseudo-chips were done with the existing experimental loop, by varying the circulating single-phase fluid's temperature. To control the temperature, the thermostatic bath in the condenser was used while maintaining adiabatic conditions in the test section. The temperature is taken as the average of MMEs' inlet and outlet temperatures.

3.3.2 Pressure

A total of 14 units of pressure transmitters were used in this facility, made by Keller, which were PAA 30bar and PAA 100bar with two different full scale ranges. All the pressure transmitters were calibrated against a standard dead weight balance following a well-defined procedure before being installed on the experimental facility (BARNET_INSTRUMENTS_LIMITED 1980).

3.3.3 Differential pressure

A total of seven units of differential pressure transmitters were installed, manufactured by Impress Sensors & Systems, calibrated by using a U-tube manometer filled with alcohol F25 MEK (Methyl Ethyl Ketone) which has a density of 806 kg/m^3 at 20 °C (based on standard DIN 51757 (DEUTSCHES_INSTITUT_FUR_NORMUNG 2011)).

3.3.4 Mass flow rate

A coriolis flow meter was used to measure the mass flow rate of the working fluid. The specification is a Micro Motion Elite CMF010M323, 1700R11 MVD with calibrated certificate, i.e. ±0.051% of rate accuracy and repeatability ±0.025% of rate. The 4-20 mA output current from the meter was acquired by the National Instrument Data Acquisition System, and the mass flow rate was calculated by the following linear correlation:

$$\dot{m} = 4999.900 \cdot I - 19.312 \qquad\qquad 3.1$$

where

$\dot{m}$ is the mass flow rate (kg/h),

I is the output amperage from the Coriolis meter which was acquired by NI DAQ.

3.3.5 Volumetric flow rate

Two turbine flow meters were installed in the two water loops, i.e. one for the condenser and another one for the subcooler. Both were calibrated by using a precise Coriolis flow meter as a standard. More details can be found in Appendix A.

3.3.6 Power consumption

Six units of power transducers were installed for measuring electrical parameters such as current, voltage, power and electrical consumption for several key components such as drivers and electrical valves. Two types of power transducers were used, i.e. for AC components (i.e. post heater, liquid pumps) and DC components (i.e. compressor, SMV and EEV), respectively, all made by GMC Instrument with the accuracy of ±0.5% of full scale from manufacturer's calibration report. A series of calibrations were carried out before being installed.

3.3.7 The MMEs' outlet vapor quality (x_o)

The MMEs'outlet vapor quality (x_o) was calculated considering Equations 3.2 to 3.4. It is an important parameter to be controlled to avoid conditions of critical heat flux or dryout which is associated with the critical vapor quality. The uncertainty was determined by means of the propagation of errors (ASME 1998) associated with the power suppliers, Coriolis mass flow meter, differential and absolute pressure transducers and K-type thermocouple, which showed a value of ±0.5%. For data processing, all thermodynamic and thermophysical properties were calculated by REFPROP (Tillner-Roth and Baehr 1994; Lemmon 2010).

$$h_i = f(P_i, T_i) \text{ , determined by REFPROP} \qquad 3.2$$

$$h_o = \frac{W_{input}}{\dot{m}} + h_i \text{ , energy balance between inlet and outlet of the two parallel MMEs' assembly (\textit{viz.}Figure 3.15)} \qquad 3.3$$

$$x_o = f(h_o, p_o) \text{ , determined by REFPROP} \qquad 3.4$$

where h_i is the specific enthalpy at the inlet junction of the two MMEs, h_o the specific enthalpy at the outlet junction of the two MMEs, $\dot{m}$ the total mass flow rate and W_{input} the total input power of the two pseudo-CPU chips. An adiabatic condition of the ambient was assumed between inlet and outlet of the MMEs, i.e. no heat loss.
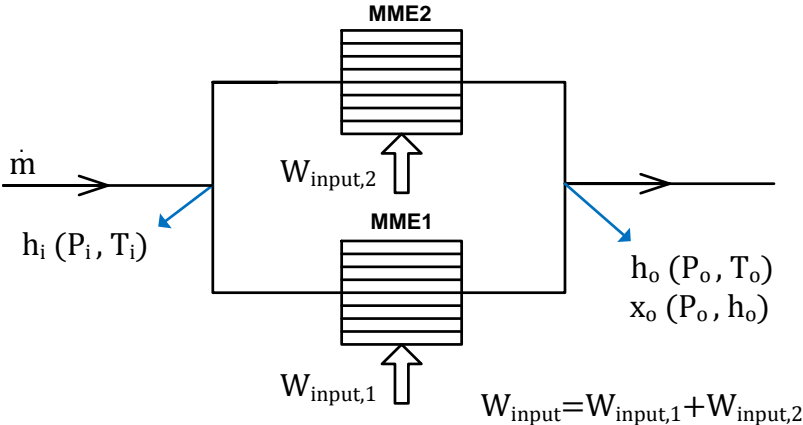
Figure 3.15 Energy balance in the MMEs assembly

4 Controls

In the previous chapter, the facility and main components were described and the issues that need to be addressed how to make the system work properly to fulfill the goals were presented. In this chapter, the control strategies will be introduced first and then the control development and evaluation of each cycle will be presented.

4.1 Control strategy

Based on previous explanations, the first goal is to maintain the chip temperature below a pre-established level, which is currently defined to be 85 °C, by controlling the inlet conditions of the micro-evaporator (pressure, subcooling and mass flow rate). It is imperative to keep the multi-microchannel evaporator (MME) outlet vapor quality below that of the critical vapor quality, which is associated with the critical heat flux. Due to this exit vapor quality limitation (it was decided not to surpass one-half of the critical vapor quality as a tentative safety margin), additional latent heat is available, which can be used by other lower heat flux generating components. The critical heat flux and critical vapor quality are predicted using methods developed by Ong and Thome (2011), which are a function of micro-evaporator inlet conditions, flow rate and microchannel dimensions.

Another parameter that must be controlled is the condensing pressure (condensing temperature). The major purpose of doing this is to recover the energy transferred by the refrigerant in the condenser to heat buildings, residences, district heating, or to be used for other applications such as preheating boiler feed water in thermal power plants, etc.

Since each cycle has its dedicated actuators and specific characteristics, to reach the objectives described above specific controllable variables were defined and particular

strategies were developed accordingly. It is worth noting that even though these controllers were defined for current research objectives, in fact there are also other possible options which can be used to fit for a variety of applications. <u>Furthermore, because of the marginal bandwidth available on CPUs of real data centers for monitoring their operating temperature, the control scheme must be a simple one, if that is feasible, and hence that will be an objective here.</u>

4.1.1 Liquid pumping cycle

In the liquid pumping cycle, the outlet vapor quality (x_o) was controlled by a stepper motor valve (single input single output, SISO strategy) and the condensing pressure (P_{cond}) by a variable speed liquid pump (SISO strategy), which modulates the flow rate of the secondary fluid (distilled water) at the condenser. The driver of the working fluid in the main loop, i.e. another variable speed liquid pump, was kept running at constant speed. Figure 4.1 shows the control strategies used in a block diagram of the closed loop scheme. It is important to assume that the coupling effects among the controlled variables can be neglected, which means that each controller can be developed independently.
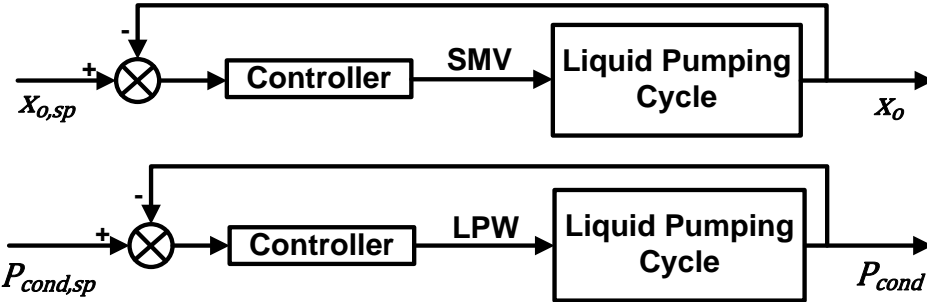
Figure 4.1 Block diagram of control strategies of the liquid pumping cycle

4.1.2 Vapor compression cycle

In the vapor compression cycle, the exit vapor quality x_o was controlled by a variable volumetric displacement vapor compressor and a stepper motor valve (single input multiple output, SIMO strategy), and the temperature difference between the water outlet

and working fluid inlet (ΔT_{cond}) by a variable speed liquid pump (SISO strategy). Figure 4.2 shows the control strategies used in a block diagram of the closed loop scheme.
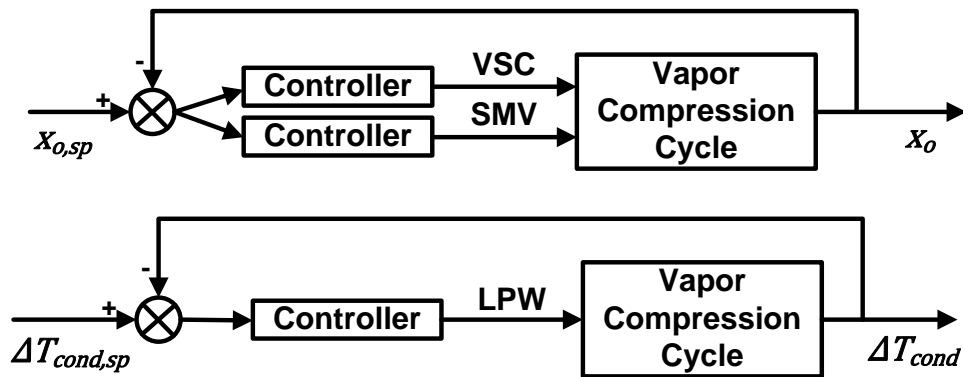
Figure 4.2 Block diagram of control strategies of the vapor compression cycle

4.1.3 Hybrid cycle

In the hybrid cycle, the exit vapor quality x_o was controlled by a variable speed liquid pump and a stepper motor valve (SIMO strategy), the P_{cond} by a variable volumetric displacement vapor compressor and a pulsating electric expansion valve (SIMO strategy), and the ΔT_{cond} by another variable speed liquid pump (SISO strategy). Figure 4.3 shows the control strategies used in a block diagram of the closed loop scheme. As mentioned before, it is important to assume that the coupling effects among the controlled variables can be neglected, which means each controller can be developed independently.
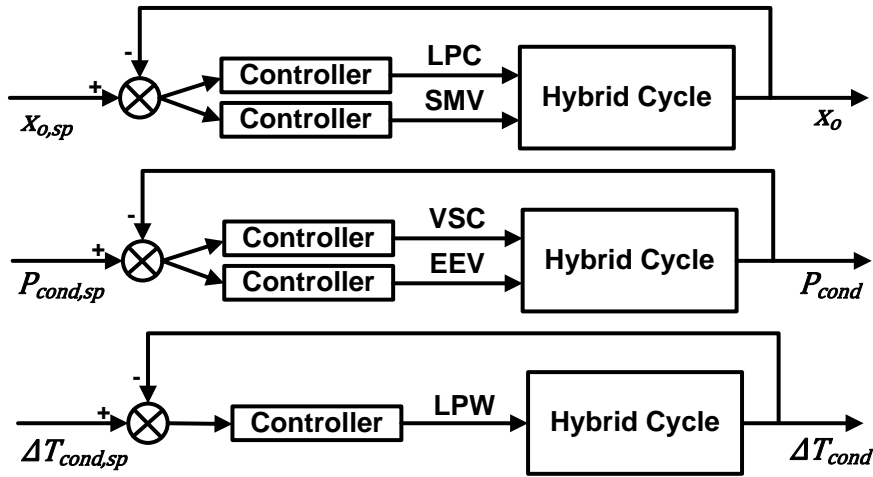
Figure 4.3 Block diagram of the control strategies of hybrid cycle

4.2 Control structure

The controllers were developed by deriving mathematical models capable of representing the dynamic behavior of the system under consideration by means of a system identification process. A PI structure was used for the controllers since the systems showed low order dynamics. A linear first-order model with delay was used for the modeling. Equations 4.1 and 4.2 show the model in time and Laplace domains, respectively.

$$\tau \frac{dy(t)}{dt} + y(t) = K_p u(t - \theta) \qquad 4.1$$

$$G(s) = \frac{y(s)}{u(s)} = \frac{K_p e^{-\theta s}}{\tau s + 1} \qquad 4.2$$

The input u and output y are values of the actuators and controlled variables, respectively, while G is the transfer function, τ is the system time constant, K_p is the gain and θ is the transport delay.

An anti-wind up strategy was also adopted to reduce the accumulated integral error of the controller when the output of the controller sets the value outside the nominal range of the actuators. Equation 4.3 shows the PI controller transfer function in the Laplace domain:

$$C(s) = K_C \left(1 + \frac{1}{T_I s} \right)$$

4.3

where K_C is the PI proportional gain and T_I is the integral time.

4.3 Control development of the liquid pumping cycle

The first controller developed was to modulate the condenser liquid pump speed (LPW_s), i.e. the distilled water (secondary fluid) flow rate to the condenser, in order to maintain the condensing pressure (P_{cond}) at the setpoint value ($P_{cond,sp}$). The second controller was developed to control the MMEs' outlet vapor quality (x_o) by modulating the stepper motor valve aperture (A_{SMV}).

The system identification, controller design and preliminary evaluation by tracking tests, which are conventional steps in the development of new controllers, are presented below. In sequence, a thorough evaluation of the controllers operating together is shown for the so-called dual SISO control strategy. Such a strategy was evaluated by disturbance rejection and flow distribution tests; for the latter, the effects of different heat loads applied on the two micro-evaporators were investigated.

4.3.1 LPW$_s$ controller

Figure 4.4 illustrates the block diagram of the first control loop, where the P_{cond} is the controlled variable ($P_{cond,sp}$ is the setpoint) and LPWs (speed of the pump and thus water flow rate to the condenser) is the manipulated variable.
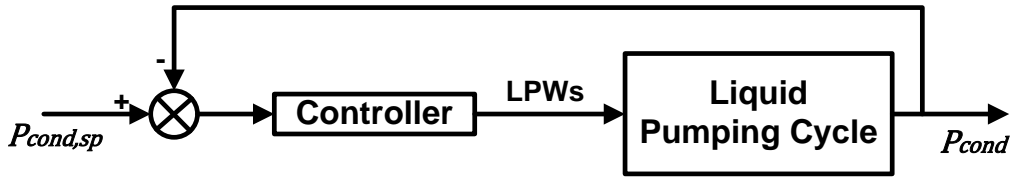
Figure 4.4 Block diagram of LPW$_S$ controller

4.3.1.1 System identification and controller design

The system identification process has the objective of deriving a mathematical model capable of representing the dynamic behavior of the system. A linear first-order model with delay was used to correlate P_{cond} with the LPW_s variations. The condensing pressure was measured with a calibrated pressure transducer at the inlet of the condenser. For such a system, the pressure drop between the inlet of the MMEs and the inlet of the condenser is negligible (< 0.03 bar), so the condensing pressure controller can also be considered as an evaporating pressure controller. As explained in section 4.2, Equations 4.1 and 4.2 show the model in the time and Laplace domains, and the input (u) and output (y) parameters are LPW_s and P_{cond}, respectively.

The model parameters were obtained by varying the LPWs from 1620 rpm to 1800 rpm (step response experiment, *viz.* Figure 4.5). The cycle's liquid pump speed, the water temperature (secondary fluid) at the inlet of condenser, the SMV's aperture and the heat load on the MMEs were maintained at 3000 rpm, 40 °C, 25%, and 90 W for MME1 and 75 W for MME2, respectively. These operating conditions are from now on referred to as the *standard conditions*.

It is important to mention that during the initial tests it was observed that the subcooler was redundant for this cycle and this level of heat load investigated. This was due to the heat losses in the piping, which ensured that there was always enough subcooling at the inlet of the liquid pump and micro-evaporators. Such a situation might not be the same for the case of better piping insulation and higher heat load, as for an entire blade center (*e.g.*

54

IBM blade center QS22 with a heat load of about 5000 W, IBM (2011)). The subcooling at the inlet manifold of the MMEs in all evaluations considered in this work remained between 2 to 8 K, avoiding the necessity for special controllers to avoid saturation conditions (that is, unwanted vapor in the inlet headers of MME1 and MME2), which would otherwise jeopardize the MMEs' performance by potentially introducing flow maldistribution.

The model parameters K_P, τ and θ were estimated in order to minimize the least square error between the model predictions and the experimental data. For this controller K_P, τ and θ were estimated as -0.8 mbar/rpm, 90.85 s and 2.59 s, respectively. Figure 4.5 and Figure 4.6 depict part of the identification tests, showing the P_{cond} time response to a step change in the LPW_s and the P_{cond} model predictions against the experimental data, respectively, with excellent agreement.
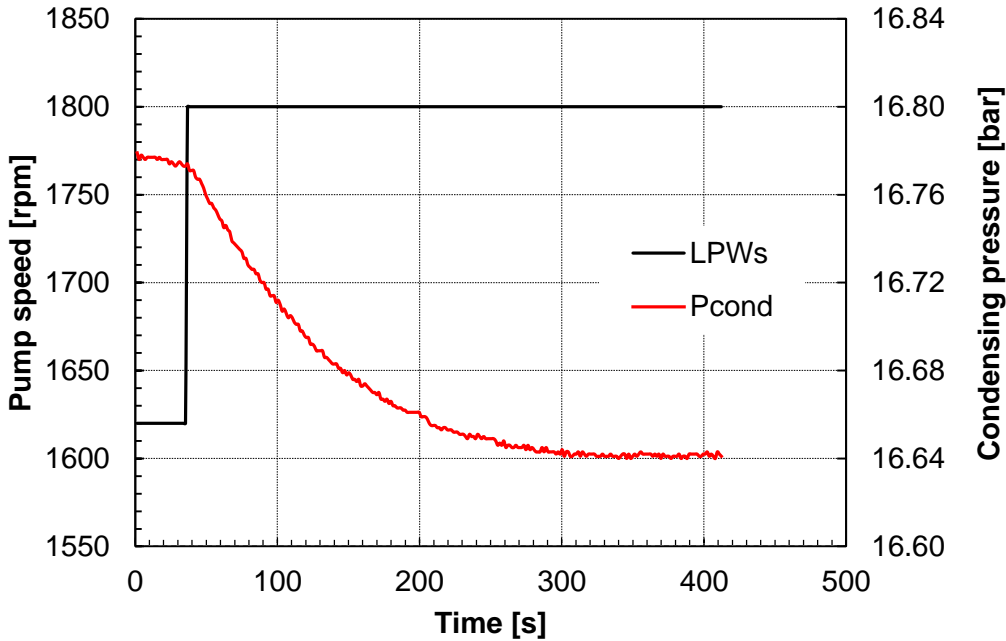
Figure 4.5 LPW$_S$ model identification
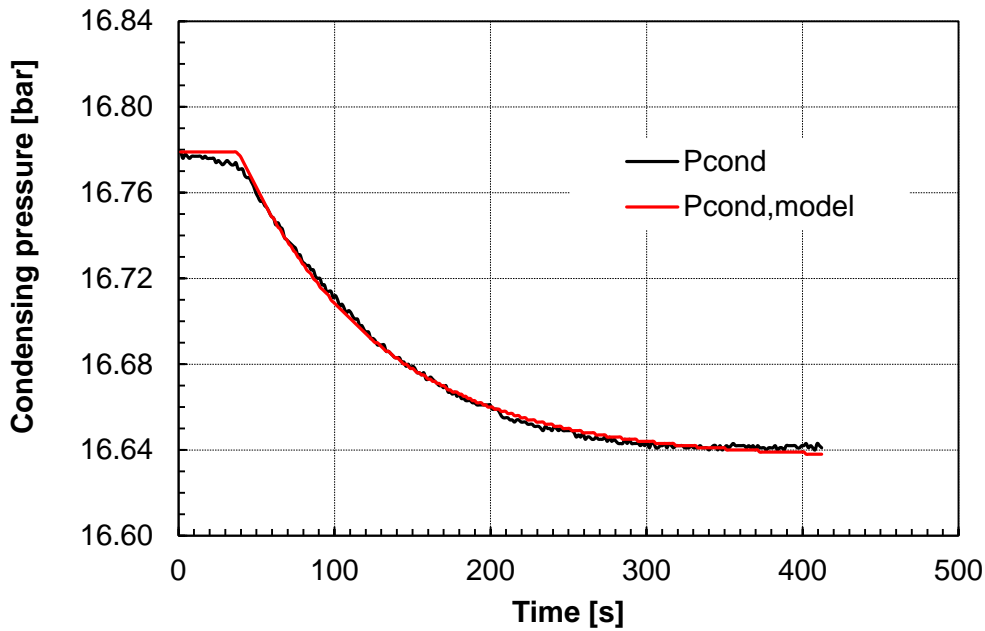
Figure 4.6 LPW$_S$ experimental vs. prediction

The PI controller was designed using the method proposed by Karimi *et al.* (2007), which is based on linear programming. It was computed to guarantee a phase margin of 30°, a gain margin of 2 and a crossover frequency two times larger than in an open loop. The T_I (integral time) and K_C (proportional) parameters were calculated as 90.85 s and -9816 bar/rpm, respectively.

4.3.1.2 *Controller evaluation*

Tracking tests were carried out with the experimental apparatus running under the *standard operating conditions* to evaluate the controller performance. It is important to notice that for each test of evaluation general principles were adopted to determine whether the current state has reached steady-state before kicking in the disturbance for the next step. Figure 4.7 and Figure 4.8 show the results for five steps along the pressure setpoints between 16.8 bar and 17.0 bar for the *LPW$_S$* controller. As can be noticed, the controller increased or decreased the liquid pump speed, in response to a decrease or increase in the pressure setpoint value.
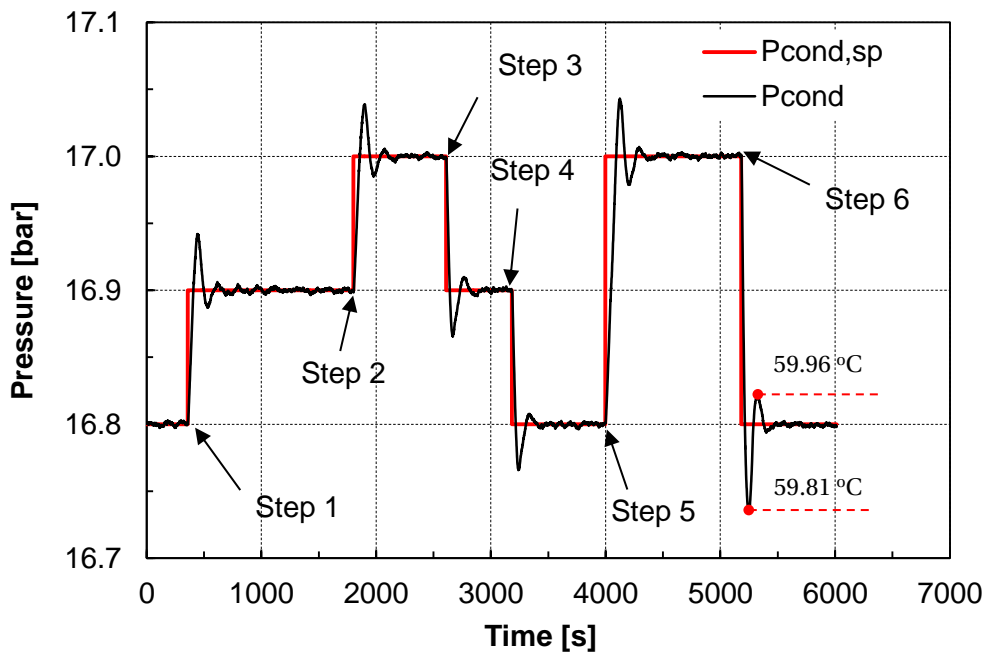
Figure 4.7 P_{cond} setpoint tracking test
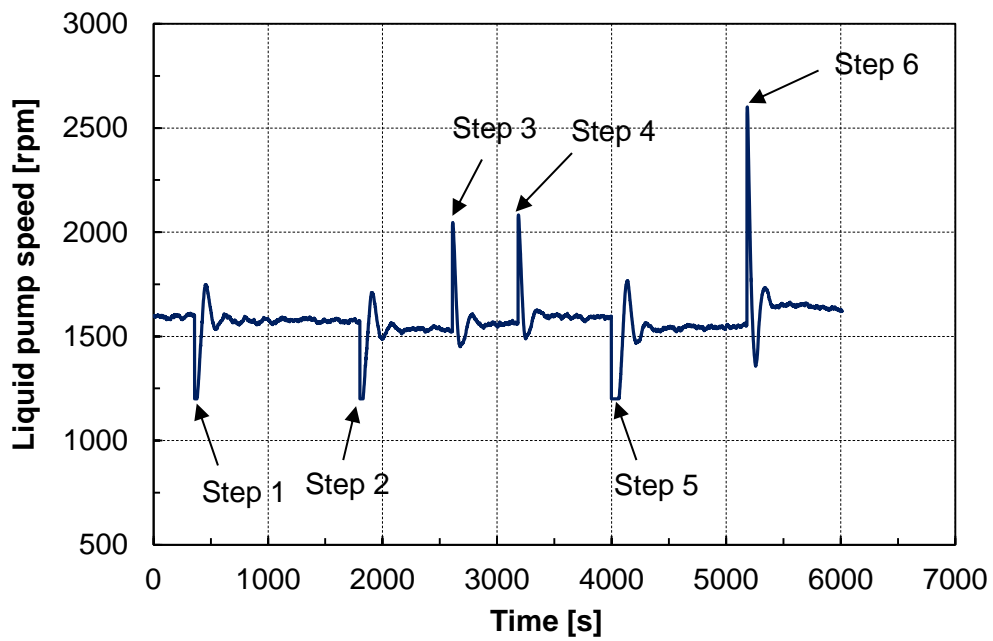
Figure 4.8 LPW_s variation

The results showed that the controller is effective and efficient to track the setpoint of pressure in a short time ($\cong$ 3.5 min after step 6, *viz.* Figure 4.9) with a maximum overshoot in the condensing temperature of only about 0.15 °C (*viz.* Figure 4.7).
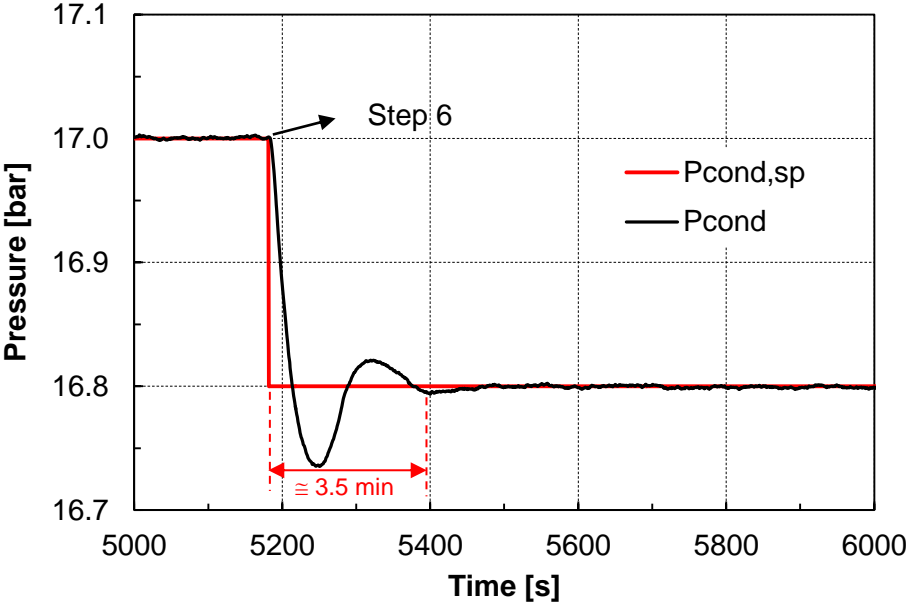
Figure 4.9 P_{cond} variation for step 6

4.3.2 SMV controller

The controller developed for the MMEs' outlet vapor quality considered the SMV as the actuator. It is worth mentioning that this variable has a considerable effect on the performance of the MME (Olivier and Thome 2010), and as a consequence on the overall system. Therefore, for safe operating reasons, such a controller must avoid the critical vapor quality (on setpoint of dryout of the microchannels), a condition where the pseudo-chips could be damaged. Figure 4.10 illustrates the controller's block diagram.
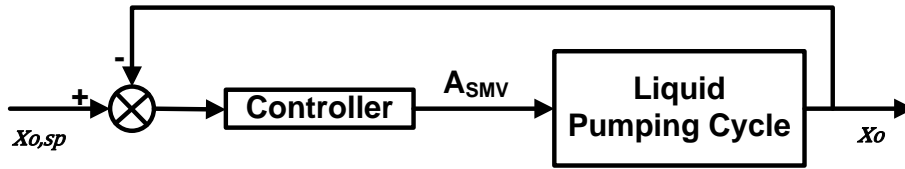
Figure 4.10 SMV controller

4.3.2.1 System identification and controller design

The system identification was developed considering the *standard condition* as a starting point and a change in SMV aperture of 2% each 10 s between 22% and 40% of aperture. The average of vapor quality for the last 5 seconds of each change was considered as the value for each aperture, i.e. the values shown in the Figure 4.11.
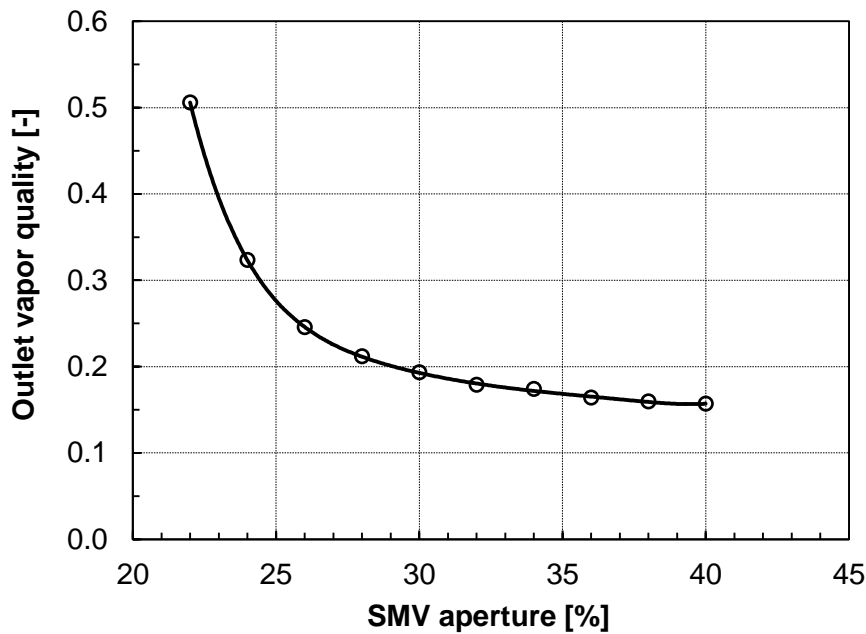
Figure 4.11 System identification: x_o vs. SMV aperture

During the system identification it was observed that small changes in the aperture resulted in a fast response (2s…3s) in the exit vapor quality, as can be seen in Figure 4.12.

Thus, the model of the system was approximated by its static gain (K_P), which varied nonlinearly with the SMV aperture change, as can be seen in Equation 4.4.

$$K_P = \frac{\partial x_o}{\partial A_{SMV}} = -7.8 \times 10^{-6} \cdot A_{SMV}^4 + 10.4 \times 10^{-4} \cdot A_{SMV}^3 - 5.2 \times 10^{-2} \cdot A_{SMV}^2 + 1.16 \cdot A_{SMV} - 9.63 \qquad 4.4$$
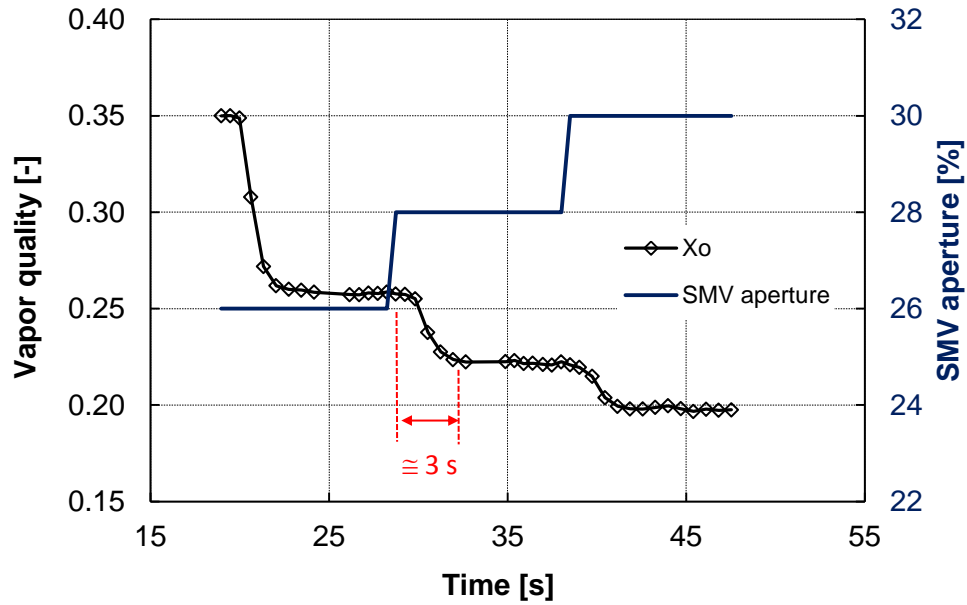
Figure 4.12 System identification: response time of exit vapor quality by changing the SMV aperture

Therefore, a gain-scheduled PI controller was developed whose gain is a function of A_{SMV}. That is, the closed-loop transfer function was represented by Equation 4.5, where the time constant (τ) is given by Equation 4.6.

$$H(s) = \frac{x_o}{x_{o,sp}} = \frac{\frac{K_c}{K_i}s + 1 \qquad \{zeros}{\frac{s(1 + K_c \cdot K_p)}{K_i \cdot K_p} + 1 \quad \{poles}} \qquad 4.5$$

$$\tau = \frac{1 + K_c \cdot K_p}{K_i \cdot K_p} \qquad\qquad 4.6$$

Defining τ_D as the desired closed-loop time constant, and C as a parameter relating the closed-loop pole (p) and zero (z) such that $p = C \cdot z$, Equations 4.7 and 4.8 were obtained for the integral and proportional constants, i.e. K_I and K_C:

$$K_C = \frac{1}{(C-1)K_P} \qquad\qquad 4.7$$

$$K_I = \frac{C}{C-1} \cdot \frac{1}{\tau_D \cdot K_P} = \frac{T_I}{K_C} \qquad\qquad 4.8$$

The gains K_I and K_C of the controller are functions of the static gain of the system K_P and are updated during runtime. C and τ_D can be seen as tuning parameters, which were experimentally adjusted for 15 and 5 s, respectively. Moreover, an anti-wind up strategy was implemented to reduce the accumulated integral error when the output of the controller moved outside the SMV's range (22% to 40% of aperture). It is worth highlighting that other techniques to design the gain-scheduled controller could also be used, for example, the method proposed in (Kunze *et al.* 2007).

4.3.2.2   *Controller evaluation*

Figure 4.13 shows the outlet vapor quality tracking test, where it can be seen that the controller reacted fairly quickly for the 4 steps considered. In the worst case, the controller took about 30 s to stabilize the system; however only a small overshoot was observed, i.e. a maximum of 1.5% in vapor quality. Finally, it can be concluded that the controller was efficient and effective for the actual application, showing a small overshoot and settling time. It is noticed that there is a maximum of 0.005 residual error or offset during the evaluation tests, which is comparably small and potentially could compensate for a load change. Furthermore, from the control theory point of view, it is possible to minimize this offset such as by means of increasing the gain of the controller. However, an increase in gain tends to increase the settling time and may increase the maximum value of error as

well. The optimum response is always achieved through some sort of compromise (Bateson 2002).
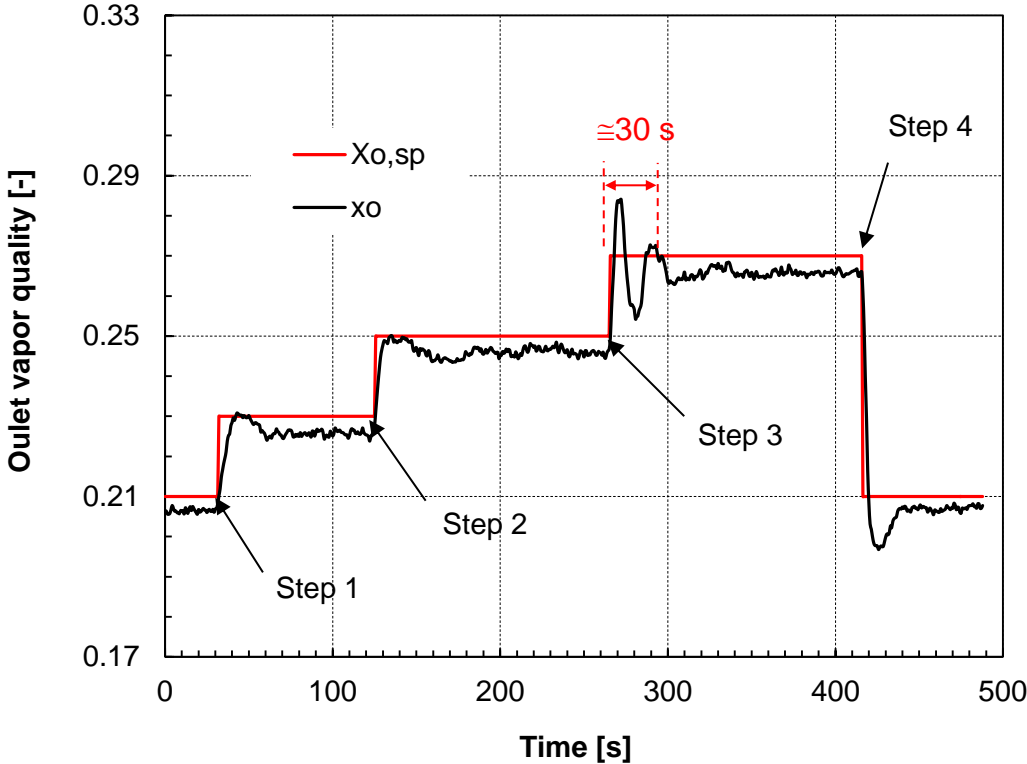
Figure 4.13 Outlet vapor quality tracking test

4.3.3 Dual SISO controller

The dual SISO control strategy was derived from the two individual controllers, as illustrated in the block diagram in Figure 4.14. This allowed the simultaneous control of P_{cond} and x_o to match the thermal load with the cooling capacity for the condensing temperature and vapor quality desired.
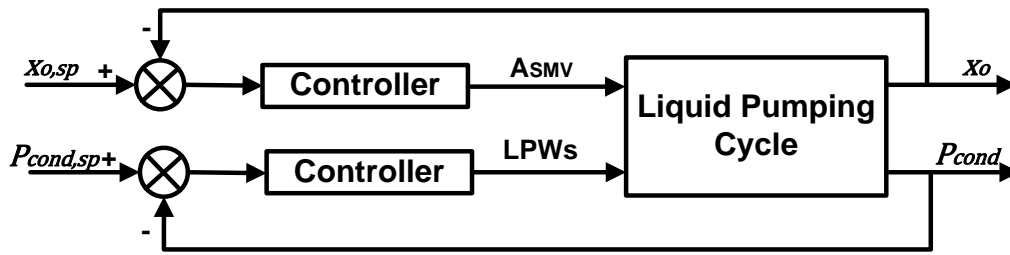
Figure 4.14 The dual SISO controller

Disturbance rejection and flow distribution tests were performed with the experimental apparatus running under a *standard operating condition* to evaluate the controllers' performance. In these tests, after the apparatus was in a steady state regime, the input power on the pseudo-chips (heat load on the MMEs) was changed periodically for a constant period of time between two levels for the disturbance rejection tests and changed to different levels until the steady state condition was established for the flow distribution tests, as will be shown below.

4.3.3.1 Heat load disturbance rejection

The integrated controller or decentralized control structure was first evaluated by considering the *standard conditions* at the beginning of the test, and setpoints of condensing pressure ($P_{cond,sp}$) and outlet vapor quality of 16.8 bar and 22%, respectively. The performance of the control strategies regarding disturbance rejections was evaluated by periodically changing the heat load on the micro-evaporators. As the heat load changed, so did the condensing pressure and vapor quality disturbances, which were detected automatically by the controllers. These in turn increased or decreased the LPW$_S$ and SMV aperture to maintain the pressure and vapor quality at the setpoint.

The heat loads on MME1 and MME2 were changed from 90 W and 75 W to 75 W and 60 W, respectively, considering a periodic disturbance time of 1.4 s. Figure 4.15 shows the input power disturbance on the pseudo-chips and the effect on the average temperature of each chip. This temperature was obtained by averaging the temperature from 11 well distributed

sensors on each pseudo-chip. It can be observed that there was a maximum temperature variation of 1.5 °C, which can be considered to be acceptable when compared to the temperature gradient along such a chip for on-chip single-phase cooling using water (about 2-3 K for uniform heat flux and without heat load disturbance (Ganapati 2009; Meijer *et al.* 2009; Brunschwiler *et al.* 2010)).
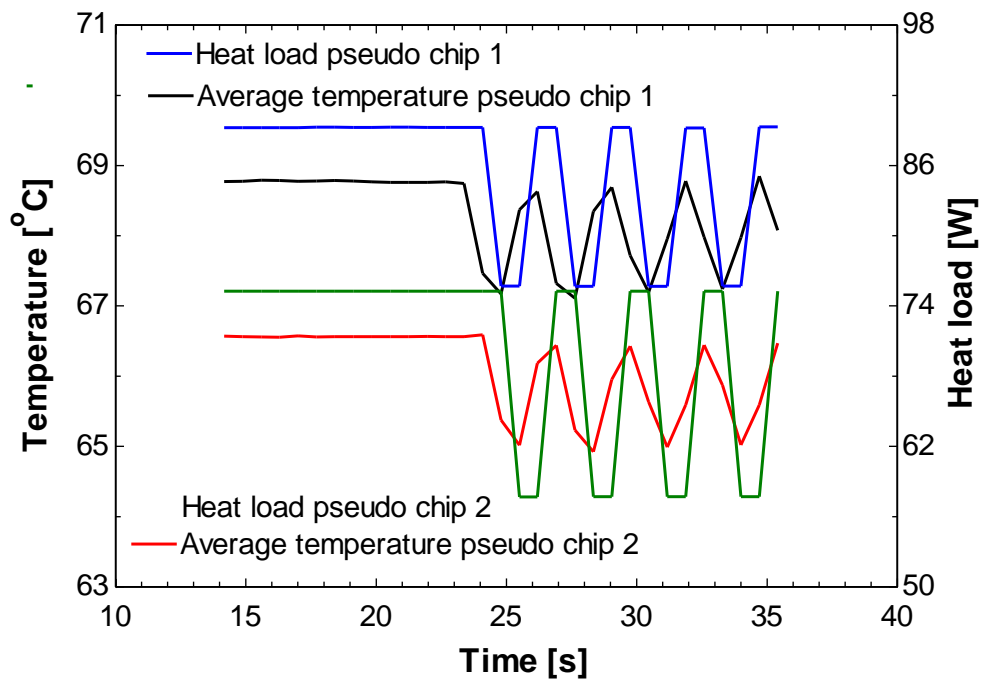
Figure 4.15 Heat load disturbance and pseudo-chip temperatures

Figure 4.16 and Figure 4.17 show the controllers' reaction under the situation of a disturbance. It can be seen that the SMV controller was able to maintain the exit vapor quality to within ±5% of the setpoint. What is important to observe is that the controller was effective, i.e. it showed fast response for the induced disturbance and no instability was observed.

The LPW$_S$ controller (*viz.* Figure 4.17) showed an initial offset when the heat load disturbance started, which represents a condensing temperature deviation of only 0.05 bar or 0.1 °C (it also represents a very small evaporating temperature variation) and it can be seen that the controller was able to reset the offset after about 2.5 minutes. Once again the controller proved to be effective and efficient in maintaining the setpoint.

64
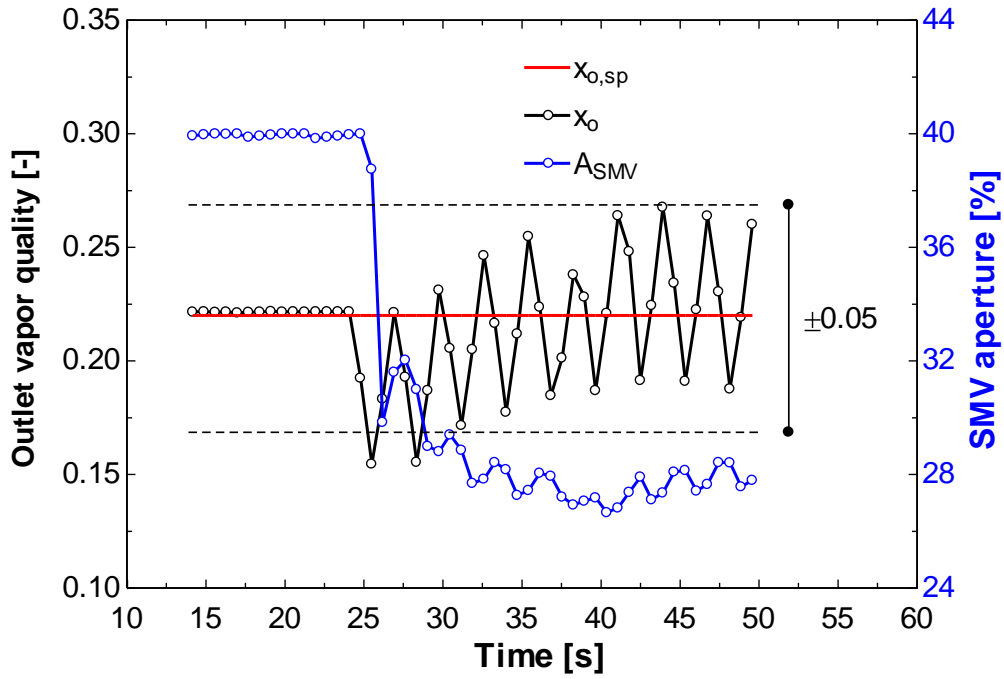
Figure 4.16 Outlet vapor quality and A_{SMV} controller
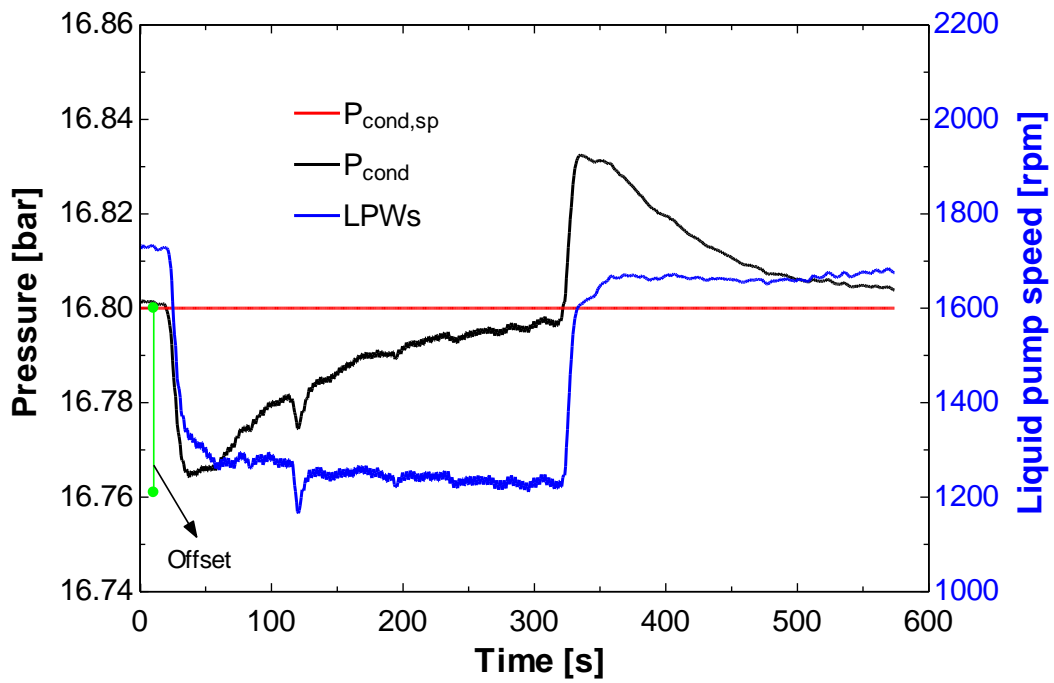
Figure 4.17 Condensing pressure and LPW_S controller

4.3.3.2   Flow distribution for non-uniform heat load

To evaluate the effect of a non-uniform heat load applied to the two MMEs on the flow distribution and, consequently, on the pseudo-chips' temperature and performance of the controllers, tests were developed for different heat loads between 30 W and 90 W and setpoints of outlet vapor quality between 15% and 22%. A total of eight different combinations of such heat loads and three outlet vapor qualities were evaluated, as shown in Figure 4.18.
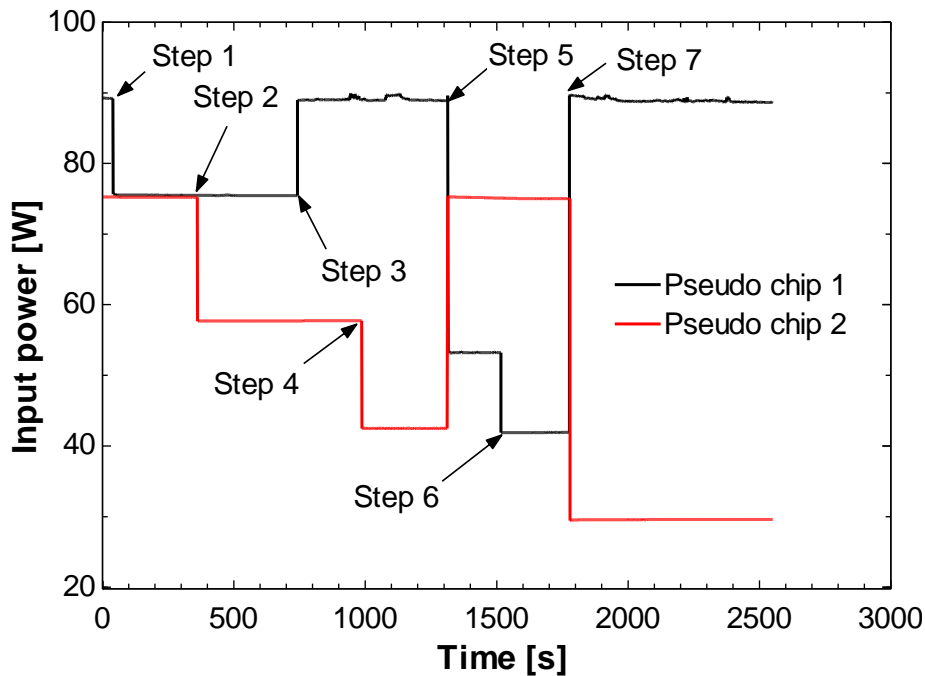
Figure 4.18 Different heat loads on the MMEs

The tests started with the *standard condition*, a setpoint of condensing pressure and outlet vapor quality of 16.8 bar and 22%, and heat loads on MME1 and MME2 of 90 W and 75 W, respectively. Seven steps of heat load combinations were then imposed, with the last one considering three different vapor quality setpoints: 22%, 18% and 15%. The steady state condition was obtained before each new change in heat load or setpoint of vapor quality, Figure 4.19 and Figure 4.20 show the results obtained for the average temperature on the pseudo-chips, the MMEs' outlet vapor qualities and the SMV aperture (action of the controller).
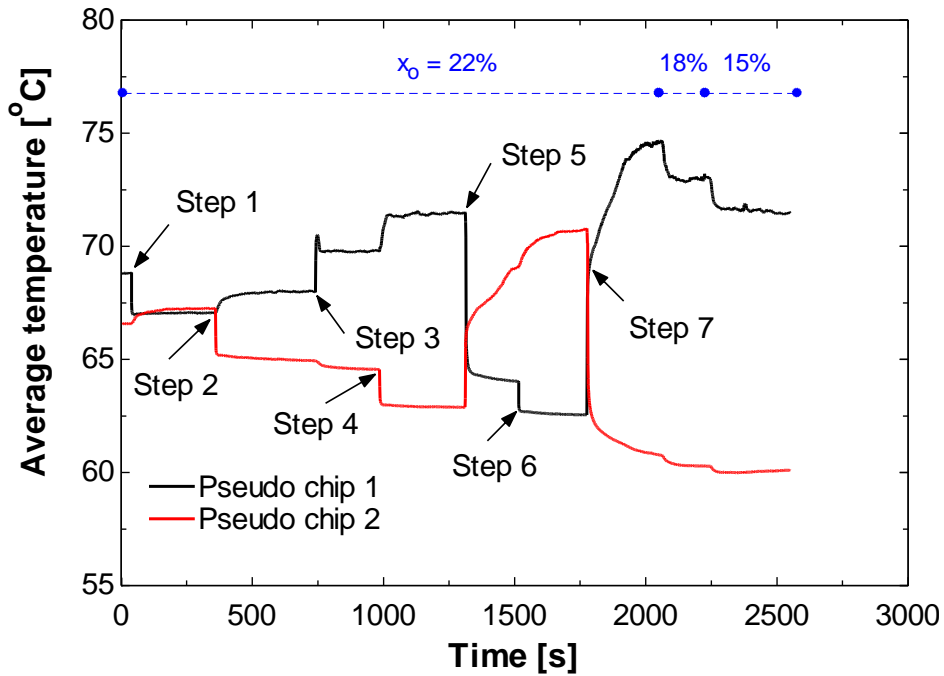
Figure 4.19 Average temperature on the pseudo-chips
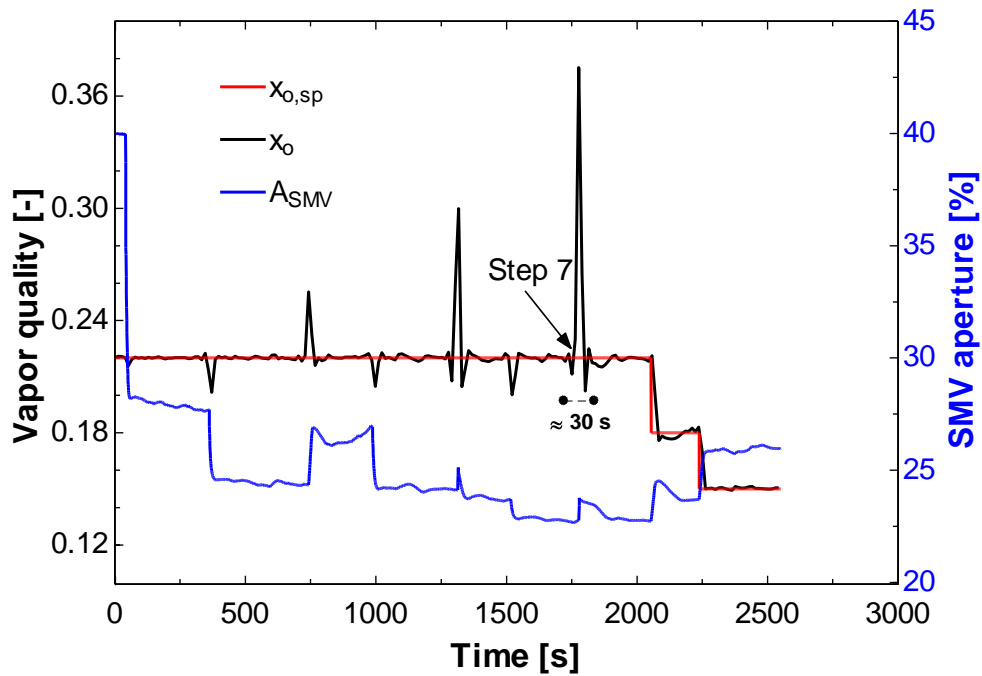
Figure 4.20 Outlet vapor quality and SMV aperture

Firstly, it can be seen that the SMV controller was effective and efficient in controlling the outlet vapor quality under different conditions of heat load and setpoints of outlet vapor

quality. The controller proved to be very fast in reaching the steady state condition, with the maximum transient time observed to be about 30 s in step 7, meanwhile maintaining the pseudo CPU average temperatures well below 85 °C.

Regarding the pseudo-chips' temperatures (*viz.* Figure 4.19), the following aspects were observed:

I. For the same heat load at step 2, the average temperature of both pseudo-chips was the same, i.e. about 67 °C. This implies that the distributors (piping) before and after the MMEs were well designed and that both MMEs have the same mass flow rate.

II. The maximum temperature difference observed was, as expected, in step 7, which considered 90 W on pseudo-chip 1 and 30 W on pseudo-chip 2. A difference of 14.5 K was obtained, where pseudo-chip 1 reached a temperature of 75 °C vs. 60.5 °C on pseudo-chip 2. Despite of this difference, the safety threshold of 85 °C is still far away.

III. The chips' temperature difference and the absolute temperatures were reduced when the setpoint of the outlet vapor quality was reduced. A difference of 11.5 °C and a temperature of 71.5 °C were obtained for pseudo-chip 1 when the outlet vapor quality setpoint was reduced to 15%.

Figure 4.21 shows the effect of a non-uniform heat load on the LPW_s controller. It can be seen that for all ranges of heat loads investigated, the controller was able to control and stabilize the condensing pressure at the setpoint. The maximum disturbance observed was stabilized after 5 min and provoked an overshoot of only 0.1 °C in the condensing temperature.
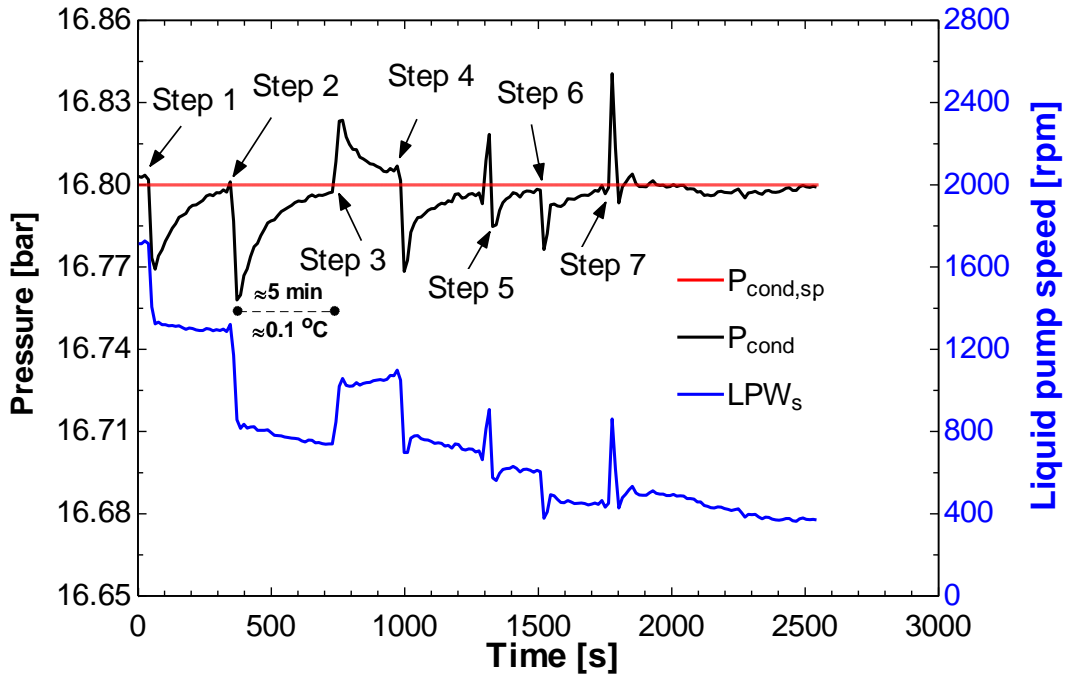
Figure 4.21 Condensing pressure and LPW_s

Finally, it can be highlighted that the dual SISO strategy proved to be a simple and effective way of controlling the condensing pressure and vapor quality while maintaining the pseudo-chips within a safe operating range. The coupling effect between the two controllable variables was not strong, in other words the controllers have low interaction effects, implying that it was not necessary to apply a more complex centralized MIMO controller.

4.4 Control development of the vapor compression cycle

For the vapor compression cooling system, alternative control strategies were adopted due to its cooling cycle concept being different. In this system, the objective is not only to cool the pseudo-chips but also to potentially recover the energy removed in the condenser, since a higher condensing temperature is possible to be obtained (higher exergy thus available). From this point of view, the differential temperature between outlet water flow and inlet water flow in the condenser (ΔT_{cond}, which is also called the minimum approach temperature difference.) and the MMEs' outlet vapor quality were defined as the variables to be controlled. The manipulated variables were, for the former, the LPW$_S$ and for the

latter the SMV aperture and the mini-compressor stroke. It is worth mentioning that preliminary evaluations for the LPW_S controlling the condensing pressure, which was used in the liquid pumping cooling system, were carried out. However, it showed a strong coupling effect between the condensing pressure and the outlet vapor quality, which provoked instabilities in the system when the controllers were operating together.

The SMV was used as an expansion device (Figure 3.5) and also as an actuator to control the outlet vapor quality together with the mini-compressor. The results obtained in this work, as will be shown, proved that since the system is well designed and controlled, a SMV for each MME is not necessary, as was initially proposed by Marcinichen *et al.* (2010) and schematically given in Figure 3.5, i.e. only one SMV or EEV is sufficient to operate as an expansion device and actuator for the outlet vapor quality controller. It should be mentioned that this is probably only valid when two MMEs are considered (only one blade), with a more general statement only being valid once a complete blade center has been evaluated. The mini-compressor is a linear oil-free compressor capable of modulating the volumetric displacement, here defined as the stroke, according to the manufacturer's scale, between zero and ten.

Regarding the thermodynamic conditions at the inlet of the mini-compressor and MMEs, all tests presented in this work showed superheating and subcooling conditions, respectively. The values remained between 1 K and 10 K, and in the same way as was observed in the previous system, special controllers were not required to avoid saturation conditions. The reason is partly associated with the performance obtained by the iHEx and LPR components (*viz.* Figure 3.1). As will be discussed in *Chapter 5*, they demonstrated high exergetic efficiency and consequently ensured the conditions mentioned beforehand.

4.4.1 SMV and mini-compressor controllers

System identification, controller design and reference tracking evaluation were done, as for the previous system. To control the MMEs' outlet vapor quality, the SMV aperture and the mini-compressor stroke were used as the manipulating variables. Therefore, two PI controllers were designed independently. The SMV controller used the same strategy, i.e. a gain-scheduling PI controller whose parameters are actualized/updated for each

acquisition time. The relationship between the manipulated and the controlled variables can be considered static, which is a function of the SMV and is given by Equation 4.9 (static gain K_P):

$$K_P = \frac{\partial x_o}{\partial A_{SMV}} = 3.5 \times 10^{-2} \cdot A_{SMV}^3 - 1.1 \cdot A_{SMV}^2 + 10.9 \cdot A_{SMV} - 36.2 \qquad\qquad 4.9$$

The desired closed-loop time constant was adjusted to τ_D = 15 s, the constant C = 35 and the *anti-wind up* set to 0.5. Due to the SMV operating as an expansion device, the range of operation was limited to between 6.5% and 9% of aperture.

For the mini-compressor controller, the transfer function obtained from the system identification is given by:

$$G(s) = \frac{y(s)}{u(s)} = \frac{-0.0573e^{-0.0741s}}{8.23s+1} \qquad\qquad 4.10$$

Using the linear programming method proposed in (Karimi *et al.* 2007) and considering a phase margin of 60°, a gain margin of 2 and a crossover frequency twice as large as in the open loop, the mini-compressor's PI parameters, i.e. K_C and T_I, were determined as -34.3%/stroke and 8.23 s, respectively.

4.4.2 LPWs controller

To control the difference of temperature between outlet water and inlet in the condenser, i.e. ΔT_{cond}, the LPW_S was used as the manipulating variable. The transfer function obtained from the system identification is given below by Equation 4.11, and the LPW_S controller parameters were adjusted to 82.04 °C/rpm and 33.76 s, respectively for K_C and T_I. The same criteria and method used for the design of the mini-compressor controller was used, resulting in:

$$G(s) = \frac{y(s)}{u(s)} = \frac{0.0234e^{-0.01s}}{33.76s+1} \qquad\qquad 4.11$$

4.4.3 Controller evaluation

A *standard condition* was defined to start each evaluation, i.e., mini-compressor stroke of 4, SMV aperture of 7.7%, LPW$_S$ of 1100 rpm, inlet water temperature in the condenser of 14 °C and input heat loads of 75 W, 75 W and 150 W on pseudo-chips 1 and 2, and on the post heater wrapped on the piping after the MMEs (post heater *viz.* Figure 3.1), respectively.

The post heater was necessary to guarantee superheated conditions at the inlet of the VSC and subcooled liquid at the inlet of the MMEs. The post heater simulates the auxiliary electronics described beforehand and in Marcinichen *et al.* (2010). A fixed value of 125 W was used, which, combined with the input power on the pseudo-chips, added up to a total heat load of about 290 W, which is equivalent to the heat load associated with IBM's QS22 blade (IBM 2011).

Figure 4.22 and Figure 4.23 show the results for the MMEs' outlet vapor quality tracking test, where ΔT_{cond} was set to the value of 15 K. The *standard condition* was defined as the starting point and six steps of vapor quality from 40% to 60% were investigated.
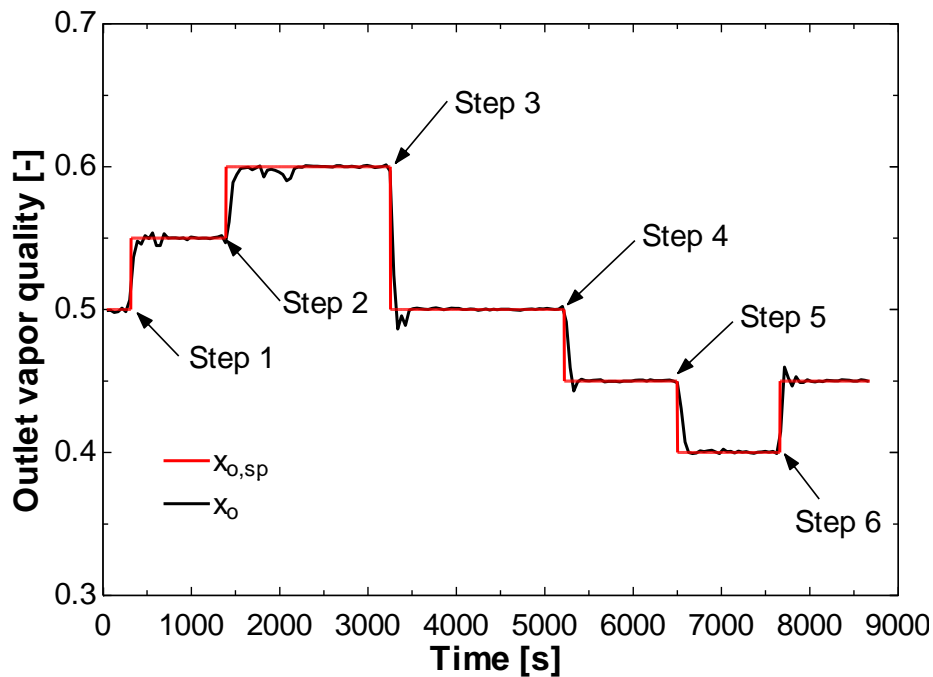
Figure 4.22 Outlet vapor quality tracking test
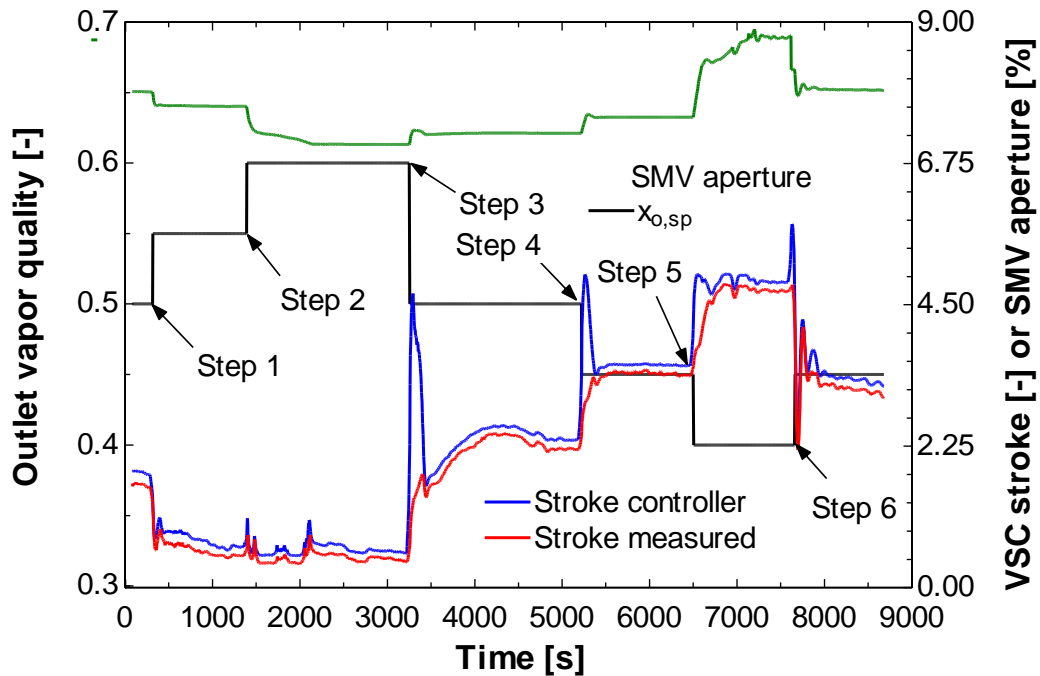
Figure 4.23 SMV and mini-compressor actuators

The outlet vapor quality proved to be well controlled by the two actuators operating together. It can be said that a negligible overshoot was observed and the controllers, mini-compressor and SMV, are efficient and effective in tracking the outlet vapor quality since no instabilities were observed in the outlet vapor quality. In the worst case, i.e. step 3, the controller took about 60 s to stabilize the system.

An anomalous operation was observed in the controller of the mini-compressor, as can be seen in Figure 4.23. When the mini-compressor controller tried to increase the stroke, defined by the stroke controller, the actual stroke or stroke measured did not respond as defined by the controller. Such a situation was observed during steps 3, 4 and 5, and certainly has some negative effect in the performance of the controller, which was not observed in the present work probably due to the SMV controller compensating for this deficiency. A possible reason is that the mini-compressor was not designed for such extreme operating conditions (evaporation at about 60 °C and condensation at about 80 °C compared to its normal design operating condition of about 5 °C and 45 °C).

Figure 4.24 shows the effect of x_o tracking tests on the LPW$_S$ controller, where it can be observed that the coupling effect between the controlled variables ΔT_{cond} and x_o was negligible, since the controller was shown to be effective and efficient in maintaining the desired $\Delta T_{cond,sp}$. The maximum overshoot observed for such a controller was ±0.2 °C.
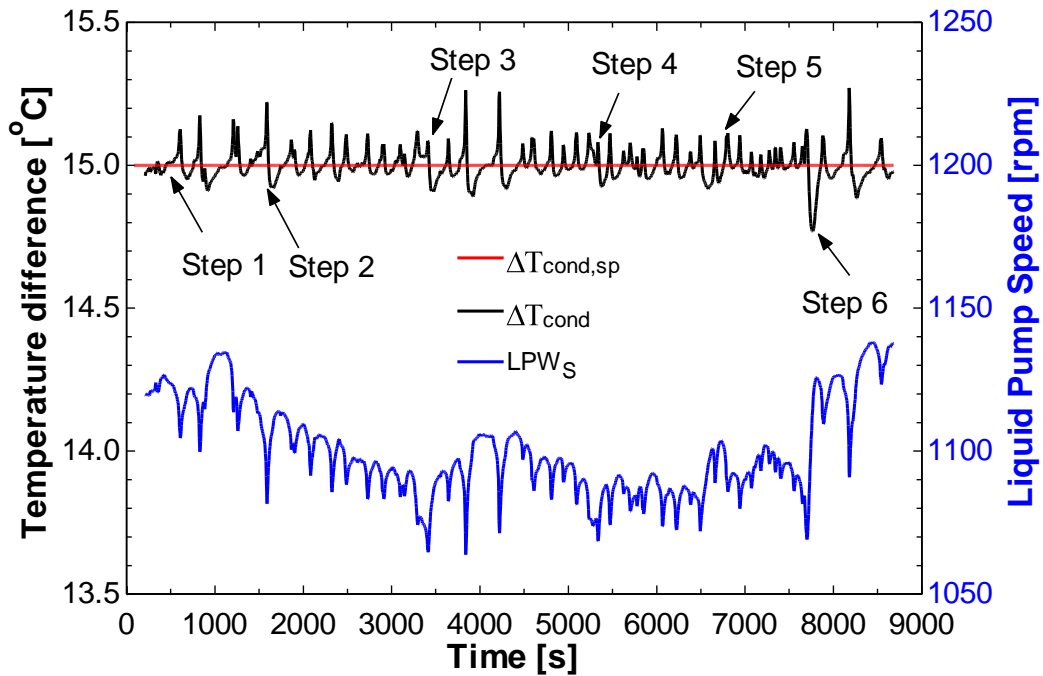
Figure 4.24 Evaluation of coupling effect between ΔT_{cond} and x_o

4.4.3.1 SISO-SIMO controller

The controllers designed previously, LPS controller (SISO strategy) and mini-compressor and SMV controllers (SIMO strategy), were integrated and evaluated through heat load disturbance rejection and flow distribution tests. The *standard condition* previously defined was used as a starting point.

Figure 4.25 shows the block diagram that represents such an integrated control strategy.
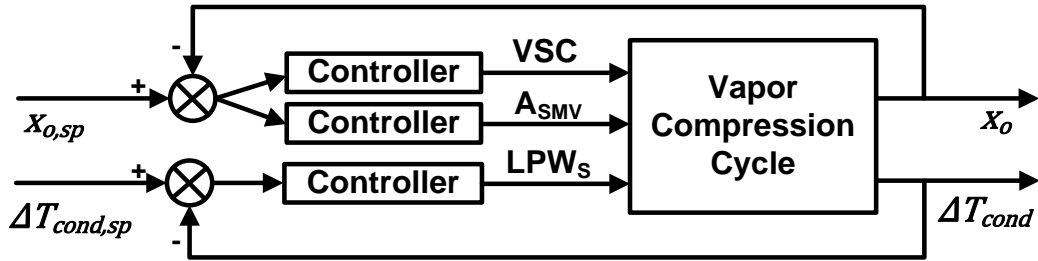
Figure 4.25 The SISO-SIMO controller of the vapor compression cycle

4.4.3.1.1 Heat load disturbance rejection

The heat load disturbance tests followed the same inputs considered for the previous system, i.e. periodic changing in the heat load on the MMEs for a time period of 1.4 s. The input heat loads changed between 75 W and 90 W on pseudo-chip 1 and 75 W and 60 W on pseudo-chip 2. The setpoint of x_o was considered to be 45%. Figure 4.26 to Figure 4.28 show the results obtained for the average temperature of the pseudo-chips, the variables under control (ΔT_{cond} and x_o) and the action of the controllers.

The maximum temperature variation observed was 1.5 °C, the same as for the previous system (*viz.* Figure 4.15 and Figure 4.26). Additionally, as can be seen in Figure 4.27, the SIMO controller, i.e. the SMV and mini-compressor actuators controlling x_o, was effective in controlling x_o, showing a continuous process of searching associated with the periodic changing in the heat load. The maximum variation of x_o regarding the setpoint was only 5%. It was also observed that the SMV controller did not show any significant effect on this test, with its aperture remaining constant.
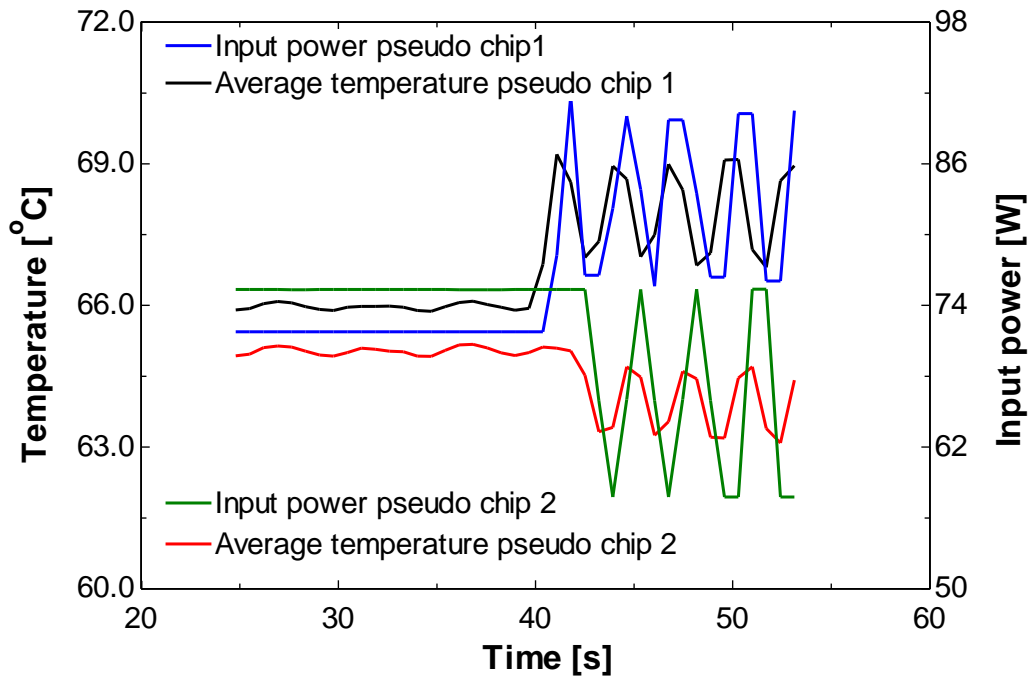
Figure 4.26 Heat load disturbances and pseudo-chip temperatures
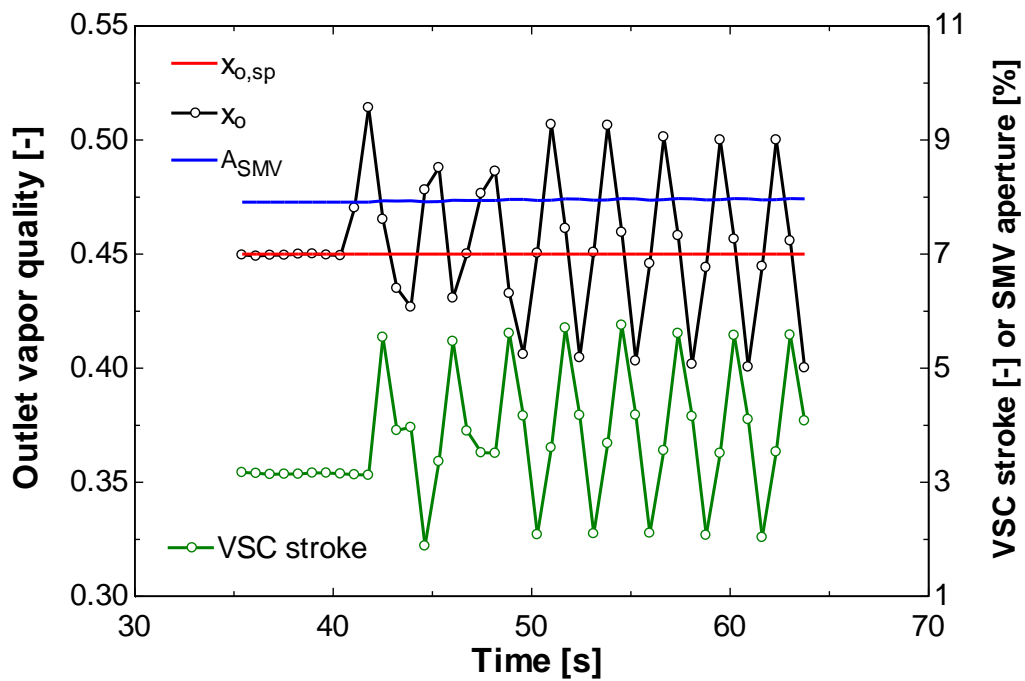
Figure 4.27 Outlet vapor quality and SMV and mini-compressor's controllers

The coupling effect between the parameters being controlled once again proved to be negligible, as can be seen in Figure 4.28. To conclude, the integrated SISO-SIMO controller proved to be effective in the disturbance rejection of heat load, ensuring the stability of the system inside an acceptable level, i.e. the system control did not show instabilities or loss of control.
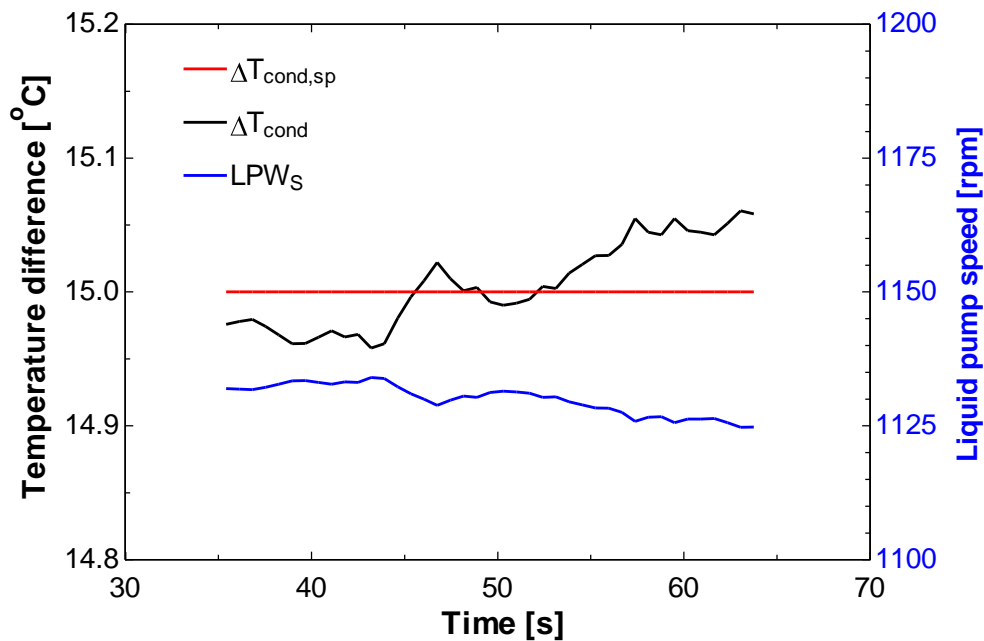
Figure 4.28 ΔT_{cond} and LPW_S controller

4.4.3.1.2 Flow distribution for non-uniform heat load

To evaluate the effect of unbalanced heat loads on the two pseudo-chip temperatures and the controllability of the vapor compression cooling system, four different steps were given in the input powers to pseudo-chips 1 and 2, which were changed between 40 W and 90 W. The setpoint of x_o and ΔT_{cond} were fixed at 45% and 15°C, respectively. Figure 4.31 and Figure 4.32 show the input power changes, the average temperature of the pseudo-chips and the action of the controllers to maintain the controllable parameters at their respective setpoints.

It can be observed from Figure 4.29 and Figure 4.30 that the difference of temperature between the chips increases when the difference in the applied input heat load increases. A

higher heat load on one of the MMEs generates a higher outlet vapor quality. To maintain the same pressure drop between the two MMEs, which are in parallel flow, the mass flow rate needs to be reduced, with the consequence that there is an increase in temperature due to the increase in heat flux. The highest difference observed was for step 3, where, after steady state has been reached, a difference of 12 °C was observed. However, the limit of 85 °C was still far away.
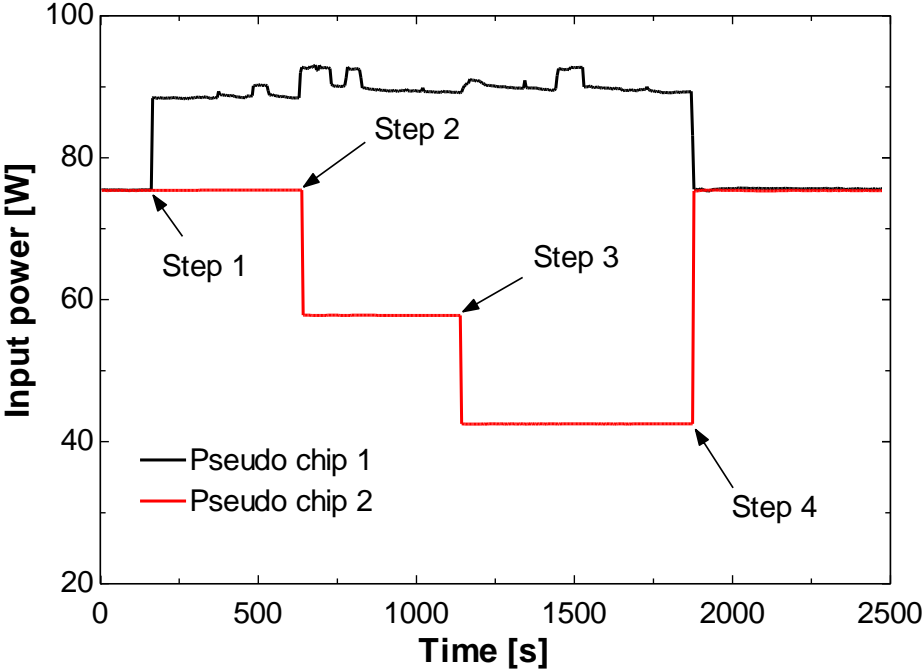
Figure 4.29 Non-uniform heat loads on the MMEs
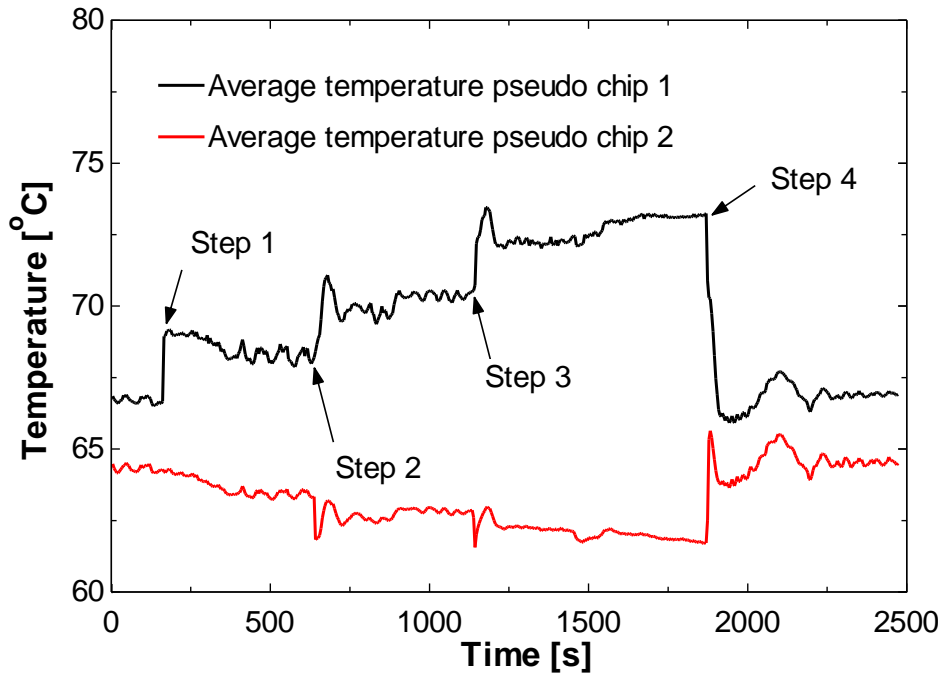
Figure 4.30 Average temperatures on the two pseudo-chips

The SIMO controller, which uses the SMV and mini-compressor as actuators, proved to be effective and efficient in controlling x_o. The maximum overshoot observed in step 4 was only 0.07% in vapor quality (*viz.* Figure 4.31). In this case, especially for steps 1 and 4, it can be seen that the SMV showed a more pronounced change in the aperture when compared with that obtained in the disturbance rejection tests. The SMV actuator can be seen as a fine adjustment of x_o. The anomalous operation to adjust/control the mini-compressor's stroke continued, i.e. the actual stroke is shorter than that requested by the controller.

Regarding the LPS controller, Figure 4.32 shows that it was effective in maintaining the 15 °C setpoint, independent of changes in the heat loads on the MMEs. The maximum overshoot remained between ± 0.5 °C while no instabilities were observed.
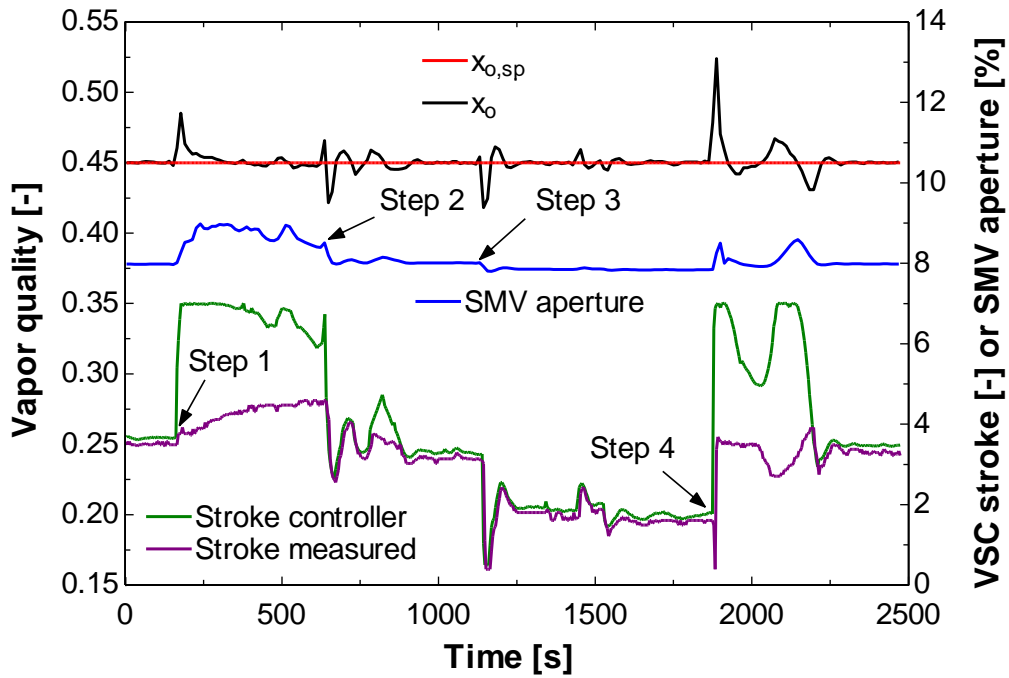
Figure 4.31 x_o and A_{SMV} and $Stroke$ controllers
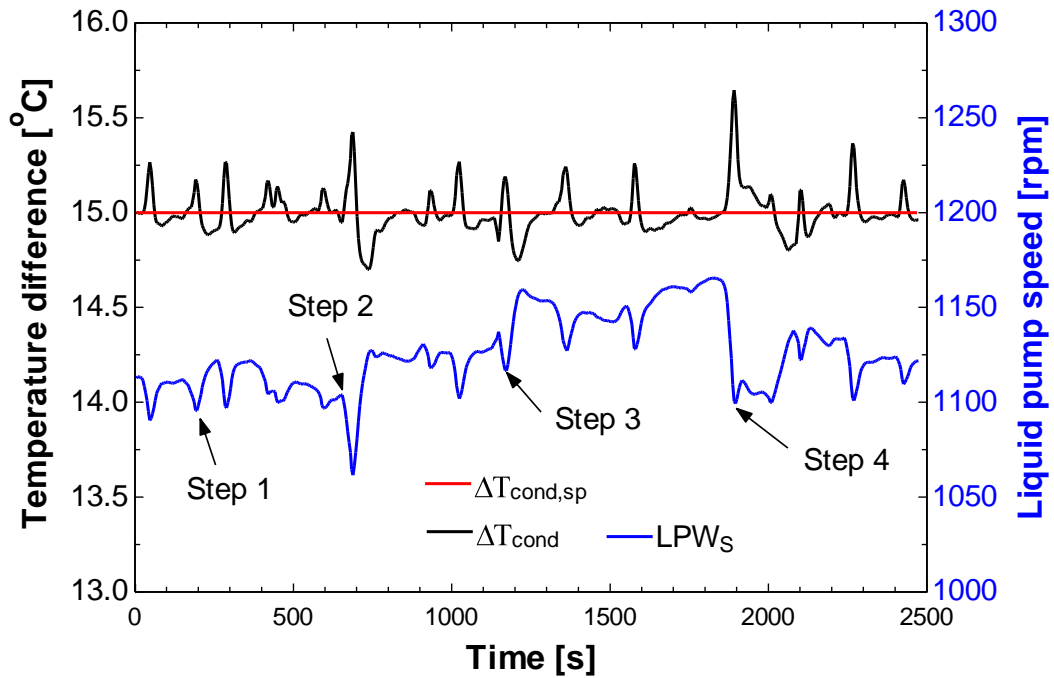
Figure 4.32 ΔT_{cond} and LPW_s controller

4.5 Control development of the hybrid cycle

In the following section, the controller development of the hybrid cycle is presented. As introduced previously, this cycle is very versatile with more drivers than the other two cycles, which permits a wider range of operating conditions. To fully explore the potential of such a cycle, the control development has been extended significantly compared with the previous controller development. Three specific controllable variables were defined, which were associated with five potential actuators. In summary, the outlet vapor quality was controlled by a variable speed liquid pump and a stepper motor valve (SIMO strategy), the condensing pressure by a variable volumetric displacement vapor compressor and a pulsating electric expansion valve (SIMO strategy), and the temperature difference between water outlet and working fluid inlet at the condenser (ΔT_{cond}) by another variable speed liquid pump (SISO strategy). Finally, the controllers were evaluated further on the system level via disturbance rejection and non-uniform heat load tests.

4.5.1 Vapor quality (x_o) controller

The system identification was developed considering several steady state conditions as the starting point and a change in SMV aperture (A_{SMV}) of 2% each 10 s between 10% and 50% of aperture. Table 4.1 shows the different levels of heat load on the MMEs and liquid pump speed (LPC_S) that were considered. The idea was to adjust the model for a range of heat load and actuators "position" large enough to emulate conditions of a real microprocessor operation (idle, normal and maximum clock speed).

Table 4.1. Heat load and LPC_s for system identification

Overall heat load [W]	LPC_s [rpm]
60	750 to 1750, steps of 250
110	1000 to 2750, steps of 250
160	1750 to 3250, steps of 250

A quadratic polynomial equation (*viz.* Equation 4.12) was adjusted with the experimental data obtained which considers x_o as a function of A_{SMV}, LPC_s and HL_{MMEs} (overall heat load on the MMEs).

$$x_o = (1 \ HL_{MMEs} \ HL^2_{MMEs}) \begin{bmatrix} a_0 & b_0 & c_0 & d_0 & e_0 & f_0 \\ a_1 & b_1 & c_1 & d_1 & e_1 & f_1 \\ a_2 & b_2 & c_2 & d_2 & e_2 & f_2 \end{bmatrix} \begin{pmatrix} 1 \\ LPC_S \\ A_{SMV} \\ LPC_S^2 \\ A_{SMV}^2 \\ LPC_S \cdot A_{SMV} \end{pmatrix} \qquad 4.12$$

Table 4.2 shows the coefficients adjusted and Figure 4.33 depicts the experimental results and adjusted curves for the highest value of HL_{MMEs}. A R^2 value (coefficient of determination) of 94.8% was obtained for the adjusted equation.
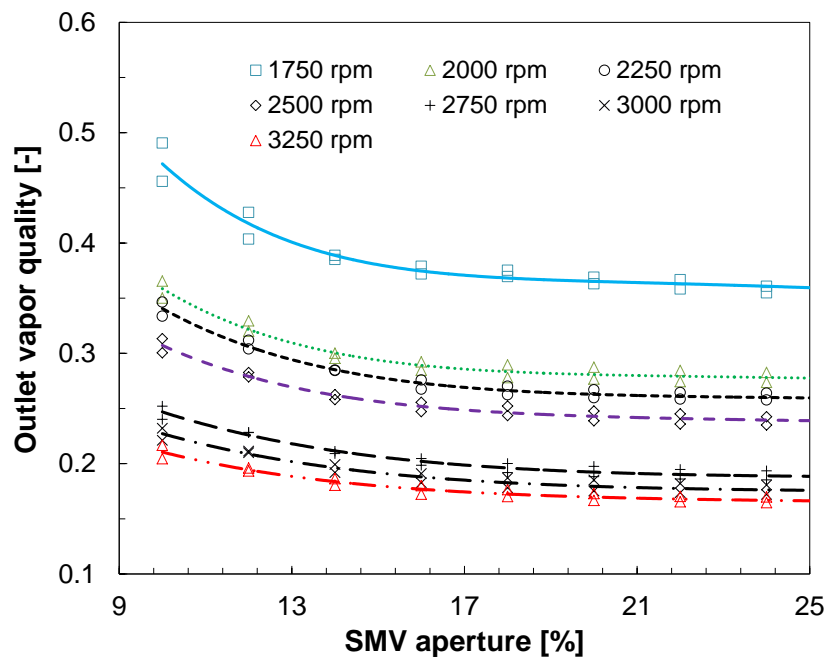
Figure 4.33 Experimental results and adjusted curves for the highest value of HL_{MMEs}

Table 4.2. Coefficients of Equation 4.12

	0	1	2
a	1.070384E+00	1.474077E-03	-8.418410E-06
b	-1.528771E-03	1.137309E-05	-2.917296E-08
c	-7.517046E-03	-2.537077E-04	1.503885E-06
d	5.285910E-07	-5.636055E-09	1.696211E-11
e	3.966723E-05	5.519641E-06	-3.174776E-08
f	5.966975E-06	-3.791135E-08	3.687400E-11

The models of the system were approximated by its static gain (K_p), which is the derivative of the equation obtained in the system identification with respect to the SMV aperture and LPC_s (*viz.* Equations 4.13 and 4.14 / SIMO strategy), i.e. the same method as presented in sections 4.3.2 and 4.4.1.

$$K_{P,SMV} = \frac{\partial x_o}{\partial A_{SMV}} \qquad\qquad 4.13$$

$$K_{P,LPC} = \frac{\partial x_o}{\partial LPC_s} \qquad\qquad 4.14$$

Therefore, a gain-scheduled PI controller was developed whose gains are a function of A_{SMV}, LPC_s and HL_{MMEs} and both are updated simultaneously with running time. C and τ_D were experimentally adjusted for 35 and 15 s (SMV controller), and 20 and 15 s (LPC_S controller), respectively.

It is important to mention that system identification was also developed for a fixed value of A_{SMV} and different steps of LPC_s. A new quadratic polynomial equation was adjusted which matched with that one previously shown. It means that both equations were able to capture the effects of steps in the LPC_s on the x_o, independent of the first system identification which did not consider dynamic aspects of LPC. The reason is that the same behavior observed when changing the A_{SMV} on the x_o was also observed when changing the LPC_s (*viz.* Figure 4.35), i.e. a very fast response so that the models of the system can be approximated by its static gain.
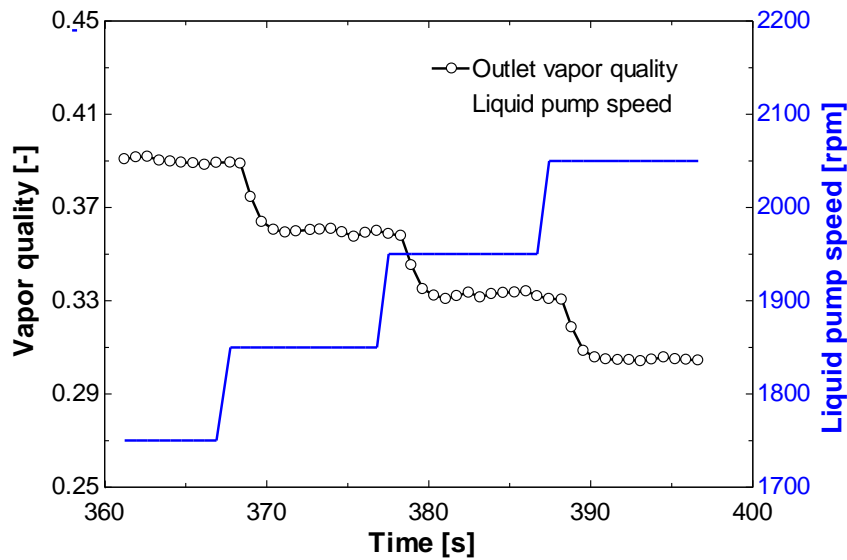
Figure 4.34 System identification: response time of outlet vapor quality by changing the LPC speed

The SIMO strategy for controlling of the outlet vapor quality was implemented and evaluated by tracking tests. A *standard condition* was defined to start the evaluation of controllers in tracking tests, i.e. mini-compressor stroke of 2.5, EEV duty cycle of 20% at the frequency of 0.5 Hz, LPW_S of 1500 rpm, inlet water temperature in the condenser of 14 °C and input heat loads of 75 W, 75 W and 125 W on pseudo-chips 1 and 2, and on the post heater wrapped on the piping after the MMEs (post heater in the Figure 3.1), respectively. The post heater simulates the auxiliary electronics as described beforehand. A fixed value of 125 W was imposed.

Figure 4.35 and Figure 4.36 show the tracking test results, where it can be seen that the controllers (SMV and LPC) reacted fairly quickly for the 4 steps considered. In the worst case, the controllers took about 5 s to stabilize the system; however only a small overshooting was observed, a maximum of 0.2% in vapor quality at Step 3. It can be concluded that the controllers were efficient (negligible steady state error) and effective (short settling time) for the actual application, showing negligible overshooting and settling time.
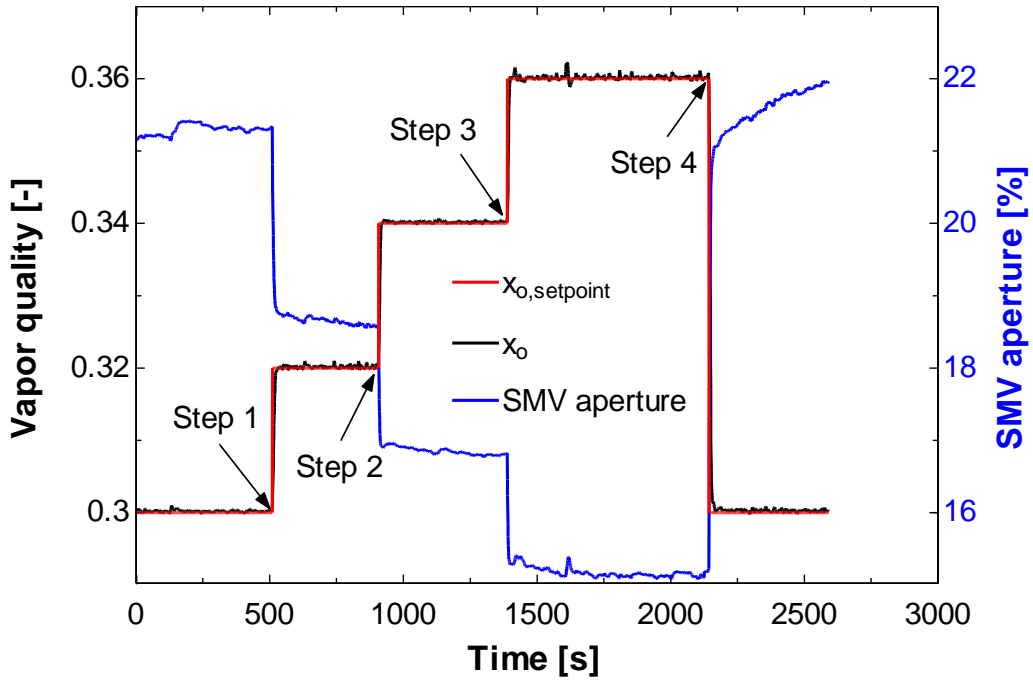
Figure 4.35 Outlet vapor quality x_o setpoint tracking and SMV response
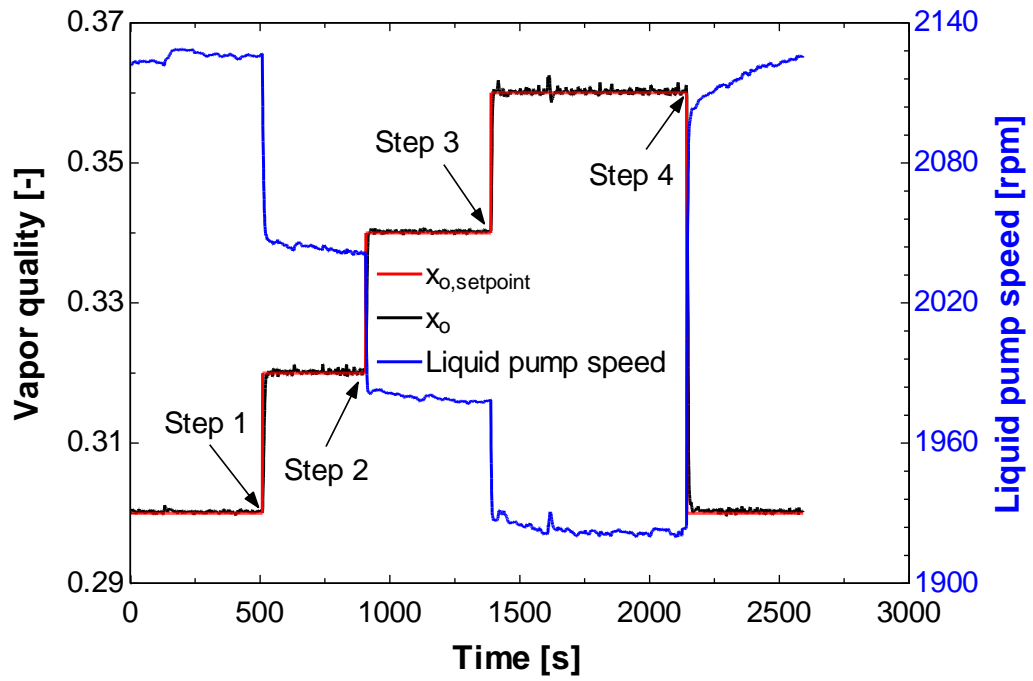
Figure 4.36 Outlet vapor quality x_o setpoint tracking and LPC response

4.5.2 Condensing pressure controller (P$_{cond}$)

The mini-compressor stroke (associated with the volumetric displacement) and the duty cycle of the EEV were used as manipulated variables to control the condensing pressure. Therefore, two PI controllers were designed independently. It is worth mentioning that the EEV is a pulse width modulated valve with a duty cycle range of 0 % to 100 % and a frequency of 0.5 Hz, and the mini-compressor is a linear oil free mini-compressor capable of modulating the volumetric displacement, here defined as stroke, according to the manufacturer's scale, between zero and ten.

For each controller a set of system identifications was carried out with three levels of heat load, which were also considered as the scheduling parameter in the design of the PI controllers. Both of the two controllers were designed by using the method proposed by Karimi *et al.* (2007), which is based on linear programming. The gain-scheduled controllers were designed to guarantee a phase margin of at least 45° and a gain margin of at least 2. Table 3 lists the parameters obtained.

Table 4.3 Summary of gain-scheduled PI controllers' parameters

	P_{cond} controller (VSC as actuator)	P_{cond} controller (EEV as actuator)
Desired bandwidth	0.035	0.01
Phase Margin	52.8538	47.373
Gain Margin	6.96	3.96
$K_C{}^{(*)}$	$P^2 \cdot (-0.0001741) + P \cdot (0.05261) - 0.76083$	$P^2 \cdot (0.0081625) + P \cdot (-3.2224) + 239.0932$
$K_I{}^{(*)}$	$P^2 \cdot (-8.5363e-6) + P \cdot (0.0029234) - 0.11605$	$P^2 \cdot (1.8951e-4) + P \cdot (-0.072894) + 5.2153$

(*) P is the HLMMEs

The SIMO strategy for condensing pressure control was implemented and evaluated by tracking tests starting with the *standard condition* defined in the previous section. Four steps of condensing pressure between 20 bar and 21 bar were investigated, as can be seen in Figure 4.37 and Figure 4.38. It can be observed that the condensing pressure proved to be well controlled by the two actuators operating together, i.e. a negligible overshooting

was observed and the mini-compressor and EEV controllers, respectively, were efficient and effective in tracking the condensing pressure (no instabilities were observed). In the worst case, i.e. step 4, the controllers took about 50 s to stabilize the system.
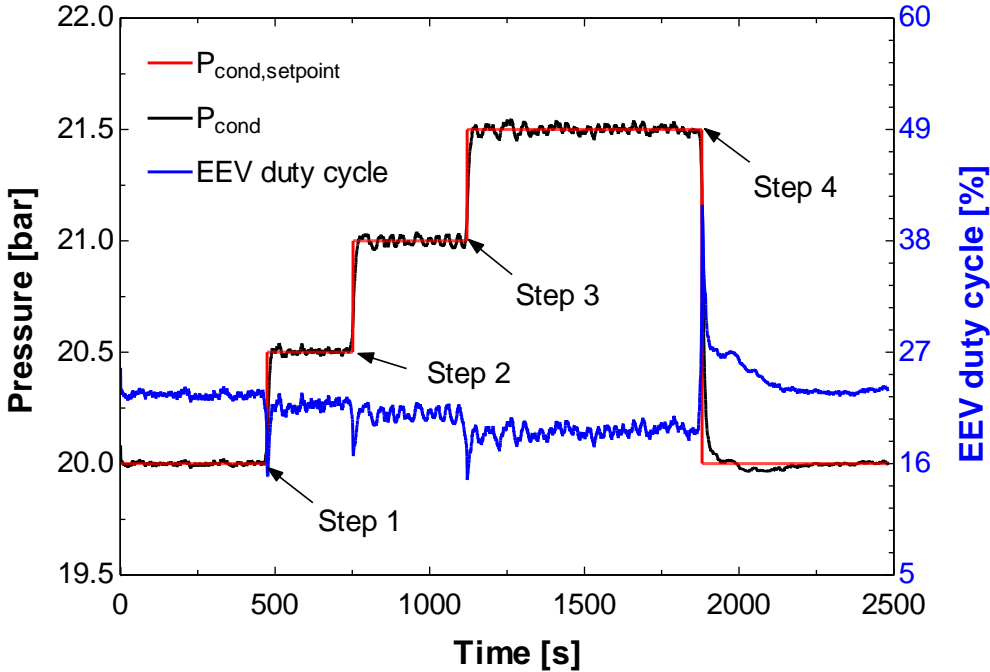
Figure 4.37 P_{cond} setpoint tracking and EEV response
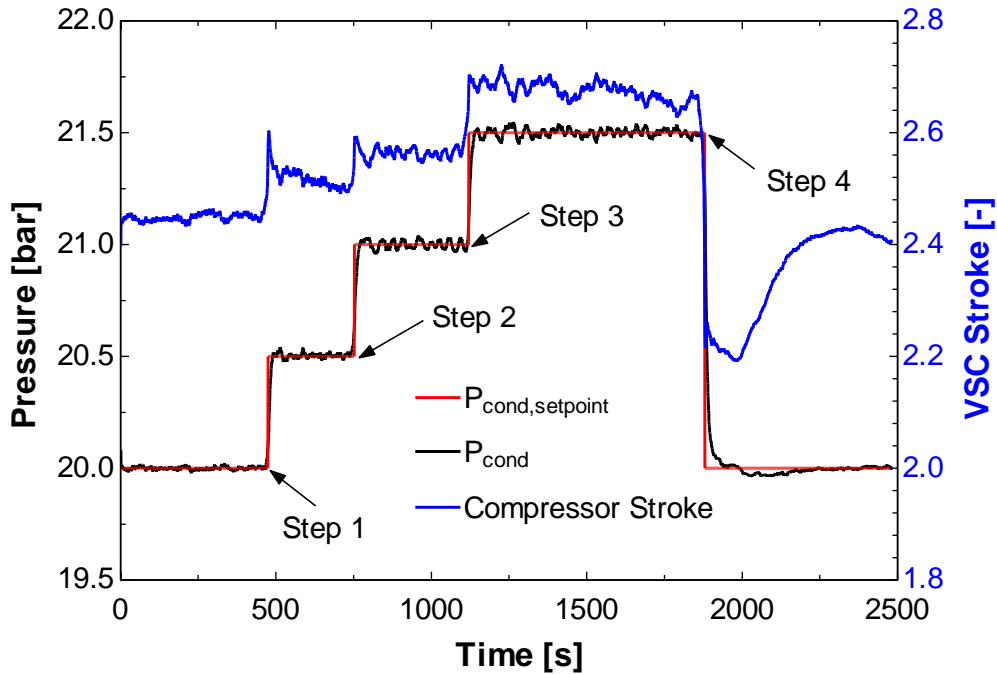
Figure 4.38 P_{cond} setpoint tracking and VSC response

4.5.3 ΔT_{cond} controller

The ΔT_{cond} controller, which uses the water loop's variable speed liquid pump (LPW) as the actuator, was developed by the same method used for the condensing pressure controller, i.e. linear programming method. The K_C and K_I parameters can be seen in Table 4.4. The reference tracking tests starting under the *standard condition* used previously were also done to evaluate the controller performance, as shown in Figure 4.39. It can be observed that the ΔT_{cond} controller was effective, with negligible overshooting. In the worst case, i.e. step 2, the controller took about 60 s to stabilize the system with negligible overshoot.
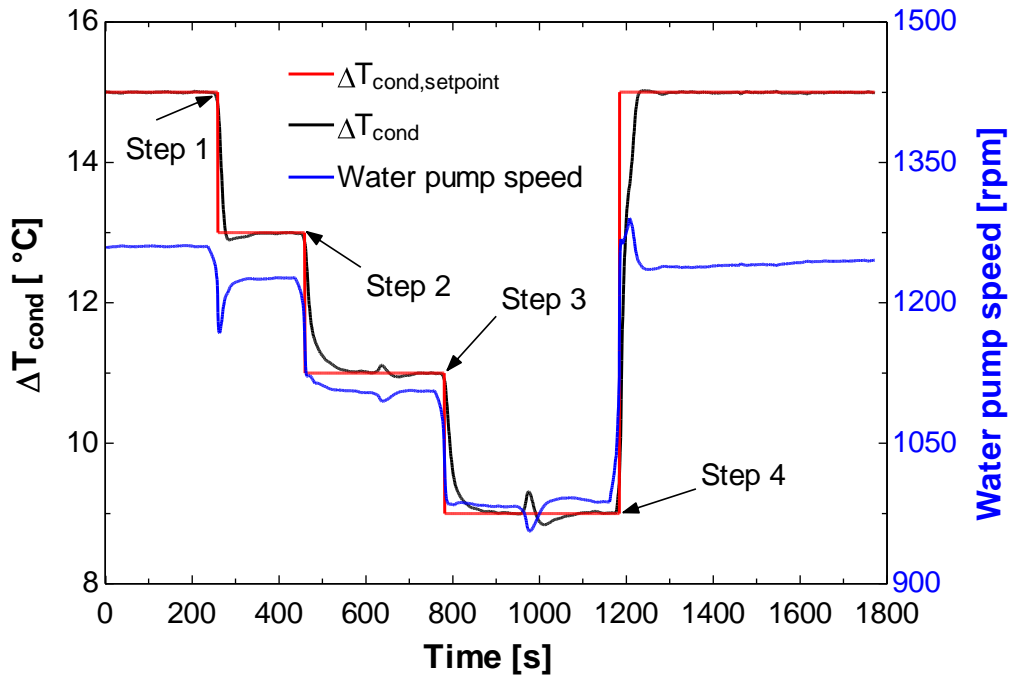
Figure 4.39 ΔT_{cond} setpoint tracking and LPW response

Table 4.4 Gain-scheduled PI controllers' parameters

	ΔT_{cond} *controller (LPW as actuator)*
Desired bandwidth	0.07
Phase Margin	58.2981
Gain Margin	2.66
$K_C^{(*)}$	$P^2 \cdot (-0.0042734) + P \cdot (1.7869) - 71.214$
$K_I^{(*)}$	$P^2 \cdot (-7.0007e-6) + P \cdot (-0.018509) + 10.5343$

(*) P is the HLMMEs

4.5.4 SISO-SIMO control strategies

The controllers developed previously, vapor quality and condensing pressure (SIMO strategies), and T_{cond} (SISO strategy), were integrated (decentralized control structure) and evaluated through heat load disturbance rejection and non-uniform heat load tests. The *standard condition* defined to start each evaluation are shown in Table 4.5, which also lists the range of heat load evaluated.

Table 4.5 Standard conditions and heat load range

	Standard condition	Heat load values
Disturbance rejection	Heat load: 75 W per pseudo-chip and 125 W for post heater $x_{o,sp}$=30%, $T_{cond,sp}$=80 °C, $\Delta T_{cond,sp}$ =10 °C	Between 75 and 90 W for pseudo-chip 1 Between 75 and 60 W for pseudo-chip 2 (changing for a period of 1.4 s)
Non-uniform heat load	Heat load: 75 W per pseudo-chip and 125 W for post heater $x_{o,sp}$=30%, $T_{cond,sp}$=80°C, $\Delta T_{cond.sp}$ =10 °C	75 and 90 W for pseudo-chip 1 40, 60 and 75 W for pseudo-chip 2

4.5.4.1 Disturbance rejection test

For the disturbance rejection test the heat loads on MME1 and MME2 were changed from 90 W and 75 W to 75 W and 60 W, respectively, considering a periodic disturbance time of 1.4 s. As the heat load changed, so did the condensing pressure, minimum approach temperature of condenser and outlet vapor quality disturbances, which were detected by the controllers. These in turn increased or decreased the LPCs, A_{SMV}, EEV duty cycle, VSC stroke and LPWs to maintain the controlled variables in the desired setpoints.

Figure 4.40 shows the disturbance of input power on the pseudo-chips and the effect on the average temperature of each pseudo-chip. It can be observed that there is a maximum temperature variation of 2.5 °C, which can be considered acceptable when compared with the temperature gradient along the chip for on-chip single-phase cooling using water (about 2 - 3 °C,(Ganapati 2009; Meijer *et al.* 2009; Brunschwiler *et al.* 2010)). Figure 4.41 and Figure 4.42 show the controllers' reaction, where it can be seen that the actuators SMV and LPC were able to maintain the exit vapor quality to within ±5% of the setpoint. What is important to observe is that the controller was effective, *i.e.* it showed fast response for the induced disturbance and no instability was observed.

Additionally, it can be seen that the disturbance rejection test showed no effect on the T_{cond} and P_{cond} controllers, as it can be seen in Figure 4.43 to Figure 4.45. Such result reinforces the assumption of decoupling between controlled variables considered in the

design of controllers. It can also be observed, once again, that the controller proved to be effective and efficient to maintain the respective setpoints.
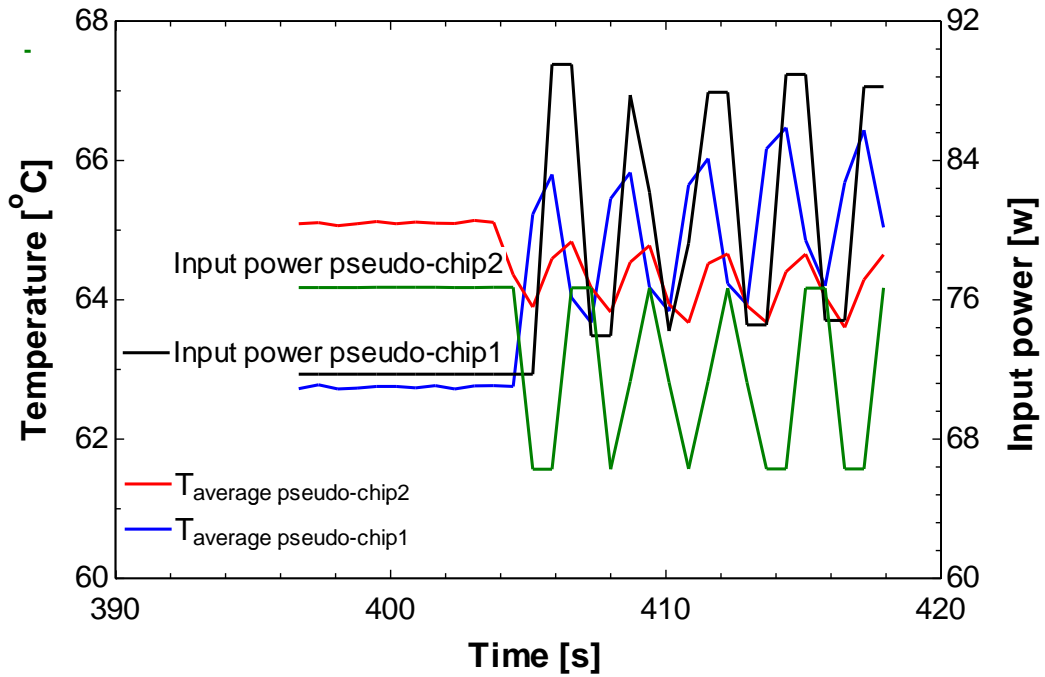
Figure 4.40 Heat load disturbance and Pseudo-chip temperature
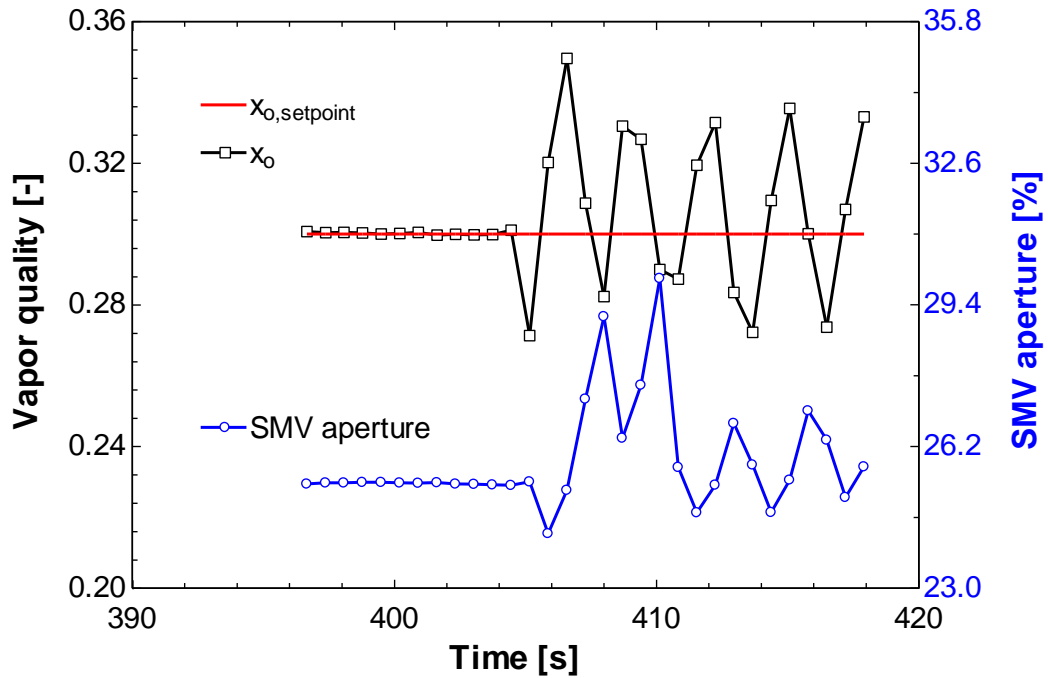
Figure 4.41 Outlet vapor quality and SMV response
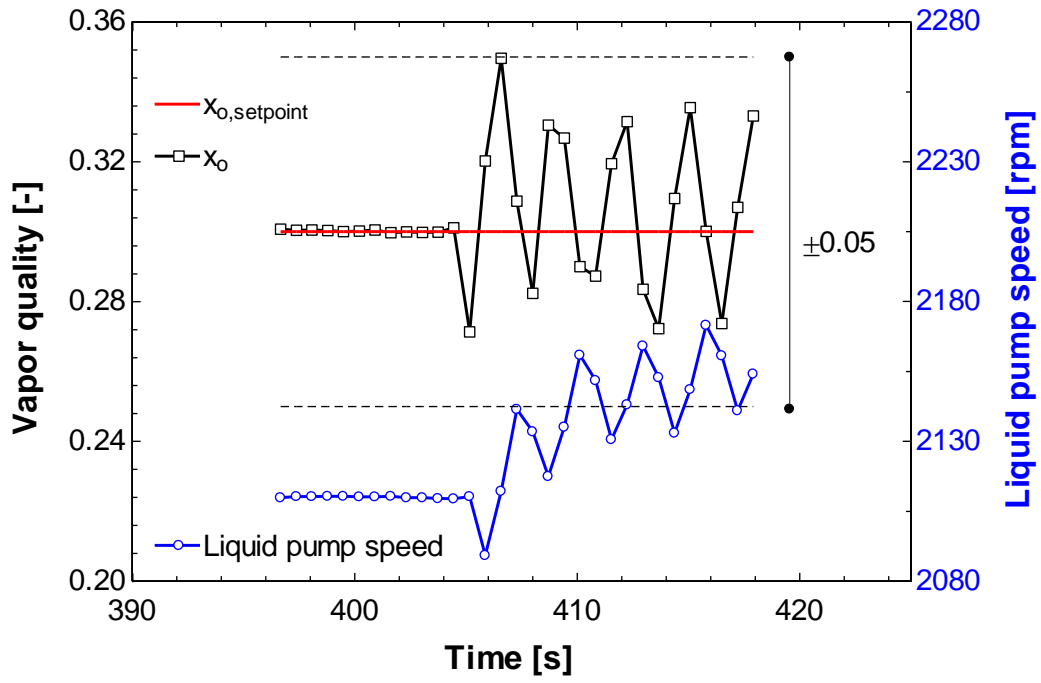
Figure 4.42 Vapor quality x_o and LPC response
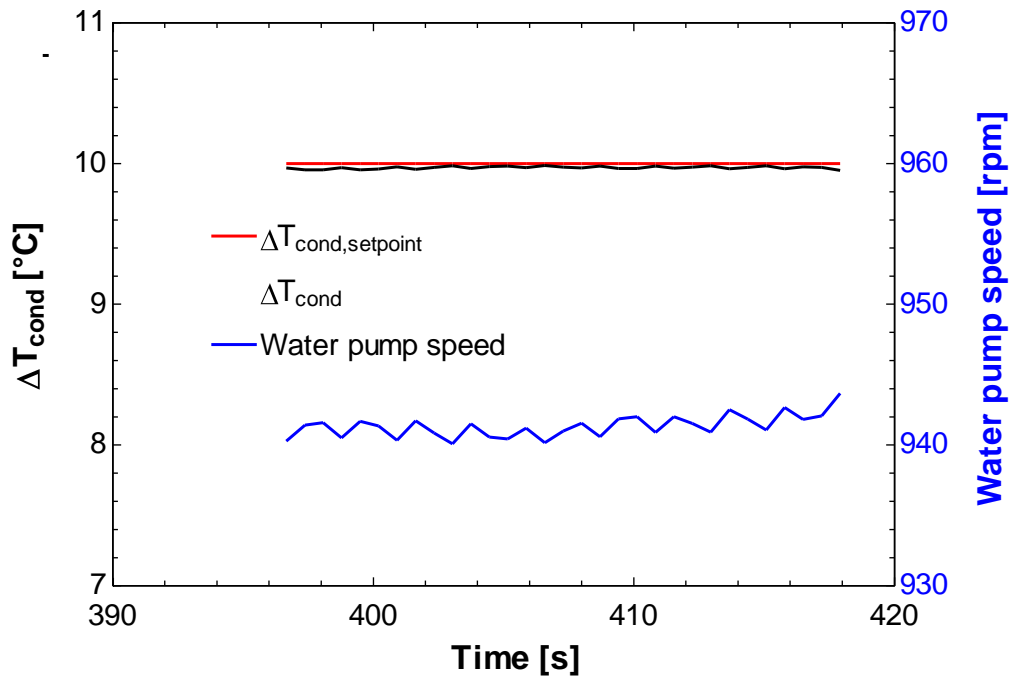
Figure 4.43 ΔT_{cond} and LPW response
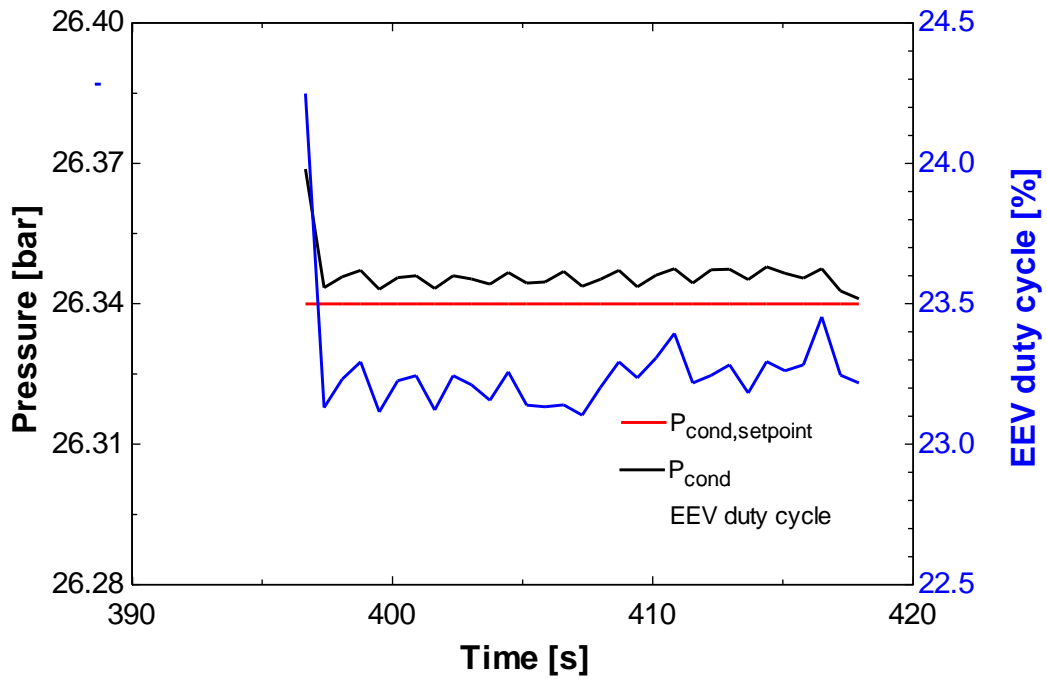
Figure 4.44 ΔT_{cond} and LPW response
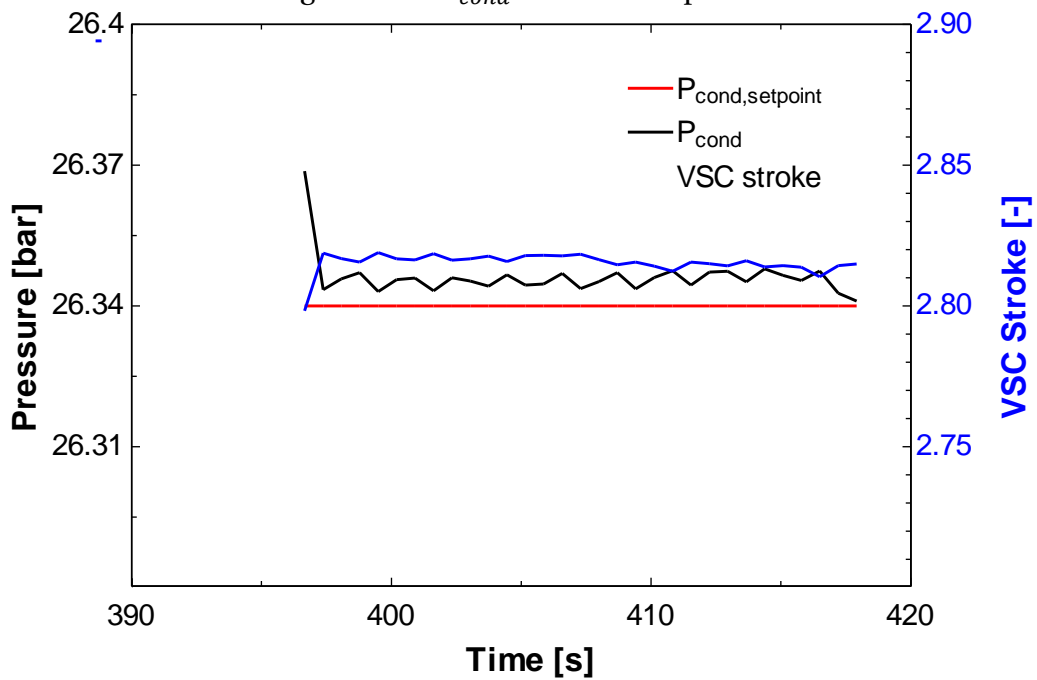
Figure 4.45 P_{cond} and VSC response

4.5.4.2   Non-uniform heat load test

To evaluate the effect of unbalanced heat loads on the two pseudo-chip temperatures and on the controllability of the hybrid cooling system, four different steps of input power were applied on the pseudo-chips 1 and 2, i.e. they were changed between 40 W and 90 W

(standby and full operation of typical CPUs). The setpoints of x_o, P_{cond} and ΔT_{cond} were fixed at 30%, 26.3 bar (80 °C of saturation temperature) and 10 °C, respectively.

It can be observed from Figure 4.46 and Figure 4.47 that the difference of average temperatures between the pseudo-chips increases when the difference of heat loads increases. The highest difference was observed for step 4, where, after steady-state has been reached, a difference of 12 °C was established. However, the limit of 85 °C was still far away even when operating at an evaporation temperature of about 60 °C.
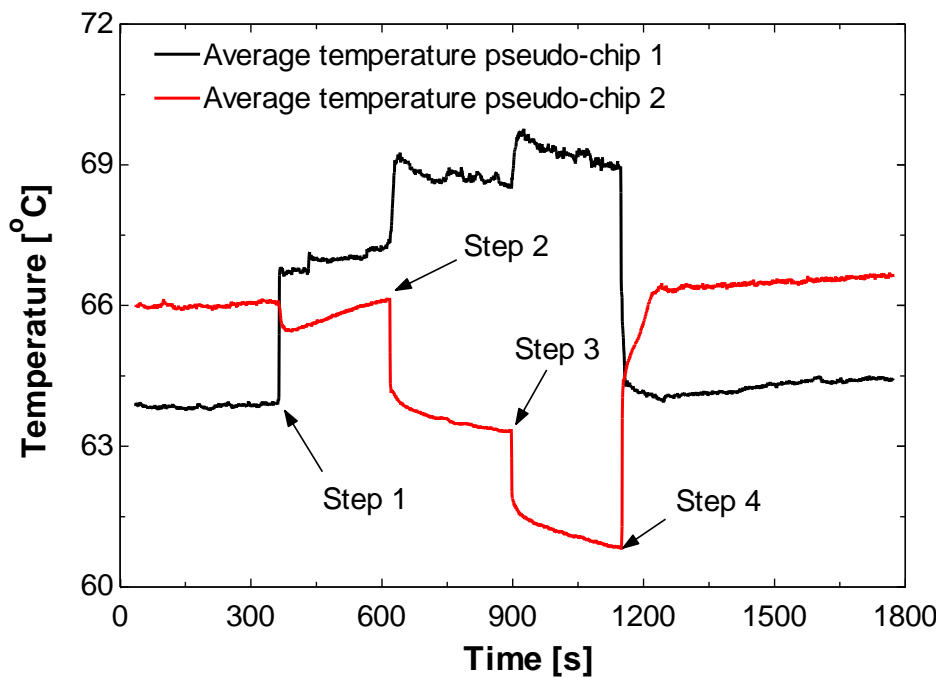
Figure 4.46 Average temperatures on the two pseudo-chips
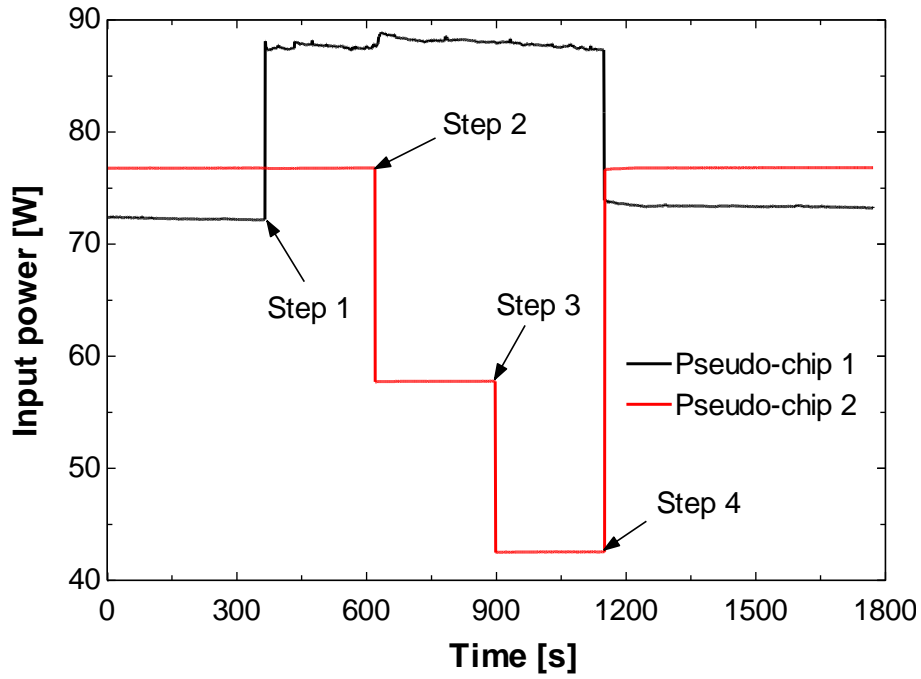
Figure 4.47 Non-uniform heat loads on MMEs

Figure 4.48 and Figure 4.49 show the results of controlling vapor quality by the actuators SMV and LPC. The maximum overshooting observed was 6% in vapor quality (step 4). It can be noticed that for each heat load change, both SMV and LPC act simultaneously towards stabilizing the vapor quality, which accelerates the settling process.
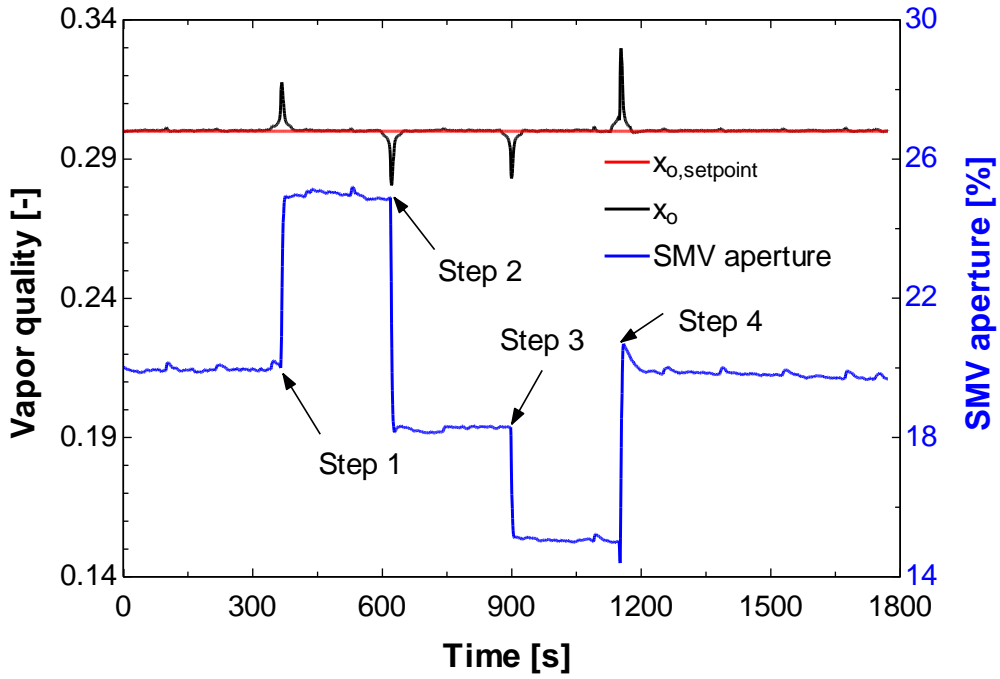
Figure 4.48 Outlet vapor quality and SMV controller
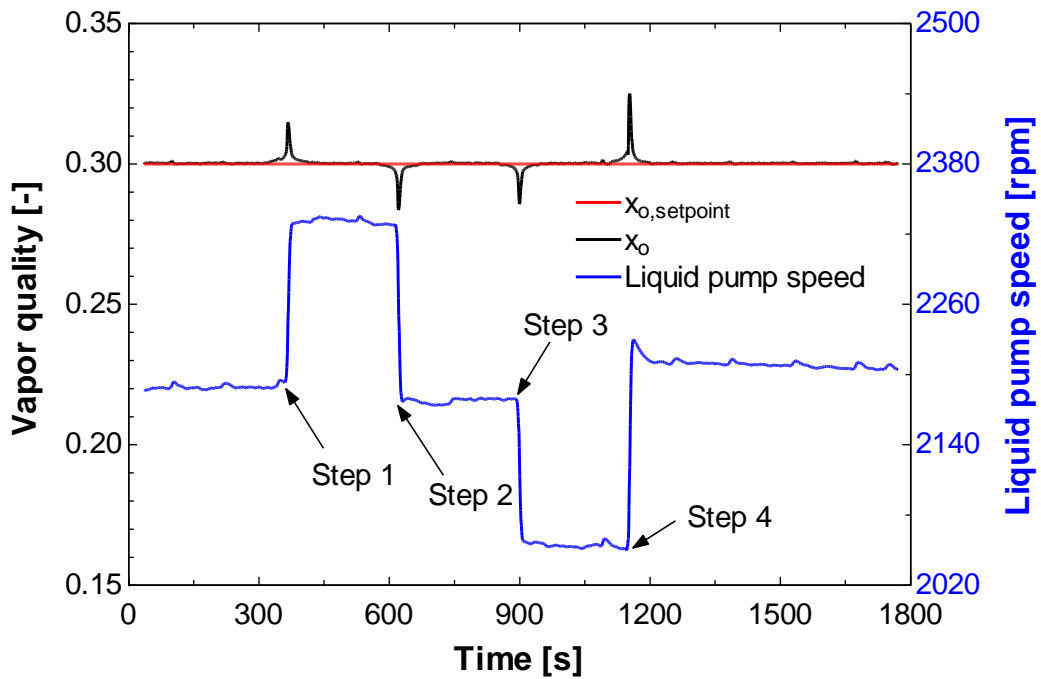
Figure 4.49 Outlet vapor quality and LP_C controller

Figure 4.50 and Figure 4.51 show the effect of non-uniform heat load on the condensing pressure controllers. It can be seen that neglegible effect/instability was observed when the

steps were done, and the maximum overshoot was of only 0.08 bar or 0.14 °C. Such a result was expected, since the change in heat load (disturbance) takes place in the *cooling loop* and the P_{cond} controllers are placed on the *condensing loop*. In other words, due to the inertia of the system, the P_{cond} controllers had enough time to absorb the change in heat load without significant instabilities.
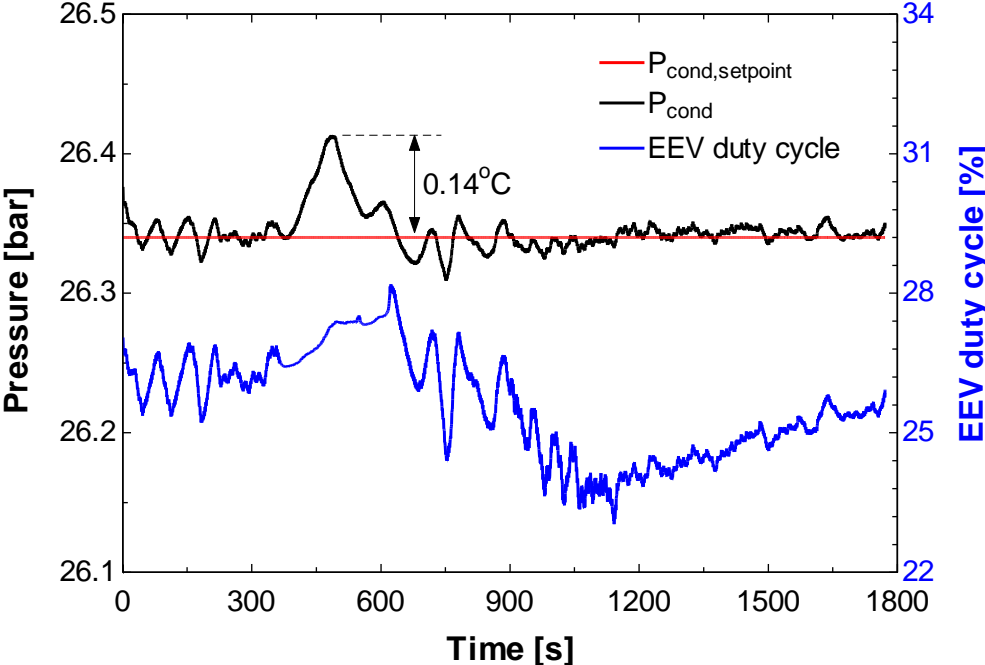
Figure 4.50 Condensing pressure and EEV duty cycle
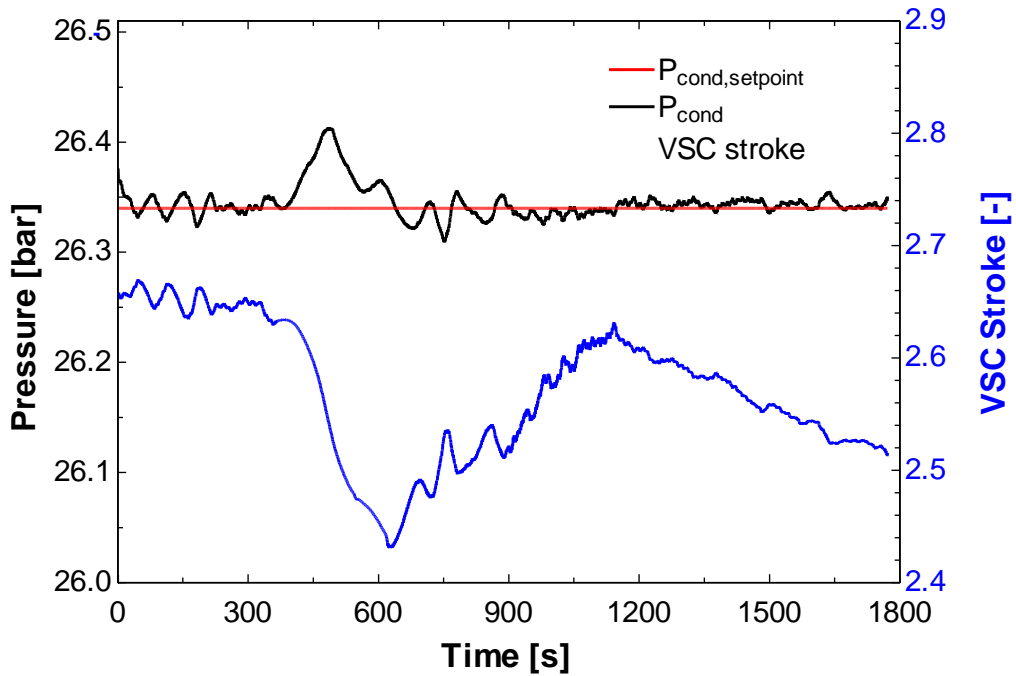
Figure 4.51 Condensing pressure and VSC stroke

Figure 4.52 shows the effect of non-uniform heat load on the ΔT_{cond} controller, which proved to be effective to maintain the 10 °C of setpoint for all ranges of heat loads investigated. The maximum overshoot remained within ±0.5 °C while no instabilities were observed.
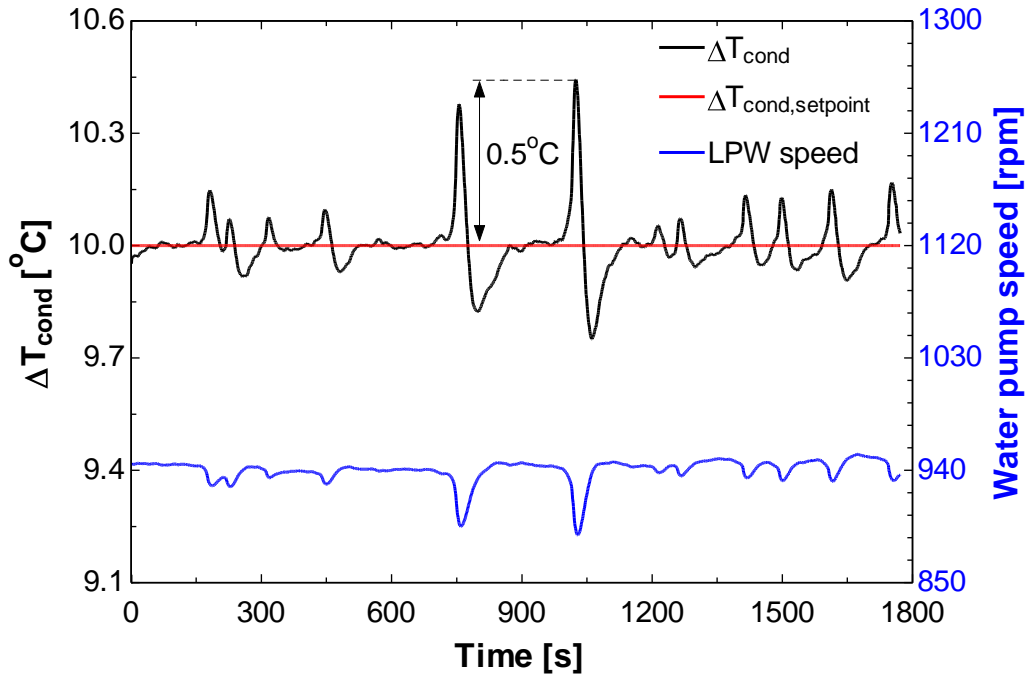
Figure 4.52 ΔT_{cond} and LPW controller

Finally, it can be highlighted that the SISO-SIMO strategy proved to be a simple and effective way of controlling the x_o, P_{cond} and ΔT_{cond} while maintaining the pseudo-chips within a safe operating range. The coupling effect between the controllable variables was not strong, in other words the controllers have low interaction effects, implying that it was not necessary to apply a more complex centralized MIMO controller.

4.6 Conclusions

Three different cooling systems were tested (pump only, compressor only, and pump plus compressor driven) for a single pseudo-CPU, two pseudo-CPU's in parallel operation, and for transition heat load operation of the CPU's. A very extensive experimental campaign was implemented to test all these numerous operating conditions. In all cases, effective and precise system control was achieved. This work demonstrates the two-phase flow control of direct on-chip two-phase cooling is not only effective when setting the coolant's saturation temperature to about 60 °C (maintaining always the CPU's temperature well below it operating limit of 85 °C), but that various "simple" control strategies work very well for achieving this for all three cooling system schemes.

5 Energy and exergy analysis

This chapter shows a comparative analysis among the three cooling systems, where a deeper investigation of exergy is made. To compare the liquid pumping, vapor compression and hybrid cooling systems from energetic and exergetic perspectives, a steady state condition was selected from the non-uniform heat load tests in the previous chapter. Such a comparison mainly evaluates the difference between the power consumption of the drivers and the heat recovery in the condenser. The experimental condition selected for the comparison was that the input power on pseudo-chips 1 and 2 were both 75 W (34.7 W/cm^2) and the junction outlet vapor quality after the two multi-microchannel evaporators was 50%.

5.1 Energy consumption – first law analysis

Table 5.1 shows the results of each driver and actuator's power consumption and overall efficiency, the latter was calculated as the ratio between the energy gained by the working fluid via isentropic pumping or compression and the total electrical input power measured by the calibrated power transducers. It also shows the three systems' input and output energies associated with components and piping and the thermodynamic conditions in the condenser for the main and secondary working fluids.

The results show that the drivers' input power for the VC and hybrid systems is about 6 times higher than for the LP system. It is worth observing that the driver has a low overall efficiency (defined by the ratio between the isentropic pumping/compression power and driver input power), which for the pump is mainly a result of its inverter's high energy consumption (about 10 W when the pump is not working) and also leakage and slip of

HFC134a in the gears. The last two aspects are due to the low viscosity of the working fluid (123.61 mPa·s for HFC134a against 466.40 mPa·s for water at 60 ˚C), which is at the lower limit for the specified pump (hence a pump specifically designed for the liquid refrigerant would be advisable). This also justifies why the difference in driver input power was higher for computational than for experimental evaluations, where the former did not consider the actual driver inefficiencies.

Table 5.1 Energy in and out in the systems and thermodynamic conditions in the condenser

	LP cycle	VC cycle	Hybrid cycle
Energy in			
Pump input power, W	13.92	--	13.82
compressor input power, W	--	81.43	89.67
Isentropic pumping power, W	0.18	--	0.23
Isentropic compression power, W	--	12.59	28.44
Driver overall efficiency, %	1.29	15.46	1.66 (LPC) 31.72 (VSC)
Input power on the pseudo-chips, W	146.13	147.55	149.16
Input power on the post heater, W	130.42	116.53	121.28
SMV input power, W	1.02	0.71	1.17
EEV input power, W	--	--	1.56
Energy out			
Heat transfer in the condenser, W	197.39	133.47	113.15
Heat loss in the driver, W	13.74	68.84	75.98
Heat loss in the piping, W	80.36	143.91	188.69
Thermodynamic conditions in the condenser			
Condensing temperature, ˚C	64.04	78.07	84.96
Inlet water temperature, ˚C	15.16	17.46	18.23
Outlet water temperature, ˚C	39.72	62.53	69.86
Mass flow rate of water, kg/h	6.92	2.55	1.89

Regarding the mini-compressor, despite the high overall efficiency, it is actually considered to be low, especially when comparing with conventional household compressors, which have values normally between 50% and 70% (Hermes *et al.* 2009; Gonçalves *et al.* 2011). Such a low efficiency is potentially associated with the fact that the mini-compressor is operating at much higher suction/discharge pressures than its actual design conditions (domestic refrigerators).

It can also be seen that about 28.9%, 51.9% and 62.5% of the energy out of the LP, VC and Hybrid systems, respectively, are associated with heat losses, which increase with temperature as expected. It shows that improvements can be made to improve the overall performance of the system, which would be accomplished with the reduction of the driver and piping losses and, consequently, to increase the energy recovered in the condenser. Note however that the test bench was designed to be versatile for changing its components with the inclusion of extensive instrumentation, so it is not compact to reduce heat losses, pressure drops in pipings, etc. As such, no "optimal" system design was attempted here since the main focus was on two phase flow control.

Finally, the results show a much higher temperature for the secondary fluid at the outlet of the condenser for the hybrid system, which is related to the higher condensing temperature and better controllability. The higher temperature is attributable to potentially imply that a higher economic value is obtained for the energy available in the condenser.

5.2   Energy recovery – the second law analysis

To better explore and understand the difference among the three candidate cooling systems (liquid pumping, vapor compression and hybrid cycles) regarding energy recovery, i.e. exergy available in the condenser for a secondary application, the second law analysis was introduced.

5.2.1   Theoretical analysis

The steady state exergy rate balance is defined by Equation 5.1 (Moran *et al.* 2010). The first and second terms on the right side of the equality represent the exergy transfer accompanying heat and work, the third and fourth are the time rate of exergy transfer

accompanying mass flow and flow work and, finally, the last term is the rate of exergy destroyed.

$$0 = \underbrace{\sum_j \left(1 - \frac{T_0}{T_j}\right) \dot{Q}_j - \dot{W}_{cv} + \sum_i \mathrm{EX}_{f,i} - \sum_e \mathrm{EX}_{f,e}}_{rate\ of\ exergy\ transfer} - \underbrace{\mathrm{EX}_d}_{\substack{rate\ of \\ exergy \\ destruction}} \qquad 5.1$$

It must be noted that an exergy reference environment should be defined. Such an environment represents the state of equilibrium or the dead state. This equilibrium state defines the exergy as the maximum theoretical work obtainable when another system in a non-equilibrium state interacts with the environment to the equilibrium.

The goal of the analysis is to determine, for each major component and system, the exergy supplied, recovered and destroyed for a control volume enclosing the cooling system. With this, the overall exergetic efficiency, defined as the ratio between the recovered and supplied exergies, can be determined. The exergetic efficiency of each component is also evaluated. Furthermore, all the pressure drops in the system were considered in the analysis here. It qualitatively identifies and classifies the components that present higher irreversibilities, helping to decide which component to optimize to improve the thermodynamic performance of the cooling cycle. Detailed theoretical analysis of exgertic balance for each component can be found in Appendix C.

5.2.2 Results and discussions

Table 5.2 shows the results obtained from the exergy analysis, while Figure 5.1 to Figure 5.3 show the exergy flow of the three cycles.

Table 5.2 Exergetic analysis of the cooling systems

	LP cycle	VC cycle	Hybrid cycle
Exergy supplied, W	58.99	123.48	144.26
Exergy destroyed, W			
Liquid Pump	13.90	--	14.00
compressor	--	68.85	61.23
Condenser	21.26	13.58	12.95
MME1	1.01	1.42	1.42
MME2	2.55	2.37	2.72
Post heater	6.29	6.92	9.78
iHEx	--	1.31	1.60
LPR	--	0.10	--
SMV	1.27	1.35	1.32
EEV	--	--	4.90
Piping	9.09	20.00	31.53
Total	**55.37**	**115.90**	**131.64**
Exergy recovered, W	3.63	7.56	7.72
Exergetic efficiency, %			
Liquid Pump	0.13	--	1.25
Compressor	--	15.46	31.71
Condenser	14.58	35.75	37.36
MME1	88.94	85.78	83.42
MME2	76.99	77.99	71.60
Post heater	72.68	66.40	54.36
Overall	**6.15**	**6.12**	**5.35**
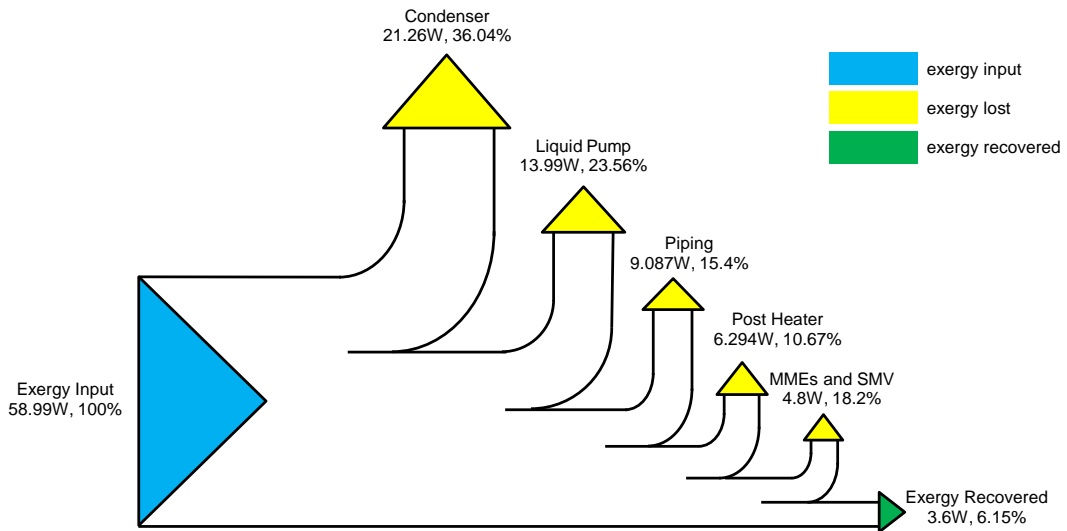
Figure 5.1 Grassmann diagram (exergy flow) for the liquid pumping cycle
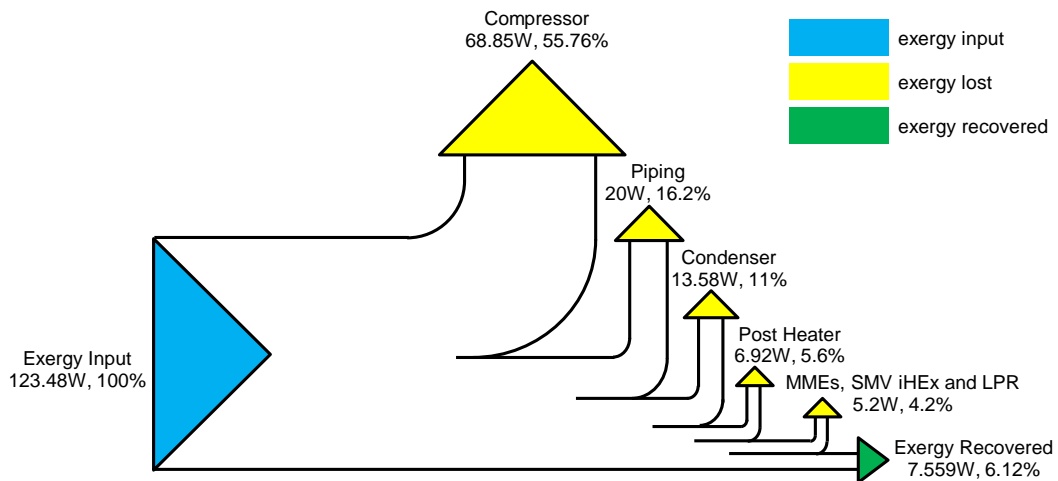
Figure 5.2 Grassmann diagram (exergy flow) for the vapour compression cycle
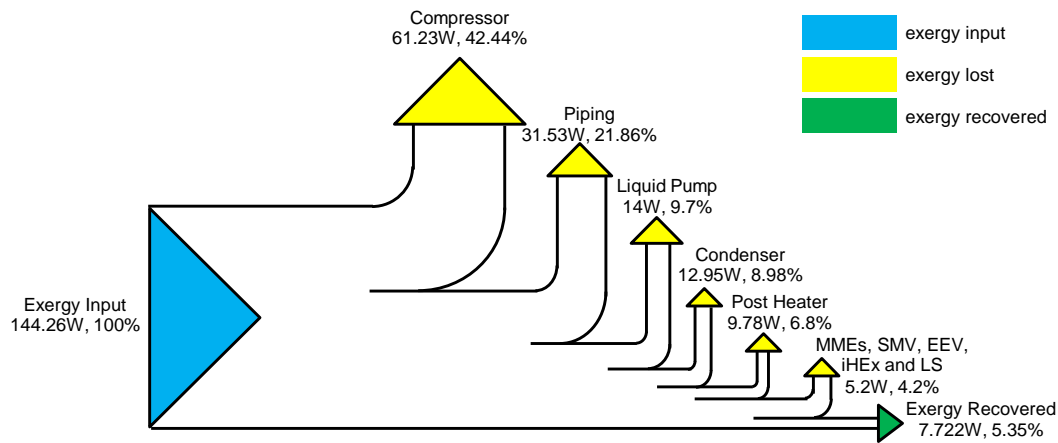
Figure 5.3 Grassmann diagram (exergy flow) for the hybrid cycle

Firstly, it is can be seen that the total exergy recovered is higher for the vapor compression and hybrid cooling systems, which is the combined consequence of the higher exergy supplied by the drivers and higher condensing temperature. However, it is highlighted that this higher exergy is the subject of interest of the owner of a secondary application of the recovered heat.

Regarding the exergetic efficiency of the components considered in the cooling systems, the driver and the condenser showed the lowest values, which implies that to improve the thermodynamic performance of the cooling systems such components must be optimized in the design. As previously noted, the drivers were not tailor-made for the current application and thus have low efficiencies. Special attention must also be given to the exergy destroyed in the piping, which represents about 16.4%, 17.26% and 23.5% of the overall exergy destroyed in the LP, VC and hybrid systems, and for the last two systems being higher than that in the condenser. This implies that a better thermal insulation and a more compact system with shorter pipings are required to minimize the heat losses, i.e. exergy lost or destroyed.

It can also be observed that the overall exergetic efficiency was lower for the hybrid cooling system, with the drivers, condenser and piping being the main culprits. The overall exergetic efficiency also shows that there is a huge need to improve the thermodynamic

performance of the cooling systems, since only an average of 6% of the supplied exergy is recovered.

The results and analyses above may lead one to conclude that the LP system is better in terms of exergy and energy. However, such a conclusion is not fair, especially when looking for the potential to improve the components' exergetic efficiencies and to reduce the piping's exergy destroyed. It seems all of the three systems can be optimized, i.e. better designed so that improvements will be generated, since the present setups were the first of a kind. It is also important to mention that the results shown here represent only the initial step in a much larger term plan where two phase flow control is the first priority and that will then followed by efficiency, and these present results will be used as the starting benching marks.

To consider the influence of improving the drivers' overall efficiency (the worst component in terms of exergetic efficiency) on the overall exergetic efficiency of the systems, a thermodynamic simulation was conducted considering as inputs the experimental results used in the previous analysis. Figure 5.4 and Figure 5.5 show the exergy efficiency plotted versus the pump and compressor efficiencies, respectively. There is a point where the exergetic efficiencies of the VC and hybrid systems surpasses that of the LP system (especially at about 25% an 50%). From an exergetic point of view, only after this point do the VC and hybrid cooling systems become competitive with the LP cooling system. It is also important to remember that the other exergy losses must be considered and the matching point of exergetic efficiency showed in Figure 5.4 and Figure 5.5 can be changed to higher or lower values in that case.
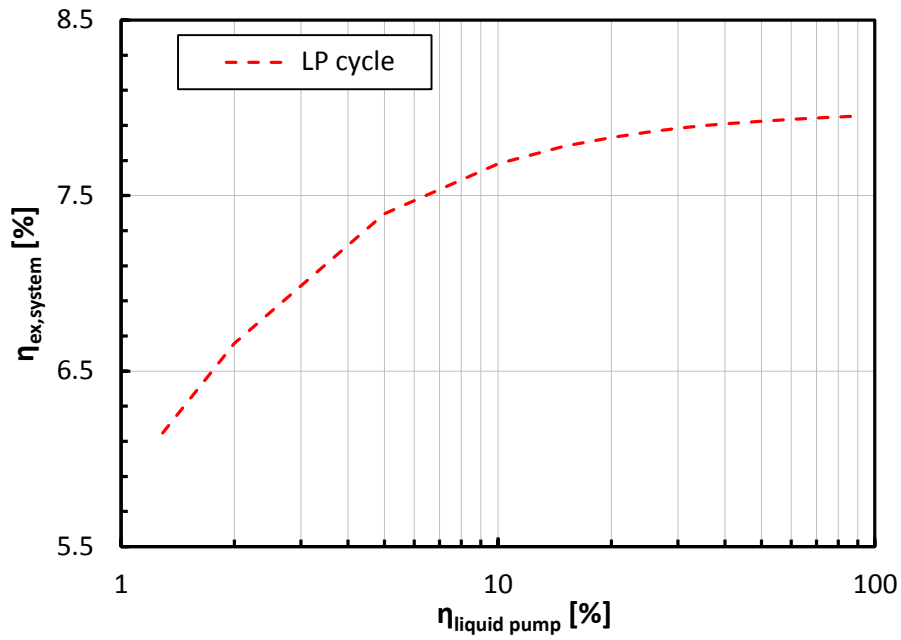
Figure 5.4 Exergetic efficiency versus driver overall efficiency for liquid pumping cycle
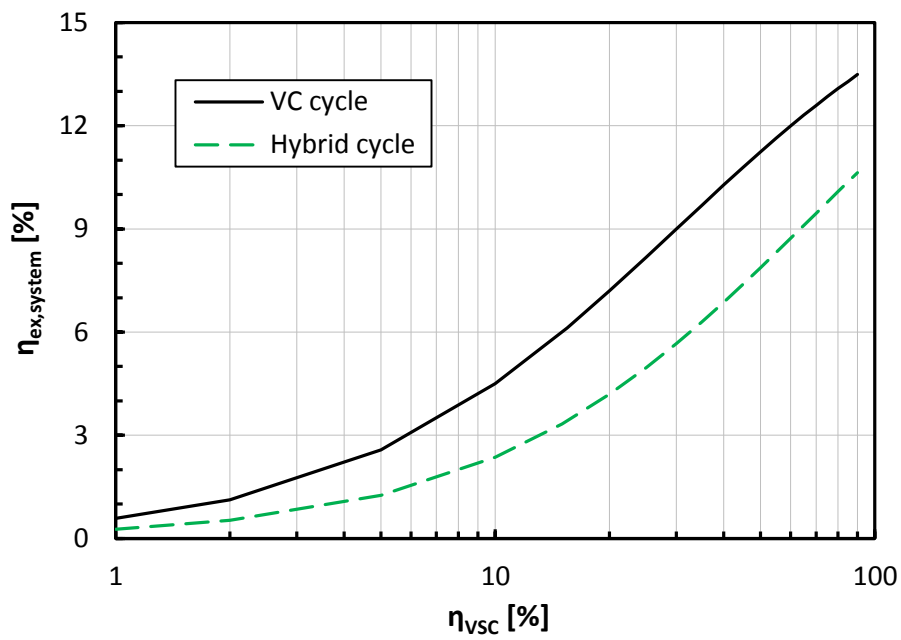
Figure 5.5 Exergetic efficiency versus driver overall efficiency for VC and hybrid cycles

Finally, it is important mentioning that the thermodynamic performance alone (energy balance) does not permit implementing the analysis shown beforehand. Exergy analysis clearly identifies the directions of efficiency improvements and reductions in thermodynamic losses attributable to green technologies. Additional advantages of such analyses are the potential to evaluate green technology aspects such as environmental impact or sustainable development (normally associated with carbon dioxide emissions) and economics ("exergy, not energy, is the commodity of value in a system, and assign costs and/or prices to exergy-related variables." (Rosen *et al.* 2008)).

6 Map of performance

The main objective in this chapter is to develop maps of performance for each cycle when taking into consideration energy consumption (cooling cycle energy performance) and the potential for energy recovery. To do this, different ranges and combinations of controlled variables were evaluated under steady state conditions to explore their effects on the cycles' performance.

Additionally, empirical and semi-empirical correlations for overall thermal conductance and performance of all components and piping of each cycle were developed and adjusted based on the experimental results obtained. This permits better analysis of the main culprits of the cycles in terms of thermal losses, and also can be used for simulations and validations of potential codes developed to design and/or evaluate the performance of these two-phase cooling cycles. This chapter then ends with an overall energy balance for each cycle using the correlations developed.

Table 6.1 shows the setpoints of controlled variables used in the performance mapping tests. A total of 120 tests were developed. The conditions were selected in order to cover the expected range in an actual cooling system.

Table 6.1 Experimental setpoints for the map of performance

	LP cycle	*VC cycle*	*Hybrid cycle*
Heat Load (W)	150 (pseudo-chips), 125 (post heater)	150 (pseudo-chips), 125 (post heater)	150 (pseudo-chips), 125 (post heater)
x_o (%)	30, 40, 50, 60	45, 50, 55, 60, 65	20, 30, 40, 50, 60
T_{cond} (°C)	58.1, 59.3, 60.6, 61.7, 63.0, 64.1	--	70, 75, 80, 85
P_{cond} (bar)	16.0, 16.5, 17.0, 17.5, 18.0, 18.5	--	21.3, 23.7, 26.3, 29.3
ΔT_{cond} (°C)	--	7.5, 10.0, 12.5, 15.0	7.5, 10.0, 12.5, 15.0

6.1 Energetic efficiency analysis

To analyze the performance of each system from an energetic point of view, two figures of merit were defined. The first one COP is the co-efficiency of performance, which is the total input power applied on the pseudo-chips and post heater (Q_{input}) divided by the sum of input power applied on drivers and actuators (W_{input}). It indicates how efficient is the system to transfer the heat dissipated by chips and power components on a board:

$$COP = \frac{Q_{input}}{W_{input}} \qquad 6.1$$

The second one η_{hr} is heat recovery efficiency, which is the condenser heat transfer rate (Q_{cond}) divided by the sum of total input power (W_{input}) and total heat load (Q_{input}) defined:

$$\eta_{hr} = \frac{Q_{cond}}{Q_{input} + W_{input}} \qquad 6.2$$

6.1.1 Liquid pumping cycle

It is important to mention that an update in the controller of outlet vapor quality was considered in this cycle, i.e. the SIMO controller (vapor quality controlled simultaneously by A_{SMV} and LPC_S) developed for the hybrid cycle was implemented. The SMV is characterized by a very low input power (about 1 W), thus with negligible effect on the overall input power of the cycle. It is used in the present cycle as an actuator that does the fine adjustment of x_o, especially under conditions of small external disturbance. For more details, see Appendix D where a comparison between SIMO and SISO control strategies in a non-uniform heat load test is shown.

As shown in Figure 6.1, COP increases when increasing x_o, which is a consequence of the decrease in the liquid pump input power (*viz.* Figure 6.2). The controller of outlet vapor quality decreases the liquid pump speed, which has a proportional relationship with the input power. It can also be observed that P_{cond} seems do not to affect COP, since no tendencies were observed and the maximum change under the same x_o was only 0.75.
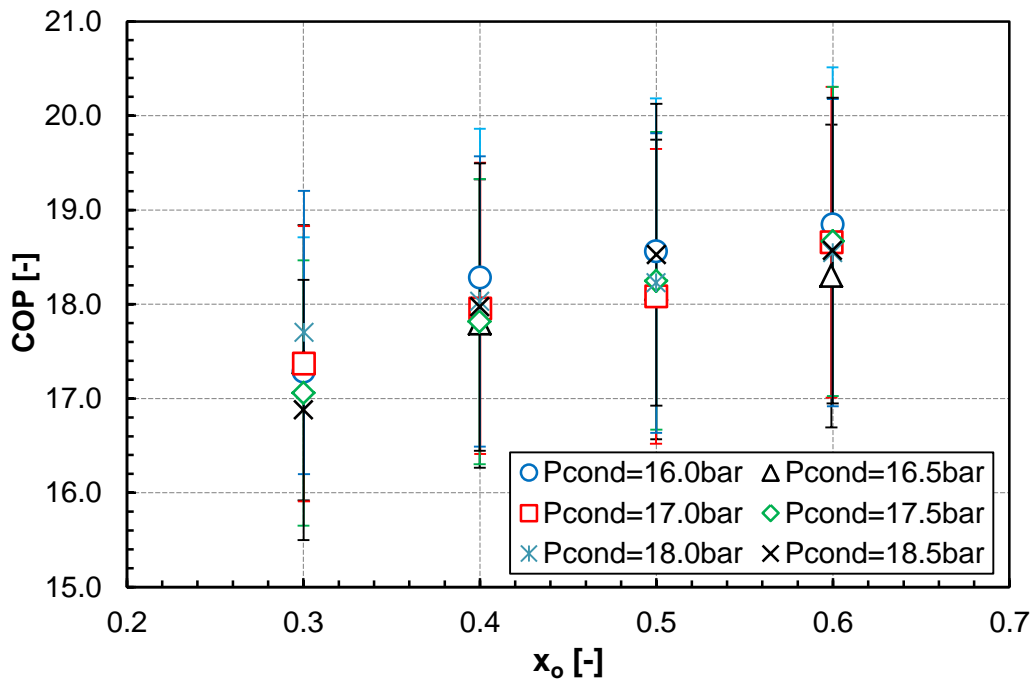
Figure 6.1 COP vs. x_o at different P_{cond}
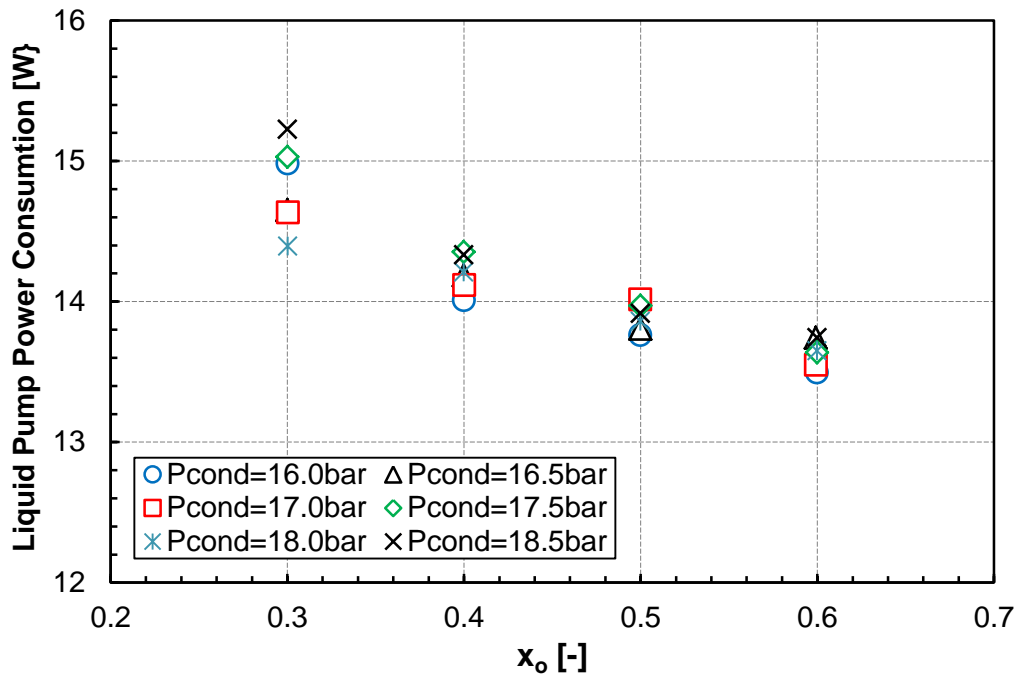
Figure 6.2 Liquid pump power consumption vs. x_o at different P_{cond}

Figure 6.3 depicts the heat recovery efficiency η_{hr} as a function of x_o and P_{cond}. A peak of η_{hr} was observed for x_o of 50% and also that the increase of P_{cond} has a negative effect on η_{hr}. The tendencies observed in η_{hr} are better interpreted when looking at the heat transfer rate at the condenser (Q_{cond}, *viz.* Figure 6.4), where the same behavior was obtained, i.e. increases with x_o and decreases with P_{cond}. Thus, as the changes in driver's input power are negligible when compared with the changes in Q_{cond} (*viz.* Figure 6.2 and Figure 6.4), it is possible to conclude that the performance of the condenser poses the major influence on heat recovery efficiency.

Finally, the reason for the decrease in η_{hr} after 50% of x_o is the inlet condition at the condenser. For 60% of exit vapor quality of MMEs x_o, the conditions at the inlet of the condenser are slightly superheated, which results in a loss of the condenser's performance since part of the condenser is used for sensible heat transfer instead of only latent heat transfer.

114
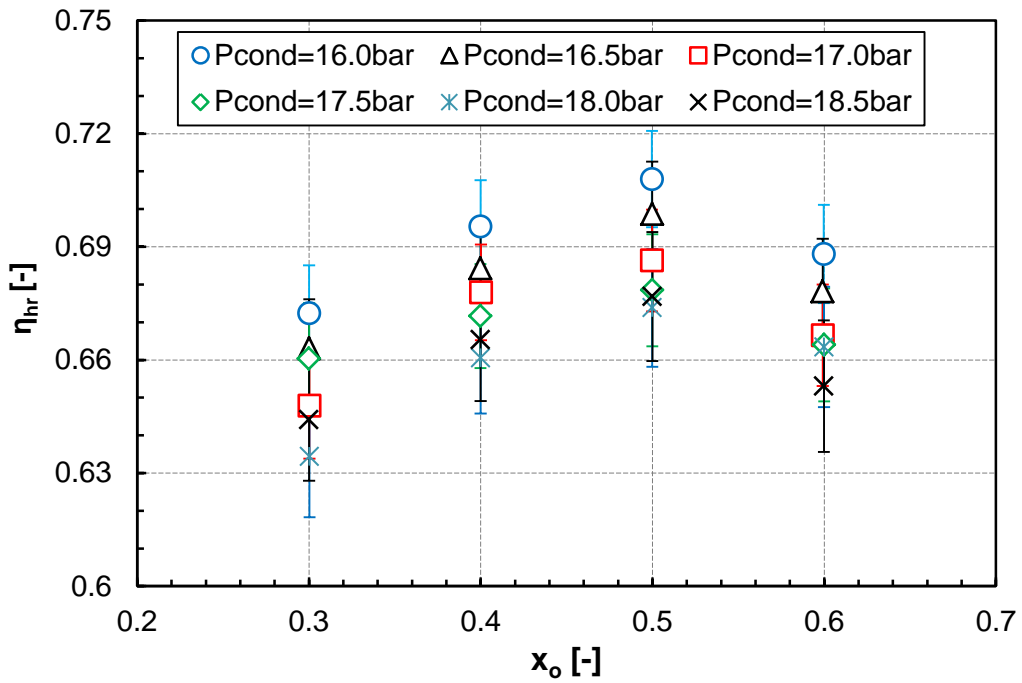
Figure 6.3 Heat recovery efficiency η_{hr} vs. x_o at different P_{cond}
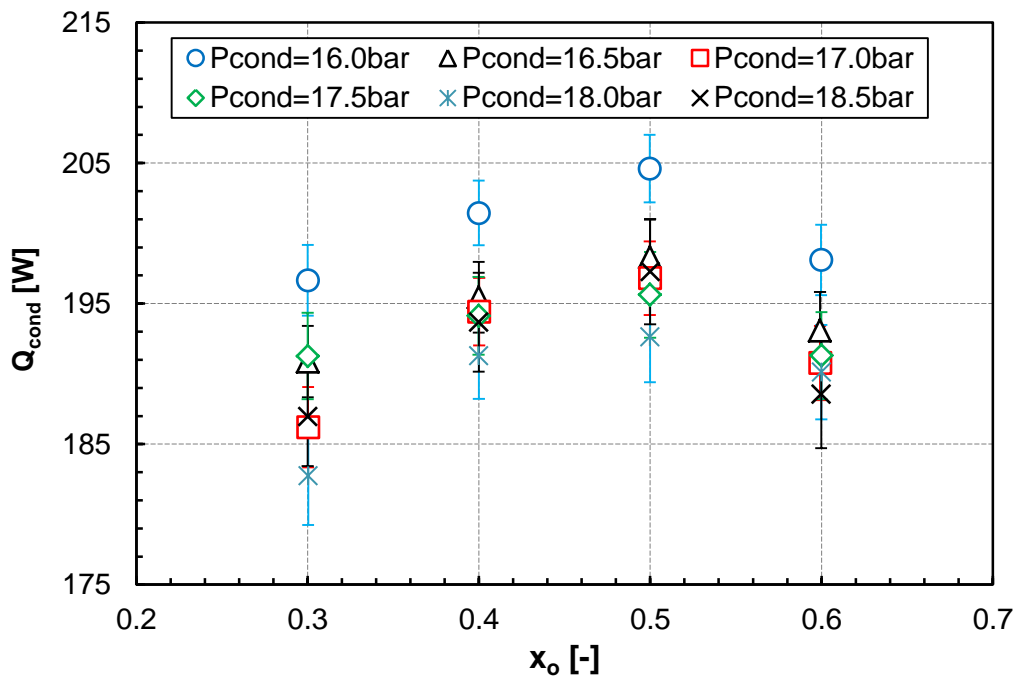
Figure 6.4 Heat transfer rate in the condenser Q_{cond} vs. x_o at different P_{cond}

Figure 6.5 shows the overall conductance of the condenser (UA_{cond}) as a function of T_{cond} and x_o. As expected, when the setpoint of x_o changes the effect on UA_{cond} is negligible. The

controller of x_o is changing the mass flow rate of HFC134a (two-phase flow), and it has a minor effect on the UA_{cond} since the main thermal resistance is due to the water side (single-phase flow). However, an increase of P_{cond} showed a decrease in UA_{cond}. The controller of P_{cond} decreases the mass flow rate of water to increase the P_{cond}, which consequently reduces the heat transfer coefficient on the water side (dominant side of the overall thermal resistance) and thus the value of UA_{cond}.
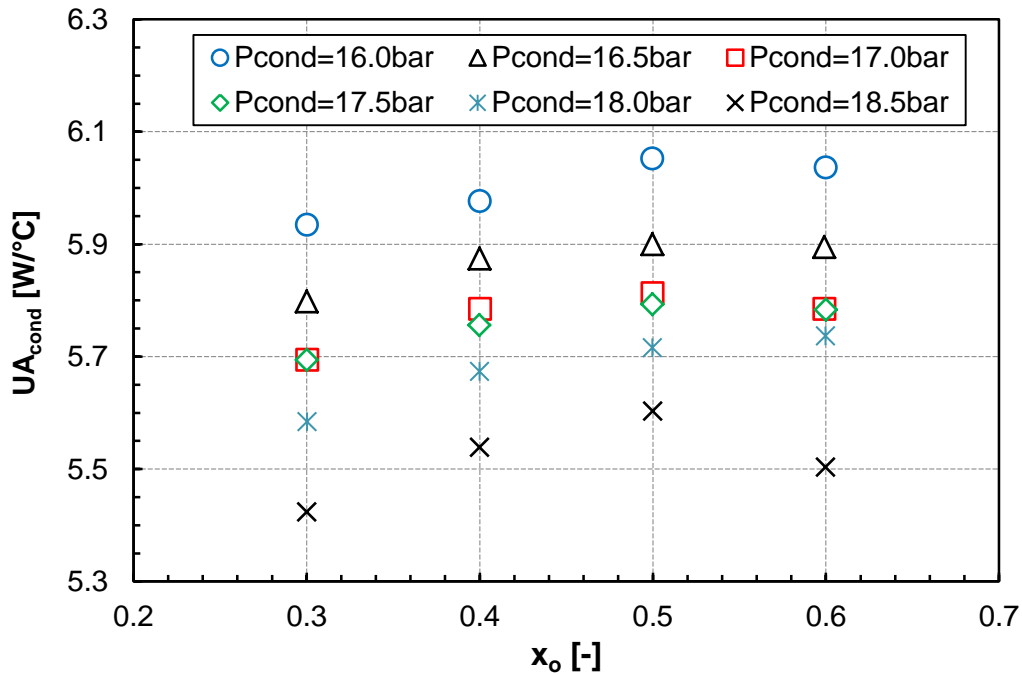
Figure 6.5 Overall conductance of condenser UA_{cond} vs. x_o at different P_{cond}

6.1.2 Vapor compression cycle

For this cycle, as explained in the Chapter 4, the controlled variable P_{cond} was changed to ΔT_{cond} due to the strong coupling effect observed between x_o and P_{cond}.

Figure 6.6 shows that COP undergoes a significant change (increase) with the increase of x_o for ΔT_{cond} of 15 °C. The same can be observed in the Figure 6.7 for W_{vsc}, which decreases with x_o mainly for ΔT_{cond} of 15 °C. The reason is that to increase in the setpoint of x_o, the controller reduces the VSC stroke and consequently the input power. Such an effect is higher for ΔT_{cond} of 15 °C due to the lower condensing pressure observed (*viz.* Figure 6.8),

which reduced significantly due to the higher heat transfer rate in the condenser, as will be seen below.
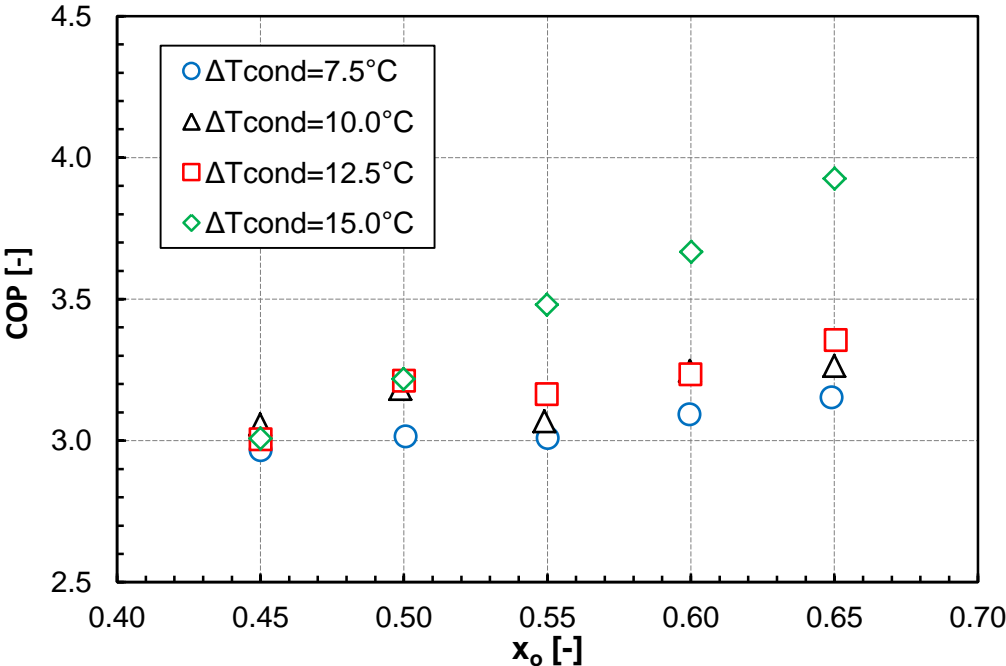
Figure 6.6 COP vs. x_o and ΔT_{cond}
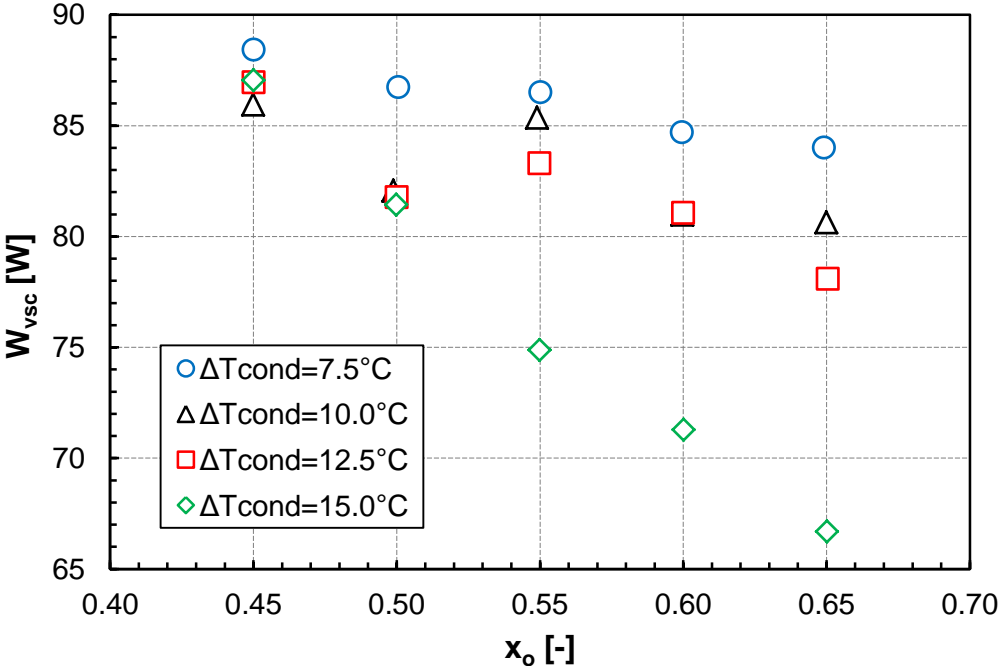
Figure 6.7 Input power of compressor W_{vsc} vs. x_o and ΔT_{cond}
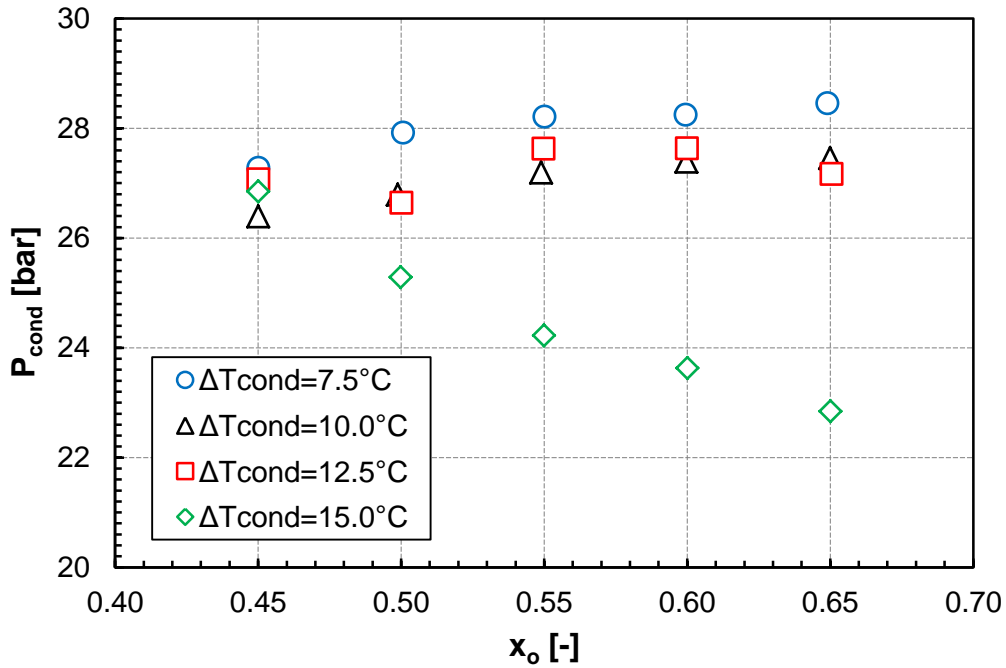
Figure 6.8 Condensing pressure P_{cond} vs. x_o and ΔT_{cond}

Figure 6.9 to Figure 6.11 show respectively the parameters η_{hr}, Q_{cond} and UA_{cond} as a function of controlled variables x_o and ΔT_{cond}. All have higher values for higher ΔT_{cond}, which is a consequence of the higher mass flow rate of water to guarantee the setpoint of ΔT_{cond} (*viz.* Figure 6.12, water mass flow rate vs. x_o and ΔT_{cond}).

Additionally, as expected, the value of x_o does not seem to affect η_{hr}, Q_{cond} and UA_{cond}, since the setpoint of x_o has a strong effect on the mass flow rate of the working fluid and the main thermal resistance in the tube-in-tube counter flow condenser is due to the secondary fluid side (single-phase flow).

Finally, as already discussed for the liquid pumping cycle, the SMV does not affect the overall power consumption due to the low input power of this actuator (about 1W). The SMV and VSC are together controlling the x_o, and the first can be considered as an actuator for fine adjustment of the x_o when in the presence of small external disturbances.
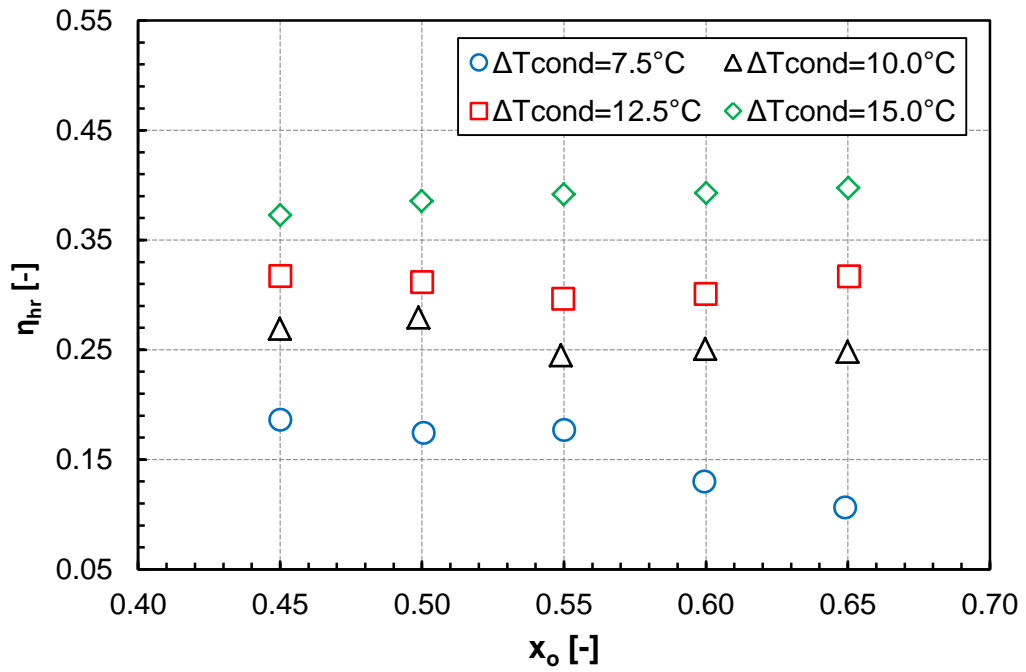
Figure 6.9 Heat recovery efficiency η_{hr} vs. x_o and ΔT_{cond}
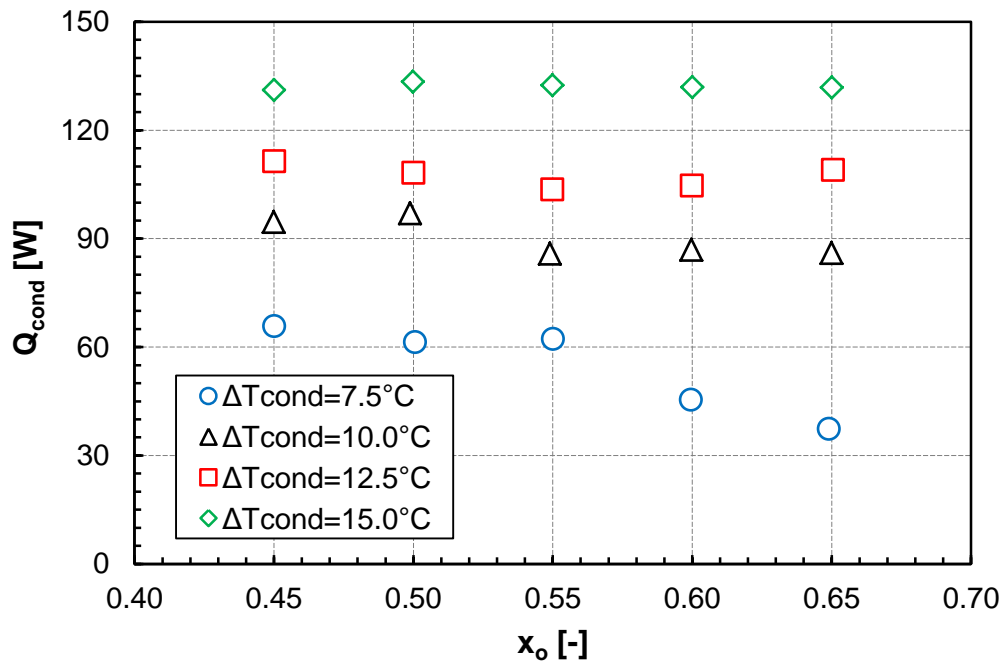
Figure 6.10 Heat transfer rate of condenser Q_{cond} vs. x_o and ΔT_{cond}
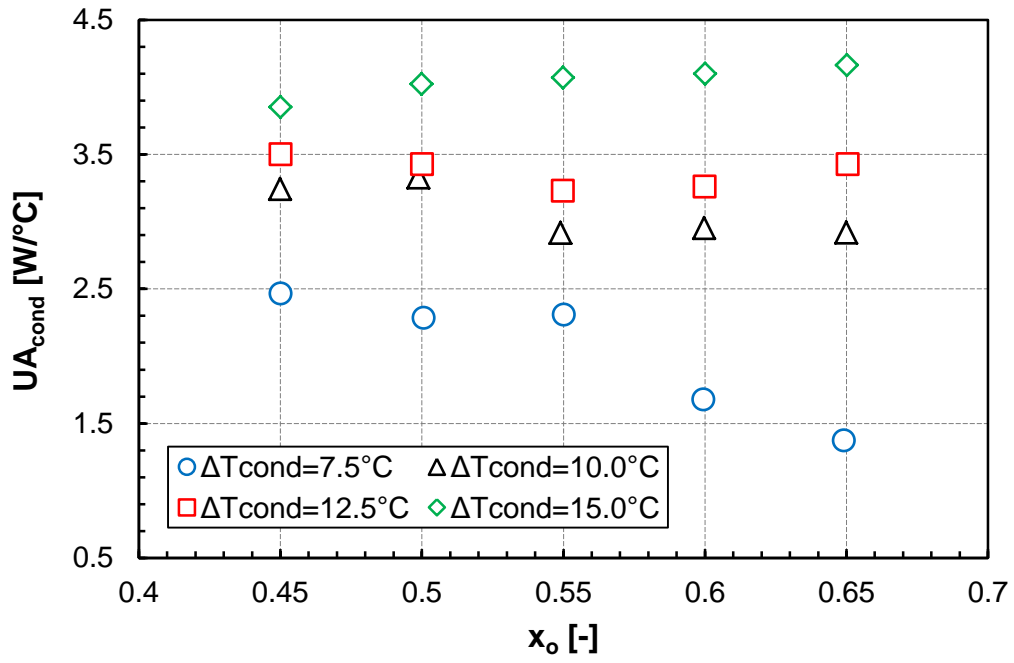
Figure 6.11 Overall conductance of condenser UA_{cond} vs. x_o and ΔT_{cond}

Figure 6.12 Water mass flow rate vs. x_o and ΔT_{cond}

120
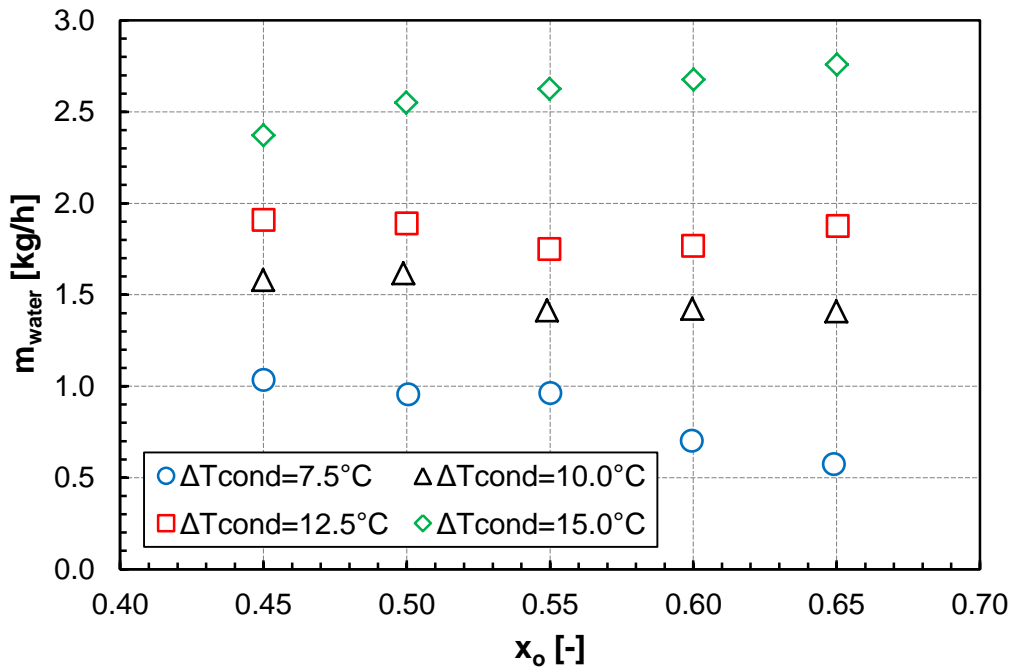
6.1.3 Hybrid cycle

Figure 6.13 and Figure 6.14 respectively show the results of LPC power consumption and heat transfer rate in the condenser (Q_{cond}) as a function of x_o and ΔT_{cond} at a value of T_{cond} of 85 °C. A decrease in power consumption can be seen with the increase of x_o, which is a consequence of the decrease in the LPC speed (controlled to guarantee the setpoint of x_o). On the other hand, x_o did not show an effect on Q_{cond} and it seems the controlled variable ΔT_{cond} does not affect the LPC power consumption. In contrast, the size of ΔT_{cond} showed a significant effect on Q_{cond}, which increases when increasing ΔT_{cond}. It is justified mainly by the higher mass flow rate of water imposed by the LPW_s controller to reach the higher ΔT_{cond}, consequently increasing the heat transfer coefficient on the water side. It is worth mentioning that similar effects were observed for the other setpoints of T_{cond}.

Based on the previous results, it was decided from now to consider the hybrid cycle separated into a *cooling loop* and a *condensing loop*, since the effects of changes in the setpoint of controlled variables appear to be concentrated inside the loop in which the controller is acting. Thus, as the x_o did not show any effect in the *condensing loop*, all analysis that follows was developed for a constant value of x_o, i.e. 20%.
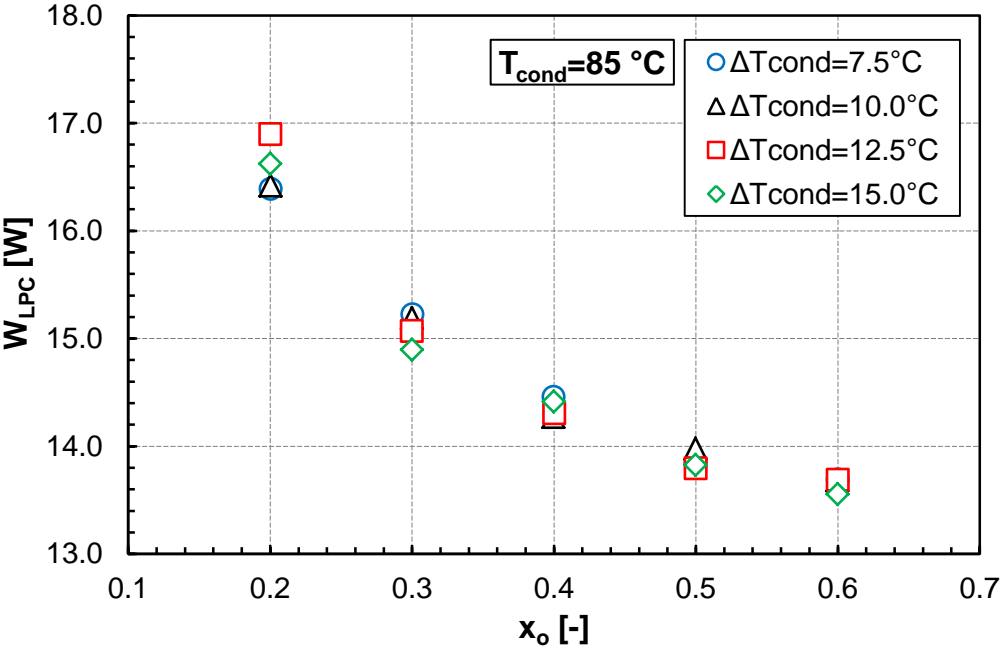
Figure 6.13 Input power of liquid pump vs. x_o and ΔT_{cond} at T_{cond}=85 °C
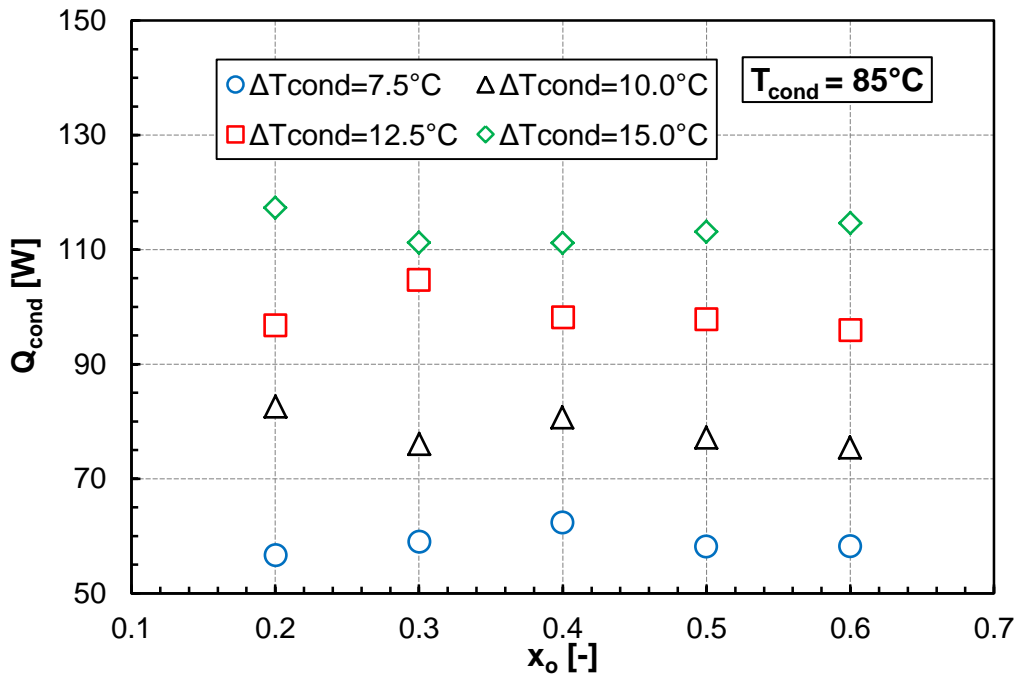
Figure 6.14 Heat transfer rate of condenser Q_{cond} vs. x_o and ΔT_{cond} at T_{cond}=85 °C

Figure 6.15 shows the effect of ΔT_{cond} and T_{cond} on η_c. It can be seen that there is a tendency of a decrease in η_c when increasing T_{cond}, which is mainly associated with the increase of compressor input power (W_{vsc}). Regarding the setpoint change of ΔT_{cond}, one can say it seems to have an effect only for T_{cond} of 80 °C (η_c ranges from 2.8 to 3.1). In fact, when ΔT_{cond} increased for this T_{cond}, the VSC controller increased the stroke to maintain the same condensing temperature, consequently increasing the power consumption of the compressor, as shown in Figure 6.16 and Figure 6.17, respectively. Additionally, it is observed that the EEV duty cycle remained constant (*viz.* Figure 6.18), which means constant input power (*viz.* Figure 6.19). The final result, as can be seen in Figure 6.15, was a decrease of the cooling cycle efficiency with ΔT_{cond}.

For the other condensing temperatures, the effect of ΔT_{cond} on COP seems to be cancelled/minimized by the opposite action of the actuators, i.e. increase the stroke (power) of VSC and decrease the duty cycle (power) of EEV (both controllers have an opposite response for a change in ΔT_{cond}, which cancelled out their combined effect on COP).

122
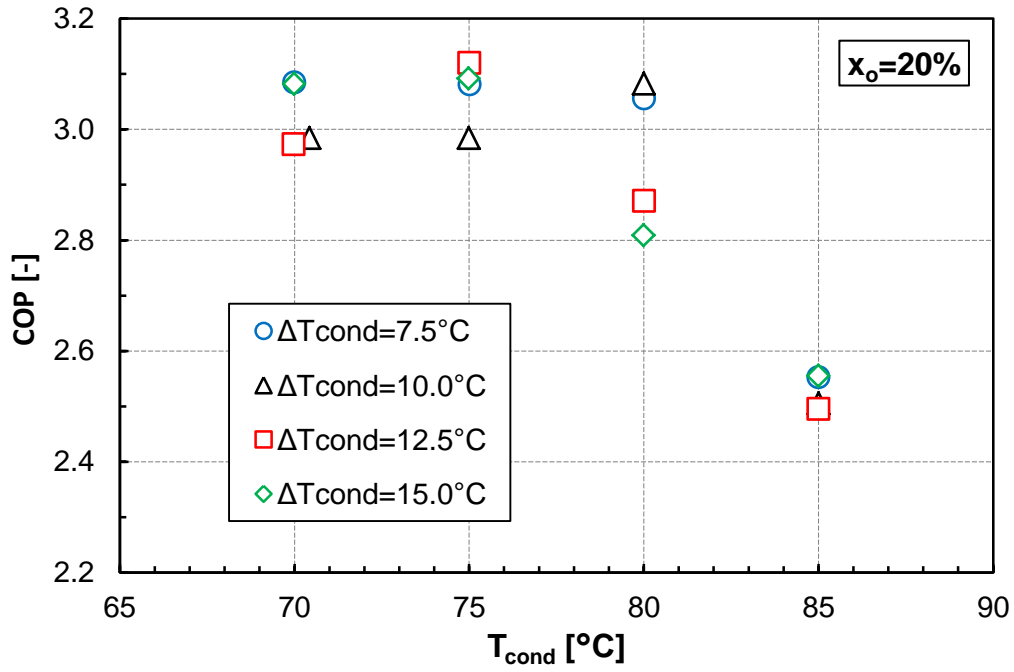
Figure 6.15 COP vs. T_{cond} and ΔT_{cond} at $x_o =20\%$
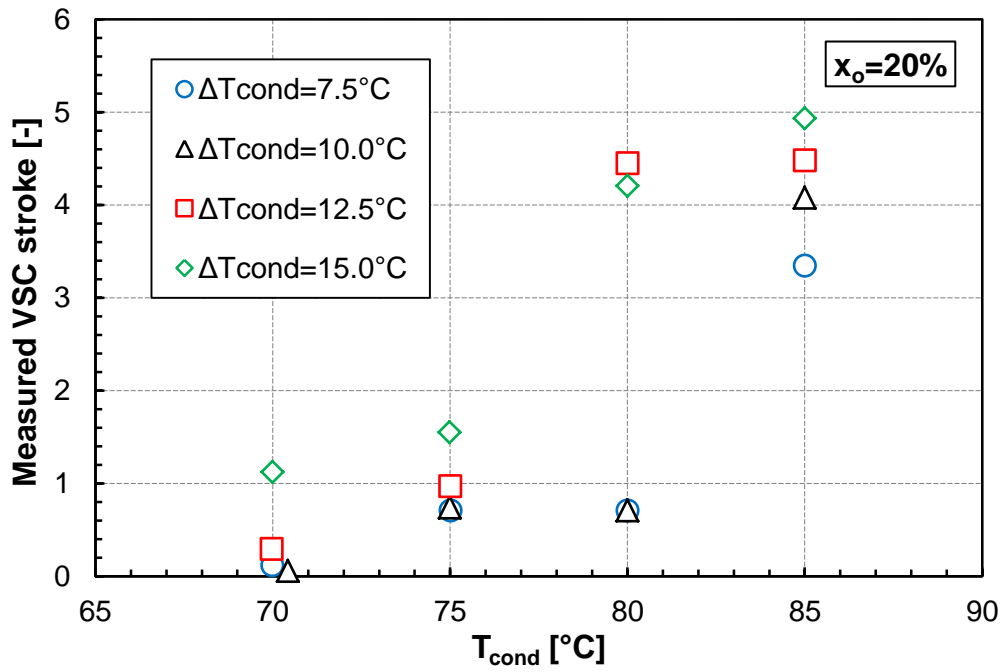
Figure 6.16 Measured VSC stroke vs. T_{cond} and ΔT_{cond} at $x_o =20\%$
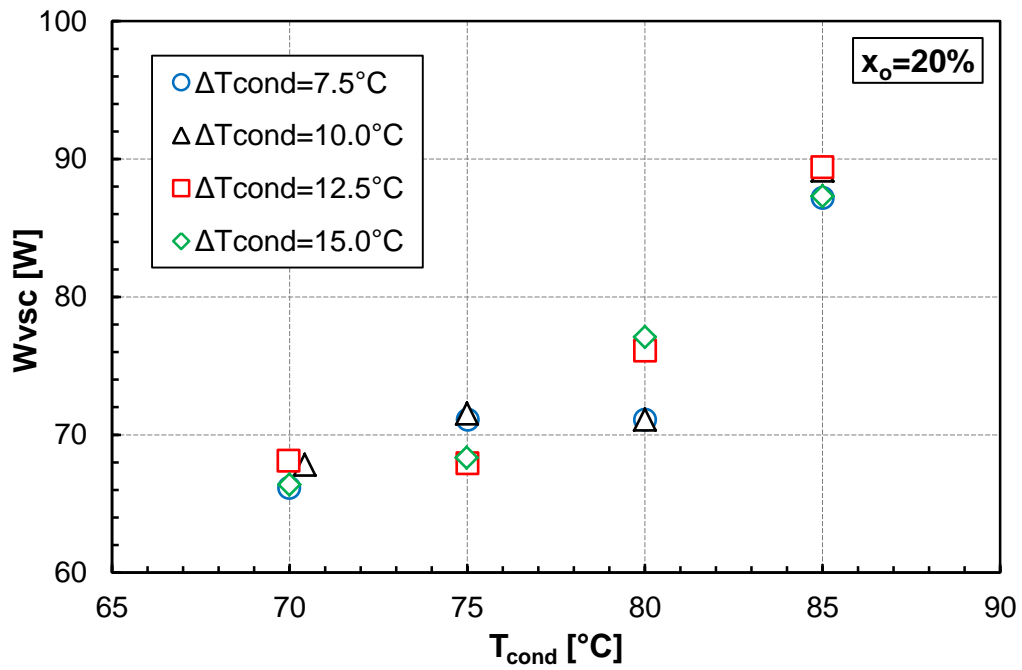
Figure 6.17 Power consumption of VSC vs. T_{cond} and ΔT_{cond} at $x_o = 20\%$
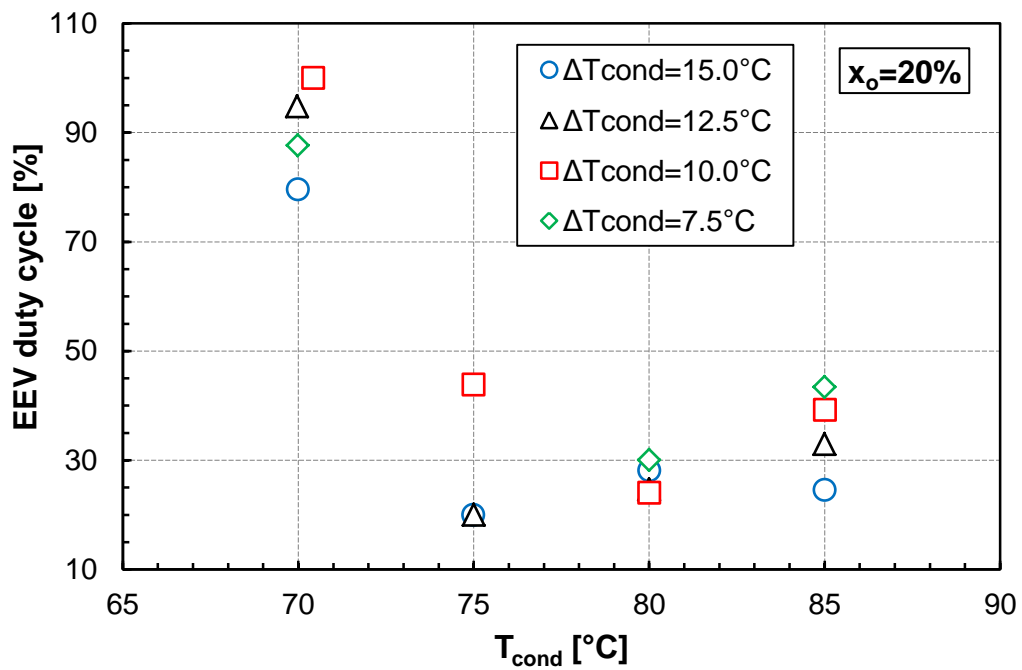
Figure 6.18 EEV duty cycle vs. T_{cond} and ΔT_{cond} at $x_o = 20\%$
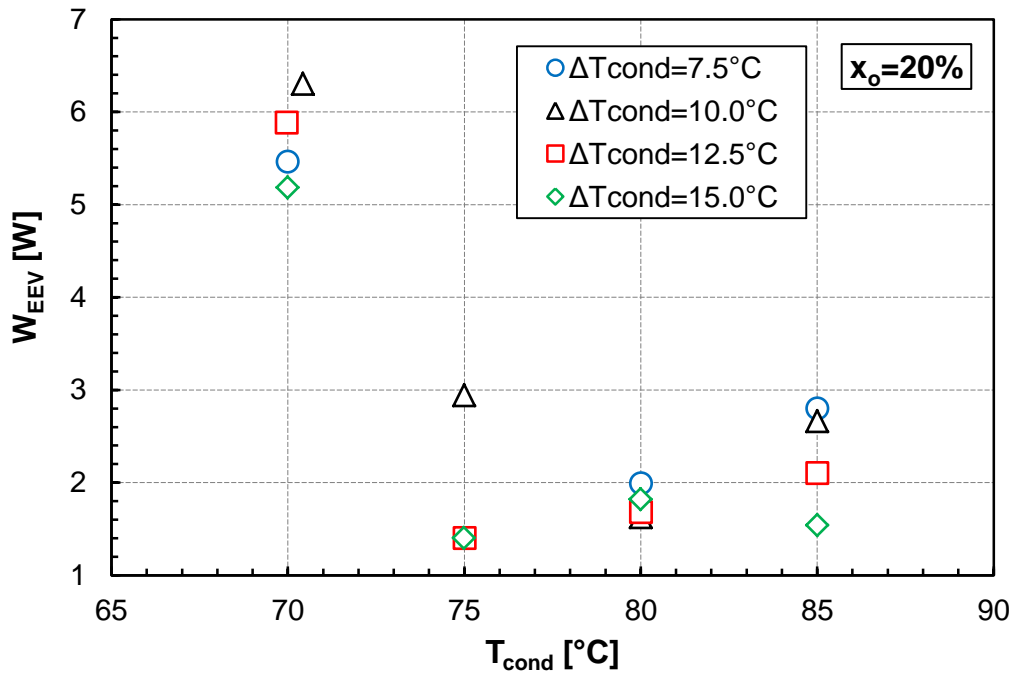
Figure 6.19 Power consumption of EEV vs. T_{cond} and ΔT_{cond} at x_o=20%

Figure 6.20 shows the map of heat recovery efficiency (η_{hr}). It can be observed that the effect of an increase in ΔT_{cond} was to increase η_{hr}, as a consequence of the higher Q_{cond} (*viz.* Figure 6.21). On the other hand, the effect of an increase in T_{cond} was to decrease η_{hr}, where such an increase causes an increase of W_{VSC} and the expectation would be also an increase in Q_{cond}. However, as observed in Figure 6.21, Q_{cond} slightly decreases, which means that the heat losses increase in the cycle due to a higher T_{cond}. Thus, as W_{VSC} increases and Q_{cond} decreases, it elucidates the reduction of η_{hr} with T_{cond}.
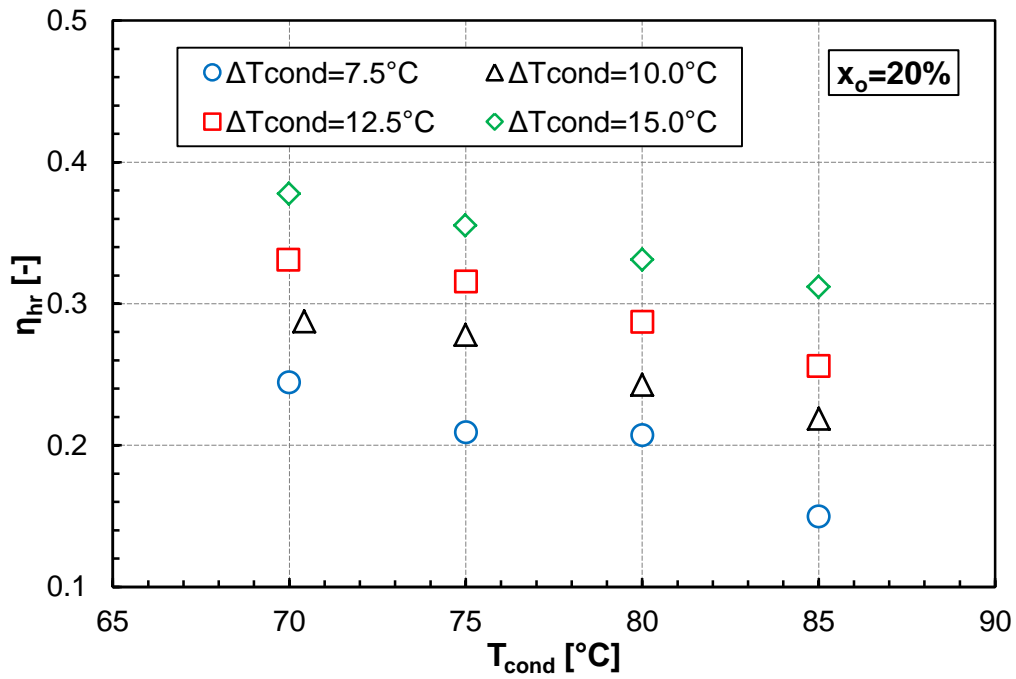
Figure 6.20 Heat recovery efficiency η_{hr} vs. T_{cond} and ΔT_{cond} at $x_o=20\%$
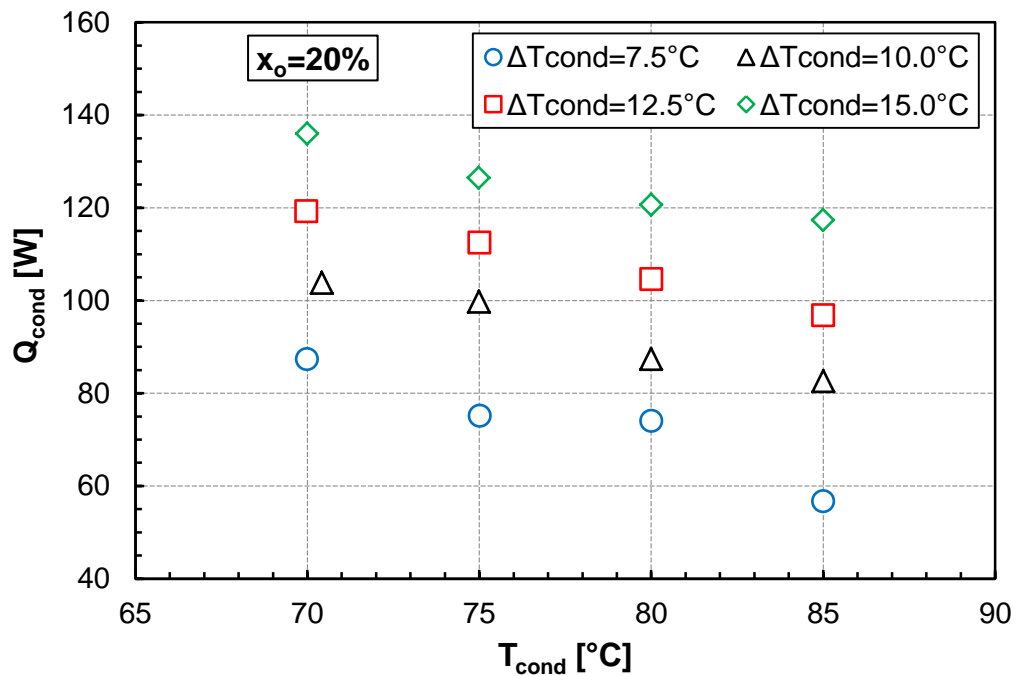
Figure 6.21 Heat transfer rate of condenser Q_{cond} vs. T_{cond} and ΔT_{cond} at $x_o=20\%$

Finally, Figure 6.22 and Figure 6.23 show the condenser's effectiveness (ε_{cond}) and overall conductance (UA_{cond}), respectively. The ε_{cond} increase when increasing T_{cond} and

decreasing ΔT_{cond}. However, UA_{cond} is decreasing when considering the same analysis. One can say that this condenser is not well designed/adjusted to work in high T_{cond} and low ΔT_{cond} due to the lower value of UA_{cond}, in spite of the higher value of ε_{cond}. From the heat recovery point of view, the idea would be to work with a high T_{cond} and low ΔT_{cond}, i.e. a condition where a high exergy level is established (high temperature of secondary fluid). Thus, to achieve such a condition, either an increase of condenser's area or an enhancement of the overall heat transfer coefficient is desired.
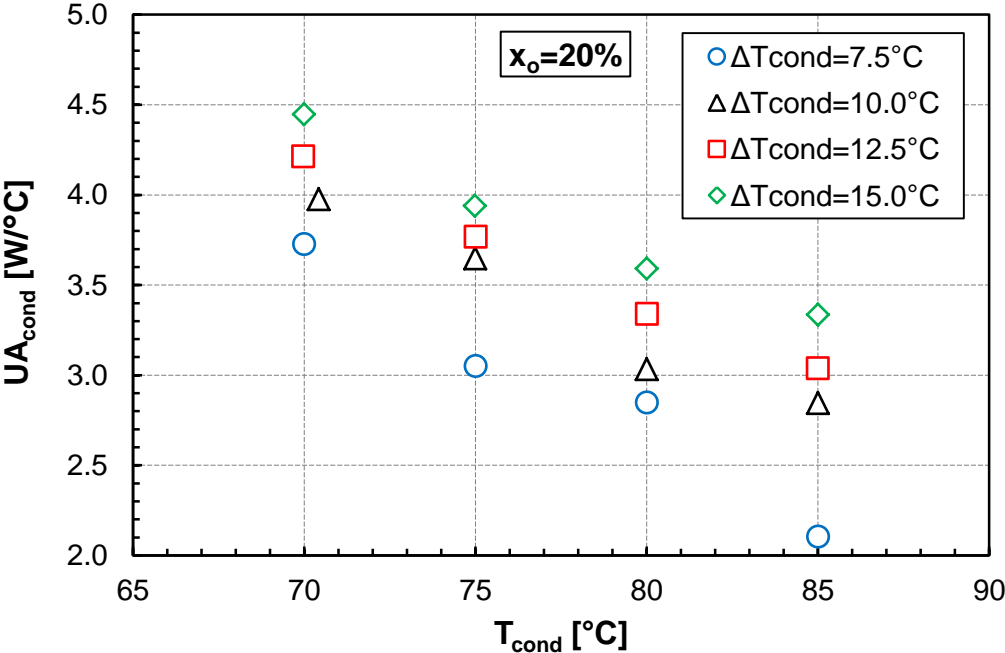
Figure 6.22 Overall conductance of condenser UA_{cond} vs. T_{cond} and ΔT_{cond} at $x_o=20\%$
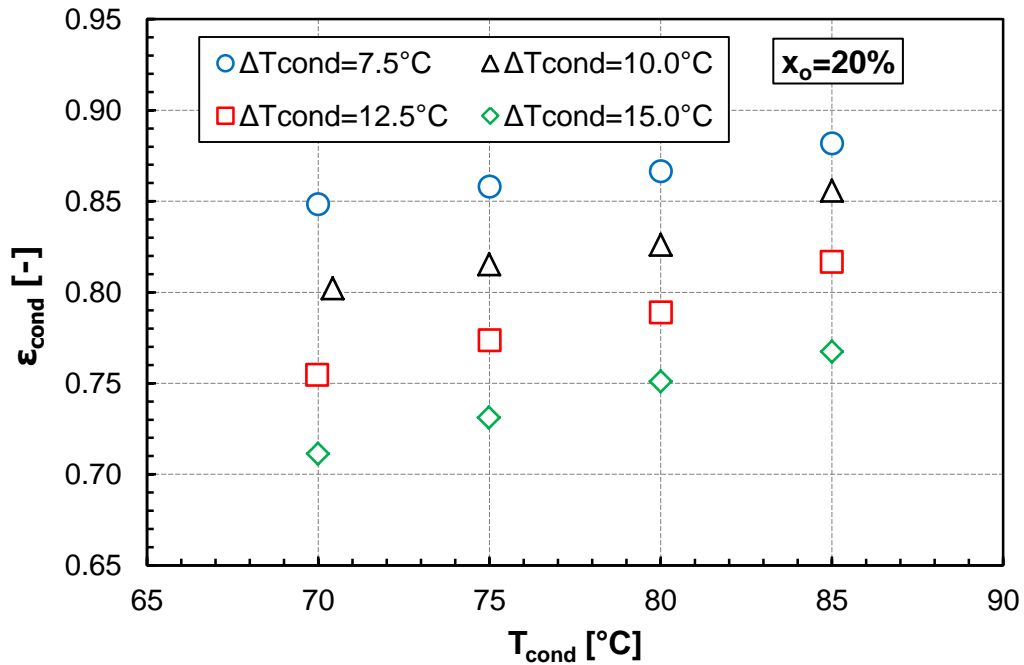
Figure 6.23 Effectiveness of condenser ε_{cond} vs. T_{cond} and ΔT_{cond} at x_o=20%

6.1.4 Overall comparison

Figure 6.24 to Figure 6.27 show the general comparison among the three cycles regarding the cooling cycle and heat recovery efficiencies, condenser's outlet water temperature and overall conductance.

The higher η_c observed for the LP cycle is explained due to the low driver input power. The gear pump is used only for flow circulation, while the mini-compressor is used to guarantee a difference of pressure between the evaporator and the condenser, and, consequently will present a higher input power and lower COP.

Regarding η_{hr}, the maximum values obtained were about 70% for the LP cycle and 40% for the other two cycles. The difference observed is due to the higher heat losses (piping and drivers, the latter being associated with their low overall efficiencies) for the cycles with higher condensing temperature, i.e. VC and hybrid cycles. Such a difference can be significantly reduced if a better thermal insulation and a more efficient driver are implemented or designed.

128

The main idea behind the VC and hybrid cycles, as described in Chapter 3, is to increase the quality (exergy) of the heat recovered at the condenser and for which the condensing temperature has to be increased. It results in a higher water temperature at the outlet of the condenser, which can be easily observed in Figure 6.26. A maximum value of about 78 °C for VC and hybrid cycles were observed against only 42 °C for the LP cycle.

It is important to mention using one of the cycles with the compressor is only justified for the cases where the secondary application of the heat recovery limits the result for a minimum in temperature. Additionally, as the quantity of energy currently rejected (waste heat) in CRAC units of data centers is huge (many MW), an exergy-economic analysis must be done for each specific application to answer if the additional energy spent to increase the exergy is compensated by the overall gains (economic energetic, and environmental) of the data center and the secondary application.
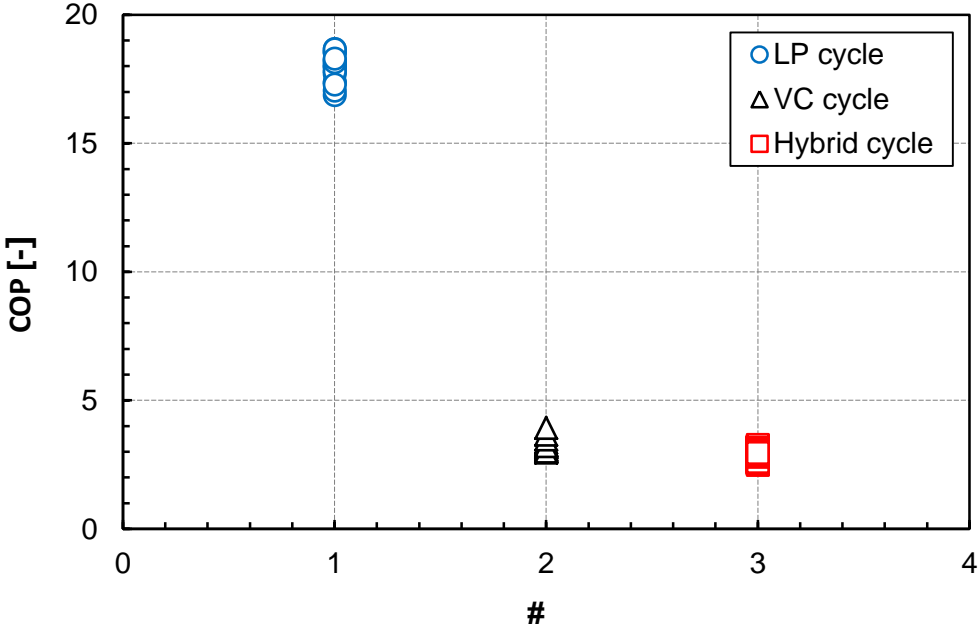
Figure 6.24 COP for the three cycles
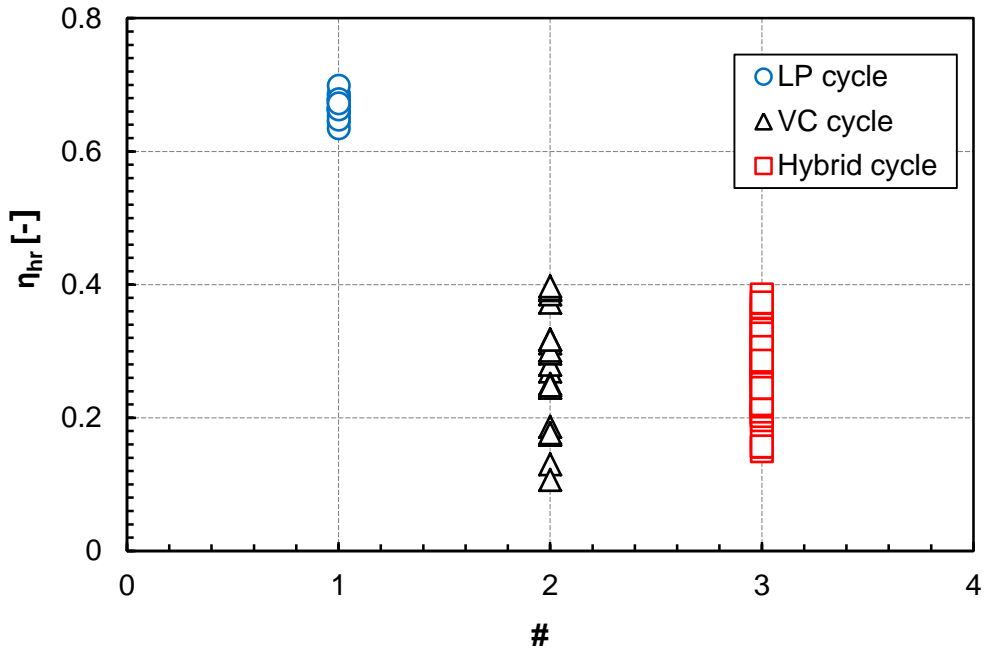
Figure 6.25 Comparison of heat recovery efficiency η_{hr} for the three cycles
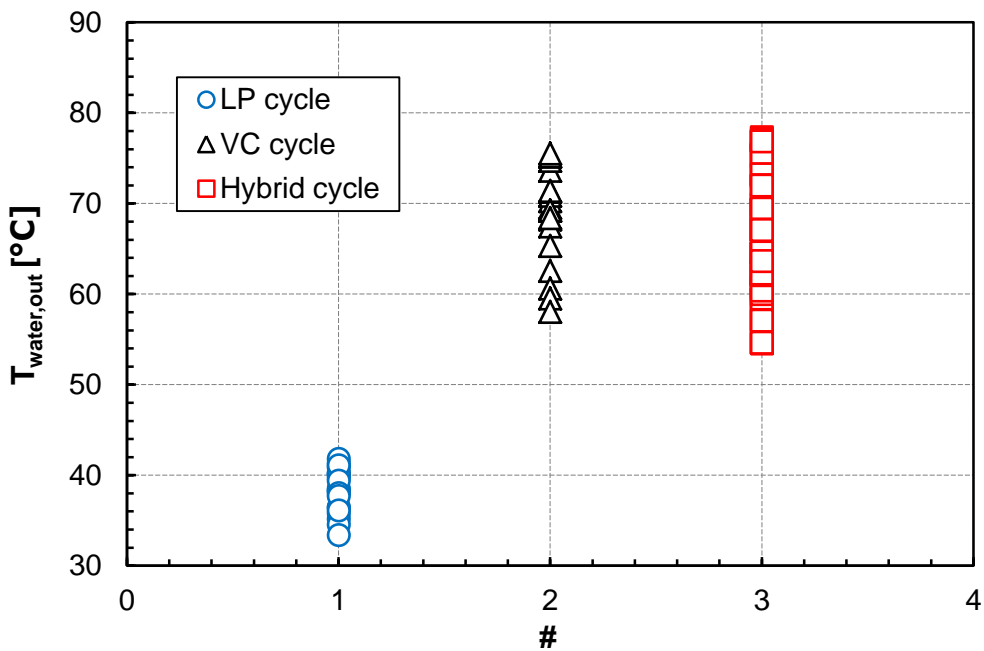
Figure 6.26 Comparison of outlet water temperature for the three cycles

Figure 6.27 and Figure 6.28 show respectively the condenser's overall conductance (UA_{cond}) and effectiveness (ε_{cond}) determined from the map of performance tests with all cycles as a

function of water mass flow rate, where it can be seen it has a well-defined behavior. As the overall thermal resistance is dominated by the single-phase flow side of the tube-in-tube condenser (water side), the results observed for UA_{cond} were expected, i.e. the single-phase side heat transfer coefficient increases with the water mass flow rate. The thermal resistance due to conduction and convection in the two-phase side (HFC134a side) of condenser are negligible:

$$Overall\ thermal\ resistance = \frac{1}{UA_{cond}} = \left(\frac{1}{\frac{1}{h_{sp}A_{sp}} + \frac{\ln(d_o/d_i)}{2\pi kL} + \frac{1}{h_{tp}A_{tp}}} \right)^{-1} \qquad 6.3$$

where:

h_{sp} and h_{tp} are respectively the heat transfer coefficients for the single phase and two phase flows, W/(m^2·K);

A_{sp} and A_{tp} are respectively the heat transfer areas for the single phase and two phase flows, m^2;

L is the length of the condenser tube, m;

k is the thermal conductivity of the tube, W/(m·K);

d_o and d_i are respectively the inner and outer diameters of the bute, m.

On the other hand, the condenser effectiveness showed an opposite effect when increasing the water mass flow rate. Such a result is explained by the fact that the outlet water temperature is decreasing with the water mass flow rate and the inlet water temperature is constant, which results in a natural decrease in effectiveness (Figure 6.29):

$$\varepsilon_{cond} = \frac{T_{w,o} - T_{w,i}}{T_{cond} - T_{w,i}} \qquad 6.4$$

where

$T_{w,o}$ and $T_{w,i}$ are the inlet and outlet temperatures of the water flow in the condenser, °C;

T_{cond} is the condensing temperature, °C.
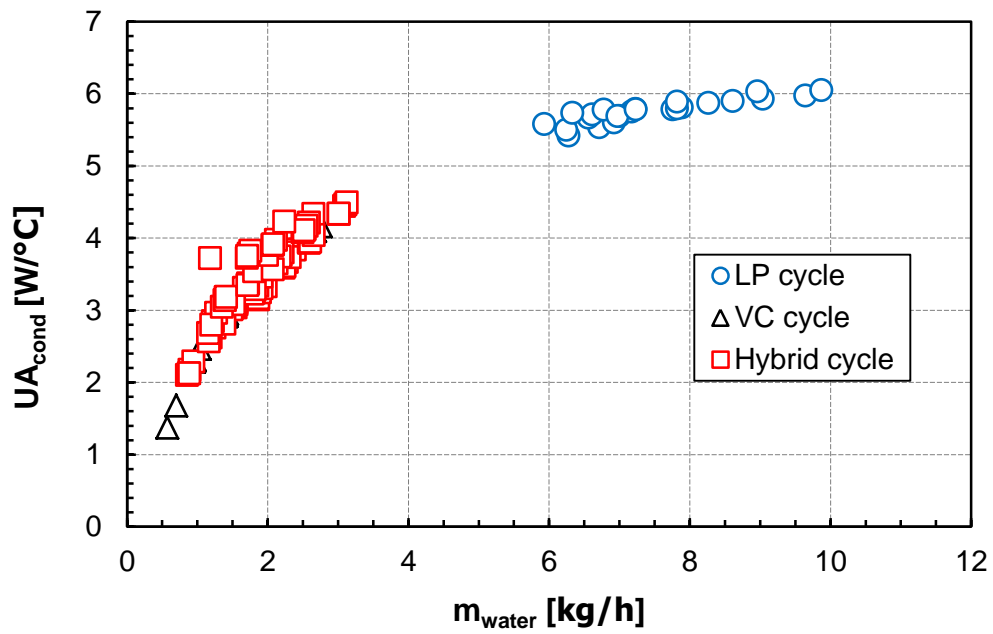
Figure 6.27 Comparison of condenser overall conductance UA_cond vs. $\dot{m}_{water}$ for the three cycles
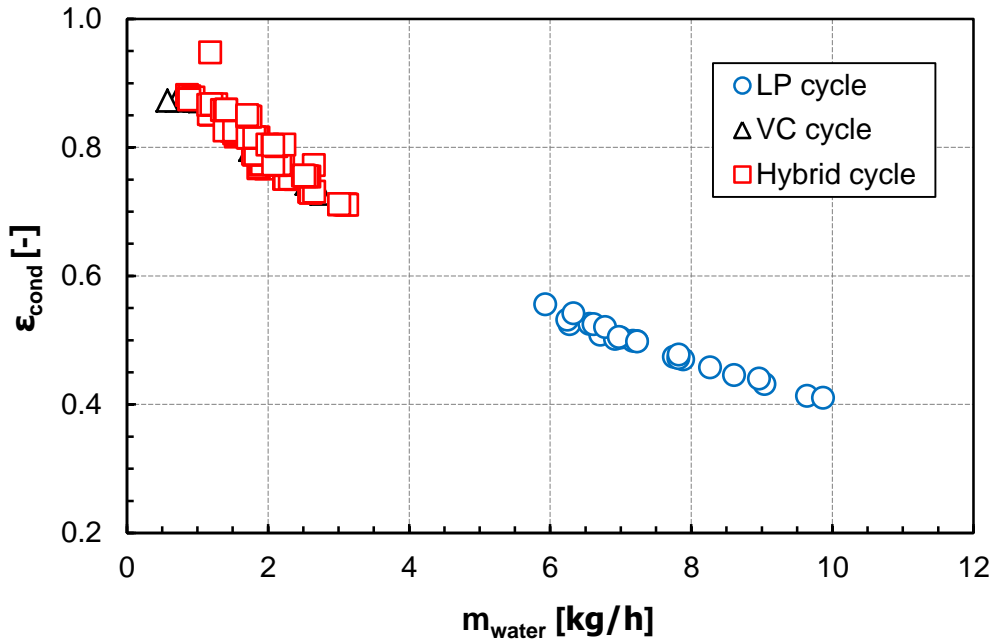
Figure 6.28 Comparison of condenser effectiveness ε_{cond} vs. $\dot{m}_{water}$ for the three cycles
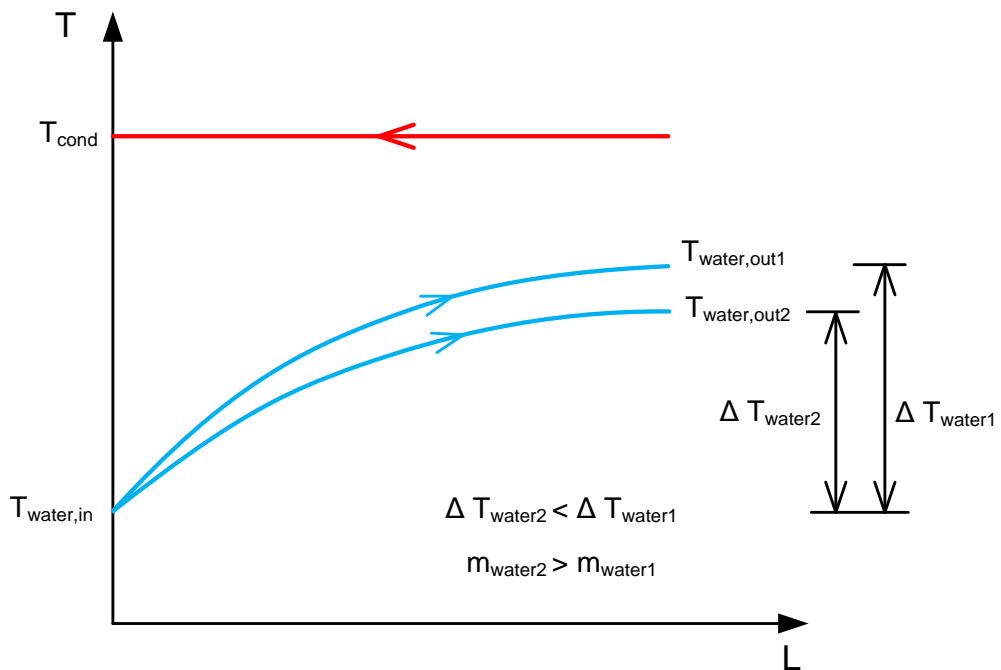
Figure 6.29 $\dot{m}_{water}$ affects the effectiveness of the condenser

6.2 Components' empirical and semi-empirical correlations

Empirical and semi-empirical correlations for characterizing the piping and components of the three cycles in terms of heat loss and thermal performance (for the drivers) were developed, based on the experimental database previously analyzed. Such correlations permit a better interpretation of the main thermal losses in the cycles and also can be used for the design and performance evaluation of potential future cooling systems.

6.2.1 Piping

Based on the performance mapping tests, a correlation for the overall heat loss conductivity (λ_{HL}, W/(m·K)), which characterizes the heat lost per length of piping, was developed as a function of the average temperature of the piping ($T_{avg,piping}$). It was assumed that all piping has a uniform thickness of thermal insulation material. The correlation obtained is as follows:

$$\lambda_{HL} = 0.0065 \times T_{avg,piping} - 0.2384 \qquad 6.5$$

Thus, the heat loss is determined by

$$HL_{piping} = \lambda_{HL} \times L \times \left(T_{avg,piping} - T_{amb} \right) \qquad 6.6$$

where:

L is the nominal length of pipe [m].

Table 6.2 lists the length of all pipes for the three cycles considered in the present study. Appendix D shows the diagram with the numbered positions of each section along the cycles.

Table 6.2 Pipe length for the three cycles

Cycle	Section	Length (cm)
LP cycle	2 to Coriolis	120
	Coriolis to 38	104
	Junction after 12/13 to 6	150
	9 to 15	107
	16 to 17	70
	18 to 1	104
VC cycle	2 to Coriolis	120
	Coriolis to 38	104
	Junction after 12/13 to 6	150
	9 to 15	107
	16 to 17	70
	18 to 1	104
Hybrid cycle	2 to Coriolis	120
	Coriolis to 38	104
	Junction after 12/13 to 6	150
	9 to 27	189
	28 to 29	85
	30 to 19	65
	20 to 15	110
	16 to 21	90
	22 to 23	34
	24 to 25	63
	26 to 1	76

6.2.2 Inlet and outlet piping (distributors) and MMEs

Based on the "diodes" (sensors of temperature assembled in each pseudo-chip) and calibration tests, the heat loss of each MME section was determined, which includes the pipe after/before the flow distribution/mixer and the MME (*viz.* Figure 6.30). This enabled an overall thermal conductance for each section to be determined, as can be seen in Equation 6.7. It is highlighted that the heat loss was determined by an energy balance in the MME sections, which considered the input power for the pseudo-chips and the increase in the enthalpy of the subcooled working fluid.

a) MME1 CV   b) MME2 CV
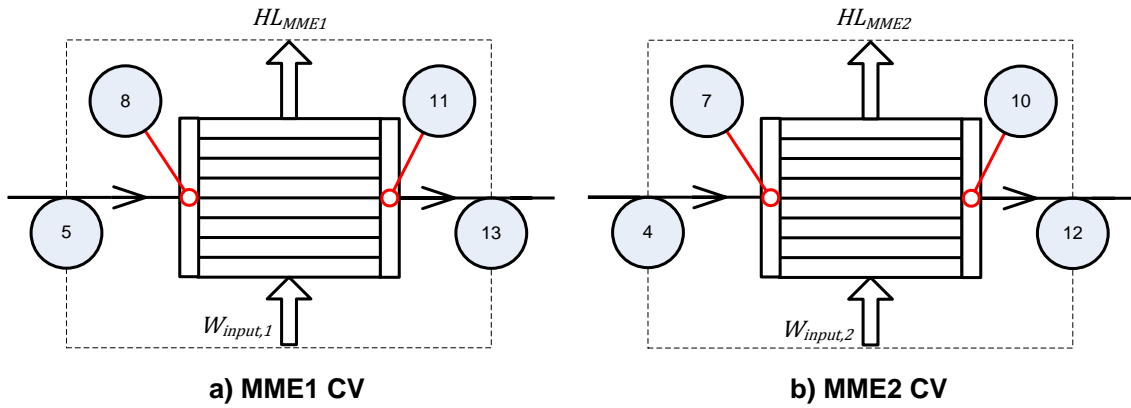
Figure 6.30 Control volumes to determine the UA of MME sections

$$HL_{MME} = UA_{MME} \times \left(T_{avg,MME} - T_{amb}\right)$$ 6.7

where:

$UA_{HL,MME}$ is the overall heat loss conductance for each MME control volume [W/(m·K)];

$T_{avg,MME}$ is the weighted temperature based on the area of inlet and outlet piping and MME [°C].

The expression to calculate the $T_{avg,MME1}$ for the MME1 section is:

$$T_{avg,MME1} = \frac{T_{avg,5-8} \times A_{5-8} + T_{avg,8-11} \times A_{8-11} + T_{avg,11-13} \times A_{11-13}}{A_{5-8} + A_{8-11} + A_{11-13}}$$ 6.8

Table 6.3 shows the areas of each pipe and the MMEs.

Table 6.3 Areas of piping and MMEs

Section	4-7	7-10	10-12	5-8	8-11	11-13
Area (m²)	0.00329	0.00383	0.00359	0.00339	0.00383	0.00499

The UA$_{MME1}$ and UA$_{MME2}$ were respectively 0.2583 W/(m·K) and 0.1889 W/(m·K).

136

Finally, it is worth mentioning that the heat losses of MME sections were not considered in the development of the controllers in the Chapter 4, i.e. the energy balance to determine the outlet vapor quality does not consider the heat losses. This means a more conservative and safer control was developed, since the actual vapor quality is lower than the calculated value (more far away of the critical vapor quality). Figure 6.31 shows a comparison between the corrected and not corrected x_o. There is an over prediction of about 10-20% in the x_o.
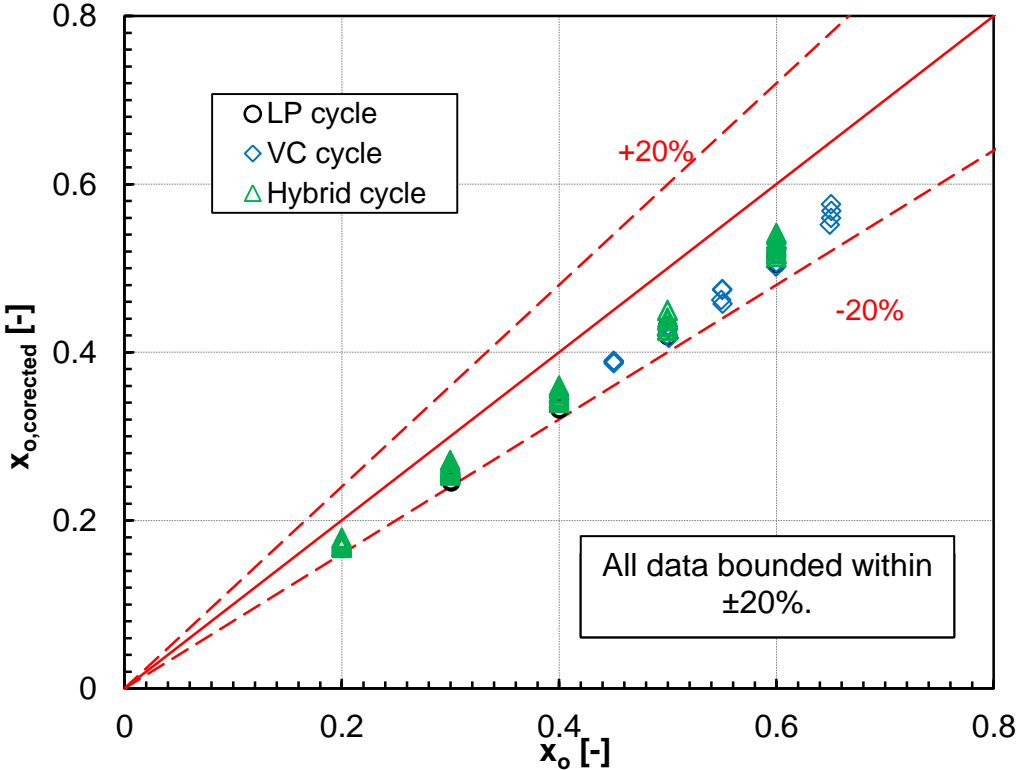
Figure 6.31 Comparison of corrected and not corrected results of x_o

6.2.3 Post heater

Based on an energy balance on the post heater, the heat loss was determined and an overall thermal conductance adjusted. Equations 6.9 and 6.10 show the expressions obtained:

$$UA_{PH} = -0.2830 + 0.006308 \times T_{PH} \qquad 6.9$$

$$HL_{PH} = UA_{PH} \times (T_{PH} - T_{amb}) \qquad 6.10$$

where:

UA_{PH} is the overall thermal conductance of post heater [W/K];

T_{PH} is the temperature at the inlet of post heater [°C];

and T_{amb} is the ambient temperature [°C].

6.2.4 Mini-compressor

6.2.4.1 Heat loss

Considering an energy balance around of the mini-compressor (*viz.* Figure 6.32) the heat loss (HL_{VSC}) was determined, as showed in Equation 6.11.
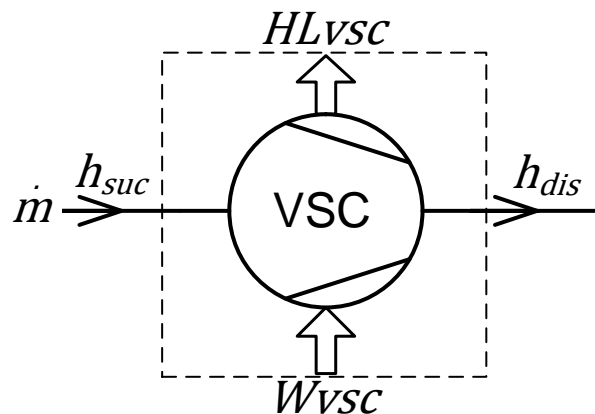
Figure 6.32 Control volume in the VSC

$$\dot{m}h_{suc} + W_{vsc} = \dot{m}h_{dis} + HL_{vsc} \qquad \qquad 6.11$$

where:

$\dot{m}$ is the mass flow rate of the compressor [kg/s];

h_{suc} and h_{dis} are the enthalpy at the suction and discharge of VSC, respectively [kJ/kg];

W_{vsc} is the VSC input power [W];

HL_{vsc} is the heat loss to the ambient [W].

Based on the method proposed by Gonçalves *et al.* (2011), the overall thermal conductance was determined. Equations 6.12 and 6.13 show the results obtained. The UA is a function of the condensing and evaporating temperatures, which were determined based on the compressor's discharge and suction pressures, respectively.

$$UA_{VSC} = 2.4358 + 0.0590 \times T_{cond} - 0.0772 \times T_{evp} \qquad \qquad 6.12$$

$$HL_{VSC} = UA_{VSC} \times \left(T_{evp} - T_{amb} \right) \qquad \qquad 6.13$$

where:

UA_{VSC} is the thermal conductance [W/K];

T_{cond} is the condensing temperatrue which is based on the discharge pressure [°C];

T_{evp} is the evaporating temperature which is based on the suction pressure [°C];

T_{amb} is the ambient temperature [°C].

Figure 6.33 shows a comparison between predicted and experimental results of UA_{VSC}, where all of the data were bounded with ±10%.
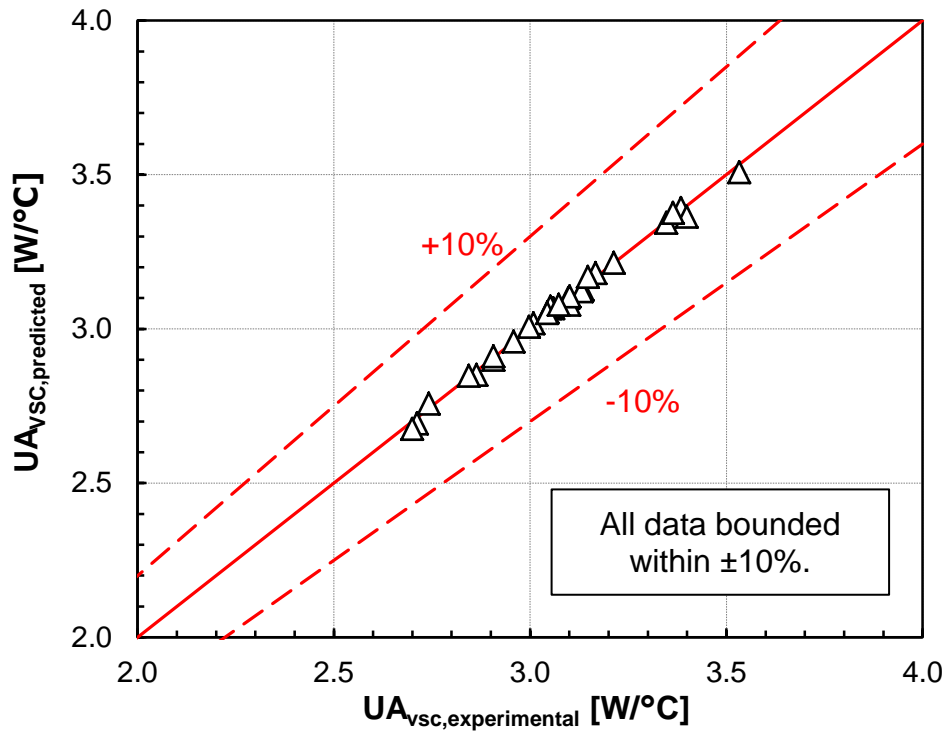
Figure 6.33 Comparison of predicted and experimental results of UA$_{VSC}$

6.2.4.2 Isentropic efficiency

The isentropic efficiency, which is the ratio between the isentropic compression and total input power, was adjusted as a function of stroke and pressure ratio, as shown below:

$$\eta_{ise} = 0.1730 + 0.04055 \times \text{Stroke} - 0.02800 \times \Upsilon_P \qquad 6.14$$

where:

Stroke is the measured stroke of the mini-compressor [-];

Υ_P is the pressure ratio between the discharge and suction lines [-].

Figure 6.34 shows a comparison between predicted and experimental results of isentropic efficiency, where the result obtained is satisfactory since 89% of the data were bounded with ±10%.
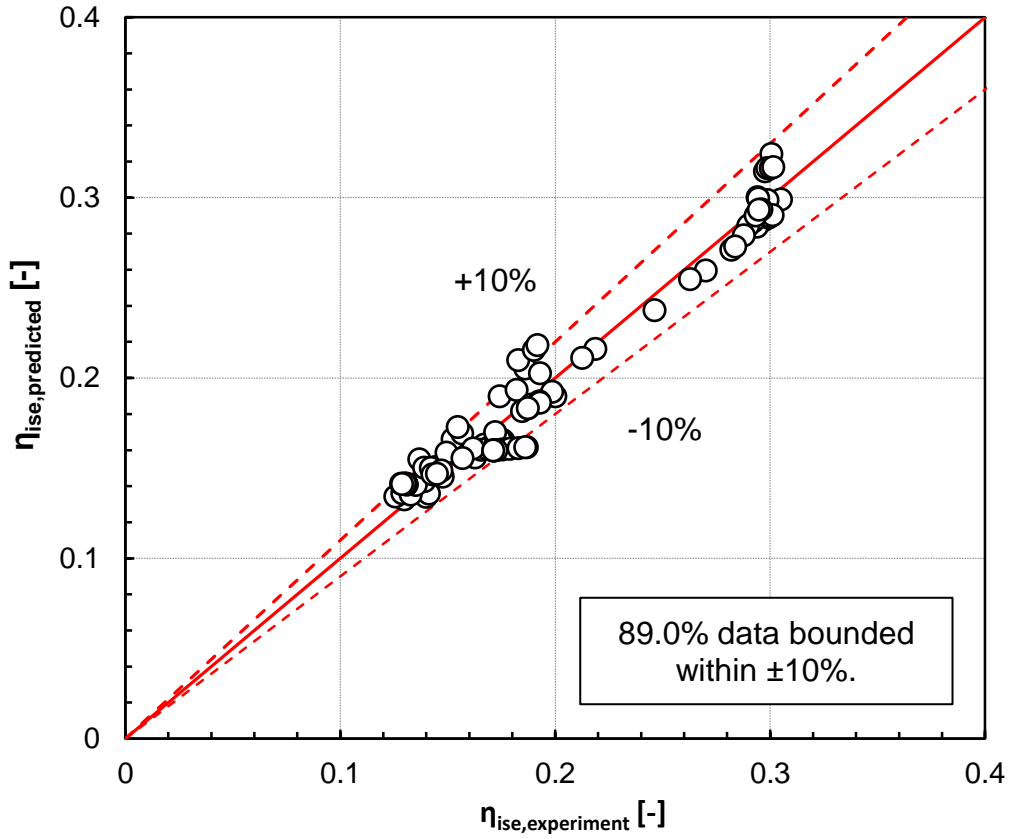
Figure 6.34 Comparison of predicted and experimental results of η_{ise}

6.2.4.3   Volumetric efficiency

Volumetric efficiency η_v is defined as the ratio between actual and theoretical mass flow rate:

$$\eta_v = \frac{\dot{m}_{act}}{\dot{m}_{the}} = \frac{\dot{m}_{act}}{NV_{sw}/v_{suc}} \qquad 6.15$$

where:

$\dot{m}_{act}$ and $\dot{m}_{the}$ are the actual and theoretical compressor mass flow rates [kg/s];

N is the speed [rpm/s];

V_{sw} is the compressor swept volume [m^3];

v_{suc} is the specific volume at the suction [m^3/kg];

A semi-empirical model was adjusted based on the theoretical equation of volumetric efficiency deduced by Gosney (1982):

$$\eta_v = 1 - \frac{V_d}{V_{sw}} \left(\Upsilon_P{}^{1/\kappa} - 1 \right) \qquad\qquad 6.16$$

where:

V_d is the dead volume [m³];

Υ_P is the ratio of the discharge and suction pressures [-];

k is the index of isentropic compression, which is calculated as:

$$k = \frac{\ln \Upsilon_P}{\ln\left(V_{suc}/V_{dis}\right)} \qquad\qquad 6.17$$

where:

v_{suc} and v_{dis} are the specific volume at the suction and discharge lines, respectively [m³/kg].

To obtain the semi-empirical model, necessary corrections were made in the suction specific volume and the swept volume, as can be seen in Equations 6.18 and 6.19. They are the main parameters that affect the volumetric efficiency during the compression process. The maximum swept volume (Vsw,max, 0.267 cm³), dead volume (Vd, 0.007854 cm³) and speed (N, 336.4 rpm/s) were given by the manufacturer. It is highlighted that the mini-compressor is characterized by a variable stroke, i.e. the Vsw changes depending on the stroke desired (stroke can be adjusted by an external controller). Equation 6.20 and Table 6.4 show respectively the adjusted model and the coefficients of Equations 6.18 and 6.19.

$$V_{sw,adj} = V_{sw,max} + C_1 \text{Stroke} + C_2 \Upsilon_P + C_3 \Upsilon_p^2 \qquad\qquad 6.18$$

$$v_{suc,adj} = v_{suc} + C_4 \Upsilon_P \qquad\qquad 6.19$$

$$\eta_v = 1 - \frac{V_d}{V_{sw,ajd}} \times \left(\Upsilon_P{}^{1/k} - 1 \right) \qquad\qquad 6.20$$

Table 6.4 Coefficients for Equations 6.18 and 6.19

	C1	C2	C3	C4
Value	1.7905E-08	-2.0357E-07	3.3043E-08	-1.1529E-03

The expression to calculate the mass flow rate, which was used in the *condensing loop* of the hybrid cycle since the Coriolis was used to measure the mass flow rate in the *cooling loop* is shown below:

$$\dot{m} = \frac{NV_{sw,max}}{v_{suc,adj}}\eta_v$$

6.21

Finally, Figure 6.35 shows the comparison between predicted and experimental results of $\dot{m}_{vsc}$, and it can be seen that 91% of the data were bounded with ±10%.
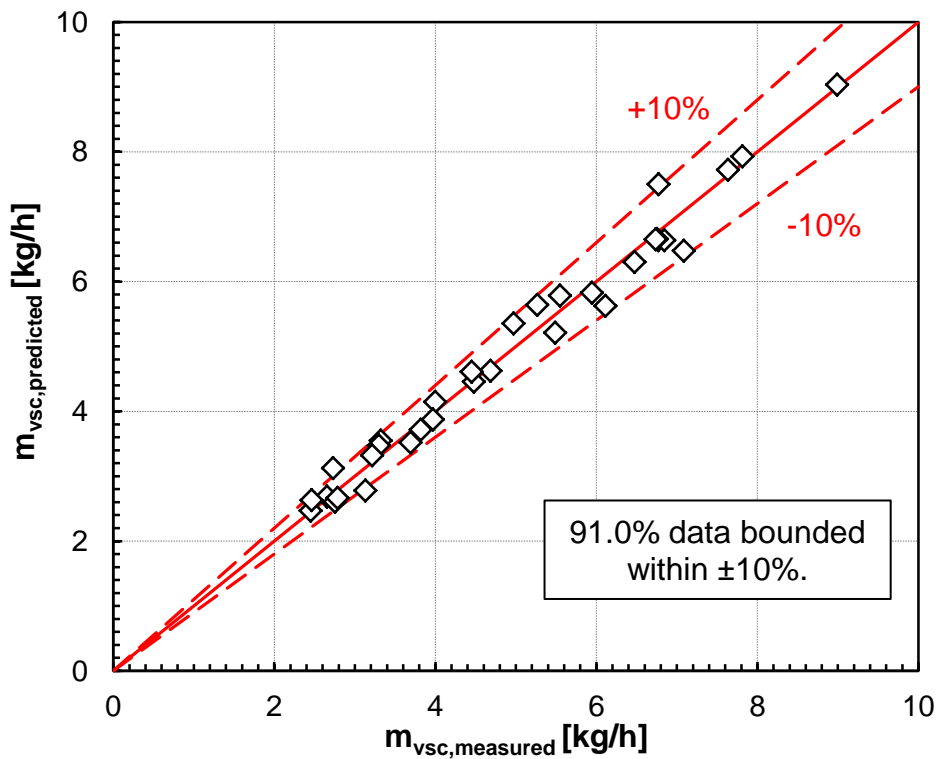
Figure 6.35 Comparison of predicted and experimental results of $\dot{m}_{vsc}$

6.2.4.4 Electrical input power

The electric input power of the mini-compressor can be calculated by Equation 6.22, which considers the values/adjusted correlations of volumetric and isentropic efficiencies previously determined. Figure 6.36 shows a comparison between the experimental results obtained during the map of performance tests (vapor compression and hybrid cycles) versus the values calculated by the correlations. It can be seen that 96.0% of data were bounded within ±10%.

$$W_{vsc} = \frac{NV_{sw,max}}{v_{suc}} \frac{\eta_v}{\eta_{ise}} \left(h_{dis,s} - h_{suc} \right) \qquad 6.22$$

where

h_{suc} is the enthalpy at the suction [kJ/kg];

$h_{dis,s}$ is the enthalpy at the discharge considering an isentropic compression [kJ/kg].
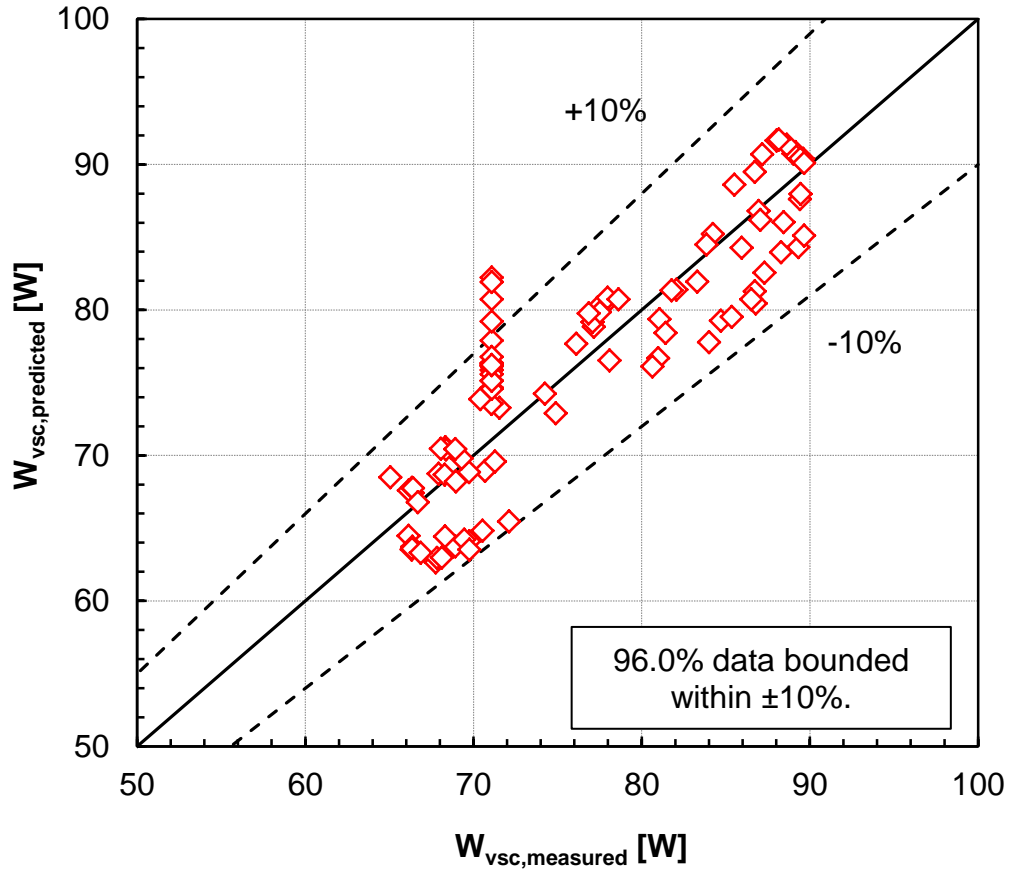
Figure 6.36 Comparison of predicted and measured W$_{vsc}$

6.2.5 Gear pump

The same methodology used for the mini-compressor analysis was also employed for the gear pump. Thus, the final results, i.e. Equations 6.23 to 6.28 respectively show the correlations for overall conductance, heat loss, isentropic efficiency, volumetric efficiency, theoretical mass flow rate and input power. The swept volume (V$_{sw}$) of the gear pump was 0.091667 cm^3 (manufacturer's data).

$$UA_{LPC} = 1.2144 - 0.01379 \times T_{dis} + 0.00008481 \times N \qquad 6.23$$

$$HL_{LPC} = UA_{LPC} \times (T_{dis} - T_{amb}) \qquad 6.24$$

$$\eta_{ise} = \frac{\dot{m}(h_{dis,s} - h_{suc})}{W_e} \qquad \text{6.25}$$

$$\eta_v = 1 - C_1 e^{-C_2 N} \Delta P / \mu_{suc} \qquad \text{6.26}$$

$$\dot{m}_{the} = 60 \times 10^{-6} N V_{sw} \rho_{suc} \qquad \text{6.27}$$

$$W_{LPC} = \frac{10^5 \dot{m}_{the} \eta_v N V_{dis} \Delta P}{\eta_{ise} \rho_{suc}} \qquad \text{6.28}$$

where:

UA_{LPC} is the thermal conductance of liquid pump [W/°C];

T_{dis} is the temperature at discharge [°C];

HL_{LPC} is the heat loss of the liquid pump [W];

ΔP is the increase of pressure (lift) given by the gear pump or the system pressure drop [bar];

$\dot{m}$ is the mass flow rate [kg/h];

$\dot{m}_{the}$ is the theoretical flow rate [kg/h].

It is highlighted that for the volumetric efficiency η_v, a simplified Poiseuille's Law, as defined by Herzog *et al.* (2002), was used. The coefficients C_1 and C_2 were adjusted with experimental data, and are 8.0045×10^{-4} and 7.6128×10^{-4}.

Figure 6.37 and Figure 6.38 show respectively the comparison between the predicted and experimental results of overall conductance (UA$_{LPC}$) and electrical input power (W$_{LPC}$). It can be seen that all data for UA$_{LPC}$ and 93.1% of data for W$_{LPC}$ were bounded within ±10%.
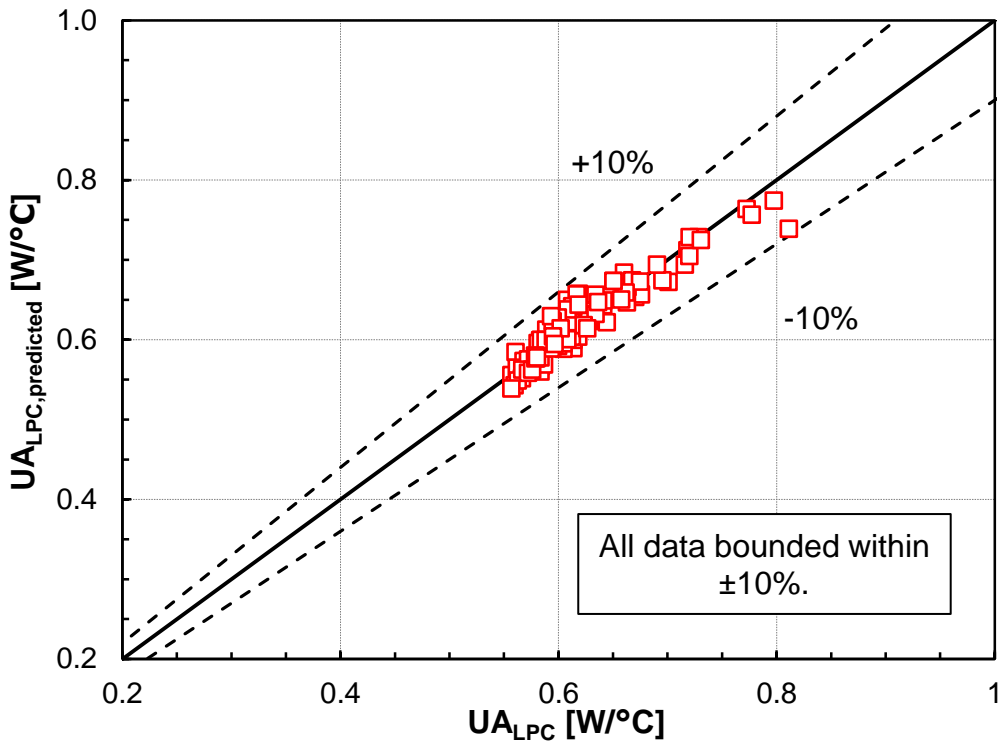
Figure 6.37 Comparison of overall conductance of liquid pump
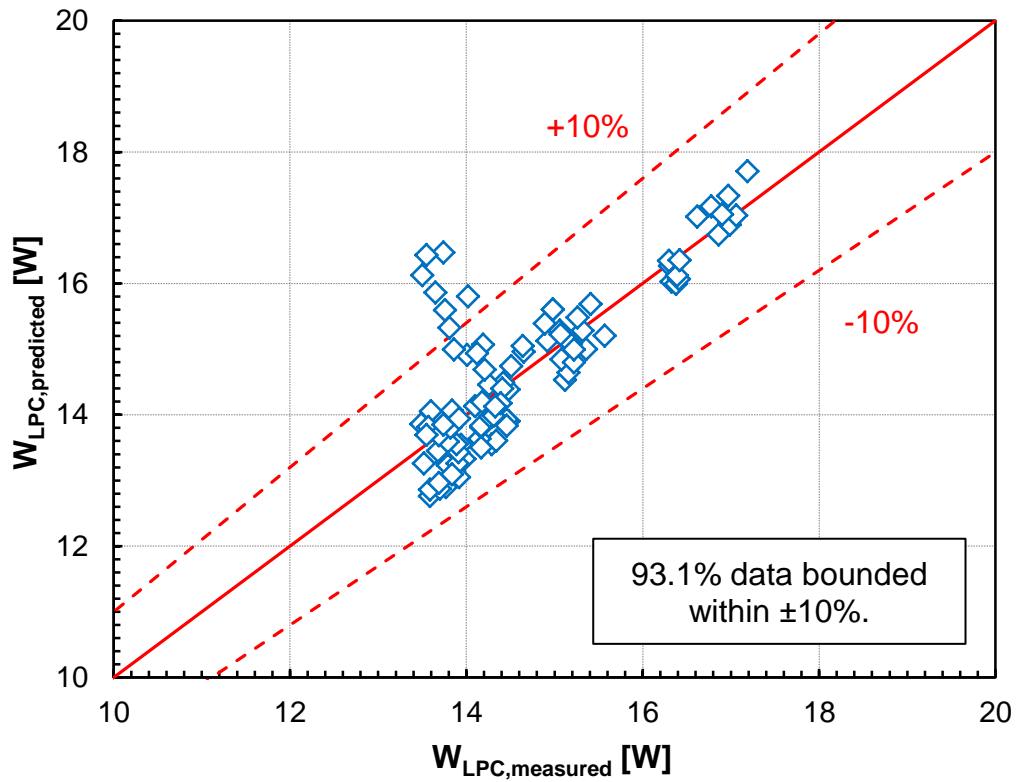
Figure 6.38 Comparison of liquid pump input power

6.2.6 Reservoirs

The overall heat loss conductances of the 3 reservoirs, LS, LA and LPR, were adjusted using the results of the performance mapping tests, and the values obtained are show in Table 6.5.

Table 6.5 Constants of UA for LS, LA and LPR

Component	LS	LA	LPR
UA [W/°C]	0.7815	0.6520	0.0739

The heat loss is determined by

$$HL = UA \times (T_{avg} - T_{amb}) \qquad 6.29$$

where:

HL is the heat loss [W];

UA is the thermal conductance [W/°C];

T_{avg} is the average temperature of the component [°C];

T_{amb} is the ambient temperature [°C].

6.3 Overall energy balance analysis

The models and correlations previously adjusted were used to determine the overall energy balance of the 3 different cooling cycles considering the performance mapping tests. In summary, the overall output of energy was determined through the correlations (piping and components) and compared with the overall input of energy measured by the calibrated power transducers. Figure 6.39 shows the results obtained, where it can be seen that 99.17% of the data were bounded within ± 10%. This permits concluding that the models and correlations captured well the thermal losses and performances of piping and drivers, and can be used for performance and/or design simulations of the cooling systems under different operating conditions.
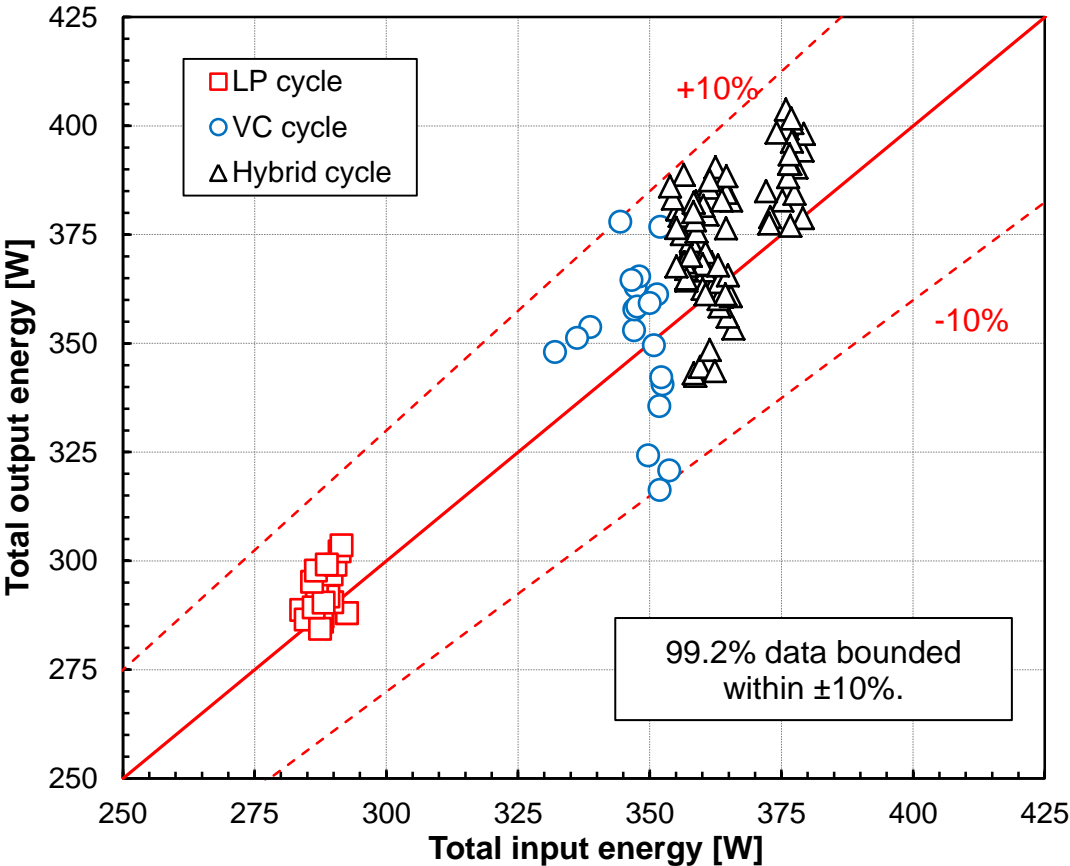
Figure 6.39 Comparison of overall energy balance for performance mapping tests

7 Conclusions and recommendations

The main objective of the present thesis was to design, build and evaluate the thermodynamic performance of three different concepts of two-phase multi-microchannel cooling systems for direct cooling of chips and additional electronic components on a typical blade server board of data centers. The specific focus was to work with two-phase cooling using the dielectric refrigerant HFC134a, a liquid pump and/or a vapor compressor to drive the working fluid, multi-microchannel evaporators for cooling of the pseudo-CPU chips and, for now, a conventional tube-in-tube condenser for heat recovery, which can reduce the demand of cooling energy with respect to air cooling and water cooling by an impressive amount. A multi-purpose test bench was constructed to experimentally evaluate the performance of the cooling systems under various typical blade server operating conditions of transient, steady state, balanced and unbalanced heat loads on the system's two pseudo CPU's, which were directly cooled by means of multi-microchannel evaporators.

The experimental campaign developed was presented in three chapters, i.e. chapter 4 for development and evaluation of controllers, chapter 5 for an energetic and exergetic comparison of the three cycles considering a test in a specific condition of heat load and thermo-hydrodynamic parameters (steady state regime) and chapter 6 for the development of a map of performance of each cycle considering an extense range of several variables (heat load, condensing pressure and temperature, MMEs' outlet vapor quality and approach temperature at the condenser). The correlations were developed for overall thermal conductance and performance of all components and piping of the three cycles based on the experimental data, which can be used for system design and performance

evaluation, and validation of simulation codes. Below is a summary of the main achievements presented in the chapters 4 to 6.

Chapter 4 showed the development of different control strategies considering the simplified PI structure, which was mainly due to the different systems showing low order dynamics. Development of such controllers of the two-phase cooling system was in fact the primary objective of the thesis. These controllers were developed based on three steps, i.e. i) system identification, where linear first order models were adjusted, ii) controller design, and iii) evaluation, where the controllers were evaluated by conventional tracking tests, disturbance rejection and flow distribution tests. The last two evaluations were done considering all controllers developed for each cycle working simultaneously in simple control structures such as SISO and MISO. The controllers were characterized by their simplicity, and high efficiency and effectiveness. The coupling effect between the different controllable variables was not strong; in other words, the controllers have low interaction effects, implying that it was not necessary to apply a more complex centralized MIMO controller.

Chapter 5 considered an energetic and exergetic comparison between the three cycles highlighting the main thermal losses. A steady state regime test was considered for a uniform heat load on both parallel pseudo-chips. The main culprits of thermal losses (inefficiencies) were the drivers followed by the piping and the condenser. It was highlighted that the drivers are operating out of their normal design range, justifying their low efficiency. There is a huge potential to improve the performance of all the cycles in terms of cooling and heat recovery, since better designs of drivers and condenser, and thermal insulation of piping are done. Finally, a simplified thermodynamic analysis extrapolating the experimental data obtained was developed considering a potential increase in the overall performance of the drivers. The result obtained in terms of overall exergetic efficiency (output of exergy at the condenser divided by the total input of exergy) showed that the VC and hybrid cycles are competitive with the LP cycle only after the compressor shows an overall performance respectively of 25% and 50%.

Chapter 6 presented the map of performance of each cycle considering basically two figures of merit, i.e. co-efficiency of performance and energy recovery efficiency.

Comparing the results among the cycles, it was observed that the LP cycle showed higher values for both parameters. A co-efficiency of performance of 18.8 versus 3.9 and 3.3, and a heat recovery efficiency of 70.8% versus 39.7% and 38.5% were obtained for the LP cycle versus respectively VC and hybrid cycles. It was highlighted that the appeal for the VC and hybrid cycles is energy recovery. Thus, a better thermal insulation and drivers' performance were recommended to increase the heat recovery efficiency. Additionally, it was observed higher values of water temperature at the outlet of condenser for both cycles, which represents a higher exergy and, consequently, economic value for the heat recovered. It was concluded that the three cycles are potential options for cooling data centers, being the choice associated with the kind of data center, level of heat load and which secondary application will reuse the heat recovered. It was also recommended for each cycle/application a deep exergo-economic analysis. Finally, an overall energy balance of the three cooling cycles considering as output (heat losses and heat transfer rate at the condenser) the values determined by semi-empirical and empirical correlations adjusted with the experimental data, showed a satisfactory result with 99.17% of the experimental data bounded within ±10%.

For future investigations, some topics can be highlighted as following:

1) Increase the thermal insulation in the sections (piping) that showed high irreversibilities;
2) Use of drivers better designed for the actual application;
3) Evaluate the use of a micro-condenser instead of a tube-in-tube counter flow condenser;
4) Evaluate the overall cooling system performance when non-uniform heat flux is considered on the chips (hot spots); and
5) Develop a thermo-hydrodynamic simulation code for the cooling system and validate it with the experimental results for steady state and transient regimes.

- Finally, it is worth of note that the present thesis is the first detailed study in the literature when looking at overall experimental aspects of two-phase electronic cooling system. A substantial amount of work was done to design, build, calibrate, make preliminary tests/adjustments, develop the controllers and evaluate their

performance, together with an overall analysis of three different cooling cycles, and also a success for a short 3-year time. And, most important, these different concepts of two-phase on-chip cooling systems were proved to be reliable and applicable for data centers of high performance computers. Thus the main contribution of the thesis included successful development and evaluation of controllers for three novel cooling cycles characterized by their simplicity, high efficiency and effectiveness; carried out first-hand performance map experimental campaign and concluded that the proposed three cycles are potential options for cooling data centers to achieve high efficiency.

A. Calibration and uncertainty

This appendix starts with a short introduction about the uncertainty theory, in sequence the calibration methodology and results are presented for each type of sensors including thermocouple, pressure transmitter, differential pressure transmitter and turbine flow meter. Finally, the results of the uncertainty analysis of the calibration are summarized.

A.1   Uncertainty theory

The uncertainty analysis followed ASME PTC standard (ASME 1998) which provides a systematic procedure and helps to determine the most critical uncertainty source. It is also in accordance with ISO "Guide to the Expression of in Measurement".

According to the theory stated in the standard two uncertainty components are taken into the consideration: systematic uncertainty and random uncertainty.

Equation A.1 shows the systematic uncertainty (B).

$$B = \left[\sum_{i=1}^{K} b_i^2 \right]^{1/2} \qquad\qquad \text{A.1}$$

where K is the total number of systematic error sources and b_i is the elemental systematic uncertainty.

For each error source in the measurement, the elemental systematic uncertainty must be estimated from the best available information. There are many sources of systematic error in a measurement, such as calibration process, instrument systematic errors, transmitter

errors, and fixed errors of method. Also environmental effects such as radiation effects in a temperature measurement can cause systematic errors of method.

Random uncertainty is the variation or scatter in repeated measurement which can be calculated by Equation A.2.

$$S_X = \sqrt{\sum_{k=1}^{N} \frac{\left(X_k - \overline{X}\right)^2}{N-1}} \qquad \text{A.2}$$

where X_k is the kth value of the variable and the degrees of freedom is $N - 1$.

Then the estimate of the standard deviation of the mean of N measurements can be calculated by Equation A.3.

$$S_{\overline{X}} = \frac{S_X}{\sqrt{N}} \qquad \text{A.3}$$

where S_X is the standard deviation of a data sample, N is the number of measurements.

Finally, the uncertainty considering 95% of confidence interval is determined by Equation A.4.

$$U_{95} = t\sqrt{\left(\frac{B}{2}\right)^2 + \left(S_{\overline{X}}\right)^2} \qquad \text{A.4}$$

where B is the 95% confidence estimate of systematic uncertainty, and $S_{\overline{X}}$ is the standard deviation of the mean and it can be calculated by Equation A.3, t is the Students' associated with the composite degrees of freedom.

A.2 Thermocouple

In the experimental facility a wide range of temperature was considered, K-type thermocouples with 0.5 mm diameter sheath were used. K-type (chromel - alumel) shows a sensitivity of approximately 41 µV/°C (chromel is positive relative to alumel) and a wide range of measurement (-200 °C to 1350 °C). Furthermore, the maximum expected temperature for the present work, i.e. around 90 °C in the vapor compression cycle, is lower than the Curie point (around 354 °C for K-type thermocouples). Thus, no abrupt change in characteristics during experiment (linear behavior is expected.).

To measure temperature a junction—normally defined as the cold junction—is maintained at a known reference temperature. In the National Instrument module there is a cold junction compensation for each thermocouple to minimize any temperature gradient between terminals along the module.

All thermocouples were calibrated before assembling in the experimental facility, the procedure of calibration is described below.

a. Insert the thermocouples in a thermally controlled thermostatic bath;
b. Vary the temperature of bath within predetermined range;
c. Record the temperatures of the thermocouples by the data acquisition including the standard reference thermometer, which is a certified platinum thermometer and bundled with all thermocouples together inside the bath.

Table A.1 shows the specifications of all instruments used during the calibration.

Table A.1 Instruments f or thermocouple calibration

Instrument	*Description*
Standard Thermometer	DP251 high precision PT100 thermometer (±0.01 °C) with PT-100 1/10DIN (±0.12 °C at 100 °C range).
National Instrument Data Acquisition System	SCXI-1001 12-Slot Chassis; SCXI-1112 8-channel thermocouple input module with Cold-junction compensation per channel; PCI-6221 (37pin) 16-Bit, 250 kS/s, 16 Analog Inputs with 37-Pin D-Sub.
Thermostatic Bath	LAUDA RE207 with Temperature control ± 0,02 °C.

The calibration considered a temperature variation from 10 °C to 50 °C, and reverse (to avoid hysteresis effects), with steps of 4 °C. Two sets of data were obtained for each thermocouple, i.e. one with uncalibrated values from the DAQ $\{\theta_i\}$ and one from the reference temperature $\{T_i\}$. The two sets are then correlated linearly (*viz.* Equation A.5) by using least-squares interpolation.

$$T = \mathrm{a} + \mathrm{b}\theta \qquad \qquad \text{A.5}$$

where the two coefficients were calculated by Equations A.6 and A.7.

$$a = \frac{\sum \theta^2 \sum T - \sum \theta \sum \theta T}{N \sum \theta^2 - (\sum \theta)^2} \qquad \qquad \text{A.6}$$

$$b = \frac{N \sum \theta T - \sum \theta \sum T}{N \sum \theta^2 - (\sum \theta)^2} \qquad \qquad \text{A.7}$$

Table A.2 shows the coefficients adjusted for all K-type thermocouples calibrated. It is also shows the R^2 value, i.e. coefficient of the determination which shows values very close to ideal (1). It means that an excellent prediction is obtained with the linear correlation proposed and high quality of the thermocouples.

Finally, it is worth mentioning that the range of calibration was not extended to 90 °C (maximum value to be acquired) in the experimental facility due to the limitation in the thermostatic bath used. However, based on the results obtained in the calibration (especially R^2) and general experience with this type of thermocouple in the LTCM lab, it was judged that the range calibrated is enough to represent the linearity of the thermocouples, i.e. reliable extrapolation can be considered.

$$R^2 = 1 - \frac{\sum(T - \theta)^2}{\sum(T^2) - \overline{(\sum T)^2}} \qquad \text{A.8}$$

Table A.2 Calibration results of thermocouples

No.	a	b	R^2
600	0.01154165	0.99579395	0.99988631
601	0.05731087	0.99488986	0.99988408
602	0.00496720	0.99602848	0.99988376
603	0.04313340	0.99613374	0.99988712
604	0.14745903	0.99510029	0.99988595
605	0.05072614	0.99662724	0.99990011
606	0.05299189	0.99604142	0.99989076
607	0.14716749	0.99659034	0.99988954
700	-0.05131218	0.99633971	0.99991933
701	0.02581129	0.99585287	0.99987921
702	-0.05224367	0.99608401	0.99988685
703	0.15078424	0.99625904	0.99989092
704	0.17943014	0.99671247	0.99989804
705	0.06108446	0.99648310	0.99989075
706	0.16714370	0.99616496	0.99989582
707	0.20130177	0.99616041	0.99988657
800	0.16704667	0.99555106	0.99988259
801	0.07707668	0.99597851	0.99988273
802	0.09297620	0.99576916	0.99988496

803	0.21808165	0.99630970	0.99990057
804	0.01166200	0.99619536	0.99988328
805	0.09082588	0.99662336	0.99990330
806	0.08303565	0.99704483	0.99988050
807	0.14486145	0.99648257	0.99988494
900	0.03376528	0.99655729	0.99987939
901	0.05981285	0.99603256	0.99988265
902	0.08761732	0.99531303	0.99988007
903	0.04156111	0.99562759	0.99988092
904	0.05824209	0.99603804	0.99988303
905	0.09943720	0.99615676	0.99988145
906	0.07557399	0.99616203	0.99988577
907	0.13096312	0.99583568	0.99988349
1000	0.01877052	0.99544937	0.99988450
1001	0.04183780	0.99604964	0.99988623
1002	0.07592244	0.99469603	0.99988726
1003	0.07790072	0.99554182	0.99988403
1004	0.06046090	0.99550509	0.99988578
1005	0.02918127	0.99555987	0.99988643
1006	0.15279065	0.99591208	0.99988712
1007	0.13699355	0.99640062	0.99988538
1100	-0.11848567	0.99613667	0.99987866
1101	-0.06804885	0.99586945	0.99987959
1102	-0.07135326	0.99586965	0.99988388
1103	-0.07787870	0.99528439	0.99988368
1104	0.00792928	0.99583828	0.99988332
1105	-0.09849810	0.99640320	0.99988569
1106	0.12445288	0.99647706	0.99988016
1107	-0.10307119	0.99643659	0.99987894
1200	-0.11597452	0.99627946	0.99988306
1201	0.10067374	0.99593004	0.99988725
1202	-0.08125342	0.99603192	0.99988573
1203	-0.01106101	0.99590313	0.99990251
1204	0.00009166	0.99619593	0.99988611

1205	0.09800219	0.99564384	0.99988283
1206	0.19283925	0.99604815	0.99988860

A.3   Absolute pressure transmitter

In order to adjust the different levels of pressure in the experimental facility, two ranges of pressure transmitters were used, 0 - 30 bar and 0 - 100 bar, respectively. All pressure transmitters were calibrated through a standard dead weight tester which uses a loaded piston cylinder to make equilibrium with an applied pressure underneath the piston. The procedure of calibration consists of adding weights gradually until the full range, and then return to the start point average hysteresis effects.

The deadweight tester should be set-up to ensure that the axis of the piston is vertical, the weights carefully center on that axis, and maintain the piston rotating during the calibration. The purpose of the rotation is to spread the lubricant over the entire surface between piston and cylinder to avoid metal-to-metal contact, otherwise the lubricant film will not cover the surface properly and readings will be in error. Furthermore, when rotating the weights the operating friction coefficient becomes rolling friction instead of static friction, under that condition the friction forces reduce drastically.

Table A.3 shows the specifications of all instruments used during the calibration.

Table A.3 Instrument list for pressure transmitter calibration

Instrument	*Description*
Standard Dead Weight Tester	Combined High & Low Pressure Dead Weight Tester, Serial Number 1737/67, Barnet Instrument Limited, The maximum relative error will not exceed 0.03% with the correction table.
Standard Barometer	Mercury column type, 10^{-4}bar resolution.
National Instrument Data Acquisition System	SCXI-1001 12-Slot Chassis; SCXI-1102 32-channel thermocouple/voltage input; PCI-6221 (37pin) 16-Bit, 250 kS/s, 16 Analog Inputs with 37-Pin D-Sub.

The range of calibration was from atmospheric pressure which was read through a Standard Mercury Barometer to the full scale range of each transmitter, considering a step of 1 bar. The calibration was done by increasing and decreasing the pressure in the full range with the purpose to average the possible hysteresis effects. Two sets of data for each pressure transmitter were obtained: one of un-calibrated values acquired from the DAQ in volts, $\{\theta_i\}$ and one of reference pressure $\{P_i\}$, which is the sum of atmospheric pressure and pressure imposed by weights,. The two sets were then correlated linearly by using least-squares interpolation (*viz.* Equation A.9).

$$P = a + b\theta \qquad\qquad A.9$$

where the coefficients a and b are calculated by Equations A.6 and A.7. Table A.4 shows the adjusted coefficients for all the transducers with the coefficient of determination R^2. It can be observed that a good linear behaviour for all transmitters. It is worth mentioning that no significant hysteresis effect was obtained.

Table A.4 Calibration Results of pressure transmitters

No.	a	b	R^2
100	0.03666698	1.99876778	1.00000000
101	0.08044154	1.99842998	0.99999995
102	0.10600311	1.99663701	0.99999973
103	0.01108972	1.99909258	0.99999985
104	0.00584828	1.99796696	0.99999996
105	- 0.00630121	1.99857145	0.99999993
106	0.03613855	2.00057481	0.99999997
107	0.00247406	1.99806107	0.99999995
108	0.00378964	1.99834804	0.99999998
109	0.00794837	1.99839933	0.99999996
110	0.02237672	4.99348260	0.99999800
111	0.01213517	4.99319001	0.99999997
112	0.00886998	4.99325655	0.99999997
113	0.00158368	4.99329632	0.99999999

A.4   Differential pressure transmitter

To investigate the pressure drop of some key components in the experimental facility such as liquid pumps, condenser and evaporators, differential pressure transmitters were installed. Totally there are eight differential pressure transmitters which were configured to operate a range of 0 - 0.2 bar (seven transmitters) and 0 - 0.5 bar (one transmitter).

Figure A.1 demonstrates the setting up for calibrating differential pressure transmitters. During the calibration the Hi-Port of differential transmitters was connected with an air pump (syringe type) and one extremity of the U tube, which is filled with certified liquid with known physical properties. The other extremity of the U-tube is open to the atmosphere.
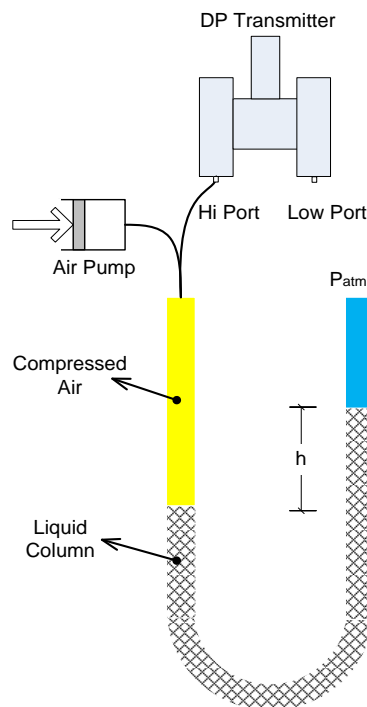
Figure A.1 Schematic of differential pressure transmitter calibration

Table A.5 shows the specifications of all instruments used during the calibration.

Table A.5 Instrument list for differential pressure transmitter calibration

Instrument	Description
Standard U-Tube Column Stand	Made by EPFL-ATME for calibrating differential pressure transmitter, with 1mm reading resolution rulers, U tubes filled with certified liquid.
National Instrument Data Acquisition System	SCXI-1001 12-Slot Chassis; SCXI-1102 32-channel thermocouple/voltage input; PCI-6221 (37pin) 16-Bit, 250 kS/s, 16 Analog Inputs with 37-Pin D-Sub.

For each point of calibration (adjusted by the air pump) the different height in the liquid column was read, which represents the differential pressure between high ports and low ports. The value of differential pressure is determined by Equation A.10.

$$DP = \rho g h \qquad\qquad\text{A.10}$$

where

ρ is the density of the fluid [kg/m^3] ;

g is the local gravitational acceleration [m^2/s];

h is the difference of height in the U-tube [m] .

For each transmitter a set of differential pressure and current value was obtained. The value was corrected by a 3rd order polynomial by using least-squares interpolation.

Table A.6 shows the correlations and R^2 obtained.

Table A.6 Calibration results of differential pressure transmitters

No.	Correlation	R^2
303	DP=1,010.41832137x3 + 795.99452811x2 - 5.79263799x + 0.01037561	0.99997813
304	DP=13.78810597x - 0.05602828	0.99991887
305	DP=13.19046488x - 0.05201460	0.99995190
306	DP=403.45094419x3 + 746.99752250x2 - 5.15772845x + 0.00864148	0.99995714
307	DP=5,965.28694507x3 + 560.13370230x2 - 2.64228089x + 0.00130044	0.99994065
308	DP=-4,194.52322890x3 + 939.06674934x2 - 7.37281102x + 0.01468178	0.99996089
309	DP=-3,324.77026723x3 + 2,069.79893594x2 - 15.39620162x + 0.02864815	0.99992421

A.5   Turbine flow meter

Two turbine flow meters were used to measure the volumetric flow rate of the water loops of condenser and subcooler. Table A.7 summarizes the specification of each turbine meter. The working mechanism of turbine meter is simple, i.e. when liquid or gas flows through the sensor and pushes the turbine to spin, it creates magnetic signal. Meanwhile the pickup coil which is installed outside the sensor picks the magnetic signal and sends it to the multifunction flow indicator which amplifies the signal and transfers to different outputs such as current, voltage and digital output.

Turbine meters provide a frequency response as a function of volumetric flow. Because this response is typically nonlinear, the manufacturers of this type of flow meter normally suggest the use of a linearization via a K factor (*viz.* Equation A.11).

$$\dot{V} = \frac{f}{K} \qquad \text{A.11}$$

where

$\dot{V}$ is the volumetric flow [l/min];

f is the frequency [Hz];

K is the linearization factor[--] .

The K factor is normally adjusted as a function of frequency and kinematic viscosity of fluid (*viz.* Equation A.12). The ratio of frequency and viscosity can be explained by its proportional relation with the Reynolds number of flow through the meter, where the frequency would be equivalent to the velocity of the flow.

$$K = g\left(\frac{f}{\nu}\right) \qquad \text{A.12}$$

where

ν is the kinematic viscosity of the fluid [m^2/s].

Thus, to obtain the volumetric flow through the turbine meter, it is necessary to use a K factor curve as a function of the ratio between the frequency and viscosity, which must be obtained experimentally.

In the present work the current output from the sensor was measured which has a linear relation with the frequency of the rotor. Table A.7 lists the specification of the two turbine flow meters.

Table A.7 Specification of turbine flow meter

Subcooler Water Loop	Condenser Water Loop
Manufacturer: Sponsler, Inc.	Manufacturer: Sponsler, Inc.
1) Sensor	1) Sensor
Model: MF20-CB-PH-A-4-MCI-N	Model: MF40-CB-PH-A-4-MCI-N
Operating range : 0.007 to 0.070 GPM	Operating range: 0.010 to 0.170 GPM
2) Multifunction Flow Indicator	2) Multifunction Flow Indicator
Model: IT400-DC-TRL-X-RF	Model: IT400-DC-TRL-X-RF
3) Pickup Coil	3) Pickup Coil
SPECTEC Digital Carrier Speed Sensor 0097	SPECTEC Digital Carrier Speed Sensor 0097

Equations A.13 and A.14 show the correlation between current ouput and frequency for MF20 and MF40, respectively.

$$f = (6.67040313 * i - 17.37161736) * 4.6 \tag{A.13}$$

$$f = (6.50491249 * i - 16.28349331) * 30 \tag{A.14}$$

where

f is the frequency [Hz] ;

i is the current [mA].

The manufacturer provides a calibration curve of the K-factor only in terms of frequency, obtained with water at the temperature of 20 °C. However, this curve is not appropriate, since the water that circulates in the condenser and subcooler can reach temperatures around 60 °C. Therefore, it was necessary to carry out a more specific calibration in order to obtain the curve of K-factor for an appropriate range of temperature. The calibration procedure is described below and was carried out separately for each of the two transmitters.

First, the transmitter is assembled in series with a standard Coriolis meter, and then connected in a closed loop with a variable speed pump for controlling the flow rate. A

thermostatic bath for varying the temperature is also in the loop. A thermocouple at the inlet of the turbine meter was used to measure the temperature, which permits to determine the density and viscosity by EFPROP. The mass flow rate was measured by a Coriolis meter. Table A.8 shows the specification of all instruments used for the calibration.

Table A.8 Instruments for turbine meter calibration

Instrument	Description
Standard Coriolis Meter	EMERSON Micro Motion Elite CMF010M323, 1700R11 MVD with calibrated certificate (0.051% F.S. accuracy)
NI DAQ	SCXI-1001 12-Slot Chassis; SCXI-1102 32-channel thermocouple/voltage input; PCI-6221 (37pin) 16-Bit, 250 kS/s, 16 Analog Inputs with 37-Pin D-Sub.
Liquid Pump	IDEX Ismatec, gear pump drive MCP-Z Process, gear pump head Z-1830
Thermostat	LAUDA WK500 with Temperature control ± 0.5 °C

The outputs of calibration are basically the following variables: mass flow, viscosity and density at the inlet of the turbine meter and frequency. The experimental K-factor, K_{exp}, determined by Equation A.15.

$$K_{exp} = \frac{f \cdot 60}{\dot{V}_{standard}} \qquad \text{A.15}$$

where

f is the frequency [Hz] calculated by the Equations A.13 and A.14, respectively.

$\dot{V}_{standard}$ is the standard volumetric flow rate [l/h]calculated by Equation A.16.

$$\dot{V}_{standard} = \frac{\dot{m}_{corolis}}{\rho_{tur}} \qquad \text{A.16}$$

where

168

$\dot{m}_{corolis}$ is the mass flow rate measured by Coriolis meter, kg/h;

ρ_{tur} is the density calculated by REFPROP using the temperature at the inlet of turbine, kg/m^3.

$$K_{exp} = a + b \cdot \left(\frac{f}{\nu}\right) + c \cdot \left(\frac{f}{\nu}\right)^2 + d \cdot \left(\frac{f}{\nu}\right)^3 + e \cdot \left(\frac{f}{\nu}\right)^4 + f \cdot \left(\frac{f}{\nu}\right)^5 + g \cdot \left(\frac{f}{\nu}\right)^6 \qquad \text{A.17}$$

$$K_{exp} = a + b \cdot \ln\left(\frac{f}{\nu}\right) \qquad \text{A.18}$$

Figure A.2 and Figure A.3 show the calibration results in terms of K factor against the ratio of frequency and kinetic viscosity. A sixth degree polynomial (Equation A.17) and a logarithmic (Equation A.18) functions were adjusted for turbines of subcooler and condenser, respectively. Those coefficients are shown in able A.9 and Table A.10.
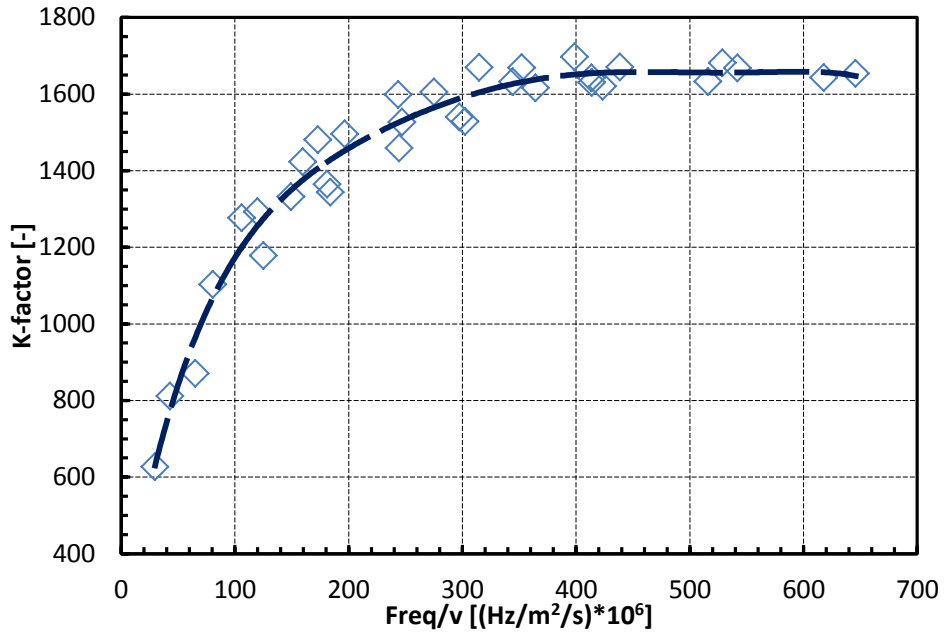
Figure A.2 K-factor vs. Ratio of frequency and kinetic viscosity - condenser
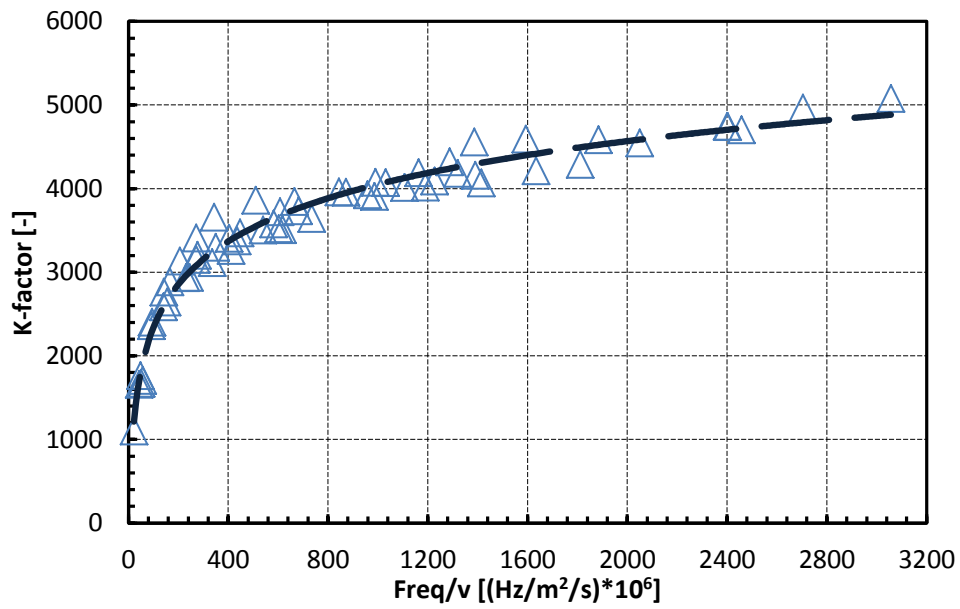
Figure A.3 K-factor vs. Ratio of frequency and kinetic viscosity – subcooler

able A.9 Coefficients of Equation A.18

a	b	c	d
2.02307280E+02	1.72835598E+01	- 1.08520261E-01	4.03554613E-04
e	f	g	R^2
- 8.47853069E-07	9.18504550E-10	-3.97712422E-13	0.966521871

Table A.10 Coefficients of Equation A.19

a	b	R^2
-1.09640321E+03	7.45200993E+02	0.972830983

A.6   Diode temperature sensor

Each pseudo-chip, with their 35 heaters and 35 diode temperature sensors, had 11 diodes calibrated (*viz.*

Figure A.4 in yellow fill) using two K-type thermocouples installed inside the inlet and outlet headers of the MMEs. The pseudo-chips were assembled at the bottom of MMEs and the section is adiabatic. Due to limited number of channels to acquire the temperature by the DAQ and also the condition of uniform heat flux for this work, only 11 sensors per pseudo-chip were calibrated.

Inlet - Column Y
Lateral orientation

11	12	13	**14**	15	16	17
21	22	23	**24**	25	26	27
31	**32**	**33**	**34**	**35**	**36**	**37**
41	42	43	**44**	45	46	47
51	52	53	**54**	55	56	57

Row X

Flow-wise orientation

Outlet
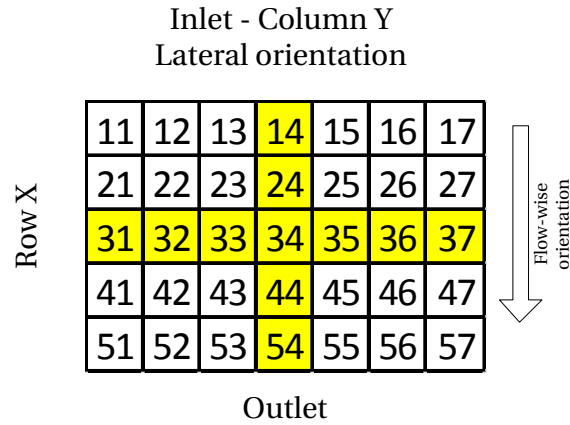
Figure A.4 Calibrated diodes sensors (in yellow)

Two sets of data were obtained for each diode sensor, uncalibrated output values in volts ($\{\theta_i\}$) as acquired by DAQ, and reference temperature by averaging the two standard thermocouples ($\{T_i\}$). The two sets are then correlated linearly by using least-squares interpolation.

$$T = a + b\theta \qquad \text{A.19}$$

Table A.11 shows the coefficients adjusted for each sensor and R^2.

Table A.11 Calibration results of diode sensor

No.	a	b	R^2
200	389.71011304	-105.29873568	0.99998261
201	388.02189074	-104.95153642	0.99999294
202	387.32130247	-104.76839840	0.99999335
203	384.09592638	-103.83983821	0.99998953
204	385.23113214	-104.23380303	0.99999421
205	386.83304343	-104.65097085	0.99999330
206	388.16822229	-105.04038310	0.99999063
207	388.65196259	-105.06809044	0.99999210
208	386.76809546	-104.64605583	0.99999276
209	387.14896752	-104.75182723	0.99999164
210	387.99636639	-104.92376229	0.99998761
211	403.81370558	-109.21492375	0.99998976
212	403.40602413	-109.21635240	0.99999342
213	403.49250389	-109.31137574	0.99999408
214	401.37904759	-108.48595634	0.99999443
215	402.68718087	-108.93960763	0.99999651
216	403.60305320	-109.35952792	0.99999515
217	404.13662482	-109.48759733	0.99999364
218	404.38092027	-109.54542793	0.99999136
219	403.74712775	-109.30853775	0.99999511
220	404.04085175	-109.33512328	0.99999349
221	403.69890847	-108.98907946	0.99998988

A.7   Power transducer

Two types of power transducers were installed, which are GMC P6EC for DC components such as compressor, SMV, EEV and GMC LQT501 for AC components such as liquid pump, post heater. To calibrate these power transducers, a regularly calibrated multimeter Agilent 33440A was used as the standard, which was connected in parallel for voltage measurement and in series for current measurement.

Table A.12 Instruments for power transducer calibration

Instrument	*Description*
Standard Multimeter	Agilent 34401A Digital Multimeter, 6½ Digit
	Basic accuracy: 0.0035% DC, 0.06% AC
National Instrument Data Acquisition System	SCXI-1001 12-Slot Chassis;
	PCI-6221 (37pin) 16-Bit, 250 kS/s, 16 Analog Inputs with
	37-Pin D-Sub.
Variable transformer	0...260 VAC 6.5 A 230 VAC

Two sets of data were obtained for each parameter of each transducer, uncalibrated output values in volts ($\{\theta_i\}$)as acquired by DAQ, and reference value by read from multimeter ($\{X_i\}$). The two sets are then correlated linearly by using least-squares interpolation.

$$X = a + b\theta$$

A.20

Table A.13 and Table A.14 show the coefficients adjusted and R^2.

Table A.13 P6EC transducers for DC components calibration results

Parameter	a	b	R^2
U_EEV1	0.99780154	- 0.02164608	0.99999611
U_SMV1	1.00213041	0.01464705	0.99999688
U_SMV2	1.00499531	- 0.12906232	0.99999270
U_VSC	0.99487637	0.00776822	0.99999780
I_EEV1	0.98474919	- 0.00041749	1.00000000
I_SMV1	0.99805339	- 0.00043758	0.99998732
I_SMV2	0.99234018	0.00128979	0.99998170
I_VSC	0.99545781	- 0.00200941	0.99999322
W_EEV1	0.99049908	0.00000003	1.00000000
W_SMV1	1.00116033	0.04752563	0.99999989
W_SMV2	0.99086999	0.04291883	0.99999901
W_VSC	0.93881657	5.06448236	0.99718186
E_EEV1	0.99221022	0.00000000	1.00000000
E_SMV1	1.00116026	0.01870280	0.99999989
E_SMV2	0.99086999	0.04291883	0.99999901
E_VSC	0.83342454	-0.00585596	0.99999967

Table A.14 LQT501 transducers for AC components calibration results

	a	b	R^2
U_LPC	0.99375707	0.00000000	0.99972314
U_LPW	0.99058007	0.00000000	0.99971926
U_Post Heater	0.99314946	0.00000000	0.99972255
I_LPC	1.14704815	0.00141691	0.99997435
I_LPW	1.14275718	0.00343971	0.99996871
I_Post Heater	1.14511778	0.00389304	0.99997958
W_LPC	0.85430785	2.30477402	0.99998508
W_LPW	0.85740554	2.28845921	0.99997421
W_Post Heater	0.85223395	2.20237252	0.99999008
E_LPC	1.00502620	0.49004869	0.99988837
E_LPW	0.99804513	0.59677711	0.99982655
E_Post Heater	0.99437974	0.51832618	0.99982272

A.8 Calibration uncertainty results

Tables A.13 to A.19 show the uncertainty results obtained for the uncertainty analysis developed for all the transmitters. The theory of propagation of errors was used.

Table A.15 Thermocouple uncertainty summary

No.	Standard Deviation (°C)	Random Uncertainty (°C)	SEE (°C)	Systematic Uncertainty, B (°C)	$U_{95, total}$ (°C)
600	0.0144	0.0282	0.1912	0.2258	0.23
601	0.0145	0.0285	0.1842	0.2199	0.22
602	0.0147	0.0288	0.1910	0.2255	0.23
603	0.0142	0.0278	0.1638	0.2030	0.20
604	0.0140	0.0275	0.1481	0.1906	0.19
605	0.0124	0.0243	0.1444	0.1878	0.19
606	0.0134	0.0263	0.1588	0.1990	0.20
607	0.0135	0.0265	0.1459	0.1889	0.19
700	0.0105	0.0205	0.2124	0.2440	0.24
701	0.0153	0.0300	0.1834	0.2192	0.22
702	0.0143	0.0280	0.2322	0.2614	0.26
703	0.0138	0.0271	0.1445	0.1878	0.19
704	0.0129	0.0254	0.1568	0.1974	0.20
705	0.0139	0.0272	0.1478	0.1904	0.19
706	0.0132	0.0258	0.1465	0.1894	0.19
707	0.0141	0.0276	0.1670	0.2056	0.21
800	0.0150	0.0293	0.1507	0.1927	0.19
801	0.0150	0.0293	0.1539	0.1951	0.20
802	0.0146	0.0286	0.1507	0.1926	0.19
803	0.0127	0.0249	0.1729	0.2105	0.21
804	0.0146	0.0287	0.1827	0.2186	0.22
805	0.0123	0.0242	0.1317	0.1782	0.18
806	0.0150	0.0294	0.1429	0.1866	0.19

807	0.0142	0.0279	0.1471	0.1898	0.19
900	0.0154	0.0302	0.1641	0.2033	0.21
901	0.0148	0.0290	0.1598	0.1999	0.20
902	0.0152	0.0298	0.1619	0.2015	0.20
903	0.0150	0.0295	0.1782	0.2148	0.22
904	0.0146	0.0286	0.1602	0.2002	0.20
905	0.0149	0.0292	0.1469	0.1897	0.19
906	0.0146	0.0285	0.1501	0.1922	0.19
907	0.0145	0.0285	0.1457	0.1888	0.19
1000	0.0145	0.0284	0.1956	0.2295	0.23
1001	0.0144	0.0282	0.1666	0.2053	0.21
1002	0.0142	0.0278	0.1764	0.2133	0.22
1003	0.0148	0.0291	0.1600	0.2000	0.20
1004	0.0145	0.0285	0.1681	0.2065	0.21
1005	0.0143	0.0281	0.1851	0.2206	0.22
1006	0.0143	0.0280	0.1460	0.1890	0.19
1007	0.0144	0.0282	0.1447	0.1880	0.19
1100	0.0155	0.0304	0.2912	0.3150	0.32
1101	0.0153	0.0300	0.2542	0.2811	0.28
1102	0.0145	0.0285	0.2557	0.2825	0.28
1103	0.0146	0.0286	0.2792	0.3039	0.31
1104	0.0147	0.0287	0.1938	0.2280	0.23
1105	0.0144	0.0281	0.2631	0.2892	0.29
1106	0.0151	0.0296	0.1457	0.1888	0.19
1107	0.0152	0.0298	0.2682	0.2938	0.30
1200	0.0144	0.0283	0.2833	0.3077	0.31
1201	0.0138	0.0270	0.1457	0.1888	0.19
1202	0.0141	0.0276	0.2590	0.2854	0.29
1203	0.0120	0.0234	0.1984	0.2318	0.23
1204	0.0141	0.0277	0.1892	0.2241	0.23
1205	0.0145	0.0284	0.1521	0.1937	0.20
1206	0.0137	0.0268	0.1602	0.2002	0.20

Table A.16 Pressure transmitter uncertainty summary

No.	Standard Deviation (bar)	Random Uncertainty (bar)	SEE (bar)	Systematic uncertainty, B (bar)	Total Uncertainty , U_{95} (bar)	U_{95} (%)
109	1.392E-04	2.729E-04	1.035E-03	5.268E-03	0.005	0.026
110	1.393E-04	2.731E-04	1.495E-02	2.013E-02	0.020	0.040
100	3.684E-04	1.443E-03	3.989E-04	5.305E-03	0.005	0.027
101	3.844E-04	1.506E-03	1.276E-03	5.441E-03	0.006	0.028
108	3.240E-04	1.269E-03	7.372E-04	5.341E-03	0.005	0.027
101	3.658E-04	1.433E-03	2.432E-03	6.044E-03	0.006	0.031
103	3.311E-04	1.297E-03	2.352E-03	6.013E-03	0.006	0.031
105	3.222E-04	1.262E-03	1.638E-03	5.771E-03	0.006	0.030
102	1.361E-04	5.328E-04	3.322E-03	5.020E-03	0.005	0.025
104	1.848E-04	7.237E-04	1.313E-03	3.986E-03	0.004	0.020
106	3.182E-04	1.248E-03	1.172E-03	3.942E-03	0.004	0.021
107	1.417E-04	5.548E-04	1.412E-03	4.020E-03	0.004	0.020
111	2.860E-04	2.799E-03	1.556E-03	1.196E-02	0.012	0.025
112	2.599E-04	2.544E-03	1.544E-03	1.196E-02	0.012	0.024

Table A.17 Differential pressure transmitter uncertainty summary

No.	Standard Deviation (bar)	Random Uncertainty (bar)	SEE (bar)	Systematic Uncertainty , B (bar)	Total Uncertainty , U_{95} (bar)	U_{95} (%)
303	1.7775E-04	3.4838E-04	2.8214E-04	3.5338E-04	0.00050	0.25
304	2.3059E-04	4.5196E-04	4.7966E-04	5.1865E-04	0.00069	0.34
305	2.0325E-04	3.9836E-04	3.6932E-04	4.1872E-04	0.00058	0.29
306	1.9382E-04	3.7989E-04	3.7308E-04	4.2999E-04	0.00057	0.29
307	3.8947E-03	7.6336E-03	4.3898E-04	4.8827E-04	0.00765	3.82
308	3.8496E-04	7.5452E-04	3.7052E-04	4.2727E-04	0.00087	0.43
309	1.2149E-03	2.3813E-03	1.1470E-03	1.2309E-03	0.00268	0.54

Table A.18 Turbine meter uncertainty analysis - subcooler

List of Uncertainty Calculation		
Thermocouple		
Random Uncertainty of Mean (°C)	Systematic Uncertainty (°C)	Total Uncertainty (°C)
0.039	1	1.003
Turbine Output Current		
Random Uncertainty (mA)	Systematic Uncertainty (mA)	Total Uncertainty (mA)
0.007	0.020	0.025
Coriolis Meter		
Random Uncertainty (A)	Systematic Uncertainty (A)	Total Uncertainty (A)
1.39E-06	3.68E-06	2.31E-06
REFPROP Uncertainty	Density Uncertainty	Viscosity Uncertainty
0.10%	0.20%	0.20%
Number of Data	Students'	Random Uncertainty (kg/h)
33	2	0.054

Table A.19 Turbine meter uncertainty results - subcooler

Temp.	$I_{Coriolis}$ (A)	$I_{turbine}$ (mA)	$\dot{m}$ (kg/h)	ρ (kg/m³)	Kin. Vis. (cm²/s)	$\dot{V}$ (l/h)	Factor K	U_{95} (kg/h)
10°C	0.0072	17.3308	16.7646	999.47	0.0124	16.77	1616.351	0.12
	0.0067	15.2829	13.9760	999.46	0.012356	13.98	1669.228	0.11
	0.0061	12.3694	11.2411	999.44	0.012302	11.25	1598.402	0.11
	0.0056	9.4781	8.5437	999.4	0.01219	8.55	1480.300	0.11
	0.0050	6.7031	5.9059	999.28	0.011887	5.91	1276.775	0.11
	0.0045	3.6974	3.2080	999	0.011283	3.21	626.708	0.11
15°C	0.0072	17.4530	16.6312	998.86	0.01102	16.65	1641.842	0.12
	0.0069	16.7903	15.3718	998.8	0.010916	15.39	1696.969	0.12
	0.0066	15.2083	13.8897	998.83	0.010977	13.91	1668.665	0.11
	0.0061	12.3468	11.1614	998.77	0.01087	11.18	1605.016	0.11
	0.0056	9.5129	8.4954	998.72	0.010786	8.51	1495.253	0.11
	0.0053	8.1761	7.1995	998.67	0.01071	7.21	1422.904	0.11
	0.0050	6.7688	5.9232	998.64	0.010677	5.93	1292.656	0.11
	0.0048	5.3720	4.6144	998.55	0.010534	4.62	1102.671	0.11
	0.0045	4.0472	3.2706	998.37	0.010294	3.28	810.911	0.11
25°C	0.0072	17.3867	16.6187	996.83	0.0087923	16.67	1632.423	0.12
	0.0066	15.2345	13.8749	996.89	0.0088366	13.92	1670.663	0.11
	0.0061	12.5296	11.1617	996.9	0.0088475	11.20	1632.036	0.11
	0.0056	9.6933	8.5209	996.85	0.0088093	8.55	1526.845	0.11
	0.0050	6.8829	5.8944	996.83	0.0087963	5.91	1332.135	0.11
42°C	0.0071	17.3504	16.3101	993.41	0.0070069	16.42	1653.527	0.12
	0.0066	15.0067	13.6022	993.45	0.0070244	13.69	1667.654	0.11
	0.0061	12.3236	10.9726	993.51	0.0070441	11.04	1620.173	0.11
	0.0055	9.5713	8.3395	993.58	0.0070728	8.39	1528.160	0.11
	0.0053	8.2569	7.0880	993.63	0.0070932	7.13	1458.857	0.11
	0.0050	6.8722	5.8132	993.71	0.007122	5.85	1343.140	0.11
	0.0045	4.1489	3.2457	994.11	0.0072862	3.26	870.986	0.11
	0.0048	5.5162	4.5225	993.76	0.0071422	4.55	1177.985	0.11
35°C	0.0072	17.4496	16.5409	994.31	0.0073719	16.64	1642.913	0.12
	0.0066	15.2572	13.7744	994.25	0.0073451	13.85	1681.409	0.11
	0.0061	12.4881	11.0983	994.21	0.0073294	11.16	1630.073	0.11

| 0.0056 | 9.7209 | 8.4591 | 994.24 | 0.0073423 | 8.51 | 1539.947 | 0.11 |
| 0.0050 | 6.9668 | 5.8546 | 994.36 | 0.0073936 | 5.89 | 1364.090 | 0.11 |

Table A.20 Turbine meter uncertainty unalysis - condenser

List of Uncertainty Calculation		
Temperature		
Random Uncertainty of Mean (°C)	Systematic Uncertainty (°C)	Total Uncertainty (°C)
0.028	1	1.002
Turbine Output		
Random Uncertainty (mA)	Systematic Uncertainty (mA)	Total Uncertainty (mA)
0.006	0.020	0.023
Coriolis Meter		
Random Uncertainty (A)	Systematic Uncertainty (A)	Total Uncertainty (A)
3.34E-06	4.49E-06	5.60E-06
REFPROP Uncertainty	Density Uncertainty	Viscosity Uncertainty
0.10%	0.20%	0.20%
Number of Data	Students'	Random Uncertainty (kg/h)
58	2	0.058

Table A.21 Turbine meter uncertainty results - condenser

Temp.	$I_{Coriolis}$ (A)	$I_{turbine}$ (mA)	$\dot{m}$ (kg/h)	ρ (kg/m³)	Kin. Vis. (cm²/s)	$\dot{V}$ (l/h)	K-factor	U_{95} (kg/h)
10°C	0.0064	6.6748	12.6977	999.41	0.012234	12.7052	3844.429	0.13
	0.0070	7.8160	15.7022	999.43	0.01228	15.7112	3959.348	0.13
	0.0084	11.3215	22.6498	999.47	0.01241	22.6618	4556.181	0.14
	0.0058	5.6678	9.5957	999.36	0.012083	9.6019	3858.942	0.13
	0.0052	4.6100	6.7401	999.32	0.011982	6.7447	3657.327	0.13
	0.0050	4.1507	5.6592	999.26	0.011824	5.6633	3405.953	0.13
	0.0048	3.7344	4.5982	999.18	0.011658	4.6020	3132.396	0.13
	0.0046	3.3324	3.5152	999.04	0.011357	3.5186	2759.008	0.14
	0.0044	3.0328	2.5801	998.83	0.010973	2.5831	2400.404	0.14
	0.0044	3.0243	2.5833	998.83	0.010979	2.5863	2358.994	0.14
	0.0042	2.7319	1.6122	998.3	0.010205	1.6149	1657.95	0.14
15°C	0.0041	2.6110	1.1452	997.59	0.009432	1.1480	1098.961	0.14
	0.0042	2.7467	1.6145	997.92	0.0097654	1.6179	1761.859	0.14
	0.0046	3.3923	3.6032	998.48	0.010441	3.6087	2884.549	0.14
	0.0050	4.0223	5.5506	998.66	0.010703	5.5581	3200.156	0.13
	0.0054	4.7356	7.6666	998.72	0.010797	7.6764	3404.953	0.13
	0.0060	5.9009	10.6777	998.79	0.010913	10.6906	3721.294	0.13
	0.0072	8.3137	16.6907	998.84	0.010992	16.7101	4071.384	0.13
	0.0078	9.7584	19.6516	998.84	0.01099	19.6744	4317.777	0.13
	0.0084	11.3898	22.6315	998.77	0.010879	22.6594	4591.962	0.13
	0.0042	2.7372	1.6338	996.95	0.0088879	1.6388	1671.218	0.14
	0.0048	3.7281	4.5395	996.84	0.0088063	4.5539	3149.366	0.13
	0.0050	4.0811	5.5837	996.83	0.0087973	5.6015	3298.182	0.13
	0.0052	4.4811	6.8426	996.9	0.0088516	6.8639	3373.937	0.13
	0.0056	5.1463	8.6273	996.9	0.0088495	8.6542	3575.916	0.13
	0.0058	5.5882	9.6498	996.87	0.0088274	9.6801	3731.481	0.13
	0.0062	6.4514	11.6485	996.89	0.0088367	11.6849	3956.238	0.13
	0.0064	6.9661	12.7910	996.84	0.0087995	12.8316	4072.395	0.13
	0.0068	7.7771	14.7014	996.9	0.0088472	14.7471	4187.329	0.13
	0.0070	7.8850	15.6477	996.87	0.0088236	15.6968	4014.442	0.13

184

	0.0074	8.7405	17.5008	996.77	0.0087502	17.5575	4159.541	0.13
	0.0082	10.9609	21.5470	996.78	0.0087564	21.6166	4581.186	0.13
	0.0044	3.0703	2.5570	995.27	0.007826	2.5692	2584.087	0.14
	0.0046	3.4023	3.5709	994.86	0.007624	3.5894	2932.857	0.13
	0.0050	4.0720	5.6052	994.45	0.0074349	5.6364	3258.729	0.13
	0.0054	4.7851	7.5470	994.34	0.0073868	7.5900	3520.073	0.13
	0.0060	6.1265	10.7468	994.33	0.0073816	10.8081	3925.221	0.13
	0.0066	7.4358	13.7378	994.13	0.0072938	13.8190	4179.388	0.13
	0.0072	8.5694	16.7651	994	0.0072418	16.8663	4211.19	0.13
	0.0078	10.1689	19.6297	994.13	0.0072953	19.7457	4545.573	0.13
	0.0082	11.3843	21.7910	993.95	0.0072189	21.9236	4743.161	0.13
	0.0082	11.3755	21.7906	993.92	0.0072058	21.9239	4738.392	0.13
	0.0086	12.5738	23.6308	994.06	0.0072669	23.7720	4960.228	0.13
42°C	0.0054	4.7821	7.5589	993.87	0.0071869	7.6056	3508.372	0.13
	0.0056	5.1990	8.6119	993.78	0.007151	8.6658	3642.357	0.13
	0.0060	6.0903	10.6815	993.64	0.0070956	10.7499	3907.068	0.13
	0.0062	6.5210	11.6506	993.6	0.0070794	11.7256	4011.976	0.13
	0.0064	6.9491	12.6463	993.56	0.0070638	12.7283	4089.794	0.13
	0.0068	7.6068	14.6038	993.5	0.0070401	14.6993	4065.271	0.13
	0.0074	9.0016	17.6227	993.39	0.0070016	17.7400	4289.07	0.13
	0.0082	11.2386	21.6143	993.21	0.0069331	21.7621	4699.918	0.13
	0.0088	13.2902	24.7087	993.08	0.0068853	24.8808	5076.283	0.13
	0.0052	4.4730	6.5428	993.68	0.007113	6.5844	3502.705	0.13
	0.0050	4.1450	5.5062	993.8	0.0071576	5.5405	3469.51	0.13
	0.0048	3.7443	4.6372	993.93	0.0072108	4.6655	3114.528	0.13
	0.0046	3.4179	3.6257	994.15	0.0073017	3.6471	2936.473	0.13
	0.0044	3.0989	2.6265	994.55	0.0074799	2.6409	2640.699	0.14
	0.0042	2.7394	1.6148	995.5	0.0079488	1.6221	1704.18	0.14

Table A.22 Diode uncertainty summary

	Standard Dev. (°C)	Random Uncertainty (°C)	SEE (°C)	Systematic Uncertainty, B(°C)	$U_{95,total}$ (°C)
200	-1.03E-03	2.13E-01	0.0447	0.1565	0.27
201	-1.56E-03	3.22E-01	0.1106	0.1565	0.37
202	-1.20E-03	2.47E-01	0.0276	0.1565	0.29
203	-1.33E-03	2.74E-01	0.0347	0.1565	0.32
204	-1.17E-03	2.42E-01	0.0258	0.1565	0.29
205	-1.08E-03	2.22E-01	0.0277	0.1565	0.27
206	-1.74E-03	3.59E-01	0.0328	0.1565	0.39
207	-1.54E-03	3.18E-01	0.0301	0.1565	0.36
208	-1.09E-03	2.25E-01	0.0288	0.1565	0.28
209	-1.50E-03	3.09E-01	0.0310	0.1565	0.35
210	-1.17E-03	2.42E-01	0.0377	0.1565	0.29
211	-1.03E-03	2.13E-01	0.0447	0.1565	0.27
212	-1.56E-03	3.22E-01	0.1106	0.1565	0.37
213	-1.20E-03	2.47E-01	0.0276	0.1565	0.29
214	-1.33E-03	2.74E-01	0.0347	0.1565	0.32
215	-1.17E-03	2.42E-01	0.0258	0.1565	0.29
216	-1.08E-03	2.22E-01	0.0277	0.1565	0.27
217	-1.74E-03	3.59E-01	0.0328	0.1565	0.39
218	-1.54E-03	3.18E-01	0.0301	0.1565	0.36
219	-1.09E-03	2.25E-01	0.0288	0.1565	0.28
220	-1.50E-03	3.09E-01	0.0310	0.1565	0.35
221	-1.17E-03	2.42E-01	0.0377	0.1565	0.29

Table A.23 Power transducer uncertainty summary

a) DC voltage

Multimeter Uncertainty					
Mean S_x (V)	U_{95} (V)	$U_{95,standard}$ (V)	Number of Data:	11	
1.12E-04	9.92E-04	6.97E-04	Students' number	1.96	
Parameter	Mean Standard Dev	Random Uncertainty	SEE	Systematic Uncertainty, B	$U_{95,total}$ (V)
U_EEV1	1.16E-03	2.26E-03	0.0088	0.0088	0.0091

Multimeter Uncertainty					
Mean S_x (V)	U_{95} (V)	$U_{95,standard}$ (V)	Number of Data:	6	
1.54E-05	1.01E-03	7.06E-04	Students' Number	1.96	
Parameter	Mean Standard Dev	Random Uncertainty	SEE	Systematic Uncertainty, B	$U_{95,total}$ (V)
U_SMV1	1.29E-03	2.52E-03	0.0047	0.0047	0.0054

Multimeter Uncertainty					
Mean Sx (V)	U_{95} (V)	$U_{95,standard}$ (V)	Number of Data:	8	
2.62E-05	9.89E-04	6.93E-04	Students' Number:	1.96	
Parameter	Mean Standard Dev	Random Uncertainty	SEE	Systematic Uncertainty, B	$U_{95,total}$ (V)
U_SMV2	1.04E-03	2.05E-03	0.0067	0.0068	0.0071

Multimeter Uncertainty					
Mean S_x (V)	U_{95} (V)	$U_{95,standard}$ (V)	Number of Data:	6	
3.04E-04	9.86E-04	7.07E-04	Students' Number:	1.96	
Parameter	Mean Standard Dev	Random Uncertainty	SEE	Systematic Uncertainty, B	$U_{95,total}$ (V)
U_VSC	1.41E-03	2.74E-03	0.0170	0.0170	0.0172

b) DC current

Multimeter Uncertainty					
Mean Sx (A)	U_{95} (A)	$U_{95,standard}$ (A)	Number of Data:	10	
1.23E-05	2.34E-05	1.75E-05	Students' Number:	1.96	
Parameter	*Mean Standard Dev*	*Random Uncertainty*	*SEE*	*Systematic Uncertainty, B*	*$U_{95,total}$ (A)*
I_SMV1	6.19E-05	1.21E-04	0.0009	0.0009	0.0009
I_SMV2	5.69E-05	0.00E+00	0.0011	0.0011	0.0011
I_EEV1	5.60E-05	0.00E+00	0.0010	0.0010	0.0010

Multimeter Uncertainty					
Mean Sx (V)	U_{95} (V)	$U_{95,standard}$ (V)	Number of Data:	13	
1.24E-02	1.45E-04	8.66E-03	Students' Number:	1.96	
Parameter	*Mean Standard Dev*	*Random Uncertainty*	*SEE (standard error of estimate)*	*Systematic Uncertainty, B*	*$U_{95,total}$ (V)*
I_VSC	1.24E-02	2.44E-02	0.012	0.0145	0.0284

c) AC voltage

Multimeter Uncertainty					
Mean S_x (V)	U_{95} (V)	$U_{95,standard}$	Number of Data	19	
3.60E-02	1.46E-01	1.04E-01	Students' number	1.96	
Parameter	*Mean Standard Dev.*	*Random Uncertainty*	*SEE*	*Systematic Uncertainty, B*	*$U_{95,total}$ (V)*
U_LPC	3.58E-02	6.97E-02	1.36	1.37	1.37
U_LPW	3.96E-02	7.71E-02	1.37	1.37	1.38
U_PostH	3.59E-02	6.99E-02	1.36	1.36	1.37

d) AC current

Multimeter Uncertainty					
Mean S_x (A)	U_{95} (A)	$U_{95,standard}$ (A)	Number of Data:	16	
1.36E-04	5.15E-04	3.67E-04	Students' number	1.96	
Parameter	*Mean Standard Dev.*	*Random Uncertainty*	*SEE*	*Systematic Uncertainty, B*	*$U_{95,total}$ (A)*
I_LPC	1.16E-03	2.58E-03	0.002	0.002	0.003
I_LPW	1.18E-03	2.63E-03	0.002	0.002	0.003
I_PostH	1.17E-03	2.62E-03	0.001	0.001	0.003

A.9   Propagation of uncertainty

A.9.1 Outlet vapor quality (x_o)

NIST (2010) REFPROP uses user inputs of pressure and temperature to calculate the correct property. The main thermo-physical properties of the fluid in question and the average uncertainties in terms of percentages are available in the *.fld* fluid files in the REFPROP directory.

Equations A.21 and A.22 show the calculation for inlet and outlet entropies of the MMEs control volume, more details were shown in section 3.37.

$$h_i = f(P_i, T_i) \tag{A.21}$$

$$\delta h_i = \left\{ \left(\frac{\partial f}{\partial P_i} \delta P_i \right)^2 + \left(\frac{\partial f}{\partial T_i} \delta T_i \right)^2 \right\}^{1/2} \tag{A.22}$$

$$h_o = \frac{W}{\dot{m}} + h_i \tag{A.23}$$

$$\delta h_o = \left\{ \underbrace{\left(\frac{\partial h_o}{\partial h_i} \delta h_i \right)^2}_{A} + \underbrace{\left(\frac{\partial h_o}{\partial W} \delta W \right)^2}_{B} + \underbrace{\left(\frac{\partial h_o}{\partial \dot{m}} \delta \dot{m} \right)^2}_{C} \right\}^{1/2} \tag{A.24}$$

Term A $\dfrac{\partial h_o}{\partial h_i} = 1$ 　　　　　　　　 Term B $\dfrac{\partial h_o}{\partial W} = \dfrac{1}{\dot{m}}$

Term C $\dfrac{\partial h_o}{\partial \dot{m}} = -\dfrac{W}{\dot{m}^2}$

$$x_o = g(h_o, P_o) \tag{A.25}$$

Finally

$$\delta x_o = \left\{ \left(\frac{\partial g}{\partial h_o} \delta h_o \right)^2 + \left(\frac{\partial g}{\partial P_o} \delta P_o \right)^2 \right\}^{1/2} \qquad \text{A.26}$$

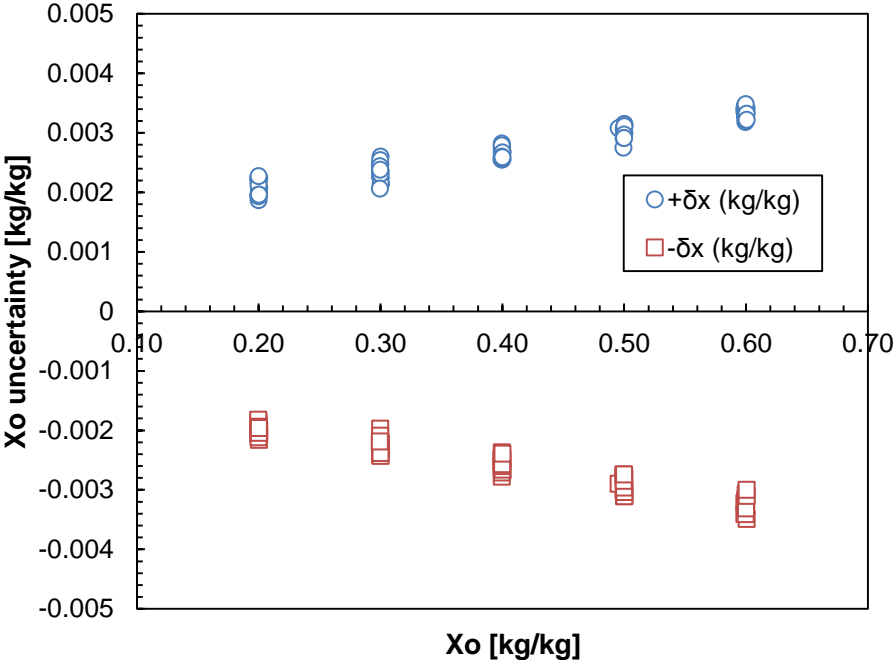Figure A.5 show the results of hybrid cycle performance map data.

Figure A.5 x_o uncertainty results of hybrid cycle performance map data

A.9.2 Heat transfer rate of condenser (Q$_{cond}$)

$$Q_{cond} = \rho_w \dot{V}_w C_{p,w} \Delta T_w \qquad \text{A.27}$$

$$\delta Q_{cond} = \left\{ \begin{array}{l} \underbrace{\left(\dfrac{\partial Q_{cond}}{\partial \rho_w} \delta \rho_w \right)^2}_{A} \quad + \underbrace{\left(\dfrac{\partial Q_{cond}}{\partial \dot{V}_w} \delta \dot{V}_w \right)^2}_{B} \quad + \underbrace{\left(\dfrac{\partial Q_{cond}}{\partial \rho_w} \delta \rho_w \right)^2}_{C} \\ + \underbrace{\left(\dfrac{\partial Q_{cond}}{\partial C_{p,w}} \delta C_{p,w} \right)^2}_{D} \quad + \underbrace{\left(\dfrac{\partial Q_{cond}}{\partial \Delta T_w} \delta \Delta T_w \right)^2}_{E} \end{array} \right\}^{1/2} \qquad \text{A.28}$$

Term A $\qquad \dfrac{\partial Q_{cond}}{\partial \rho_w} = \dot{V}_w C_{p,w} \Delta T_w$ $\qquad\qquad$ Term B $\qquad \dfrac{\partial Q_{cond}}{\partial \dot{V}_w} = \rho_w C_{p,w} \Delta T_w$

Term C $\qquad \dfrac{\partial Q_{cond}}{\partial \rho_w} = \rho_w \dot{V}_w \Delta T_w$ $\qquad\qquad$ Term D $\qquad \dfrac{\partial Q_{cond}}{\partial C_{p,w}} = \rho_w \dot{V}_w \Delta T_w$

Term E $\qquad \dfrac{\partial Q_{cond}}{\partial \Delta T_w} = \rho_w \dot{V}_w C_{p,w}$

And

$$\Delta T_w = T_{w,out} - T_{w,in} \qquad \text{A.29}$$

Thus

$$\delta \Delta T_w = \left\{ \left(\delta T_{w,out} \right)^2 + \left(\delta T_{w,out} \right)^2 \right\}^{1/2} \qquad \text{A.30}$$

A.9.3 Co-efficiency of Performance (COP)

$$COP = \frac{Q_{input}}{W_{input}} \qquad \text{A.31}$$

where

$$Q_{input} = W_{MME1} + W_{MME1} + W_{PH} \qquad \text{A.32}$$

$$\delta Q_{input} = \{\delta W_{MME1}^2 + \delta W_{MME2}^2 + \delta W_{PH}^2\}^{1/2} \qquad \text{A.33}$$

For each cycle W_{input} is different, taken liquid pumping cycle for example:

$$W_{input} = W_{LPC} + W_{SMV} \qquad \text{A.34}$$

$$\delta W_{input} = \{\delta W_{LPC}^2 + \delta W_{SMV}^2\}^{1/2} \qquad \text{A.35}$$

Finally

$$\delta COP = \left\{ \underbrace{\left(\frac{\partial COP}{\partial Q_{input}}\delta Q_{input}\right)^2}_{A} + \underbrace{\left(\frac{\partial COP}{\partial W_{input}}\delta W_{input}\right)^2}_{B} \right\}^{1/2} \qquad \text{A.36}$$

Term A $\qquad \dfrac{\partial COP}{\partial Q_{input}} = \dfrac{1}{W_{input}}$ $\qquad\qquad$ Term B $\qquad \dfrac{\partial COP}{\partial W_{input}} = -\dfrac{Q_{input}}{W_{input}^2}$

A.9.3 Heat recovery efficiency (η_hr)

$$\eta_{hr} = \frac{Q_{cond}}{Q_{input} + W_{input}} \qquad \text{A.37}$$

$$\delta\eta_{hr} = \left\{ \underbrace{\left(\frac{\partial\eta_{hr}}{\partial Q_{cond}} \delta Q_{cond}\right)^2}_{A} + \underbrace{\left(\frac{\partial\eta_{hr}}{\partial Q_{input}} \delta Q_{input}\right)^2}_{B} + \underbrace{\left(\frac{\partial\eta_{hr}}{\partial Q_{input}} \delta W_{input}\right)^2}_{C} \right\}^{1/2} \qquad \text{A.38}$$

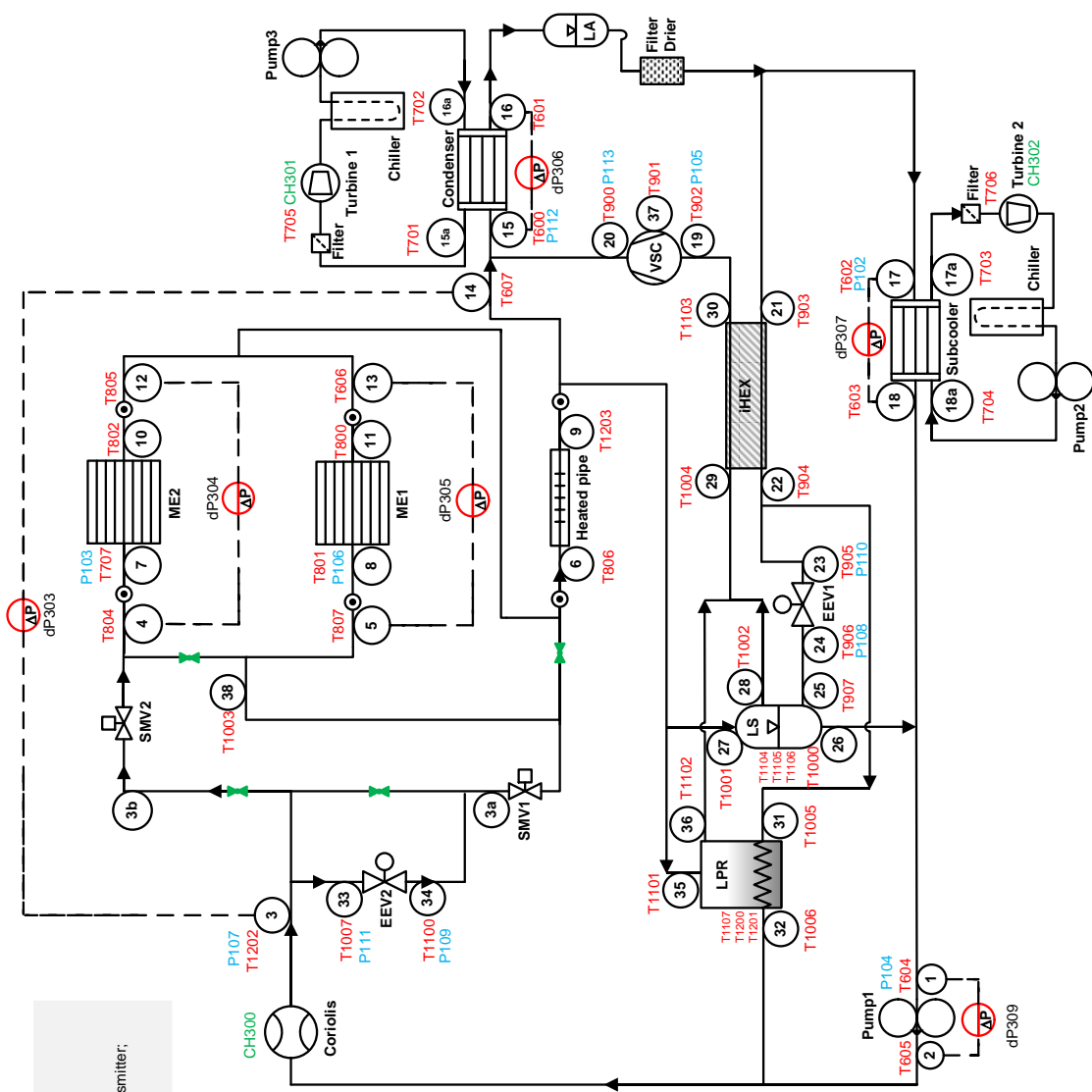Term A $\quad \dfrac{\partial\eta_{hr}}{\partial Q_{cond}} = \dfrac{1}{Q_{input} + W_{input}}$ 　　　　Term B $\quad \dfrac{\partial\eta_{hr}}{\partial Q_{input}} = -\dfrac{Q_{cond}}{\left(Q_{input} + W_{input}\right)^2}$

Term C $\quad \dfrac{\partial\eta_{hr}}{\partial W_{input}} = -\dfrac{Q_{cond}}{\left(Q_{input} + W_{input}\right)^2}$

δQ_{cond}, δQ_{input} and δW_{input} can be obtained by Equations A.28, A.33 and A.35, respectively.

B. Detailed facility diagram

C. Exergertic balance analysis for the major components

In this appendix the theoretical exergy balance analyses of the major components are presented.

C.1 Compressor

Figure C.1 shows the control volume considered for the exergy analysis on the VSC. The irreversibilities and exergetic efficiency were calculated based on a real case.
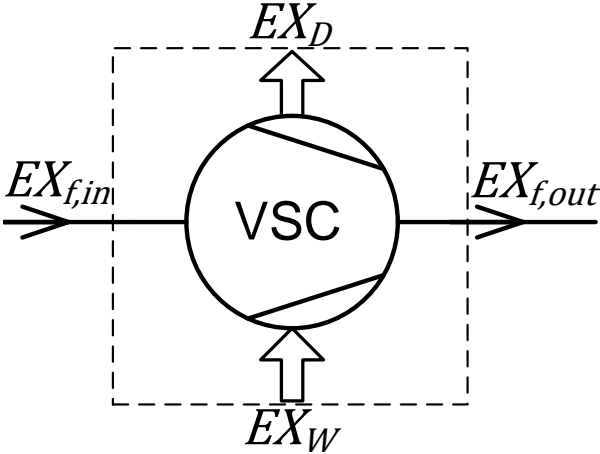

Figure C.1 Control volume for exergy balance analysis of VSC

Equations C.1 and C.2 show the formulations respectively.

$$0 = EX_W + EX_{f,in} - EX_{f,out} - EX_D \qquad \text{C.1}$$

$$\eta_{EX,VSC} = \frac{EX_{f,out} - EX_{f,in}}{EX_W} \qquad \text{C.2}$$

where

EX_w is the exergy supplied, which is the input power of the compressor [W];

$EX_{f,in}$ and $EX_{f,out}$ are the inlet and outlet flow exergies of the compressor, respectively [W];

EX_D is the exergy destroyed or irreversibility of the compressor [W].

C.2   Liquid pump

Figure C.2 shows the control volume for exergy analysis on LPC assuming isentropic pumping, based on the exergy balance the irreversibility can be calculated by Equation C.3. Equations C.3 and C.4 represent the exergy balance and the exergetic efficiency, respectively. And the same assumption as for the compressor was used, i.e. isentropic pumping.
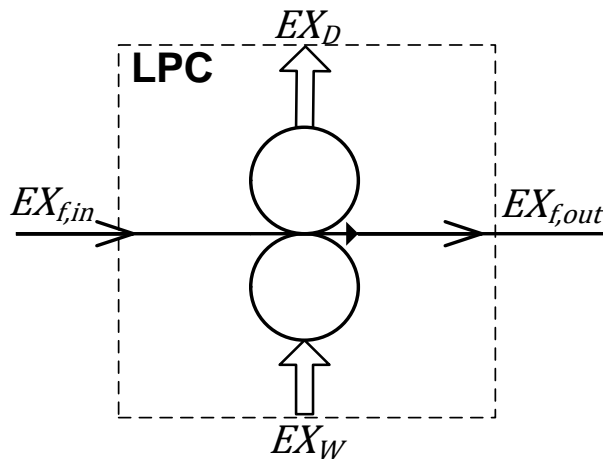
Figure C.2 Control volume for exergy balance analysis of LPC

$$0 = EX_W + EX_{f,in} - EX_{f,out} - EX_D \tag{C.3}$$

$$\eta_{EX,LPC} = \frac{EX_{f,out} - EX_{f,in}}{EX_W} \tag{C.4}$$

where

EX_W is the exergy supplied which is the electrical consumption of LPC [W];

$EX_{f,in}$ and $EX_{f,out}$ are the inlet and outlet flow exergies of LPC, respectively [W];

EX_D is the exergy destroyed or irreversibility of LPC [W].

C.3 Condenser

Figure C.3 shows the control volume for exergy analysis in the condenser. Equations C.5 and C.6 show the irreversibility and exergetic efficiency.

Figure C.3 Control volume for exergy balance analysis of condenser

$$0 = EX_{f,in,ref} + EX_{f,in,w} - EX_{f,out,ref} - EX_{f,out,w} - EX_D \tag{C.5}$$

where

$EX_{f,in,ref}$ is the flow exergy at the inlet of refrigerant side[W];

$EX_{f,in,w}$ is the flow exergy at the inlet of water side[W];

$EX_{f,out,ref}$ is the flow exergy at the outlet of refrigerant side[W];

$EX_{f,in,w}$ is the flow exergy at the outlet of water side[W];

EX_D is the exergy destroyed or irreversibility of the condenser [W].

$$\eta_{EX,LPC} = \frac{EX_{f,out,w} - EX_{f,in,w}}{EX_{f,in,ref} - EX_{f,out,ref}}$$
<div align="right">C.6</div>

It is highlighted that from a system point of view the term $\{EX_{f,out,w} - EX_{f,in,w}\}$ is also the exergy recovered from the whole system.

C.4   SMV or EEV

Figure C.4 shows the control volume for exergy analysis of the EEV and the SMV assuming adiabatic flow condition. Equations C.7 and C.6 show the irreversibility.

Figure C.4 Control volume for exergy balance analysis of EEV and SMV

$$0 = EX_W + EX_{f,in} - EX_{f,out} - EX_D$$
<div align="right">C.7</div>

where

EX_w is the exergy supplied, which is the electrical consumption for SMV and EEV [W],

$EX_{f,in}$ and $EX_{f,out}$ are the inlet and outlet flow exergies for SMV and EEV, respectively [W],

EX_D is the exergy destroyed or irreversibility of SMV and EEV[W].

C.5 MME

Figure C.5 shows the control volume for the exergy analysis on the MME, and based on the exergy balance, the irreversibility can be calculated considering Equations C.8 and C.9, and the exergetic efficiency is expressed by Equation C.11.
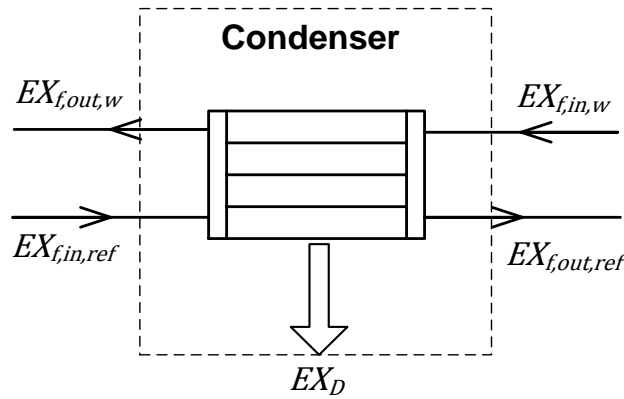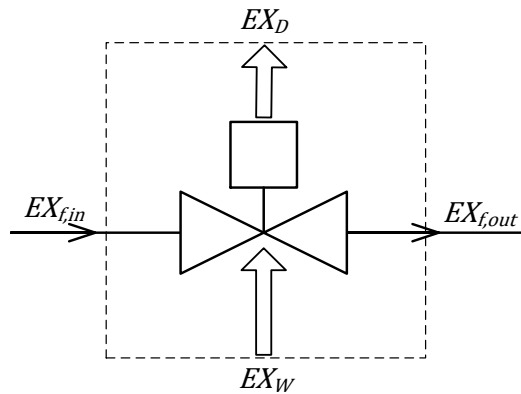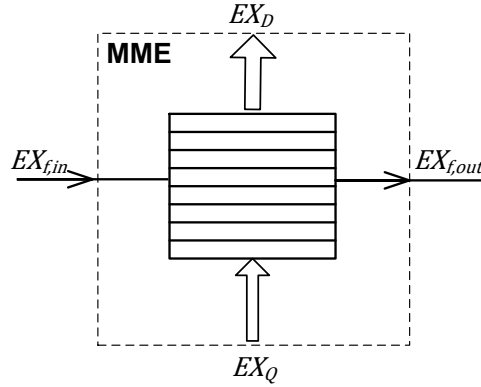

Figure C.5 Control volume for exergy balance analysis of MME

$$0 = EX_Q + EX_{f,in} - EX_{f,out} - EX_D \qquad \text{C.8}$$

$$EX_Q = Q_{pseudochip}\left(1 - \frac{T_0}{T_{avg,pseudochip}}\right) \qquad \text{C.9}$$

$$\eta_{EX,MME} = \frac{EX_{f,out} - EX_{f,in}}{EX_Q} \qquad \text{C.10}$$

where

EX_Q is the exergy supplied by the pseudo-chip, which can be calculated by Equation C.9 [W];

$EX_{f,in}$ and $EX_{f,out}$ are the inlet and outlet flow exergies of MME [W];

EX_D is the exergy destroyed or irreversibility of MME[W];

$Q_{pseudochip}$ is the heat generated by the pseudo-chip which equals to its electrical input power [W];

T_0 is dead state temperature in K;

$T_{avg,pseudochip}$ is the average temperature of the pseudo-chip in K.

It is important to mention that the exergy balance formulation of the post heater was the same as the MME.

C.6   Cooling cycle

Finally, for each cooling cycle the exergetic efficiency can be defined by Equation C.11 and C.12, respectively.

$$\eta_{ex} = \frac{EX_{recovered}}{\sum EX_{in}} \qquad \text{C.11}$$

$$EX_{recovered} = EX_{f,out,w} - EX_{f,in,w} \qquad \text{C.12}$$

where

$EX_{recovered}$ is the exergy recovered at the condenser [W];

$\sum EX_{in}$ is the overall sum of input exergy, including exergies supplied by the drivers, actuators MMEs and poster heater[W];

$EX_{f,out,w}$ and $EX_{f,in,w}$ are the inlet and outlet flow of exergy in the water side of the condenser [W]

D. Comparison of x_o control strategies applied on the liquid pumping cycle

The comparison of 2 different control strategies for the outlet vapor quality x_o was evaluated under non-uniform heat load tests. In summary, the x_o was controller by either LPS_C or LPS_C and A_{SMV}. Figure D.1 and Figure D.2 show the steps in heat load and the behavior of x_o. It can be seen that x_o was controlled efficiently and effectively for both control strategies.
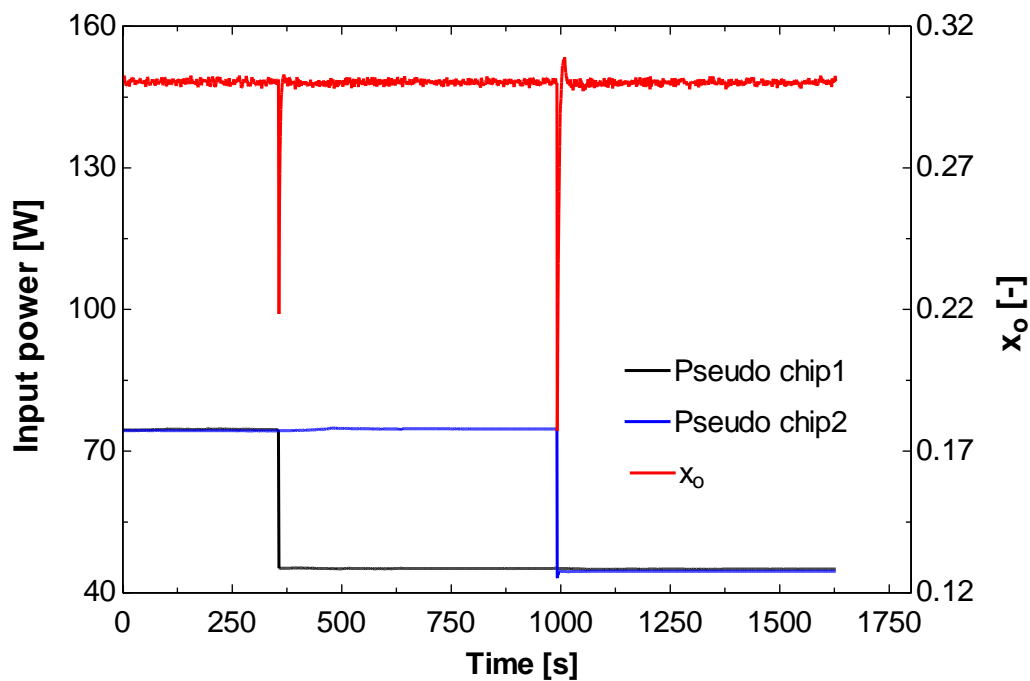
Figure D.1 Non-uniform heat load test under x_o controlled by LPSc
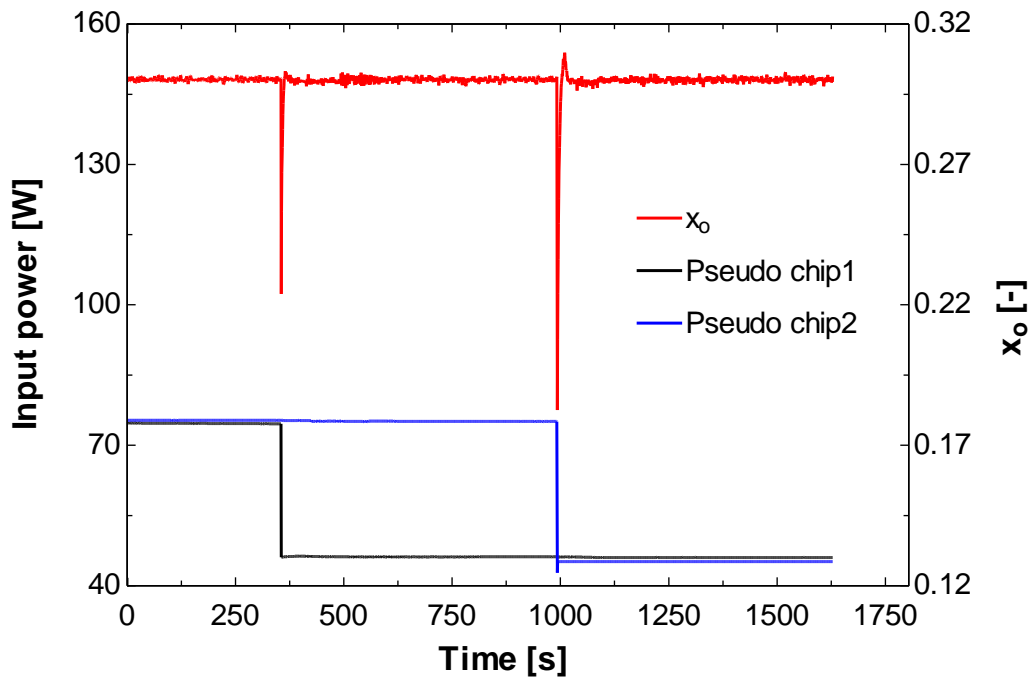
Figure D.2 Non-uniform heat load test under x_o controlled by A_{SMV} and LPSc

Figure D.3 to Figure D.5 show the actuators' response for each strategy considered. It can be seen that the overshoot in x_o is higher when considering only LPC as the actuator (viz. Figure D.3), which means that the SMV and LPC actuating together can potentially control better the x_o under situations of external disturbances (heat load disturbance).
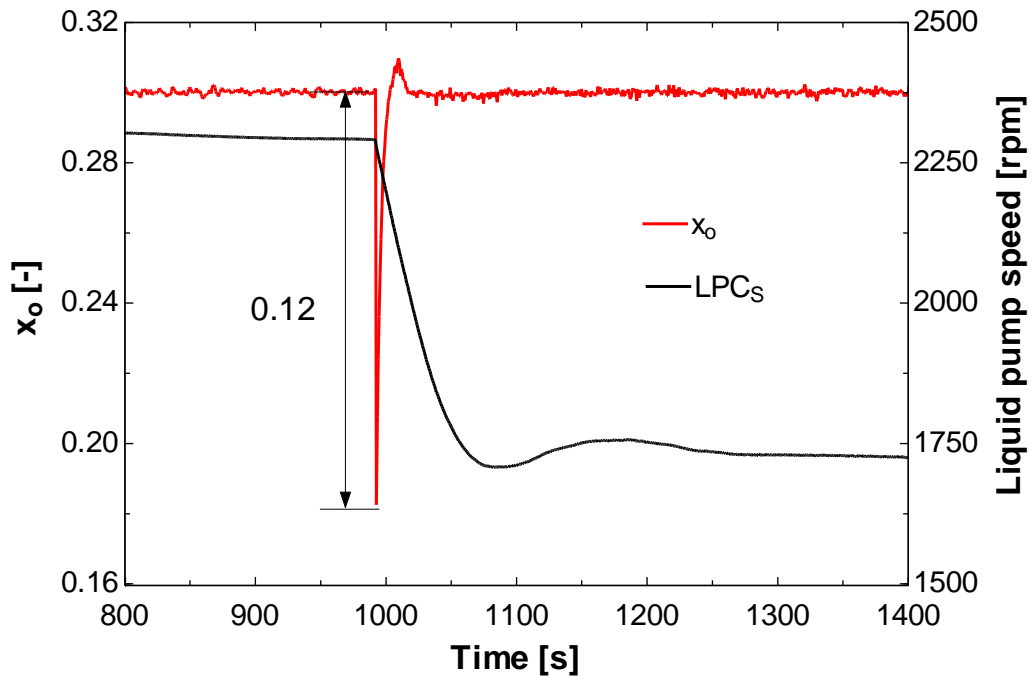
Figure D.3 LPC response under x_o controlled by LPC
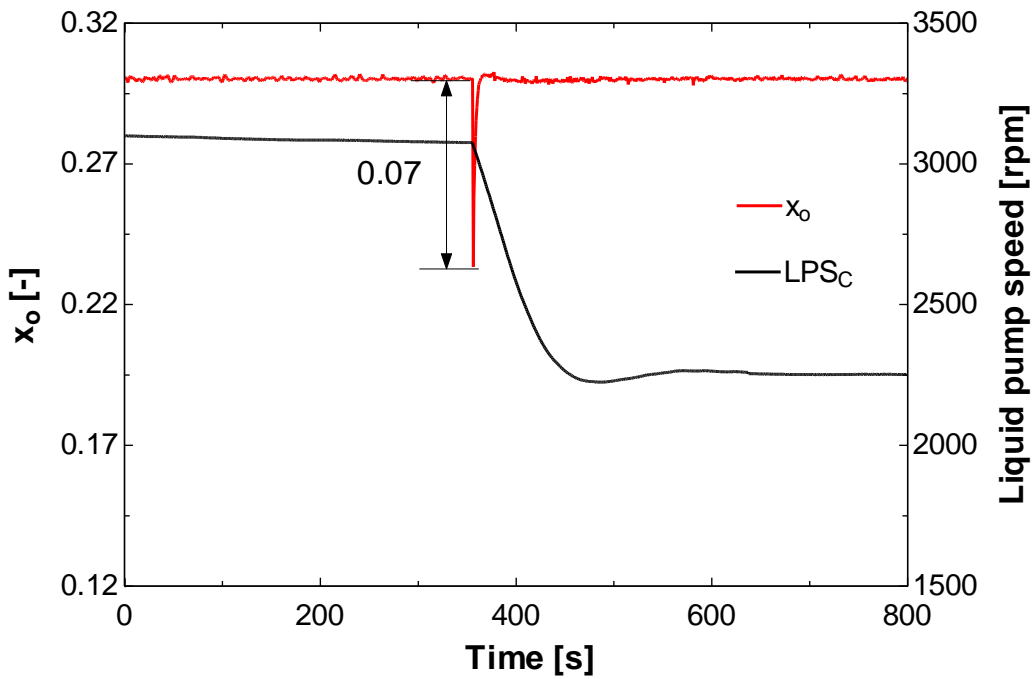
Figure D.4 LPC response under x_o controlled by A_{SMV} and LPSc
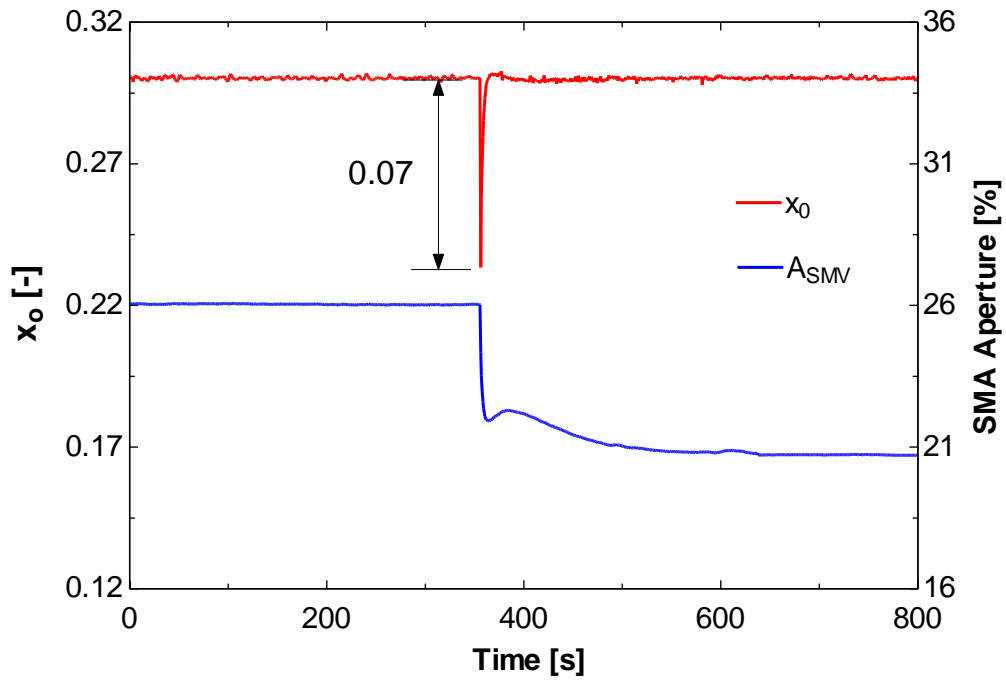
Figure D.5 SMV response under x_o controlled by A_{SMV} and LPSc

It is concluded that all 3 control strategies for x_o evaluated in the LP cycle in the present study, i.e. using as actuator either only SMV (Section 4.3), or SMV and LPC, or only LPC, have been shown to be viable and reliable (effective and efficient). The eventual decision of which control strategy to use in a real application would be associated with the design of the system and the type of data center (heat load, number of racks, etc.).

Bibliography

Agostini, B., M. Fabbri, J. Park, L. Wojtan and J. R. Thome (2007). "State-of-the-art of High Heat Flux Cooling Technologies." Heat Transfer Engineering **28**: 258-281.

Agostini, B., M. Fabbri, J. E. Park, L. Wojtan, J. R. Thome and B. Michel (2007). "State-of-the-art of High Heat Flux Cooling Technologies." Heat Transfer Engineering **28**: 258-281.

Agostini, B., R. Revellin, J. R. Thome, M. Fabbri, B. Michel, D. Calmi and U. Kloter (2008). "High Heat Flux Flow Boiling in Silicon Multi-Microchannels: Part III. Saturated Critical Heat Flux of R236fa and Two-Phase Pressure Drops." Int. J. Heat Mass Transfer.

Agostini, B. and J. R. Thome (2005). Comparison of an Extended Database for Flow Boiling Heat Transfer Coefficient in Multi-Microchannels Elements with the Three-Zone Model. ECI Heat Transfer and Fluid Flow in Microscale, Castelvecchio Pascoli, Italy.

ASME (1998). Supplement to Performance Test Coded, Instruments and Apparatuss,Test Uncertainty. New York, ASME. **PTC-19.1**.

Bar-Cohen, A., A. Kraus and S. Davidson (1983). "Thermal Frontiers in the Design and Packaging of Microelectronic Equipment." Mechanical Engineering **105**(6): 53-59.

BARNET_INSTRUMENTS_LIMITED (1980). Combined High & Low Pressure Dead Weight Tester Manual.

Bateson, R. (2002). Introduction to Control System Technology, Pearson Education, Inc.

Borkar, S., T. Karnik, S. Narendra, J. Tschanz, A. Keshavarzi and V. De (2003). <u>Parameter Variations and Impact on Circuits and Microarchitecture</u>. DAC'03 40th Annual Design Automation Conference.

Bowers, M. B. and I. Mudawar (1994). "High flux boiling in low flow rate, low pressure drop mini-channel and micro-channel heat sinks." <u>Int. J. Heat Mass Transfer</u> **37**: 321-332.

Brunschwiler, T., G. I. Meijer, S. Paredes, W. Escher and B. Michel (2010). <u>Direct Wast Heat Utilization from Liquid-Cooled Supercomputers</u>. 14th Int. Heat Transfer Conference, Aug. 8-13, Washington, DC, USA.

Brunschwiler, T., B. Smith, E. Ruetsche and B. Michel (2009). "Toward zero-emission data centers through direct reuse of thermal energy." <u>IBM Journal of Research and Development</u> **53**(3).

Costa-Patry, E. (2011). <u>Cooling High Heat Flux Micro-Electronic Systems using Refrigerants in High Aspect Ratio Multi-Microchannel Evaporators</u>. PhD, ÉCOLE POLYTECHNIQUE FÉDÉRALE DE LAUSANNE.

Costa-Patry, E., J. A. Olivier, B. Michel and J. R. Thome (2011). "Two-phase flow of refrigerants in 85 μ m-wide multi-microchannels: Part II – Heat transfer with 35 local heaters." <u>International Journal of Heat and Fluid Flow</u> **32**(2): 464-476.

Costa-Patry, E., J. A. Olivier, B. A. Nichita, B. Michel and J. R. Thome (2011). "Two-phase flow of refrigerants in 85 μ m-wide multi-microchannels: Part I – Pressure drop." <u>International Journal of Heat and Fluid Flow</u> **32**(2): 451-463.

Costa-Patry, E., J. A. Olivier, S. Paredes and J. R. Thome (2010). <u>Hot-Spot Self-Cooling Effects on Two-Phase Flow of R245fa in 85μm-wide multi-microchannels</u>. 16th International Workshop on Thermal Investigations of ICs and Systems, Spain.

Costa-Patry, E., J. A. Olivier and J. R. Thome (2010). Hot-spot effects on two-phase flow of R245fa in 85 μ m-wide multi-microchannels. <u>16th International Workshop on Thermal Investigations of IC's and Systems</u>. Barcelona, Spain.

Costa-Patry, E., N. S., J. A. Olivier and J. R. Thome (2012). "On-Chip Two-phase Cooling with Refrigerant 85 μm-wide Multi-Microchannels Evaporator Under Hot-Spot Conditions." <u>IEEE TRANSACTION ON COMPONENTS, PACKAGING AND MANUFACTURING TECHNOLOGY</u> **2**(2): 10.

Danfoss. (2012). "Heat Exchanger." from <u>http://www.danfoss.com/north_america/businessareas/refrigeration+and+air+conditioning/products/group/ra/line-components/line-components-commercial-refrigeration/he-heat-exchangers/f5fc718c-07b5-4bac-aa89-aa2b1a4087e8.html</u>.

DEUTSCHES_INSTITUT_FUR_NORMUNG (2001). Electrical laboratory devices - Laboratory circulators and baths - Part 2: Determination of ratings of heating and refrigerated circulators, Deutsches Institut fur Normung. **DIN 12876**.

DEUTSCHES_INSTITUT_FUR_NORMUNG (2011). Testing of mineral oils and related materials - Determination of density, Deutsches Institut fur Normung. **DIN 51757**.

Ganapati, P. (2009). "Water-Cooled Supercomputer Doubles as Dorm Space Heater." from <u>http://www.wired.com/gadgetlab/2009/06/ibm-supercomputer/</u>

Ganapati, P. (2009) "Water-Cooled Supercomputer Doubles as Dorm Space Heater, <u>http://www.wired.com/gadgetlab/2009/06/ibm-supercomputer/.</u>"

Gonçalves, J. M., C. Melo, C. J. L. Hermes and J. R. Barbosa (2011). "Experimental Mapping of the Thermodynamic Losses in Vapor Compression Refrigeration Systems." <u>Journal of the Brazilian Society of Mechanical Sciences and Engineering</u> **33**(2): 159-165.

Gosney, W. B., Ed. (1982). <u>Principles of Refrigeration</u>, Cambridge University Press.

Hannemann, R., J. Marsala and M. Pitasi (2004). <u>Pumped Liquid Multiphase Cooling</u>. IMECE - International Mechanical Engineering Congress and Exposition, Anaheim, CA, USA, paper 60669.

Hermes, C. J. L., C. Melo, F. T. Knabben and J. M. Gonçalves (2009). "Prediction of the Energy Consumption of Household Refrigerators and Freezers via Steady-State Simulation." International Journal of Applied Energy **86**: 1311-1319.

Herzog, S., D. Placek, R. Simko and C. Neveu (2002). "Predicting the Pump Efficiency of Hydraulic Fluids to Maximize System Performance." SAE **1**(1430): 7.

Heydari, A. (2002). Miniature Vapor Compression Refrigeration Systems for Active Cooling of High Performance Computers. 8th Intersoc. Conf. Thermal Thermomech. Phenom. Electron. Syst. (I-THERM).

IBM. (2011). "IBM BladeCenter QS22: Overview." Retrieved February 18, 2011, from www-03.ibm.com/systems/bladecenter/hardware/servers/qs22/.

Karajgikar, S., D. Agonafer, K. Ghose, B. Sammakia, C. Amon and G. Refai-Ahmed (2010). "Multi-Objective Optimization to Improve Both Thermal and Device Performance of a Nonuniformly Powered Micro-Architecture." Journal of Electronic Packaging **132**: 81-87.

Karimi, A., M. Kunze and R. Longchamp (2007). "Robust Controller Design by Linear Programming with Application to a Double-Axis Positioning System." Control Engineering Practice **15**(2): 197-208.

Koomy, J. G. (2007). Estimating Regional Power Consumption by Servers: A Technical Note. Oakland, CA, Lawrence Berkeley National Laboratory.

Kunze, M., A. Karimi and R. Longchamp (2007). Gain-Scheduling Controller Design by Linear Programming. European Control Conference, Kos, Greece.

Lazarek, G. M. and S. H. Black (1982). "Evaporating Heat Transfer, Pressure Drop and Critical Heat Flux in a Small Vertical Tube with R-113." International Journal of Heat and Mass Transfer **25**(7): 945-960.

Lemmon, E. W., Huber, M.L., McLinden, M.O. (2010). NIST REFPROP. Gaithersburg, National Institute of Standards and Technology.

Leonard, P. L. and A. L. Phillips (2005). The Thermal Bus Opportunity – A Quantum Leap in Data Center Cooling Potential ASHRAE Transactions, Denver, CO.

Madhour, Y., J. A. Olivier, E. Costa-Patry, S. Paredes, B. Michel and J. R. Thome (2011). "Flow Boiling of R134a in a Multi-Microchannel Heat Sink with Hotspot Heaters for Energy-Efficient Microelectronic CPU Cooling Applications." IEEE Transactions on Components, Packaging and Manufacturing Technology **1**(6): 873-883.

Marcinichen J.B., Olivier J. and Thome J. (2012). "On-chip two-phase cooling of datacenters: Cooling system and energy recovery evaluation." Applied Thermal Engineering **xxx**(xxx): 16.

Marcinichen, J. B. and J. R. Thome (2010). Refrigerated Cooling of Microprocessors with Micro-Evaporation New Novel Two-Phase Cooling Cycles: A Green Steady-State Simulation Code. 13th Brazilian Congress of Thermal Sciences and Engineering - Encit 2010, Uberlândia, MG, Brazil.

Marcinichen, J. B., J. R. Thome and B. Michel (2010). "Cooling of Microprocessors with Micro-Evaporation: A Novel Two-Phase Cooling Cycle." International Journal of Refrigeration **33**(7): 1264-1276.

Mauro, A. W., J. R. Thome, D. Toto and G. P. Vanoli (2010). "Saturated Critical Heat Flux in a Multi-Microchannel Heat Sink Fed by a Split Flow System." Experimental Thermal and Fluid Science **34**: 81-92.

Meijer, G. I., T. Brunschwiler and B. Michel (2009). Using Waste Heat from Datacenters to Minimize Carbon Dioxide Emissions. ERCIM News. **79:** 23-24.

Mongia, R., K. Masahiro, E. DiStefano, J. Barry, W. Chen, M. Izenson, F. Possamai, A. Zimmermann and M. Mochizuki (2006). Small Scale Refrigeration System for Electronics Cooling within a Notebook Computer. ITHERM 2006, San Diego, CA.

Moran, M. J., I. Howard and N. Shapiro, Eds. (2010). Fundamentals of Engineering Thermodynamics, John Wiley & Sons.

Ohadi, M. M., S. V. Dessiatoun, K. Choo and M. Pecht (2012). A Comparison Analysis of Air, Liquid, and Two-Phase Cooling of Data Centers. 28th IEEE SEMI-THERM Symposium, IEEE: 58-63.

Olivier, J. A., J. B. Marcinichen, A. Bruch and J. R. Thome (2011). "Green Cooling of High Performance Micro Processors: Parametric Study between Flow Boiling and Water Cooling." International Journal of Thermal Sciences and Engineering Application 3: 1-12.

Olivier, J. A. and J. R. Thome (2010). Two-Phase Cooling of Electronics with Multi-Microchannel Evaporators. NATO: AVT-178 Specialists' Meeting on System Level Thermal Management for Enhanced Platform Efficiency, Bucarest, Romania.

Ong, C. L. (2010). Macro-to-Microchannel Transition in Two-phase flow and Evaporation. PhD, École Polytechnique Fédérale de Lausanne.

Ong, C. L. and J. R. Thome (2011). "Macro-to-microchannel transition in two-phase flow: Part 2 – Flow boiling heat transfer and critical heat flux." Experimental Thermal and Fluid Science: doi:10.1016/j.expthermflusci.2010.1012.1003.

Park, J. (2008). Critical Heat Flux in Multi-Microchannel Copper Elements with Low Pressure Refrigerants. PhD, Swiss Federal Institute of Technology.

Park, J. E. (2008). Critical Heat Flux in Multi-Microchannel Copper Elements with Low Pressure Refrigerants. Ph.D. thesis, École Polytechnique Fédérale de Lausanne.

Qu, W. and I. Mudawar (2004). "Measurement and correlation of critical heat flux in two-phase micro-channel heat sink." Int. J. Heat Mass Transfer 47: 2045-2059.

Revellin, R. and J. R. Thome (2008). "An analytical model for the prediction of the critical heat flux in heated microchannels." Int. J. Heat Mass Transfer 51: 1216-1225.

Rosen, M. A., I. Dincer and M. Kanoglu (2008). "Role of Exergy in Increasing Efficiency and Sustainability and Reducing Environmental Impact." Energy Policy 36: 128-137.

Saini, M. and R. L. Webb (2003). "Heat Rejection Limits of Air Cooled Plane Fin Heat Sinks for Computer Cooling." IEEE Transactions on Components and Packaging Technologies **26**(1): 71-79.

Samadiani, E., S. Joshi and F. Mistree (2008). "The Thermal Design of a Next Generation Data Center: A Conceptual Exposition." Journal of Electronic Packing **130**: 1-8.

Thome, J. R. and A. Bruch (2008). Refrigerated Cooling of Microprocessors with Micro-Evaporation Heat Sinks: New Development and Energy Conservation Prospects for Green Datacenters. Institute of Refrigeration (IOR).

Tillner-Roth, R. and H. D. Baehr (1994). "An international standard formulation of the thermodynamic properties of 1,1,1,2-tetrafluoroethane (HFC-134a) for temperatures from 170 K to 455 K at pressures up to 70 MPa." J. Phys. Chem: 657-729.

Trutassanawin, S., E. A. Groll, S. V. Garimella and L. Cremaschi (2006). "Experimental Investigation of a Miniature-Scale Refrigeration System for Electronics Cooling." IEEE Transactions on Components and Packaging Technologies **29**(3): 678-687.

Wojtan, L., R. Revellin and J. R. Thome (2006). "Investigation of saturated critical heat flux in a single uniformly heated microchannel." Experimental Thermal and Fluid Science **30**: 765-774.

Zhang, T., Y. Peles, J. T. Wen, T. Tong, J. Chang, R. Prasher and M. K. Jensen (2010). "Analysis and active control of pressure-drop flow instabilities in boiling microchannel systems." International Journal of Heat and Mass Transfer.

Zhou, R., J. Catano, J. T. Wen, G. J. Michna, Y. Peles and M. K. Jensen (2010). "The Steady-State Modeling and Optimization of a Refrigeration System for High Heat Flux Removal." Applied Thermal Engineering.

Curriculum Vitae

PERSONAL DATA

Name	Duan Wu
Data of birth	2nd May, 1981
Nationality	China
Address	EPFL STI IGM LTCM
	ELH 010, Station 9
	CH-1015 Lausanne
Others	E-mail: duan.wu@hotmail.com
	Web profile: http://www.linkedin.com/in/wuduan

EDUCATION

2009.9-2012.12	Swiss Federal Institute of Technology (Lausanne), Ph.D., Mechanical Engineering
2003.9-2006.4	Shanghai Jiao Tong University, M.E., Refrigeration & Cryogenics Engineering
1999.9 - 2003.6	Shijiazhuang Railway Institute, B.E., Heating Ventilation & Air-Conditioning Engineering

EMPLOYMENT

2009.9 - 2012.12	Swiss Federal Institute of Technology (Lausanne), Laboratory of Heat and Mass Transfer, Doctoral Research Assistant
2006.4 - 2009.8	Emerson Electric Co., Advanced Power Electronics Technology Center (China), Heat Transfer & Packaging Engineer

PUBLICATIONS

- Duan Wu, Jackson Braz Marcinichen, John Thome, "Experimental Evaluation of Hybrid Two-Phase Multi-Microchannel Cooling and Heat Recovery System Driven by Liquid Pump and Vapor Compressor", International Journal of Refrigeration (Special issue), 2012

- Duan Wu, Jackson Braz Marcinichen, John Thome, "Experimental Evaluation of Hybrid Two-Phase multi-Microchannel Cooling and Heat Recovery System Driven by Liquid Pump and Vapor Compressor", ECI 8th International Conference on Boiling and Condensation Heat Transfer, Ecole Polytechnique Fédérale de Lausanne, 3-7 June 2012

- WU Duan, JIANG Cailing, QIAO Junsheng, CHEN Zhijiu, CHEN Jiangping, "Internal Flow Numerical Analysis on Micro-centrifugal Fan", Energy Technology, 2006 27 (3). (in Chinese)

- WU Duan, JIANG Cailing, QIAO Junsheng, CHEN Zhijiu, CHEN Jiangping, "Numerical flow characteristics analysis and research of micro-centrifugal fan", Fan and Blower Technology, 2006 27(4). (in Chinese)

- WU Duan, QIAO Junsheng, CHEN Zhijiu, CHEN Jiang-ping, "Research on Structure Optimization of Offset-Strip-Fin Oil Cooler", Energy Technology, 2006. (in Chinese)

- WU Duan, Yang Tao, CHEN Zhijiu, CHEN Jiangping, "Advances in Research of Lubricant Oil for Trans-critical CO_2 Mobile Air Conditioning System", Fluid Machinery, 2006 34 (11). (in Chinese)

- WU Duan, CHEN Zhijiu, CHEN Jiangping, "Optimization Study of Inlet Tank Structures of Air-air Charge-air Cooler", Shanghai Refrigeration Conference, 2005. (in Chinese)